Mechanical integrity and corrosion behavior of metal-composite hybrid joints produced with Friction Spot Joining

Vom Promotionsausschuss der
Technischen Universität Hamburg
zur Erlangung des akademischen Grades
Doktor-Ingenieurin (Dr.-Ing.)

genehmigte Dissertation

von
Natalia Manente Andre

aus
São Paulo

2020

1. Gutachter: Univ.-Prof. Dr.-Ing. Sergio de Traglia Amancio Filho

2. Gutachter: Prof. Dr.-Ing. habil. Bodo Fiedler

Vorsitzende: Prof. Dr.-Ing. Wolfgang Hintze

Mündliche Prüfung: 7. September 2020

Abstract

The combination of fiber-reinforced polymer composites and lightweight alloys has emerged as a lightweight solution for the transportation sector, mainly due to the optimal specific strength and stiffness associated with these materials. The possibility of joining metals and composites is an important topic for the cost-effectiveness of hybrid structures in mass production. Friction Spot Joining (FSpJ) is an alternative solid-state joining technique for hybrid structures. This technology has demonstrated its potential as a joining solution for metal-composite structures by attaining high mechanical and durability performances in previous investigations. Nevertheless, the industrial transferability of such new technology requires further assessment regarding the mechanical integrity and corrosion behavior of the joints.

Therefore, this thesis is dedicated to understand the damage evolution at the interface of AA2024-T3/CF-PPS friction spot joints. For this purpose, finite element modelling was applied and the bonding zones of the joints were discretized using the traction-separation law. It was demonstrated that the damage in friction spot joints initiates at the AZ (adhesion zone) and then propagates as a symmetric linear front from the edges towards the center of the joined area. Nevertheless, as the damage advances inside the PDZ (plastically deformed zone), its propagation became an asymmetrical linear front that evolves preferably from the free edge of the composite part due to the higher peeling stresses in this region (asymmetrical secondary bending of the structure took place due to differential stiffness of materials). Based on the findings of this study, modifications were proposed to the failure theory previously stated for friction spot joints.

In addition, the fatigue damage tolerance of the joints was evaluated under mixed-mode I/II loading. The AZ presented low crack growth resistance ($G_{I/II} = 0.85 \pm 0.01$ J m^{-2}), while the PDZ demonstrated to be the most damage tolerant zone of the joints ($G_{I/II\ max} = 274 \pm 1$ J m^{-2}). The fatigue crack growth of the friction spot joints was dictated by the bonding zones and occurred in three well-defined stages: initiation, linear region, and unstable crack growth. Steady crack growth rates were found for AZ (0.10 ± 0.03 mm/cycle) and PDZ (0.006 ± 0.001 mm/cycle). This shows that the main bonding zones of these joints have defined properties. Thereby, the mechanical behavior of the joints can be tailored by their zones. Moreover, the friction spot joints generally present inferior and more stable fatigue crack growth rates when compared to adhesive bonded joints.

The impact resistance of the joints was investigated using the drop weight test. Four levels of impact energy were tested: 2 J, 4 J, 6 J, and 8 J. The joints were aluminum-side and composite-side impacted to provide a preliminary design guideline regarding the impact damage tolerance of such hybrid joints. This study showed that a friction spot joint absorbs up to 103 kJ m^{-2} of the joined area, while the literature reports energy absorption up to 48 kJ m^{-2} for bonded joints. Shear after impact (ShAI) test was employed to evaluate the residual strength of the joints. The impact energy introduced from the aluminum-side was mostly absorbed into the global plastic deformation of the aluminum part, thereby promoting the detachment of the joint interface. Otherwise, the impact energy introduced from the composite-side was mostly absorbed into the creation/extension of internal damage through the plies of the composite. Thus, the impact energy was only partially transferred to the interface of the joint in case of composite-side impact. Consequently, these joints presented higher residual strength than the aluminum-side impacted joints.

Further, the corrosion behavior of the joints was investigated during six weeks of salt spray exposure. The process-related changes in the microstructure, precipitation state, and local mechanical performance of the aluminum part were investigated and correlated with the corrosion development on the top surface of the joints. Regarding the corrosion at the interface of the joints, four stages were identified and correlated with the global strength degradation of the joints: I – Water and NaCl migration and the consequent plasticization of the composite (-24% of ULSF); II – corrosion protection of the PDZ by the polymer layer in the AZ (-28% of ULSF); III – detachment of the polymer layer in the AZ and corrosion inside the PDZ (-44% of ULSF); and IV – generalized corrosion in the PDZ causing the final strength degradation of the joints.

Finally, as a first step for the upscaling of the FSpJ technology, a fuselage sub-component was constructed using FSpJ in combination with other friction-based technologies. A reduction of 20% in weight was reached in comparison with the full-metallic and bolted design, thereby successfully demonstrating the potential of FSpJ as a joining solution for hybrid aircraft structures in the future.

Zusammenfassung

Die Kombination von faserverstärkten Polymerverbundwerkstoffen und Leichtmetalllegierungen bietet sich für den Einsatz in Leichtbaustrukturen im Transportsektor an, hauptsächlich aufgrund der optimalen spezifischen Festigkeit und Steifigkeit dieser Materialienkombination. Die Möglichkeit, Metalle und Verbundwerkstoffe zu verbinden, ist ein wichtiger Aspekt für die Kosteneffektivität der Hybridstrukturen in der Massenproduktion. Friction Spot Joining (FSpJ) ist eine alternative Festphase-Verbindungstechnik, die ihr Potenzial als Verbindungslösung für Hybridstrukturen durch das Erzielen guter mechanischer Eigenschaften und langer Haltbarkeit in früheren Untersuchungen bewiesen hat. Die industrielle Hochskalierung dieser neuen Technologie erfordert jedoch weitere Untersuchungen hinsichtlich der mechanischen Integrität und des Korrosionsverhaltens der damit hergestellten Verbindungen.

Daher wurde diese Doktorarbeit dem Verständnis der Schadensentwicklung an der Grenzfläche von AA2024-T3/CF-PPS FSpJ-Verbindung gewidmet. Die Finite-Elemente-Methode wurde angewandt und die einzelnen Verbindungszonen wurden basierend auf einem Gesetz der Traktions-Separation diskretisiert. Es wurde beobachtet, dass der Riss in der AZ ausgelöst wird und sich als symmetrische lineare Front von den Rändern zum Zentrum der verbundenen Fläche ausbreitet. Da sich der Schaden innerhalb der PDZ ausbreitet, wird die Ausbreitung zu einer unsymmetrischen linearen Front, die sich aufgrund der höheren Schälbeanspruchung in diesem Bereich vorzugsweise von der freien Kante des CF-PPSs her entwickelte. Basierend auf den Ergebnissen dieser Studie wurden Modifikationen der herkömmlicherweise angenommenen Versagenstheorie für FSpJ vorgeschlagen.

Zusätzlich wurde die Ermüdung und Schadenstoleranz der Verbindungen unter einem gemischten I/II-Belastungsmodus bewertet. Die AZ zeigte eine geringe Risswachstumsresistenz ($G_{I/II}$ = 0,85 ± 0.01 J m^{-2}), während die PDZ die am schadenstoleranteste Zone der Verbindungen darstellt ($GI_{/II}$ = 274 ± 1 J m^{-2}). Das Ermüdungsrisswachstum der Verbindungen wird durch die Bindungszonen bestimmt und erfolgt in drei Stufen: Initiierung, linearer Bereich und instabiles Risswachstum. Eine stabile Risswachstumsrate wurde für AZ (0,10 ± 0,03 mm/Zyklus) und PDZ (0,006 ± 0,001 mm/Zyklus) gefunden. Dies zeigt, dass die Hauptverbindungszonen der FSpJ-Verbindungen definierte Eigenschaften haben, die das mechanische Verhalten der Verbindungen unter zyklischer Belastung bestimmen. Im Allgemeinen weisen die FSpJ-Verbindungen im Vergleich zu Klebeverbindungen eine geringere und stabilere Risswachstumsrate auf.

Die Schlagzähigkeit der Verbindungen wurde mit dem Fallgewichtsversuch untersucht. Vier Stufen der Aufprallenergie wurden getestet: 2 J, 4 J, 6 J und 8 J. Eine einzelne FSpJ-Verbindung absorbierte bis zu 103 kJ m^{-2}, während in der Literatur eine Energieabsorption von nur 48 kJ m^{-2} für Klebeverbindungen berichtet wurde. Die Restfestigkeit der Verbindungen nach dem Aufprall wurde durch Scherzugprüfungen bewertet. Die Verbindungen, die von der Aluminiumseite belastet wurden, absorbieren die Aufprallenergie in der globalen plastischen Verformung des Aluminiumteils, was die Ablösung der Grenzfläche verursacht. Die Aufprallenergie bei einer Belastung der Kompositseite wird größtenteils durch die Erzeugung und Ausbreitung von Beschädigungen in den Lagen des Verbundwerkstoffes absorbiert. Somit wird die Aufprallenergie im Falle eines Komposit-seitigen Aufpralls nur teilweise auf die Grenzfläche der Verbindungen übertragen. Dadurch wiesen diese Verbindungen nach dem Aufprall eine höhere Scherrestfestigkeit auf.

Zudem wurde das Korrosionsverhalten der hergestellten Verbindungen während einer sechs-wöchigen Belastung mit Salzspray untersucht. Vier Stufen wurden identifiziert und mit der globalen Festigkeitsabnahme der Verbindungen korreliert: I - Wasser- und NaCl-Migration und anschließende Plastifizierung des Verbundwerkstoffes (-24% ULSF), II - Korrosionsschutz der PDZ durch die Polymerschicht in der AZ (-28% der ULSF), III - Ablösung der Polymerschicht in der AZ und Korrosion in der PDZ (-44% der ULSF), IV - generalisierte Korrosion in der PDZ und damit Abbau der Restfestigkeit.

Zur Aufskalierung der FSpJ-Technologie wurde eine Flugzeugrumpf-Subkomponente mit FSpJ konstruiert. Im Vergleich zu Vollmetall- Nietkonstruktionen wurde eine Gewichtsreduktion von 20% erreicht, was die Einsatzbarkeit von FSpJ als Verbindungslösung für Flugzeughybridstrukturen erfolgreich demonstriert.

Symbols and Abbreviations

A	Crack area
a	Crack length
A_1, A_2, B and p	Constants of the sigmoidal model for crack growth
ANOVA	Analysis of variance
a_o	Initial crack
AR	As-received
AS	Aluminum-side
ATDCB	Asymmetric-tapered double cantilever beam
AZ	Adhesion zone
b	Width
BM	Base material
BVID	Barely visible impact damage
C	Compliance
CF	Carbon-fiber-reinforced
CFRP	Carbon-fiber-reinforced polymer
CLS	Crack lap shear
CS	Composite-side
CZM	Cohesive zone model
d	Displacement
d_s	Sleeve diameter
da/dN	Crack propagation rate
DCB	Double cantilever beam
DIC	Digital image correlation

e	Edge distance
E	Electrochemical potential
$\bar{E}$	Young's modulus
E_l	Young's modulus in plane stress state
E_a	Absorbed energy
$E_{a,max}$	Maximum energy absorption
EDS	Energy dispersive X-ray spectroscopy
E_i	Impact energy
$E_{i,el}$	Pure elastic limit of impact energy
ENF	End-notched flexure
EPM	Energy profile method
FEM	Finite element method
FML	Fiber metal laminates
FSpJ	Friction Spot Joining
G	Strain energy release rate (or fracture energy)
GBP	Guinier-Preston-Bagaryatsky
G_c	Critical strain energy release rate
GF	Glass-fiber-reinforced
GFRP	Glass-fiber-reinforced polymer
G_I	Strain energy release rate in pure mode I
$G_{I/II}$	Strain energy release rate in mixed-mode I/II
G_{II}	Strain energy release rate in pure mode II
h	Thickness
HAZ	Heat-affected zone

HZG	Helmholtz-Zentrum Geesthacht
I	Current
IW	Induction Welding
JF	Joining force
JT	Joining time
k	Shear correction factor
K	Stress intensity factor
K_c	Critical stress intensity factor
K_{nn}, K_{tt}, K_{ss}	Stiffness coefficients for normal, tangential and shear directions
L	Length
LW	Laser Welding
MMB	Mixed-mode bending
P	Force
PD	Plunge depth
PDZ	Plastically-deformed zone
PPS	Polyphenylene sulfide
R	Load ratio
R_a	Average surface roughness
RS	Rotational speed
RW	Resistance Welding
SAXS	Small angle X-ray scattering
SEM	Scanning electron microscopy
ShAI	Shear after impact
SLB	Single-leg bending

SST	Salt spray test
ST	Surface-treated
SZ	Stir zone
T_g	Glass transition temperature
T_m	Melting temperature
TMAZ	Thermomechanically affected zone
TZ	Transition zone
U	Stored elastic energy for crack propagation
ULSF	Ultimate lap shear force
UW	Ultrasonic Welding
W	External work
XPS	X-ray photoelectron spectroscopy
Y	Geometrical factor
δ_{nn}, δ_{tt}, δ_{ss}	Separations for normal, tangential, and shear directions
ν	Poisson's ratio
σ_r	Stress applied to the crack
μ	Shear modulus
2a	Crack length on an infinite plane with uniform stress distribution

Contents

Chapter 1. Introduction

Engineers and designers in the transportation sector face increasingly rigorous economic and environmental policies [1]. The reduction in fuel consumption and CO_2 emissions are the most demanded requirements. A promising solution to comply with these requirements is found in the concept of lightweight hybrid structures [1]. The combination of fiber-reinforced polymer composites and lightweight metallic alloys has emerged as a smart lightweight solution for the transportation sector, mainly due to the optimal specific strength and stiffness associated with these materials [2].

Therefore, the development of lightweight hybrid structures has recently taken the focus of the transportation sector. In the aircraft industry, for instance, the structure of the Boeing 787 is composed of over 50 wt% of advanced polymer composites, this saves 20% of the total aircraft weight compared to the conventional aluminum structure [3]. In the past 30 years, Airbus has also addressed the use of carbon-fiber-reinforced polymer composites (CFRP). Applications were developed for components, such as the wing movables and the vertical tailplane of the A310, the horizontal tailplane of the A320, the keel beam of the A340-600, the center wing box of the A380, the wing parts of the Falcon 10, the ATR 72, and the A400M [4]. Recently, the A350 XWB launch has set a new standard in its Airbus class by presenting 25% lower fuel consumption due to 53% composite use in its structure [4]. Embraer has also invested in the carbon fiber-reinforced polymers with the release of the military transport aircraft KC-390. The KC-390 presents lightweight ballistic protection solutions provided through the use of carbon fiber-reinforced polymers [5]. Additionally, in the automotive industry, a generation of fully electric and hybrid cars has been developed by BMW (e.g. i3 and i8). By replacing steel with carbon fiber-reinforced polymers, BMW engineers have considerably reduced the weight of the cars, while reductions of 50% in energy and 70% in water consumption have been accomplished during the manufacturing process [6].

Currently, mechanical fastening and adhesive bonding are the most applied techniques to join dissimilar materials [2,7]. Mechanical fastening allows the joining of dissimilar materials while retaining their specific properties [7]. In this case, the joining is performed without high thermal stresses, thereby preventing the thermal modification of the base materials properties. In the case of adhesive bonding, a larger surface is provided for load transmission in comparison with fasteners. Therefore, better homogeneity of the load distribution and good fatigue performance are generally achieved for those joints [8]. Despite the benefits, these techniques have intrinsic limitations [9]. Considering mechanical fastening, weight penalty and stress concentration due to through-holes in the structure are the primary drawbacks, whereas adhesive bonding often requires extensive surface preparation and long curing time for the adhesive [10]. Therefore, a number of joining technologies have been developed in the last decades to mitigate the limitations of these traditional joining methods [11–14].

The possibility of joining metals and polymeric composites is one, if not the major, important issue regarding the cost-effectiveness of hybrid structures in mass production industries, such as transportation [15]. Facing the high dissimilarity of physical properties between metals and polymeric composites, designing large and complex structures is not a simple task and requires advanced joining techniques. Resistance, induction, ultrasonic and laser welding have been put forward with their respective advantages and drawbacks [13,16]. The heat sources can be as diverse as electrical current, electromagnetic field, high-frequency vibration and radiation. In general, these joining techniques have presented well-established processes and high-quality joints [14,17,18]–[19]. However, disadvantages such as relatively long welding cycles (1–4 minutes), additional material consumption, equipment cost, and difficult automation motivate further scientific and engineering developments in the joining of metal–polymer structures [16].

Friction Spot Joining (FSpJ) is an alternative solid-state joining technique for hybrid structures developed at Helmholtz-Zentrum Geesthacht in Germany [20]. This friction-based technology avoids or reduces the polymer degradation due to the low heat input generated during the process. Therefore, the FSpJ process is a suitable joining solution for metal–polymer/composite structures rather than traditional fusion welding processes [21]. Among the advantages of the FSpJ process, it highlights the short joining cycles (0.5 s – 8 s) and the absence of/reduced damage to the fiber reinforcement of composites [21]. Several combinations of materials have been successfully joined using FSpJ, some examples are Goushegir *et al.* [22] with AA2024-T3/ with carbon fiber-reinforced polyphenylene sulfide (CF-PPS), André *et al.* [23] with AA2024-T3/PPS/CF-PPS, Esteves *et al.* [24] with AA6181-T4/CF-PPS, and Amancio *et al.* [21] with AZ31-O/GF- and CF-PPS in recent publications.

Goushegir *et al.* [25] recently investigated the formation and mechanical performance of AA2024-T3/CF-PPS friction spot joints. Shear strengths as high as 27 MPa and 43 MPa have been achieved using bare aluminum and alclad specimens, respectively. The authors demonstrated that the friction spot joints present static strength 50% higher than the state-of-the-art adhesive bonded joints, the main concurrent joining technology of FSpJ [25]. Additionally, the fatigue performance of AA2024-T3/CF-PPS friction spot joints was also assessed. The aircraft industry's requirement for qualifying new joining technologies at the coupon level claims a fatigue strength between 30% of the static strength of the joints at 10^5 cycles [26]. In this study, the friction spot joints presented a fatigue strength of 37% of ULSF at 10^5 cycles. Equivalent hybrid ultrasonic welds (AA5754/CF-PA66) have shown 32% of ULSF as the fatigue strength at 10^5 cycles [27].

The previous investigations on FSpJ demonstrated the potential of this technology as a joining solution for hybrid structures. Nevertheless, the increase of the technological readiness level of such new technology requires further assessment. The prediction of the damage tolerance of a structure is mandatory for the safety certification of aircraft and automotive structures. Therefore, the tolerance to fatigue and impact damage of friction

spot joints has become an essential topic to be investigated. Similarly, the assessment of the corrosion behavior of metal–composite joints is also highly important for the development of this joining method. The interest in these topics emerges not only for the industry and its requirements, but also for the research community to focus for the first time on the mechanisms of mechanical damage and corrosion development of hybrid joints produced by FSpJ. Finally, the construction of robust and safe structures demands advanced engineering and designing efforts [28,29]. Naturally, such requirements cannot be achieved merely through the coupon joints analysis [29]. The "Building Block" approach is a strategy normally adopted for the development of new structural components in the aerospace and automotive industry [28]. This upscaling strategy comprises the modeling and testing of coupons, elements, subcomponents, and components to integrate the scientific findings with the requirements and responsibilities of the industry [29].

Thus, the current doctoral work aims to fulfill the knowledge gaps related to the mechanical integrity and corrosion behavior of AA2024-T3/CF-PPS friction spot joints for future aircraft applications. The damage evolution at the interface of the joints was investigated along with the fatigue and impact damage tolerance. The corrosion behavior of the joints was also assessed and correlated with the precipitation state and the bonding zones of the joints. Finally, as a first step for the upscaling of this technology, a full-scale demonstrator containing, among others joining techniques, FSpJ joined parts was constructed. Therefore, this thesis is structured into the following chapters:

Chapter 1 comprises this introduction, where the context in which this Ph.D. work is inserted was presented.

Chapter 2 presents the motivation along with the scientific and technological objectives of this study.

Chapter 3 consists of the literature review of the topics covered in this Ph.D. thesis. This chapter starts with the introduction of the FSpJ technology. The FSpJ process, as well as the bonding mechanisms, the mechanical performance, and the failure behavior of the friction spot joints are described. Further, the fundamentals of materials mechanics are briefly summarized and discussed for overlap connections. In addition, the impact behavior of multi-material connections is concisely reviewed. This chapter follows with the outlines of the galvanic corrosion of metals and carbon fiber-reinforced polymers. Finally, an overview of the properties of the materials used in this work concludes the chapter.

Chapter 4 summarizes the development phases of this Ph.D. project.

Chapter 5 describes the materials used in this work, as well as the detailed methods applied to analyze the different aspects of the joints during the development of this thesis.

The results and their discussions were divided into five chapters. Chapter 6 is devoted to understand the damage evolution at the interface of the friction spot joints under shear stresses. For this purpose, finite element modeling (FEM) and experiments were integrated. Firstly, a finite element model to predict the static strength and damage evolution at the interface of the joints is presented and validated. The influence of the different bonding zones on the mechanical performance of the joints is also addressed using FEM. Further, the prediction of the damage evolution is coupled with loading–unloading hysteresis curves of the joints to clarify the damage micro-mechanisms in the bonding zones at different load levels. Finally, the chapter concludes with the proposal of an updated theory of failure for friction spot joints based on the new findings.

Chapter 7 presents applied fundamentals of linear elastic fracture mechanics to investigate the fracture energy and fatigue damage tolerance of single friction spot joints. The joints were subjected to mixed-mode I/II loading to simulate in-service loads. The crack was monitored throughout the static and fatigue life of the joints. The strain energy release rate at the crack tip was calculated using the linear beam theory, which incorporated transverse shear and elastic foundation effects. Thus, the mode-mixity of the fracture test was evaluated. Next, the typical R-curve for friction spot joints is presented for the first time in the literature. Additionally, the influence of the different bonding zones of the joint on the strain energy release rate and the fatigue crack growth was addressed. The chapter concludes with a preliminary model to predict the fatigue crack growth behavior of the friction spot joints.

In Chapter 8, the impact resistance of friction spot joints is investigated. Four levels of impact energy were tested: 2 J, 4 J, 6 J, and 8 J. The joints were aluminum-side and composite-side impacted to provide a preliminary design guideline regarding the impact damage tolerance of such hybrid joints. The absorbed energy and the development of the damage on the aluminum and composite surfaces were analyzed for the different impact energies under study. Laser scanning microscopy was used to monitor the damage evolution on the surfaces. Ultrasonic echo scanning was applied to evaluate the damage at the interface and inside the composite part of the joints. Finally, the transfer of the impact energy to the interface of the joint was assessed and correlated with the residual strength of the joints in accordance with the side of the joint under impact.

Chapter 9 is dedicated to the corrosion behavior of AA2024-T3/CF-PPS friction spot joints. The joints were exposed to salt spray from one up to six weeks. Firstly, the influence of the joining process on the microstructure and precipitation state of the aluminum alloy was assessed using optical microscopy and small angle X-ray scattering (SAXS). Thus, the corrosion evolution on the top surface of the joints was described in accordance with the microstructural zones formed due to the FSpJ process. Additionally, the corrosion at the interface of the joints was evaluated. Scanning electron microscopy (SEM) and energy dispersive spectroscopy (EDS) were used to identify the four stages of corrosion development at the interface of the joints. The role of each bonding zone of the joint was

elucidated within the corrosion degradation process of the interface. Finally, the global strength degradation of these joints was correlated with the corrosion damage in the bonding zones.

Chapter 10 presents the first results obtained in the upscaling of the FSpJ technology. Part of an aircraft fuselage was built using FSpJ as one of the joining methods, as a proof of concept for the use of FSpJ in aircraft structures. Metallic stringers, in an alternative design to promote weight reduction, were joined to a CFRP skin using FSpJ. In combination with other friction-based joining technologies, a hybrid fuselage was built. The weight reduction in relation to fully metallic and state-of-the-art bolted designs is presented.

In Chapter 11, the main findings of this study are summarized.

Finally, Chapter 12 presents recommendations for future work on the topics addressed in this doctoral thesis.

Chapter 2. Motivation and Objectives

The potential of FSpJ as a joining solution for hybrid structures is evident, as demonstrated in Chapter 1. Nevertheless, the knowledge gaps regarding the mechanical integrity and corrosion behavior of friction spot joints, also highlighted in Chapter 1, are of major importance for the production of safe structures joined by FSpJ in the future. Therefore, the damage evolution at the interface of the joints must be understood in a better way along with the fatigue and impact damage tolerance of these joints. Additionally, the galvanic coupling of metal alloys and CFRP is a well-known issue for hybrid structures and must also be addressed for friction spot joints. Furthermore, the construction of robust and safe structures demands advanced engineering and designing efforts in the upscaling of the FSpJ technology.

Thus, the objectives of this work are divided into two parts:

Scientific Objectives:

The scientific objectives include:

- Describe the damage evolution and its mechanisms through the different bonding zones of friction spot joints
- Evaluate the fracture energy and the fatigue damage tolerance of friction spot joints
- Evaluate the impact resistance and the capability of impact energy absorption of friction spot joints
- Understand the corrosion behavior and the related strength degradation of friction spot joints

Engineering Objective:

In the technological scope, the main objective is:

- Investigate the upscaling of the FSpJ technology for structural applications with the construction of a full-scale demonstrator in terms of design feasibility and weight reduction capabilities

Chapter 3. Literature Review

3.1 Friction Spot Joining (FSpJ) technology

Friction Spot Joining (FSpJ) is an alternative joining process for metal-polymer and metal-composite hybrid structures. This solid-state joining technology enables the connection between metallic and polymeric materials by causing limited or no damage to the polymeric part of the joint. Furthermore, FSpJ presents very short joining cycles; from 0.5 s to 8 s. Since its invention in 2011, this technology has received several prizes and therefore its potential has already been recognized in both scientific and industrial communities [30–34].

3.1.1 Principles of the process

FSpJ uses a three-piece non-consumable tool comprising a pin, a sleeve, and a clamping ring. The clamping ring is the stationary part of the tool; it is responsible for applying pressure between the parts and the backing bar during the joining process. The sleeve and the pin are the moving parts of the tool; they have axial and rotational movements independent of each other (Figure 3.1).

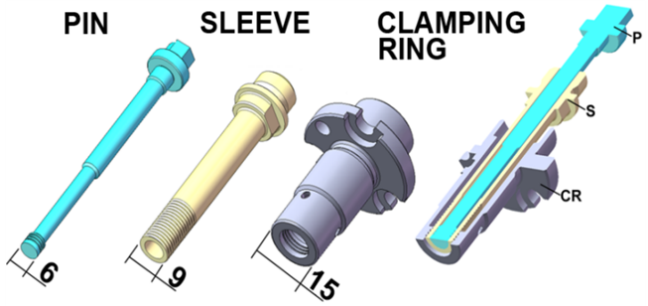

Figure 3.1 FSpJ tools used in this study (dimensions in mm) (Reproduced from [21]).

The FSpJ process occurs in three simple steps, which are schematically illustrated in Figure 3.2 [21]. In the first step, the sleeve and the pin start to rotate and the rotating sleeve plunges into the metal sheet. The sleeve plunging occurs only in the metallic part to avoid or reduce polymer degradation and damage to the fiber reinforcement if composites are used [21]. The friction between the sleeve and the metal locally increases the temperature to below the melting point of the metal [22,24]. The combination of high temperature and the axial movement of the sleeve plastically deforms a volume of the metal around the tool. Simultaneously, the pin is retracted, forming a reservoir into which flows the plasticized metal (Figure 3.2-1). Next, the sleeve and the pin are driven back to the surface of the metal part. Hence, the plasticized metal is pushed by the pin movement, refilling the keyhole formed during the plunging of the sleeve (Figure 3.2-2). Finally, the tool is retracted from the metal surface and the spot joint consolidates (Figure 3.2-3).

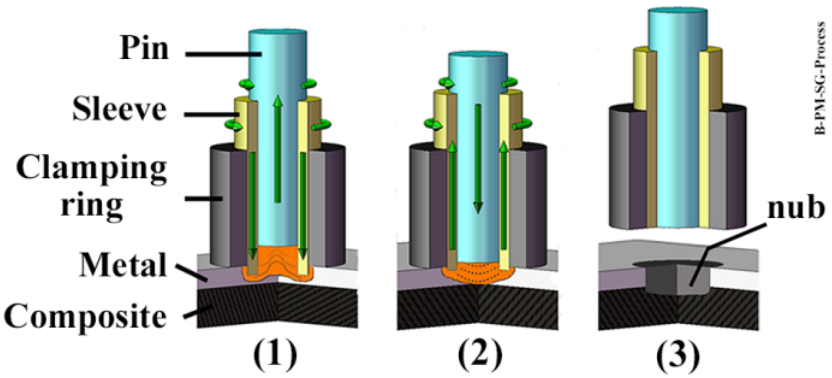

Figure 3.2 Schematic illustration of the FSpJ process steps (sleeve plunge variant) for a metal-composite hybrid structure. (1) Sleeve plunging and metal plasticizing; (2) spot refilling and (3) joint consolidation (Reproduced from [21]).

The main joining parameters of FSpJ are rotational speed (RS), plunge depth (PD), joining time (JT), and joining force (JF) [35]. RS and JT directly contribute to the heat generation and temperature evolution during the joining process [35]. PD and JF dictate the volume and geometry of the metal inserted into the composite part [35]. JF is also responsible for ensuring an intimate contact between the parts to be joined during the process and for controlling the flow of molten polymer at the metal-composite interface [35]. Other parameters, such as clamping force, consolidation time, surface finishing of the parts, as well as physicochemical and thermal properties of the materials, may also affect the joint formation [35].

3.1.2 Bonding mechanisms of friction spot joints

The bonding mechanisms of friction spot joints are divided into two categories: mechanical interlocking and adhesion forces [22]. Mechanical interlocking occurs in macro- and micro-scales. The macro-mechanical interlocking between the metal and the composite is provided by the deformation of a certain volume of the metal into the composite during the joining process (Figure 3.3-A). This geometrical feature of the joint is called “metallic nub,” and its shape and size strongly influence the mechanical strength of friction spot joints [36]. The micro-mechanical interlocking is found at the metal-composite interface through fiber attachment (Figure 3.3-B) and polymer matrix entrapment (Figure 3.3-C) of the composite on the aluminum surface.

Besides the mechanical interlocking, adhesion forces are also present at the interface of the joints. The axial movement of the tool during the joining process displaces a layer of molten/softened polymer from the center to the edges of the joined area. The arrows in Figure 3.4 indicate the layer of polymer accumulated at the borders of the joint. After the cooling of the joint, the layer of molten/softened polymer reconsolidates and establishes adhesion forces at the metal-composite interface [21]. Chemical bonds between aluminum and composite in this region of the AA2024-T3/CF-PPS friction spot joints were recently investigated by Goushegir *et al.* [37]. X-ray photoelectron spectroscopy (XPS) analysis identified Al-C bonds at the metal-composite interface created by the joining process.

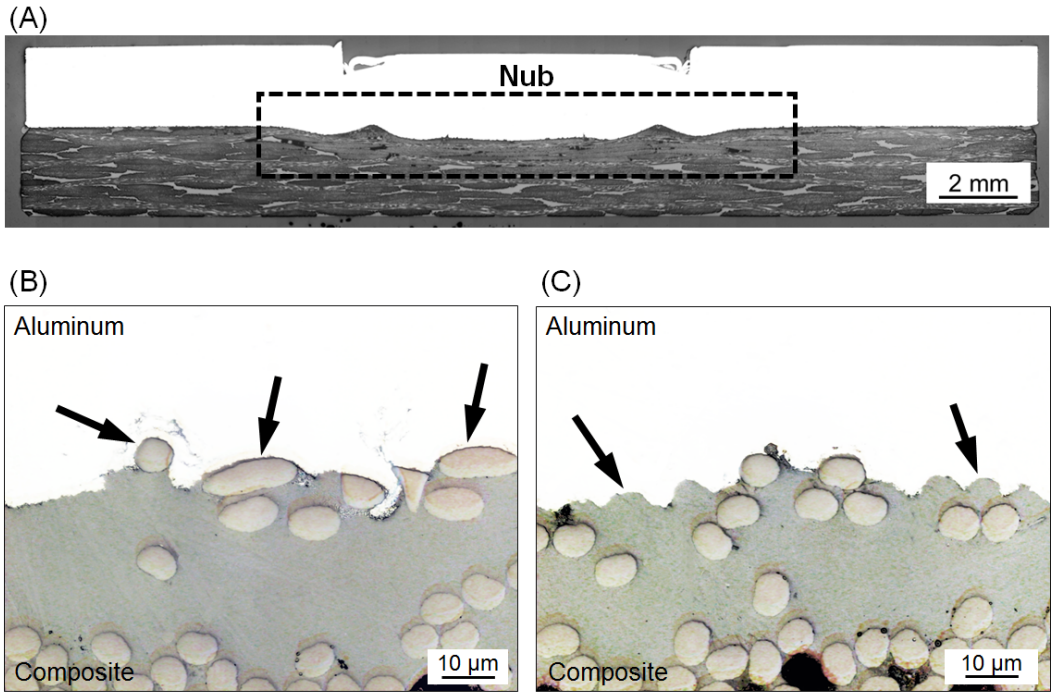

Figure 3.3 (A) Typical cross-section of AA7075-T6/CF-PPS friction spot joints; the dashed lines highlight the metallic nub. (B) and (C) show details of the metal-composite interface; the arrows indicate the micro-mechanical interlocking by polymer entrapment and fiber attachment in the aluminum irregularities. (Adapted from [36]).

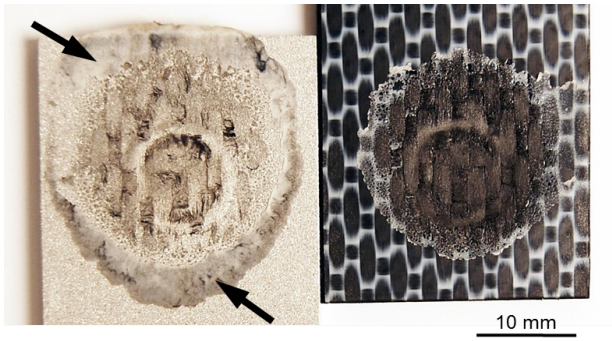

Figure 3.4 Typical fracture surface of AA7075-T6/CF-PPS friction spot joints. The arrows indicate the layer of reconsolidated polymer accumulated at the borders of the joined area (Adapted from [36]).

3.1.3 Feasibility and mechanical performance of friction spot joints

The FSpJ technology has ascertained its potential as a joining solution for several combinations of materials. Amancio *et al.* [21], for the first time, demonstrated the feasibility of the FSpJ technology. They successfully joined the magnesium alloy AZ31-O with GF- and CF-PPS. In this work, grain refinement by the dynamic recrystallization

of AZ31-O and the annealing of PPS were observed in the joining parts due to the FSpJ process. Shear strength up to 29 MPa was achieved for friction spot joints in this study without the use of any surface pre-treatment of the parts.

Further, Esteves *et al.* [24] investigated the influence of the FSpJ parameters on the microstructure and mechanical performance of AA6181-T4/CF-PPS joints. It was observed that the combination of intermediate rotational speed and long joining time produced defect-free joints with the largest bonding areas. Additionally, deeper plunge depths improved the macro-mechanical interlocking, thereby resulting in more pronounced metallic nubs. Thus, the strength of the joint was demonstrated to be maximal for the combination of intermediate rotational speed, long joining time, and deep plunge depth. The statistical analysis performed in this work showed that the joining force was the parameter with the least significant influence on the strength of the AA6181-T4/CF-PPS joints.

The joint formation and mechanical performance of AA2024-T3/CF-PPS friction spot joints were addressed by Goushegir *et al.* [22]. The authors systematically described, for the first time, the bonding mechanisms of friction spot joints. Macro-/micro-mechanical interlocking and adhesion forces were pointed as the main bonding mechanisms in friction spot joints. Additionally, it was demonstrated that the clad layer on aluminum alloys can enhance the micro-mechanical interlocking at the interface of the joints. Shear strength up to 43 MPa was achieved using alclad aluminum parts.

In another work, Goushegir [25] investigated the influence of surface pre-treatments on the mechanical performance of AA2024-T3/CF-PPS friction spot joints. Mechanical, chemical, and electrochemical surface pre-treatments were performed in the metallic part of the joints to increase the effective contact area and chemical activity of the metallic surfaces. The authors demonstrated the enhancement of the shear strength of the joints with the use of surface pre-treatments. The shear strength increased up to 800% (approximately 8 kN) compared to the as-received joints when electrochemical surface treatment was used in combination with aeronautical primer.

A qualitative comparison between the static mechanical performance of FSpJ and other welding-based technologies for metal-polymer structures is given in Figure 3.5. Induction welding (IW) [18], resistance welding (RW) [13], ultrasonic welding (UW) [38], and laser welding (LW) [39] are included in the comparison. Joints with similar materials (metals and CFRP), configuration (overlap), surface pre-treatments, thicknesses, and failure mechanisms to friction spot joints were selected for the comparison. Figure 3.5 demonstrates that friction spot joints present comparable or superior static shear strength than the concurrent technologies. The joining time is another advantage of the FSpJ technology compared to other welding-based techniques [25]. The friction spot joints are produced in a single-step joining cycle, which is performed in a few seconds (4 seconds for the joints currently under comparison). The ultrasonic and laser welding processes present joining cycles similar to that of FSpJ (3.5 s - 4 s) [38]. In contrast, the induction

welding process, for instance, lasts about 60 s [18], while the resistance welding process can take from 30 s up to 5 min [13].

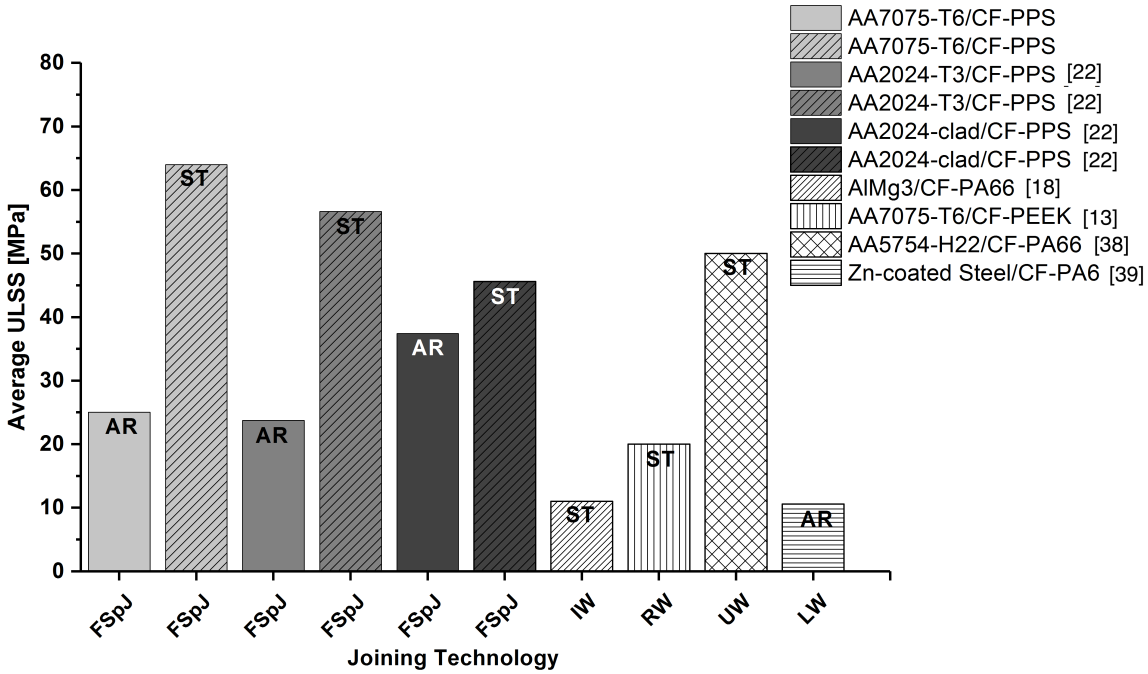

Figure 3.5 Qualitative comparison of the static shear strength (ULSS) of the concurrent joining technologies for hybrid structures (AR: as received, ST: surface treatment) (Reproduced from [36]).

The fatigue performance of friction spot joints was recently investigated by Goushegir *et al.* [25] for AA2024-T3/CF-PPS joints. The requirement of the aircraft industry for qualifying new joining technologies requires the fatigue strength of the joints to be at least 30% of their ULSS at 10^5 loading cycles. In this context, the authors showed that the fatigue strength of friction spot joints reached up to 37% of the ULSS at 10^5 cycles, thereby fulfilling the aeronautical requirement [26].

Further improvement in the fatigue performance of AA2024-T3/CF-PPS friction spot joints were investigated by André *et al.* [40]. Based on the weld-bonding concept, the authors added a thermoplastic polymer film between the AA2024-T3 and the CF-PPS. The film interlayer was melted and reconsolidated during the joining process, thereby enlarging the bonding area of the joints. Hence, additional sites of micro-mechanical interlocking were observed and the fatigue strength of the joints increased to 51% of the static strength at 10^5 cycles. Other concurrent technologies, such as ultrasonic welding [27] and resistance welding [41], have reported fatigue strengths up to 32% of the static strength of their joints at 10^5 cycles.

3.1.4 Bonding zones and failure of friction spot joints

The failure mechanisms of friction spot joints have been described by Goushegir *et al.* [42]. Three bonding zones are found in the joined area of friction spot joints: the Adhesion

Zone (AZ), the Plastically Deformed Zone (PDZ), and the Transition Zone (TZ) [22]. Figure 3.6 depicts the three bonding zones in the fracture surface of the joint.

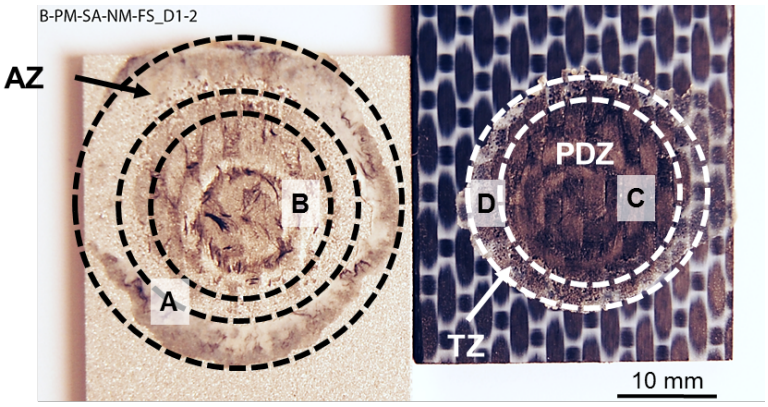

Figure 3.6 Typical fracture surface of AA7075-T6/CF-PPS friction spot joint. The bonding zones are delimited by the dashed circles (Reproduced from [36]).

The AZ is the outer region of the joined area [22]. It is originated from the layer of the molten/softened polymer displaced from the center of the joint during the joining process. After its reconsolidation, this layer of polymer provides adhesion forces at the metal-composite interface. Figure 3.7-A shows a featureless fracture surface of the reconsolidated molten polymer in the AZ [42]. It demonstrates that in this zone the failure occurs through the decoupling between the reconsolidated polymer layer and the composite surface, i.e., in the adhesive failure mode [22].

The PDZ is the central region of the joined area [22]. In this zone, the metallic nub is formed. The insertion of the metal part into the composite displaces part of the polymeric matrix, thereby exposing the fibers on the surface of the composite [22]. Thus, an intimate contact between the molten/softened matrix, fibers, and the aluminum surface is achieved, leading to the micro-mechanical interlocking described in Section 3.1.2. Figure 3.7-B displays the carbon fibers and the polymeric matrix attached to the aluminum surface after the failure of the joint. The matrix and the fibers which remained attached to the aluminum surface indicate that, in this zone, the crack propagated through the first plies of the composite [42]. Therefore, the PDZ fails predominantly through the cohesive failure mode. Additionally, one observes polymeric fibrils after the plastic deformation inside the PDZ, as shown in Figure 3.7-C. It demonstrates the predominance of a ductile micro-mechanism of failure in this zone [42]. The cohesive failure mode accompanied by ductile micro-mechanisms of failure is also reported for other metal-composite joints in Resistance Welding [17], Ultrasonic Welding [38] and Induction Welding [15].

The TZ is the transition area between the PDZ and the AZ [22]. The main characteristic of this zone is the presence of air bubbles. Such air bubbles are formed during the joining process due to the outflow of molten/softened polymer from the center to the borders of the joined area [42]. Figure 3.7-D depicts the air bubbles in this zone on the composite surface after failure. It is to be noted that the bubbles failed through plastic deformation

with final tearing (arrows in Figure 3.7-D). Thus, it is believed that the TZ fails predominantly through a cohesive mode with a mixture of brittle and ductile micro-mechanisms [42].

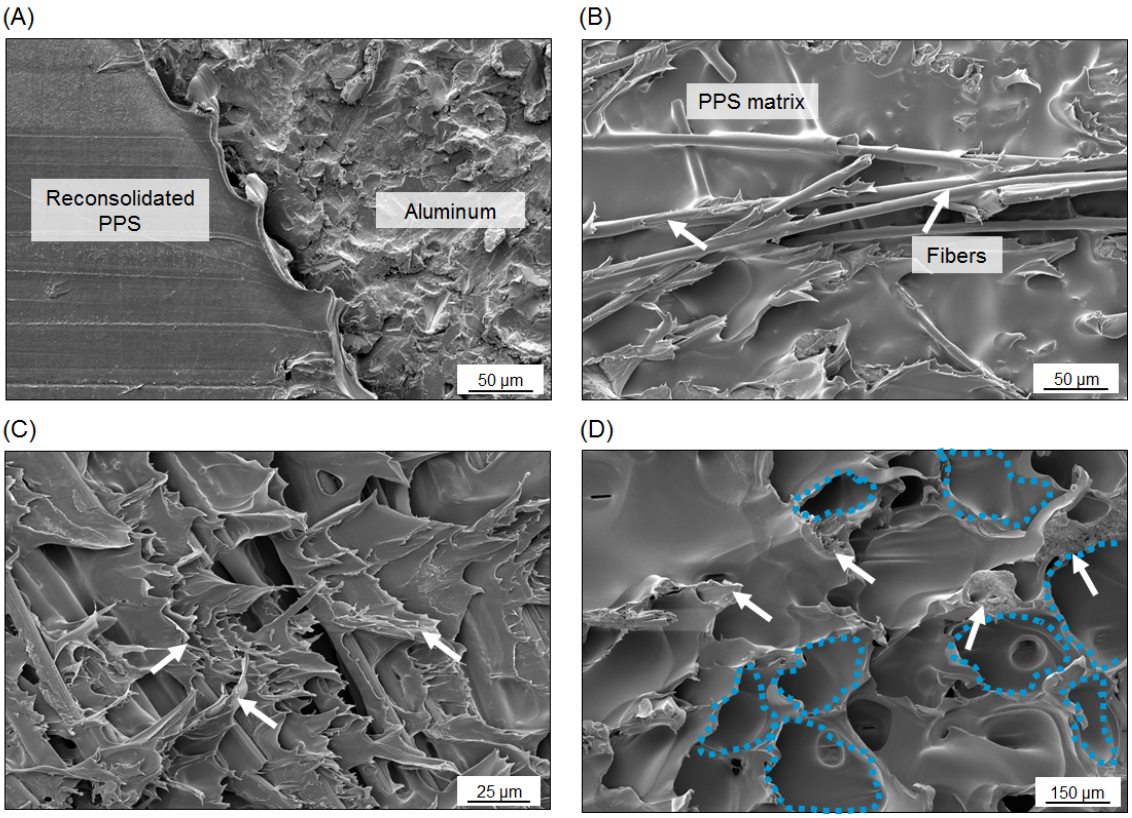

Figure 3.7 Details of the fracture surface presented in Figure 3.6. (A) Featureless fracture surface of the reconsolidate layer of polymer. (B) Polymeric matrix and fibers attached to the aluminum surface. (C) Plastic deformation of the polymeric matrix in the PDZ. (D) Teared air bubbles in the TZ (Reproduced from [36]).

Considering the bonding zones of the joints, a failure theory for friction spot joints was proposed by Goushegir *et al.* [22]. It is believed that the crack initiates at the borders of the AZ, propagating radially at the interface between the reconsolidate polymer layer and the composite surface. Further, the crack path shifts as it reaches the TZ. At this point, the crack propagates through the first plies of the composite into the PDZ, in the cohesive failure mode. Therefore, partial attachment of the polymer matrix and fibers are found on the metal surface after the fracture of the joint (Figure 3.7-B and C). Thus, it is concluded that the friction spot joints typically fail in a mixture of the adhesive-cohesive mode. Figure 3.8 summarizes the proposed mechanism for crack propagation in friction spot joints under shear loading [22].

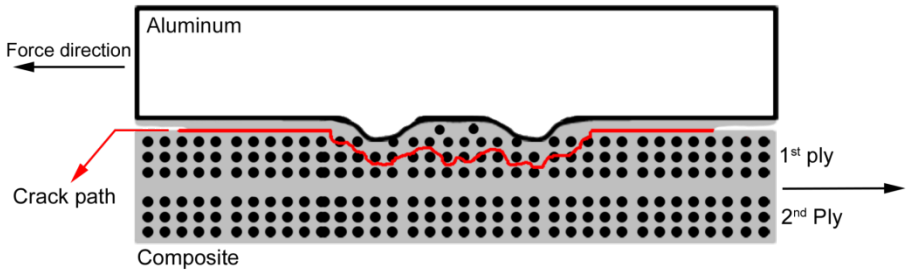

Figure 3.8 Scheme of the proposed crack propagation for metal-polymer composite friction spot joints under shear loading (Reproduced from [22]).

3.2 Materials Mechanics applied to overlap connections

The reliability and robustness of a structure are among the major concerns of engineers and designers in all industrial sectors [43–45]. Thus, the fundamental understanding of the materials mechanics is essential to the design of efficient and safe structural components [46]. Within the materials mechanics, three main approaches can be applied to understand and evaluate the mechanical behavior of materials: the continuum mechanics, the fracture mechanics, and the damage mechanics [43–45]. The optimal structural design solution is often acquired from the combination of these three approaches [43–45].

The continuum mechanics approach essentially comprises the characterization of stresses and deformations of the material in the three main loading cases: stress, shear, and peeling [47]. Further, this information is transferred to a more complex structure, usually involving a multi-axial stress state. In this approach, the materials are considered continuous [47]. Nevertheless, voids, delamination, cracks, and other damages are virtually present in all materials as a result of manufacturing processes and handling [48,49]. This strength-based approach still belongs to the core of structural design. However, generous safety factors are required to ensure the reliability of the calculations when the criterion is based on continuum mechanics [47]. The inherent flaws can significantly decrease the bearable strength of the material. The growth of preexisting or induced cracks may occur at load levels well below the maximum strength of the material, leading to a catastrophic failure of the structure over time [47]. Additionally, the design of multi-material structures become complex with the use of continuum mechanics [47,50]. In multi-material structures, the stresses are no longer uniformly distributed, and this factor will ultimately dictate the mechanical performance of such components [51].

An alternative design approach is offered through fracture mechanics [50]. The fracture mechanics approach acknowledges the presence of flaws/cracks and quantifies the driving forces required for their propagation [52]. Two criteria can be used to predict the propagation of a crack in the material: (a) the stress intensity state and (b) the energy at the tip of the crack [52,53]. The stress intensity at the crack tip is characterized by the

stress intensity factor (K), while the energetic requirement for crack propagation is given by the strain energy release rate (G) [52,53]. The subscripts I, II, and II are added to K and G to indicate the type of loading applied to determine these parameters [53]. I stands for the opening mode (stress normal to the plane of the crack); II represents in-plane shear (crack front perpendicular to the shear stress); and III is regarded as the out-of-plane shear (crack front parallel to the shear stress) [52].

K is a scalar parameter that predicts the stress state at the crack tip. It depends on the geometry of the specimen, size and location of the crack, and the magnitude, mode, and distribution of the applied stress. Considering a crack of length *2a*, in an infinite plane with uniform and perpendicular stress to the loading direction (mode I), the stress intensity factor is given by the linear elastic theory through Equation 3.1 [52]. In Equation 3.1, *Y* is a geometrical factor and σ_r is the stress applied to the crack. Ks are usually given in $MPa.m^{1/2}$. Equation 3.1 is only valid for small yielding at the crack tip [54]. Otherwise, approaches like the J-Integral may be used to account for inelastic behavior [55].

Equation 3.1 $$\mathbf{K_I = Y\,\sigma_r\sqrt{\pi a}}$$

In this case, the crack 2a will propagate when K_I at its tip exceeds a critical value; the critical stress intensity factor K_{Ic}. The $K_{Ic/IIc/IIIc}$ is the property of the material that measures its capability to suppress any crack growth [52]. Therefore, as long as the computed K at the crack tip does not exceed K_c, there will be no crack growth in the material [52].

Similarly, the energetic criterion is dictated by a critical value of the strain energy release rate (G_c), which is also known as fracture energy [53]. In this case, the crack propagation will occur when the energy at the crack tip is enough to balance the energy dissipation related to the crack growth event [47]. It includes the energy dissipation due to the creation of new fracture surfaces and other dissipation phenomena such as small yielding at the crack tip. In 1921 Griffith established the strain energy release rate as presented in Equation 3.2 [56], where *U* is the stored elastic energy for crack propagation, *W* is the external work, and *A* is the crack area. Gs are usually given in $J.m^2$; the energy available for crack propagation per unit of area. This relation is valid for systems in which the energy dissipation is restricted to the crack tip [47].

Equation 3.2 $$\mathbf{G = \frac{d\,(U-W)}{dA}}$$

For homogeneous materials, the stress intensity factor (K) and the strain energy release rate (G) are correlated, as presented in Equation 3.3. Here $\bar{E}$ is the Young's modulus for the plane stress case ($E_l/(1-v^2)$) and *v* is the Poisson's ratio.

Equation 3.3 $$\boldsymbol{G = \frac{K^2}{\bar{E}_l}}$$

Within the fracture mechanics approach, the energetic criterion has been extensively applied to overlap connections, as adhesive bonded joints and layered materials along the years [57–61]. The main advantage of this criterion is that it directly transfers its physical meaning through its values of strain energy release rate (G) in contrast to the stress intensity factor (K). Besides, stress intensity factors are difficult to obtain experimentally for non-bulk materials in which the crack grows near an interface [62]. The roughness of the crack surfaces, the crack tip yielding, the presence of eventual residual stresses, and the mismatch of the elastic properties of the interface are some of the factors that may make it difficult to calculate K [62]. Thus, the key advantage reported for the energetic criterion is the easy estimation of G from general force-displacement experimental data [47]. In 1978 Broek [63] described the first correlation between G, force, and displacement, as presented in Equation 3.4. In Equation 3.4, *P* is the force applied, *C* is the compliance (*d/P*), *d* is the displacement, and *A* is the crack area.

Equation 3.4 $$G = \frac{P^2}{2}\frac{\partial C}{\partial A}$$

The interlaminar fracture of layered materials and overlap connections have been investigated by several authors based on the pioneer study of Broek [64–66]. The determination of G is mainly accomplished through beam theories, which consider the two surfaces in between the crack as slender beams [67]. The pioneer in the development of beam theories was Timoshenko [67], who established the first correlation between compliance (C) and crack length (a) to complement Equation 3.4. The Timoshenko beam theory simplifies the solid mechanics to beam behavior by providing formulations for the deflection and internal stress in a beam [67]. In the last few decades, the relation established by Timoshenko [67] has been further developed, incorporating the influence of other factors such as plasticity at the crack tip, transverse shear, and elastic foundations effects [50].

The most diverse types of fracture tests have been developed to characterize the interlaminar fracture in different loading modes. The most common fracture tests are the double cantilever beam (DCB) for mode I and the end-notched flexure (ENF) for mode II. Nevertheless, an extensive list of options are found for such tests including highly sophisticated apparatus [50]. In the past decades, the need to evaluate the performance of structures under mixed-mode loading also instigated the development for mixed-mode fracture tests. The literature reports several mixed-mode methods such as the asymmetric tapered double cantilever beam (ATDCB) [68], crack lap shear (CLS) [69], mixed-mode bending (MMB) [70], and the single leg bending (SLB) [71].

The MMB test is the only standardized mixed-mode fracture test (ASTM D6671-06). Nevertheless, MMB requires complex clamping apparatus and loading hinges, which complicate the compliance with the standardized procedure [50,57]. In contrast, SLB is the simplest method to be performed and relies on a three-point bending equipment [50,57]. The specimen comprises two beams: The lower beam is shorter than the upper

beam. Thus, one extremity of the specimen is unsupported. Therefore, the load at the mid-span of the specimen leads to a mixture of shear and opening at the unsupported extremity [50,57]. Figure 3.9 illustrates the SLB test for an adhesive bonded joint, where *P* is force, *L* is the mid-length of the longer beam, *h* is the thickness, *a* is the crack length, and *b* is the width of the specimen.

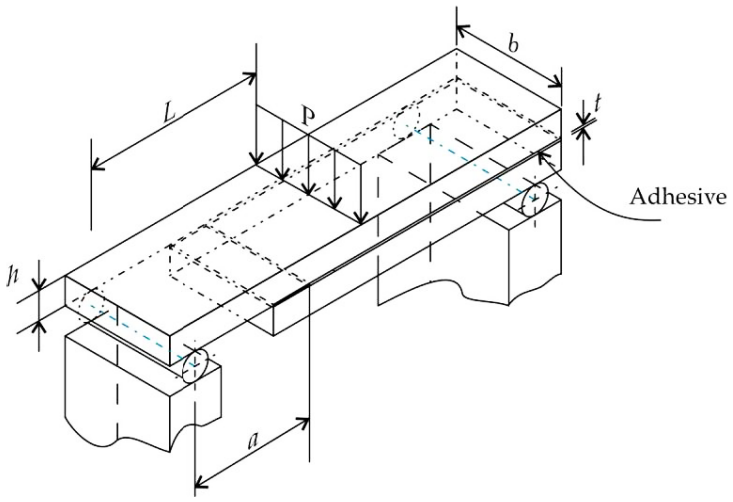

Figure 3.9 Example of the SLB test of an adhesive bonded joint (Reproduced from [50])

Ozdil and Carlsson [72] derived a formulation for the compliance as a function of the crack length for ENF composite laminate specimens based on the Timoshenko beam theory. In this study, the energy strain release rate (G) was obtained by differentiating the compliance formulation with respect to the crack length, as denoted in Equation 3.4. Further, Szekrényes and Uj [73] complemented the compliance formulation of Ozdil and Carlsson [72] to be used for SLB experiments. The authors superposed the contributions of the transverse shear and the elastic foundation effects on the compliance during the SLB test. The Winkler foundation model was considered in this analysis. This elastic foundation model assumes a linear force-deflection relation between the beam and the foundation. The model is depicted in Figure 3.10. It comprises two beams connected by perfect elastic springs. The deflection in the specimen is described by four functions (w). Thus, the potential energy of the un-cracked region is obtained using the Hooke's law and its contributions to the compliance and G can be calculated.

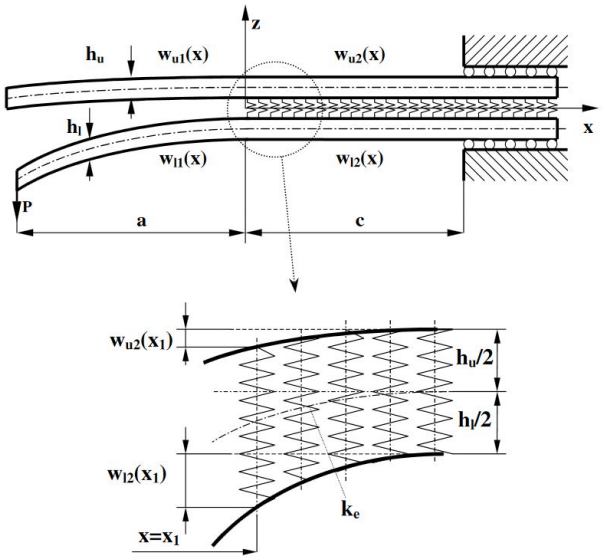

Figure 3.10 Illustration of the Winkler foundation model used by Szekrényes and Uj (Reproduced from **[73]**).

Szekrényes and Uj [73] also proposed a partitioning method to obtain the fractions of mode I (G_I) and mode II (G_{II}) in the total strain energy release rate at the crack tip under mixed-mode I/II loading ($G_{I/II}$). The final equations obtained for $G_{I/II}$, G_I, and G_{II} are given in Equations 5, 6, and 7 respectively. In Equations 5–7, P is force, a is the crack length, b is the width of the parts, h is the thickness, $\bar{E}$ is the tensile modulus, μ is the shear modulus, and k is the shear correction factor (k = 5/6).

Equation 3.5
$$G_{I/II} = \frac{21\,P^2\,a^2}{16\,b^2\,h^3\,\bar{E}} + \frac{P^2}{16\,b^2\,h\,k\,\mu} + \frac{P^2 a^2}{16\,b^2\,h^3\,\bar{E}}\left[5.42\left(\frac{h}{a}\right) + 2.45\left(\frac{h}{a}\right)^2\right]$$

Equation 3.6
$$G_I = \frac{12\,P^2\,a^2}{16\,b^2\,h^3\,\bar{E}} + \frac{P^2}{16\,b^2\,h\,k\,\mu} + \frac{P^2 a^2}{16\,b^2\,h^3\,\bar{E}}\left[5.42\left(\frac{h}{a}\right) + 2.45\left(\frac{h}{a}\right)^2\right]$$

Equation 3.7
$$G_{II} = \frac{9\,P^2\,a^2}{16\,b^2\,h^3\,\bar{E}}$$

The combination of linear elastic fracture mechanics (LEFM) and beam theories have been widely used to characterize the interlaminar fracture of adhesive bonded joints and composite laminates [58–60,74,75]. An interesting study was performed by Fernandez *et al.* [76]. The authors addressed the mixed-mode I/II fracture of CF-epoxy bonded joints under fatigue loading. They used the formulation of Szekrényes and Uj [73] to calculate the strain energy release rate at the crack tip throughout the fatigue life of the joints. It was demonstrated that for adhesive bonded joints, the strain energy release rate increases linearly regarding the cycles, thereby presenting a sudden exponential increase toward the end of the fatigue life of the joints. The authors also showed the validity of the Paris law as a function of the mode-mixity level. Their study concluded that the presence of loading in mode II is beneficial to the adequacy of the crack growth behavior in the typical Paris

law for the crack propagation rate (da/dN) and the strain energy release rate (G), which is widely used for design of damage-tolerant structures.

Razavi *et al.* [77] investigated the mixed-mode fracture response of metallic-reinforced adhesive for CF-epoxy joints. Increases of up to 13% in the strain energy release rate were achieved by the incorporation of the metallic fiber in the adhesive. Fiber bridging, pull-out, and shear bands were observed at the fracture surface of the joints with metallic-reinforced adhesive. Theses failure mechanisms introduced by the fibers are believed to be the reason for the increased fracture energy of the joints.

De Moura, Cavaleiro and Silva [75] addressed the fracture characterization in the mixed-mode for CF-epoxy/Cork laminates using SLB. In this study, the crack was virtually estimated from the measured compliance using the Compliance-Based Beam Method (CCBM). The equivalent crack derived from the CCBM was validated using finite element modeling. Additionally, the results demonstrated that the hybridization of the composite with cork stabilized the crack growth in the composite.

It is important to note that the fracture mechanics approach relies on the presence of a crack [52]. Such crack can be modeled and artificially created to simulate damage initiation [47]. Nevertheless, the method itself does not account for crack initiation but only the crack propagation [47]. The damage mechanics approach combines cohesive and continuum damage models to mitigate the limitations of continuum and fracture mechanics [47]. In this approach, the strength criteria from continuum mechanics is applied to model the damage initiation and fracture mechanics to model the crack propagation [47].

In the damage mechanics field, cohesive zone models (CZM) are the most used models to investigate the damage initiation and propagation between two surfaces [50]. The CZMs are based on the creation of cohesive elements to connect planes and tridimensional solids [78, 79]. Thus, the CZMs describe the relationship stress-displacement of each pair of adjacent elements at a given interface [80]. The application of such models requires previous knowledge of critical areas where damage is prone to occur in order to precisely place the cohesive elements [50,79]. In this way, the cohesive elements are assigned specific features related to the interface under investigation. Among these features there are: the thickness of the region under interest, its stiffness, the allowable stresses and displacements, as well as the fracture energy. In addition, cohesive softening laws can be applied to model the mechanical behavior of these zones such as the triangular, trapezoidal, linear-parabolic, polynomial, or exponential laws [81,82]. Thus, the continuum and the fracture mechanics approaches can be combined to enable the prediction of the damage initiation and evolution in such elements [81].

Although the damage mechanics provides a more complete solution to the failure behavior of the materials and structures, it is also a more complex approach. Therefore, closed-form solutions are often enhanced with the aid of finite element modeling software in damage mechanics [83–89].

De Moura *et al.* [88] investigated the residual compressive strength of composite laminates after low-energy impact. The authors used a cohesive zone model based on the triangular traction-separation law to model the delamination damage in the laminates with different stacking sequences. The model was able to predict the different compressive behavior of two types of composite laminates. In addition, the maximum bearable load was fairly accurately predicted.

In another work, Schellekens *et al.* [90] applied a mixed-mode delamination model to investigate the initiation and propagation of delamination at the free edge of graphite-epoxy composites under uniaxial tensile loading. The model was based on the orthotropic hardening–softening plasticity law. The predictions of the model were validated using in-situ X-ray radiography, which demonstrated the good agreement between computational and experimental crack growth behavior.

A damage model was also developed by Allix and Ladevèze *et al.* [91] to investigate the delamination tolerance of a homogeneously layered laminate. The interlaminar interfaces were modeled as a two-dimensional entity, and the displacement/traction were transferred from one layer to another. The authors concluded that with a few intrinsic properties of the interface such as shear strength and stiffness, it is possible to predict the tendency of a structure to delaminate. Finally, the authors validated the approach by accurately predicting the delamination initiation and propagation of a CF-epoxy laminate under static shear loading.

3.3 Impact behavior of multi-material connections

Accidental impacts on aircraft and automobile structures are often reported during manufacturing, shipping, maintenance, and daily operation [92]. Recently, Airbus performed a study in cooperation with airlines to assess the susceptibility of impact in the different regions of the airplane and the extension of such impact threats [92]. The study states that the main aircraft areas subjected to impact are the surrounding of the doors (53%), doors (15%), and the wings (13%) [92]. Most of the impact events are actually related to the ground operation of the airplanes, e. g. luggage charging, runway debris, and tool dropping during maintenance. The impact threat levels for each aircraft zone were investigated indicating that impact energies below 35 J were the most common extent of damage [92]. In-service accidental damages can strongly influence the performance and hence the safety of structural components [43]. Therefore, the prediction of how accidental damage can cause a premature failure is of significant importance for ensuring the robustness and safety of the structures [43,93].

The Energy Profile Method (EPM) has been widely applied to characterize the impact behavior of materials [94–97]. In this method, two parameters dictate the impact behavior of the material: the impact energy (E_i) and the absorbed energy (E_a) [94]. The impact energy (E_i) is defined as the total energy applied to the material due to the impact event,

while the absorbed energy (E_a) is the fraction of the impact energy actually absorbed by the material. The absorption of impact energy can occur through different phenomena, such as deformation (elastic and plastic) and creation of internal damage [94,98,99]. E_i and E_a are correlated through the so-called energy profile diagram (EPD), as shown in Figure 3.11.

Considering the impact behavior of a material, three regions can be identified in the EPD of Figure 3.11: rebounding (AB), penetration (BC), and perforation (CD) [94]. The region AB corresponds to the range of impact energy where $E_i > E_a$. In this region, the impact energy is partially absorbed by the material [94,98]. Thus, the excess of impact energy is consumed by the rebounding of the impactor after the impact event [94]. Rebounding is mostly related to the yield strength of the material and its capability to elastically recover from deformation [99,100]. The region BC comprises the range of energy where $E_i = E_a$. In this region, the impact energy is totally absorbed by the material [94]. The $E_{i,el}$ represents the pure elastic limit of the material [94,98]. As the $E_{i,el}$ is reached in Point B, the impactor penetrates the material and no longer rebounds. Finally, the region CD corresponds to the perforation range of the material. At Point C, the energy absorption capability of the material reaches its maximum ($E_{a,max}$) and the impactor usually perforates the material [94,98]. Therefore, E_a no longer changes as E_i increases [94].

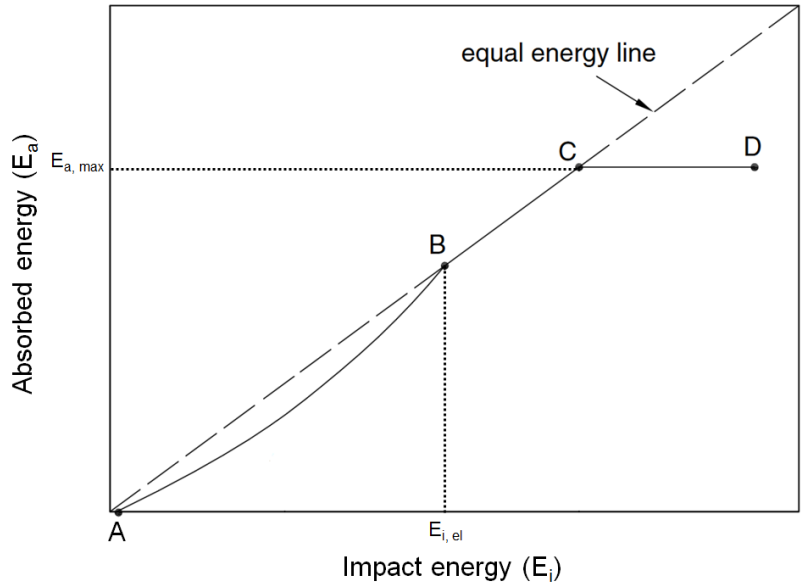

Figure 3.11 General schematic illustration of an energy profile diagram (EPD) (Adapted from **[94]**).

Owing to their highly dissimilar properties, composites and metals diversely absorb the impact energy due to accidental damage [43,101,102]. Therefore, the assessment of the impact resistance of hybrid structures is very important not only to predict premature failure and impact damage tolerance, but also to guide the design of such hybrid structures [43,103].

Most metallic materials present a strong ductile behavior [48]. Thus, when subjected to impact, the impact energy is initially absorbed through elastic deformation of the material, leaving only a surface indentation behind [48]. The impact damage usually initiates after the yield strength of the material is reached, through local plastic deformation [92]. Therefore, there is no immediate loss in performance for metallic components after impact. Besides, the impact damage – local plastic deformation – is easily detectable during regular maintenance checks [43]. Hence, the initiation and propagation of a crack due to impact can be identified and stopped before compromising the mechanical integrity of the component [43].

The heterogeneous and anisotropic nature of composites leads to very complex damage mechanisms in these materials [104]. Impact damage in composites can include: matrix cracking, matrix-fiber interfacial cracking, delamination, and fiber bridging and breakage [104]. Such impact damages may immediately reduce the performance of the material, depending on the type of the composite and the extent of damages [43,45]. Besides, such damages are all internally created and therefore undetectable by visual inspection [43,45]. Typically, accidental damages in composites are classified as barely visible impact damage (BVID), i.e., not visible within a range of 50 cm of distance [105]. Therefore, non-destructive techniques (NDT), such as acoustic emission and ultrasonic scanning, are usually employed to monitor accidental damage in composite materials [105].

Considering the impact behavior of fiber metal laminates (FML), Liu and Liaw [99] investigated the influence of the metal constituent in the impact behavior of GLARE. In the case that the AA7475-T6 was used, small deflections were identified after impact due to the high stiffness of this material. Nevertheless, earlier crack initiation was observed when the AA7475-T6 was used rather than a more ductile aluminum alloy like AA2024-T3. The researchers reported that by using AA2024-T3, instead of AA7475-T6, smaller damage zones were created after the impact. In case of AA2024-T3, more energy was attenuated through plastic deformation than when AA7475-T6 was used.

The impact damage evolution of Ti/GFRP laminates was addressed by Nakatani *et al.* [106]. The authors demonstrated that the delamination and out-of-plane deformation on the GRFP layer was suppressed by the addition of a titanium layer underneath the composite sheet. Cross-sectional analysis and finite element modeling indicated that the metallic layer absorbed the impact energy through plastic deformation and crack initiation, thereby protecting the GFRP layer from delamination.

Bieniás *et al.* [107] investigated the low-energy impact behavior of CF-epoxy and aluminum hybrid laminates. The authors observed a very complex damage mechanism that started with cracking at the matrix-fiber interface. Nevertheless, the critical decrease in strength of the laminate actually occurred due to the delamination of the aluminum-CFRP interface, as a result of the global plastic deformation of the aluminum component of the laminate.

Silva *et al.* [108] assessed the impact behavior of adhesively bonded high strength steel joints. They produced the joints using a flexible adhesive at the ends of the overlap, while a rigid adhesive was applied in the middle of the joint. This mixed-adhesive strategy improved the impact resistance of the joints. The researchers showed that 100% of the impact energy was absorbed in this case in contrast to only 50% of absorption when only one type of adhesive was employed. In another study, Machado *et al.* [109] performed a similar study for CFRP bonded joints. The effects of combining flexible and rigid adhesives were found to be similar to what was observed for the steel joints. Nevertheless, higher impact failure loads were observed for the CFRP joints than those for the steel joints. It is believed that the internal damages created in the CFRP substrates reduced the stresses in the adhesive layer of those joints compared to the steel joints, thereby preserving the strength of the joints.

3.4 Galvanic corrosion of metal-CFRP connections

The chemical composition and temperature of an environment can significantly deteriorate the mechanical performance of a structure through corrosion [110]. Airplanes and cars are designed to survive diverse environments worldwide, including marine and other corrosive atmospheres [110]. These structures are also often in contact with maintenance chemicals during its service life, which can lead to corrosion [110]. Additionally, the use of CFRPs has shown to be an advantageous alternative to reduce weight and fuel consumption of cars and aircraft [2,111]. The most famous examples are the A350 XWB [111] and the Boeing 787 [3], along with the new generation of fully electric and hybrid cars of BMW (e.g., i3 and i8) [6]. Nevertheless, the galvanic coupling of metal alloys and carbon fibers is a well-known issue for metal-CFRP connections [10,112]. Therefore, the understanding and evaluation of the corrosion behavior of metal-CFRP connections are of great interest in the transport industry [113–116].

The carbon fiber is an electrochemically noble material, i.e., it usually presents relatively high electrochemical potential [117]. In contrast, metallic alloys typically present low electrochemical potential [117]. One of the reasons for the enhanced corrosion susceptibility of metallic alloys is related to the diverse types of particles and inclusions distributed on the grains and its boundaries formed during the alloy processing [49,118]. Precipitates and intermetallic particles have different chemical compositions than the matrix of the alloy [119]. Besides, the chemical composition of adjacent areas can also be affected during the formation of such precipitates and intermetallic particles [120]. Thus, the corrosion potential of the matrix, the particles, and their adjacent areas will be different, raising the corrosion susceptibility of the material through pitting, intergranular, and self-corrosion [120].

Galvanic corrosion is considered a durability issue when the potential difference between two materials exceeds 250 mV [121]. The galvanic series (ASTM G82-98) reports values up to -1.0 V for the corrosion potential of aluminum alloys and +0.2 V for pure graphite

[122]. The potential difference between the materials is the driving force for the onset/acceleration of the corrosion reactions. The potential of the two materials in contact tend to equilibrate to achieve a thermodynamically stable condition [121]. The shift in the electrochemical potential to achieve the thermodynamic equilibrium is called polarization [121]. The polarization dictates the current flow, which will consume the anode material during the corrosion process [117]. Figure 3.12 exemplifies the encounter of the cathodic and anodic branches of the polarization curves of carbon (pure graphite) and aluminum alloys widely used in the aircraft industry respectively. The point of encounter of the cathodic and anodic branches represents the potential and current of corrosion for the coupled materials in a given environment [123].

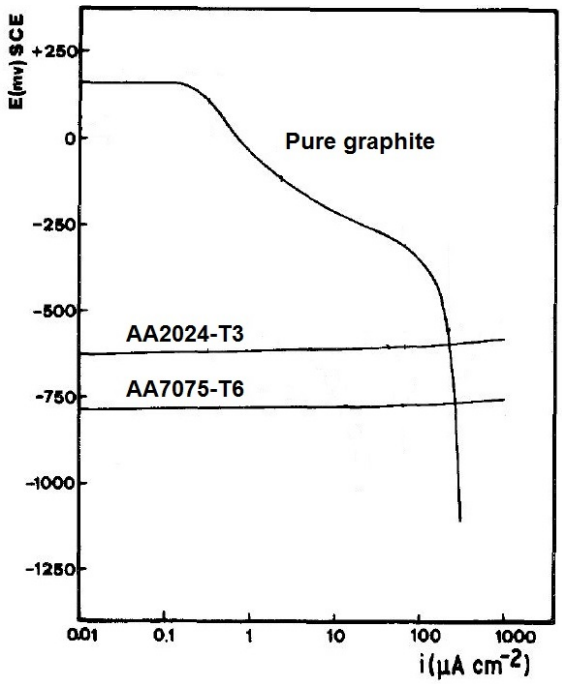

Figure 3.12 Polarization curves of pure graphite (cathodic branch) and aircraft aluminum alloys (anodic branch) in neutral air-stirred 3.5 % NaCl (Adapted from **[117]**).

The galvanic corrosion occurs through a redox reaction [123]. It means that oxidation and reduction occur simultaneously during the corrosion process [123]. The anodic reaction during corrosion dissolves the metal into ions. Equation 3.8 exemplifies the anodic reaction for aluminum [124]. The cathodic reaction will consume the electrons released from the anodic reaction. Nevertheless, a number of cathodic reactions are possible to occur during galvanic corrosion [123]. It will depend on the anode and environmental factors like the pH and concentration of oxygen in the electrolyte. In neutral electrolytes, water splitting is the favorable cathodic reaction, as shown in Equation 3.9. For neutral or basic electrolytes exposed to the atmosphere, oxygen reduction is more likely to occur (Equation 3.10). And finally, hydrogen reduction may occur as a cathodic reaction in case of acidic electrolytes (Equation 3.11). In case of aluminum-CFRP coupling, water splitting and oxygen reduction are the reactions most likely to occur [124].

Equation 3.8 $$Al_{solid} \rightarrow Al^{3+} + 3e^{-}$$

Equation 3.9 $$2\,H_2O_{liquid} + 2e^{-} \rightarrow 2\,OH^{-} + H_{2\,(gas)}$$

Equation 3.10 $$O_2 + 2\,H_2O + 4e^{-} \rightarrow 4\,OH^{-}$$

Equation 3.11 $$2\,H^{+} + 2e^{-} \rightarrow H_{2\,(gas)}$$

Galvanic corrosion as a degradation mechanism for AA2024-T3 and AA7075-T6 in contact with graphite-epoxy has been investigated by Belucci *et al.* [117]. They demonstrated that the corrosion rate of the metallic parts increases as the CF-epoxy absorbs water and the matrix-fiber interface is degraded. The corrosion rate was also affected by the surface treatment applied to the CF-epoxy. The cathodic area available for reaction can increase depending on the matrix-fiber adhesion and the surface finishing of the CF-epoxy, thereby raising the corrosion rate.

Pan *et al.* [125] addressed the electrochemical behavior of magnesium alloys (LZ91, LZ141 and AZ31) in contact with CFRP. The galvanic activity was found to increase as the lithium content of the alloys increases. In contrast, the aluminum concentration decreased the galvanic activity of magnesium alloys coupled with CFRP. Additionally, the study demonstrated that galvanic corrosion is more severe to magnesium alloys than aluminum or titanium alloys when coupled to CFRPs. The magnesium alloys in this study presented corrosion current density of approximately 70 μA/cm^2. In contrast, the corrosion current density for Ti-6Al-4V/graphite-epoxy was reported to be 0.5 μA/cm^2, while the AA2024-T3/graphite-epoxy couple presented 8.7 μA/cm^2 [126].

The corrosion of AA6060-T6/CF-epoxy riveted joints was investigated by Fiore *et al.* [127] using salt spray exposure. The researchers showed decreases of up to 46% in the strength of the joints after 15 weeks of exposure due to deterioration of the mechanical properties of the composite. Plasticization and decrease in stiffness of the composite matrix was observed due to water absorption and NaCl migration. The authors concluded that the influence of galvanic corrosion on the strength degradation of the joints was insignificant in their study.

3.5 Materials used in this work

3.5.1 Aluminum alloy 2024-T3

In 1931 the aluminum alloy 2024 was introduced by Alcoa as an alclad sheet in the T3 temper. This is a precipitation-hardening alloy, which has Cu and Mg as the principal alloying elements. The addition of copper and magnesium provides high strength to the alloy through pinning of dislocations. Copper acts through solid solution strengthening, while Mg creates precipitates by natural aging [119]. The precipitation sequence of Al-

Cu-Mg alloys depends highly on the Cu/Mg ratio [128]. The complete precipitation sequence of AA2024-T3 is still nowadays under debate [129–131]. Nevertheless, it is generally accepted that the main precipitation clusters in the T3 state of this alloy consists of Guinier Preston Bagaryatskii (GPB) zones, which are coherent phases with the aluminum matrix [132]. The literature reports that GPB zones dissolve around 250°C [132]. The resultant solute from the dissolution of these zones induces the precipitation of the metastable and semicoherent S'(S) phase around 300°C, which may decrease the local strength of the alloy [128,132]. The S' phase is a strained version of the stable S phase (Al_2CuMg), therefore the two orthorhombic phases are usually reported as a single phase: the S'(S) phase. At temperatures above 350°C, the dissolution of the S'(S) phase occurs [128,132].

Additionally, Cu-rich intermetallic particles are formed during the processing of the alloy [120]. Coarse intermetallic particles and precipitates create active sites, increasing the corrosion susceptibility of this alloy [133,134]. The coarse intermetallic particles can lead to pitting corrosion due to their high self-corrosion potential through dissolution (or surrounding matrix dissolution, depending on the composition of the particles) [133]. The precipitates are often associated with the formation of Cu-depletion zones around the grain boundaries during their formation [133]. These zones create a potential gradient at the region around the grain boundaries, consequently increasing the susceptibility of intergranular corrosion [133].

This aluminum alloy is widely used in the aeronautical industry mainly due to its excellent specific strength and fatigue performance [119]. It also presents good machinability, conformability, and surface-finish capabilities. Plate products are used in fuselage structures, wing tension members, shear webs, ribs, and other different structural areas where stiffness and fatigue performance are required [119]. Sheet products, usually alclad, are extensively used in commercial and military aircraft for fuselage skins, wing skins, and engine areas where temperatures up to 120°C are achieved [119].

3.5.2 Carbon fiber-reinforced polyphenylene sulfide

Carbon fiber-reinforced polyphenylene sulfide (CF-PPS) is an engineering thermoplastic composite that offers outstanding mechanical performance at room and high temperatures [135]. Exemplary applications of this composite in the aircraft industry includes the "J-Nose" sub-frame wings of the Airbus A380 and the engine pylon cover of the Airbus A340-500/600 [135].

The matrix PPS is a homopolymer thermoplastic comprising linear chains [136]; its structural formula is represented in Figure 3.13. The PPS matrix presents a glass transition temperature (T_g) of approximately 90°C and a melting temperature (T_m) of about 280°C. In addition, the onset of thermal degradation for this polymer lies above 450°C [137]. PPS also offers excellent thermal stability and chemical resistance due to the combination of

sulfur and the aromatic ring in its macromolecule (Figure 3.13) [138]. Low moisture absorption and high service temperature (160-240°C) are also properties of this thermoplastic [138].

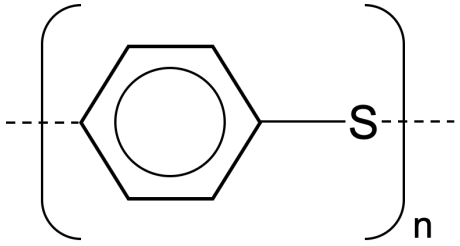

Figure 3.13 Repeat unit of PPS chain.

PPS is a semi-crystalline thermoplastic with an orthorhombic unit cell defined by a planar *zig-zag* conformation of the sulfide groups [142]. The phenyl groups are disposed alternately in angles of 40–45° on the backbone plane of the unit cell [142]. Such tridimensional disposition of the phenyl groups limits the mobility of the macromolecules. Therefore, the thermal transitions of PPS occur at relatively high temperatures, thereby increasing its service temperature when compared to aliphatic polymers [139].

The thermal degradation of PPS usually occurs in two stages. The first degradation process is the random scission of the polymer chains followed by cyclization [143]. This phenomenon usually starts at temperatures above 450°C and it is known as crosslinking. Above 550°C, the depolymerization mechanism dominates the degradation process of PPS and the molecular weight of the polymer starts to decrease [140]. The thermal decomposition of PPS was described by Budgell, Day and Cooney [141] using pyrolysis coupled to gas chromatography and mass spectrometry. The researchers identified the generation of cyclic tetramers, linear dimers, and trimers as a result of the cyclization mechanism of degradation up to 550°C. At higher temperatures (550–650°C), the presence of low molecular weight compounds was identified. Benzothiophenes and naftotiofenos were found as a result of the depolymerization of PPS.

The physicochemical and thermal properties of PPS, in combination with the high strength and stiffness of the carbon fibers, result in a tough, rigid, and chemical-resistant composite laminate [135]. Such properties suit the CF-PPS as a material for structural applications [142,143]. Additionally, the thermal properties of PPS provides the means to the application of the FSpJ process [35]. The high thermal transitions of PPS (T_g and T_m) allow the melting and reconsolidation of the polymer to generate the bonding mechanisms discussed in Section 3.1.2. Moreover, the high onset degradation temperature of PPS (450°C) ensures that there is no extensive thermal degradation of this polymer due to the FSpJ joining process, where temperatures up to 400°C are achieved [35].

Chapter 4. Experimental Approach

This doctoral work aimed to fulfill the knowledge gaps related to the mechanical integrity and corrosion behavior of AA2024-T3/CF-PPS friction spot joints for future aircraft applications. For this purpose, this work was performed in three phases, as depicted in Figure 4.1.

Phase I provided the guidelines for producing joints with the maximized level of mechanical strength. First, the FSpJ process was assessed considering the different available joining equipment to produce the joints. The formation of the joint was investigated along with the quasi-static mechanical performance and failure mechanisms. Thus, the reproducibility of the joints in comparison to the state-of-the-art friction spot joints was confirmed and the differences between the joining equipment were assessed. Further, the joining parameters were optimized using design of experiments (full-factorial 2^4) and analysis of variance (ANOVA) to maximize the lap shear strength of the joints. In addition, the influence of secondary factors like tool geometry, consolidation time, and cooling rate were addressed. Although Phase I was of major importance to the development of this work, its results are not discussed in this PhD thesis. The analyses from this phase are presented in Appendix A.

In accordance with the guidelines provided by Phase I, optimized friction spot joints were produced and evaluated in Phase II. Thus, Phase II contains a deep evaluation of the mechanical integrity and corrosion behavior of friction spot joints. In this phase, four stages are found: (a) damage evolution and failure behavior; (b) fracture energy and fatigue damage tolerance; (c) impact resistance; and (d) corrosion behavior, as indicated in Figure 4.1.

In Stage II-a, FEM was integrated with lap shear test to describe the damage evolution and failure behavior of the joints. Scanning electron microscopy (SEM) analysis was used to confirm the micro-mechanisms of failure in each bonding zone of the joint.

In Stage II-b, the single leg bending (SLB) fracture test was used to assess the fracture energy and fatigue damage tolerance of single friction spot joints under mixed-mode I/II loading. The strain energy release rate (G) was computed using the equations derived from linear elastic fracture mechanics. The crack growth resistance and fatigue damage tolerance of friction spot joints were addressed regarding the bonding zones and their bonding mechanisms.

Moreover, the impact resistance of the joints was evaluated using instrumented drop weight test in Stage II-c. The impact damage was assessed using non-destructive characterization techniques (ultrasonic scanning and laser scanning microscopy). Both aluminum and composite surfaces were subjected to impact to provide design guidelines

regarding the impact resistance of the joints. Shear after impact (ShAI) tests were performed to evaluate the residual strength of the joints after the impact.

Finally, the corrosion behavior of the joints was investigated through the salt spray test (SST) in Stage II-d. The joints were exposed during six weeks and their residual strengths were evaluated every one week using lap shear test. The corrosion phenomenon was investigated on the top surface and at the interface of the joints. The corrosion process on the top surface of the joint was correlated with the process-related microstructural changes of the aluminum part. Optical microscopy was employed to investigate the microstructure of the metallic part, while its local mechanical performance was addressed using Vickers microhardness. Small angle X-ray scattering (SAXS) was employed to assess the precipitates in the different microstructural zones of the joint. The corrosion process at the interface of the joints was correlated with the global strength degradation of the joints. SEM and energy dispersive spectroscopy (EDS) were used to describe the stages of corrosion development at the interface of the joints.

Phase III comprises a preliminary study on the upscaling of the FSpJ technology. In this phase, part of an aircraft fuselage was built using FSpJ as one of the joining methods, as a proof of concept for the use of FSpJ in aircraft structures. The design and the weight savings of the hybrid and friction-joined sub-component are presented.

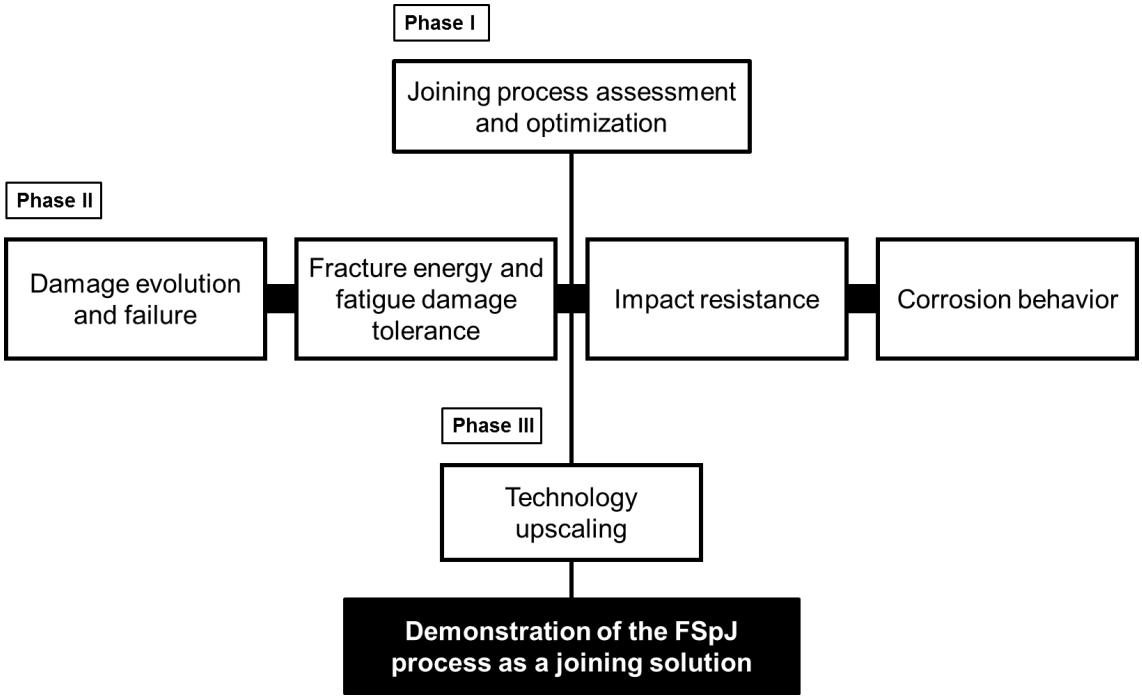

Figure 4.1 Schematic illustration of the phases included in this PhD project.

Chapter 5. Materials and Methods

In this chapter, details of the materials used in the work are presented. It also describes all the methods applied to analyze the different aspects of the hybrid joints during the development of the project.

5.1 Base materials

5.1.1 Aluminum alloy 2024-T3

The aluminum alloy 2024-T3 was selected as the metallic part to produce the joints in this investigation. This is a precipitation hardenable alloy, which has Cu and Mg as the principal alloying elements. Table 5.1 presents the nominal chemical composition of the alloy.

Figure 5.1 shows the microstructure of the aluminum alloy used in this work. The intermetallic particles are observed distributed in the grains and their boundaries.

Table 5.1 Nominal chemical composition of AA2024-T3.

Element	Cu	Mg	Mn	Fe	Zn	Si	Ti	Cr	Al
Wt%	4.55	1.49	0.45	0.17	0.16	0.10	0.02	<0.01	Bal.

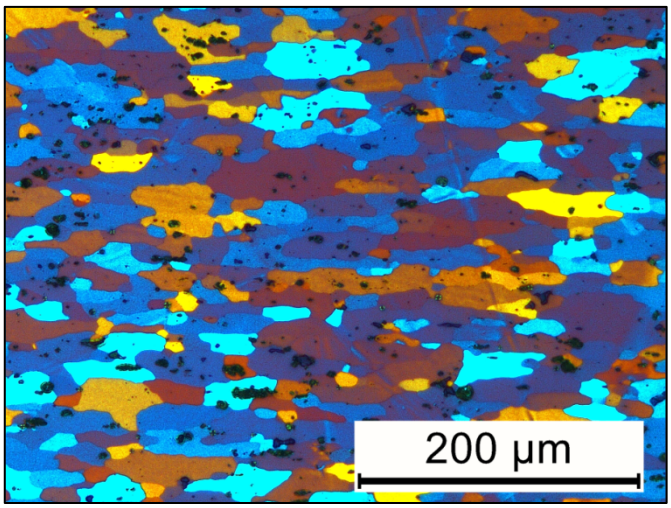

Figure 5.1 Microstructure of the AA2024-T3 parallel to the rolling direction.

In this work, 2-mm thick rolled sheets produced by Constellium were used. Table 5.2 lists the selected physical and mechanical properties of this alloy [144].

Table 5.2 Selected physical and mechanical properties of AA2024-T3 **[144]**.

Property	Value
Tensile Strength (TL direction) [MPa]	437
Yield Strength (TL direction) [MPa]	299
Tensile Modulus [GPa]	73
Shear Modulus [GPa]	28
Incipient Melting Temperature [°C]	502
Thermal Conductivity [W m^{-1} K^{-1}]	121
Coefficient of Thermal Expansion, 20–300°C [µm m^{-1} $°C^{-1}$]	24.7
Density [$g.cm^{-3}$]	2.78
Poisson ratio	0.33

5.1.2 Carbon fiber-reinforced polyphenylene sulfide

Carbon fiber-reinforced polyphenylene sulfide (CF-PPS) was selected as the composite part to produce the joints in this investigation. The composite used in this work consists of a quasi-isotropic laminate. It is composed of seven plies of carbon fiber fabric reinforcement in the $[(0.90)/(\pm45)]_3/(0.90)$ sequence. Laminate sheets of 2.17-mm in thickness and with 43 wt% carbon fibers woven fabric (5H satin configuration), produced by Tencate, were used. Figure 5.2 exhibits the microstructure of CF-PPS. Table 5.3 presents a selection of the relevant physical and mechanical properties of CF-PPS.

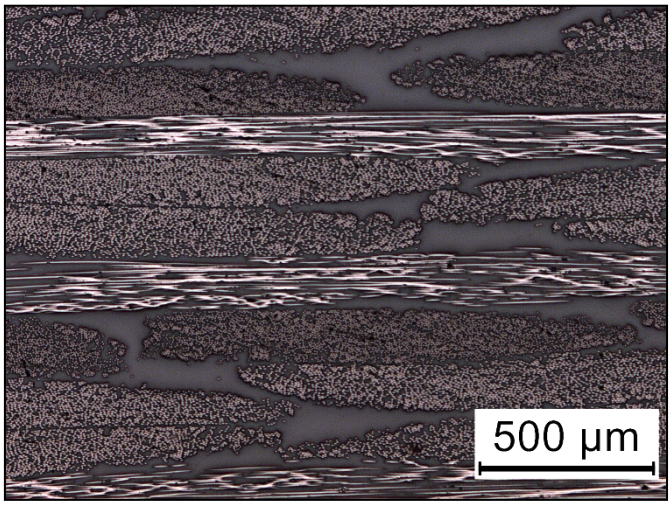

Figure 5.2 Microstructure of CF-PPS in the weft direction.

Table 5.3 Selected physical and mechanical properties of CF-PPS **[135]**.

Property	Value
Tensile Strength (warp/weft) [MPa]	790/750
In-Plane Shear Strength [MPa]	119
Tensile Modulus [GPa]	53
Flexural Modulus (warp/weft)	60/45
Glass Transition Temperature [°C]	120
Melting Temperature [°C]	280
Thermal Conductivity [W m^{-1} K^{-1}]	0.19
Coefficient of Thermal Expansion, 23–300°C [µm m^{-1} $°C^{-1}$]	52.2
Density [$g.cm^{-3}$]	1.35
Poisson ratio	0.2

5.2 Methods

5.2.1 Surface preparation

The aluminum part was sandblasted before the joining process to increase its surface roughness. Previous investigations [25,145] showed that such mechanical surface pre-treatment enhances the adhesion between aluminum and composite. The medium blast used was corundum (Al_2O_3, average particle size: 100 – 150 µm). The aluminum parts were sandblasted for 10 s at a distance of 20 cm and an incidence angle of 45° of the blasting pistol. The average surface roughness (R_a) of 6.7 ± 0.4 µm was obtained.

5.2.2 Joining procedure

FSpJ equipment

The friction spot joints were produced using an RPS 200 welding equipment (Harms & Wende, Germany), as depicted in Figure 5.3. This equipment was customized for the research purposes found in the Helmholtz-Zentrum in Geesthacht. The machine has a welding head, where the FSpJ tool is assembled, and a movable table where the parts to be joined are placed. In the welding head, both axial and rotational movements of the pin and the sleeve are individually actuated with electromechanical transducers. The RPS 200 is also equipped with 11 load cells to accurately measure the axial loads applied by the pin, the sleeve, and the clamping ring on the materials during the joining process. Besides, the torque of the sleeve and the pin are measured using load sensors attached to the

respective motors via lever arms. The load cells and sensors are connected to a data acquisition system, which provides live measurements of rotational speed, displacement, force, and torque during the joining process.

The RPS 200 has a torque capacity of 60 N.m along with 35 kN for the maximum joining force. Rotational speeds from 500 rpm up to 3300 rpm can be applied by this equipment. Besides, the upstroke (Z-axis) of RPS 200 can achieve 300 mm. It enables the joining of coupon specimens of thick materials as well as larger structures like structural subcomponents and components.

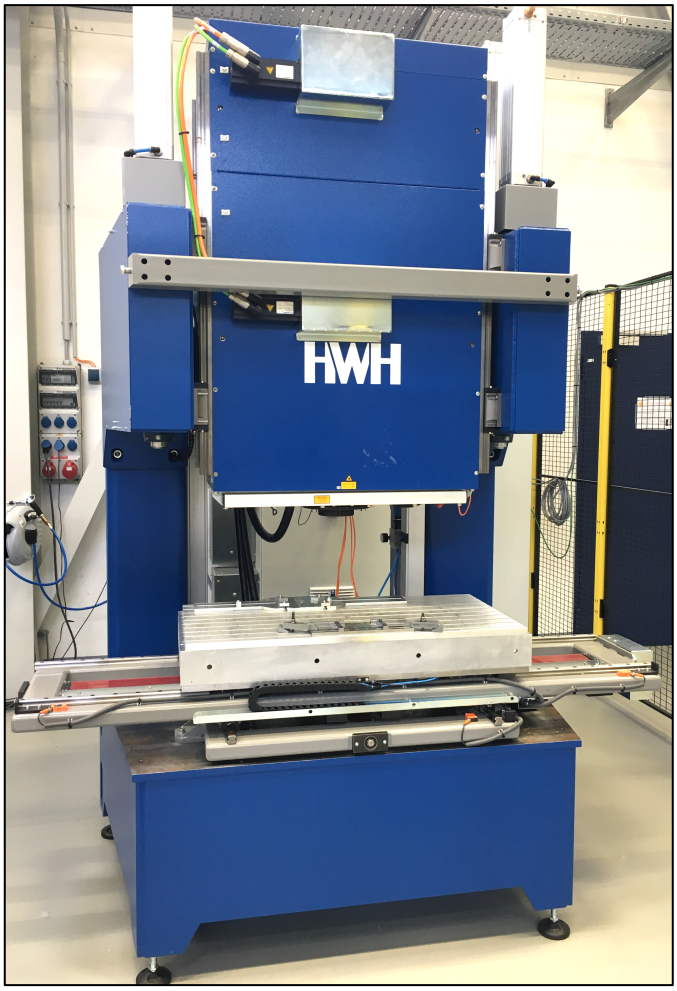

Figure 5.3 RPS 200 welding equipment used in this work.

The FSpJ tool used in this work was made of molybdenum-vanadium hot-work tool steel. The dimensions of the tool follow the description provided in Section 3.1.

A sample holder and manual clamping system were used to produce the joints (Figure 5.4). The sample holder was made of low alloy steel, while the manual clamping system consists of 8 mm thick 7XXX series aluminum alloy.

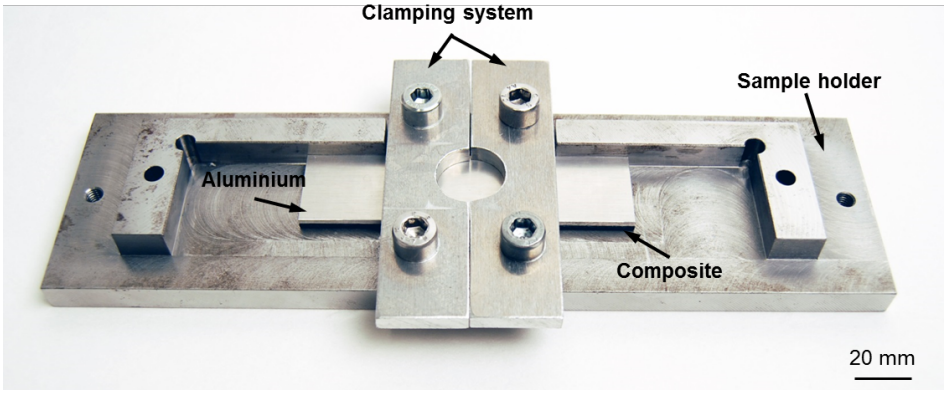

Figure 5.4 Sample holder and manual clamping system used to produce lap shear specimens.

Joining parameters

The joints were produced using the following joining parameters: 2900 rpm of rotational speed, 0.8 mm of plunge depth, 8 s of joining time, and 6 kN of joining force. This combination of the joining parameters was obtained from a statistical optimization to maximize the lap shear strength of the joints. A full-factorial design of experiments, in combination of analysis of variance (ANOVA), was employed. Appendix A summarizes the performed statistical analysis.

Temperature monitoring

The temperature evolution during the process was monitored with an infrared thermo-camera (Infratec, Germany) set within the range of 150–700°C. The data acquisition frequency was 80 Hz. The measurements were performed on the aluminum surface around the tool. The set-up for the thermography measurements is presented in Figure 5.5. The maximum process temperature was considered as the highest temperature measured on the aluminum surface around the tool.

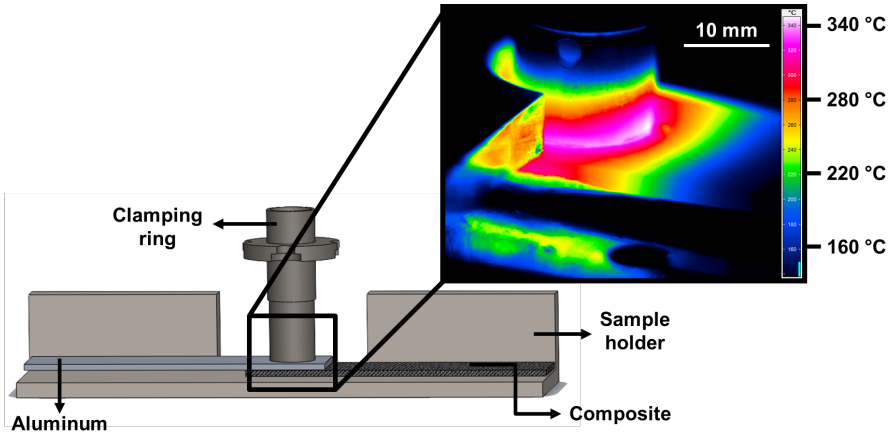

Figure 5.5 Illustration of the set-up for infrared thermography along with an example of the snapshot during the joining process.

5.2.3 Microstructural analysis

Optical microscopy

Optical microscopy (DM IR microscope, Leica, Germany) with polarized light was employed to investigate the changes in the microstructure of the aluminum part of the joint after FSpJ. The top surface of the joint was embedded and prepared following standard grinding and polishing procedures. Further, the specimen was electrochemically etched to reveal the microstructure of the aluminum. A standard Barker solution was employed. The specimen was etched at 25 V during 60 s and then observed in the microscope.

Scanning electron microscopy (SEM)

The microstructure of the joints was also analyzed using scanning electron microscopy (SEM) for high-contrast images of the corroded specimens. In this case, the cross-section of the joints was embedded and prepared following standard grinding and polishing procedures. Further, the samples were gold-sputtered and then analyzed by SEM (FEI, QUANTA FEG 650, USA). A voltage of 10 kV and a working distance of 10 mm were utilized.

Small-angle X-ray scattering

The changes in size and volume fraction of the precipitates in the aluminum part of the joint after FSpJ were investigated using small angle X-ray scattering (SAXS). The measurements were performed along a line crossing the center of the joint to cover the different microstructural zones of the spot joint, as indicated in Figure 5.6. The scan line was 50 mm long with a step size of 1 mm between measured points. The measurements were performed using X-rays with an energy level of 87.1 keV. The beam had a cross-section of 0.2 mm × 0.2 mm; the distance between the sample and the detector was 3460 mm, and a beam stop with 1mm diameter was used. A Perkin-Elmer area detector with a pixel size of 200 μm and an exposure time of 20 s was also employed. An empty measurement (i.e. without sample), corrected for the sample transmission, was subtracted from each image. The images were then reduced to scattering curves by azimuthal integration using the program Fit2d [146]. The scattering curves were analyzed based on the two-phase model of the particles in a homogeneous matrix. All the precipitates were modeled as spheres. Two lognormal size distributions were applied to fit the measured scattering curves using a least-squares algorithm. Inter-particle interference was taken into account using the local monodisperse approximation [147]. A constant isotropic contribution was added to the scattering of the precipitates.

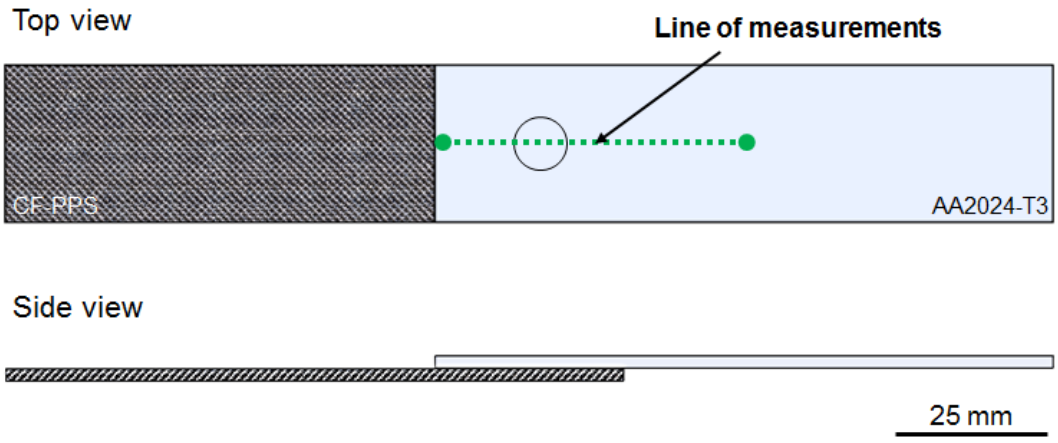

Figure 5.6 Schematic drawing showing the SAXS measurements on the aluminum surface of the joint.

5.2.4 Local mechanical properties

Microhardness measurements were performed on the top surface of a friction spot joint to evaluate the influence of FSpJ on the local mechanical performance of the aluminum alloy. The indentations were performed on half of the overlap area of the joint (25 mm x 12.5 mm) in consideration of the symmetry of the joints. The indentation force was 200 g (applied for 10 s) and the distance between indents was 0.3 mm in agreement with the ASTM E384-10 standard procedure.

5.2.5 Global mechanical properties

Lap shear test

Lap shear tests were employed to evaluate the quasi-static mechanical performance of the joints in this study. The tests were carried out using a universal testing machine, Zwick/Roell 1478 (Germany), with a cross-head speed of 1.27 $mm.min^{-1}$ at room temperature. A load cell of 100 kN was used. The distance between jigs was 125 mm. Specimens with 645.16 mm^2 of overlap area were tested; dimensions details of the specimen are given in Figure 5.7. The average shear strength of the joints was evaluated based on five replicates.

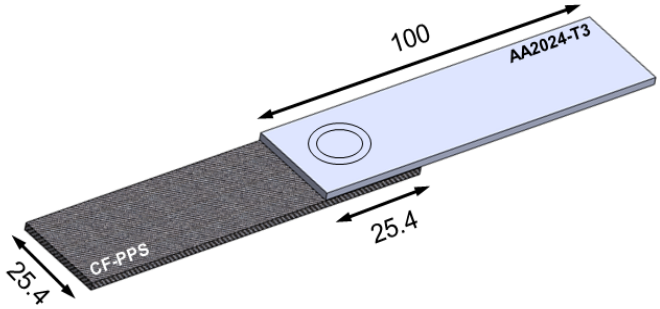

Figure 5.7 Configuration and dimensions of the joints used for lap shear test (in mm).

Single leg bending (SLB) test

The fracture energy as well the fatigue crack growth behavior of single friction spot joints were evaluated using the single leg bending test (SLB). The SLB is a mixed-mode I/II test, which is widely used to characterize the interlaminar fracture of wood, composites, and adhesive bonded joints [50,57,71]. In this interlaminar fracture test, the aluminum and the composite work as slender beams. The test is performed using a three-point bending test apparatus, as depicted in Figure 5.8. The composite part of the joint is shorter than the aluminum part. Thus, one extremity of the composite part is unsupported, creating the mix of modes I and II at the joint interface during loading (Figure 5.8). The geometry of the joints used to carry out this test is given in Figure 5.8. The length (L) of the specimens in this study was 85 mm, comprising 33 mm of initial crack (a_0), 25 mm of joined length, and 27 mm of unbonded length to guarantee the stabilization of the test. Although there is no standardized geometry of SLB specimens, the geometry used in this work was based on several studies of mixed-mode fracture characterization for composites and adhesive bonded joints [73,76,148]. The literature indicates that when $0.25L<a_0<0.45L$ is satisfied, a stable crack propagation is achieved.

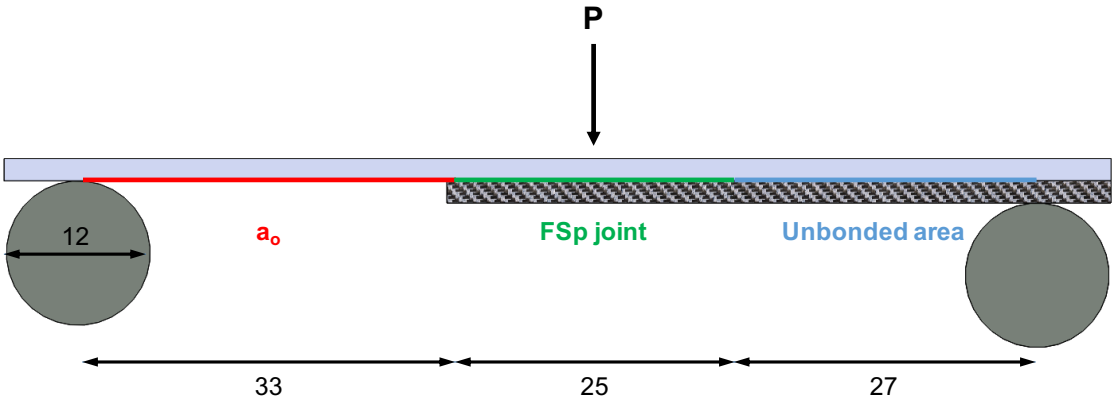

Figure 5.8 Configuration and dimensions of the joints used for SLB test (in mm).

The static SLB test was employed to characterize the resistance of the joint interface to crack extension. The side of the joints was painted matte-white to facilitate the visualization of the crack tip. Additionally, a paper ruler was attached along the joined length to assist the crack length reading. The crack size was visually monitored and recorded using a high-speed camera. The data acquisition frequency of the camera was 1 Hz. The tests were performed using a transverse speed of 0.5 $mm.min^{-1}$ at room temperature using a universal testing machine, Zwick/Roell 1478 (Germany). A load cell of 100 kN was used in this work. The force-displacement curve and the crack measurements were obtained for three replicates.

The cyclic SLB test was performed to simulate in-service mixed-mode loading of the joints. The fatigue crack growth behavior of the joints was investigated under 50% of the

respective static strength using a load ratio of R = 0.1. Combined with a frequency of 1 Hz, appropriate monitoring of the crack propagation is ensured. The side of the joints was also painted matte-white to facilitate the visualization of the crack tip. Additionally, a paper ruler was attached along the joined length to assist the crack length reading. The crack size was visually monitored and recorded using a high-speed camera. The data acquisition frequency of the camera was 4 Hz and pictures were taken every 100 cycles. The crack growth rate was computed using the secant method recommended in the ASTM E647-10. Three replicates were tested.

In both cases (static and cyclic SLB), the strain energy release rate was calculated in accordance with the linear elastic fracture mechanics concepts and the beam theory described in Section 3.2.

Drop weight test

The impact resistance of the friction spot joints was assessed using drop weight testing. An instrumented drop weight tower was used to perform the impacts. The tower was equipped with an anti-rebound system to avoid secondary impacts. The configuration of the joints for the drop weight test is presented in Figure 5.9. The overlap area of the joints was clamped between the cylindrical pneumatic clamping fixtures, as shown in Figure 5.10. A semi-spherical impactor with a radius (r) of 6.25 mm was used (Figure 5.10). The specimens were impacted at the center of the overlap area where the spot joint was produced. Four levels of impact energy were investigated: 2 J, 4 J, 6 J, and 8 J. These levels of impact energy were chosen after a first assessment of the impact resistance of the friction spot joints. In this way, damages starting from barely visible up to the complete failure of the joint were covered. To provide a design guideline regarding the impact damage tolerance of such hybrid joints, the specimens were impacted from both facets, i.e., one set of specimens from the aluminum side (AS) and another set from the composite side (CS). The load applied by the indenter on the specimens was measured during the impact events by a strain gauge full bridge placed on the head of the impactor. Three replicates were tested for each energy level.

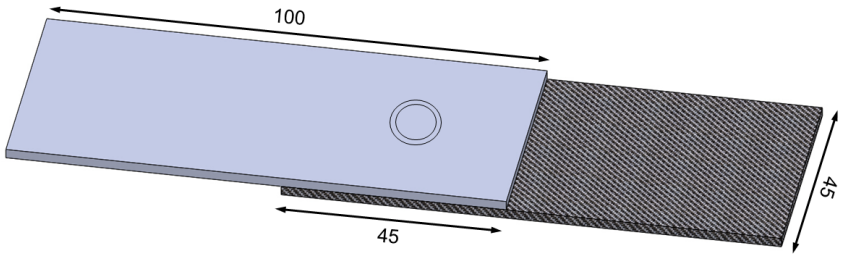

Figure 5.9 Configuration and dimensions of the joints used for the drop weight test (in mm).

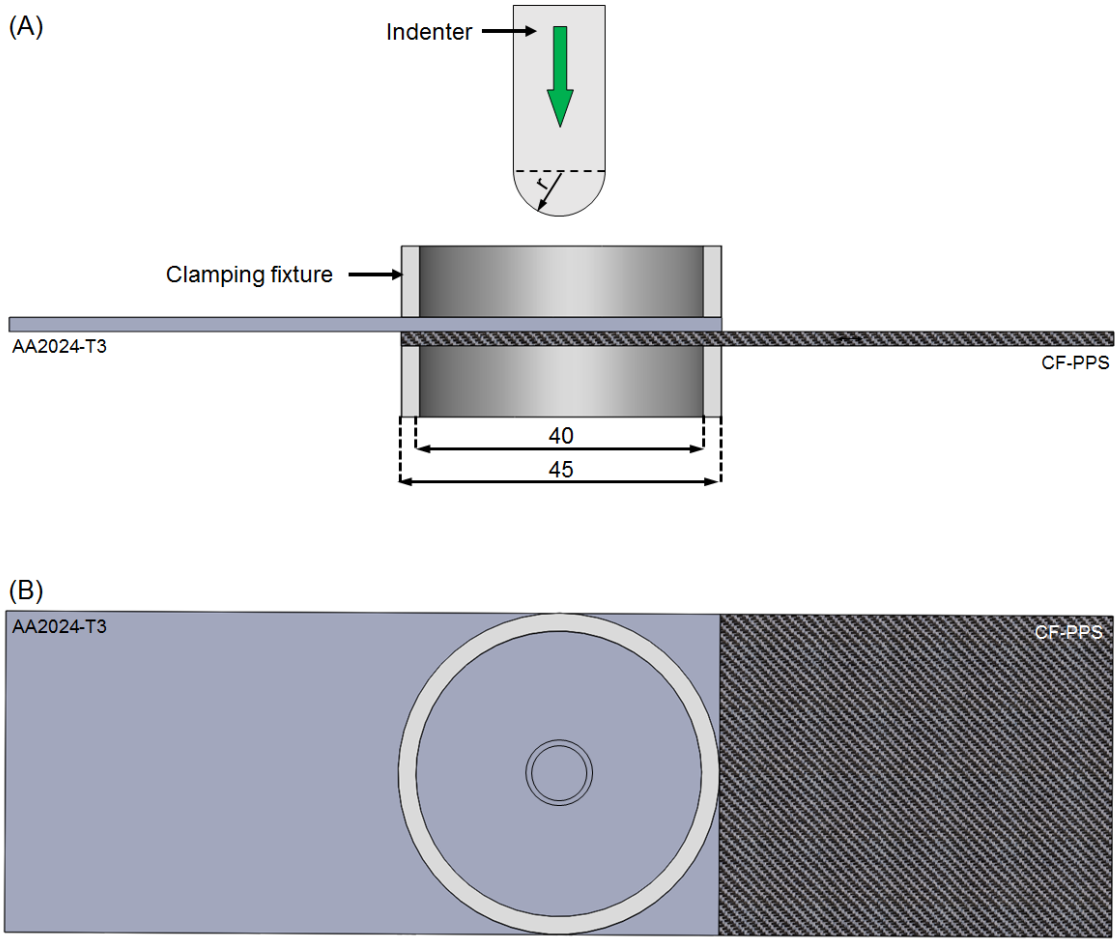

Figure 5.10 Schematics of the clamping of the specimens during drop weight test. (A) Cross-sectional view and (B) top view of the configuration used in this work.

Furthermore, the lap shear test was employed to assess the residual strength of the joints after impact. Such tests are known as shear after impact (ShAI); they are widely applied in the aircraft industry to assess the impact damage tolerance of composite structures [149]. The tests were performed in accordance with the procedure described earlier in Section "Lap shear test." The average residual shear strength of the joints was evaluated based on three replicates for each impact condition.

5.2.6 Salt spray testing (SST)

The corrosion behavior of friction spot joints was evaluated using salt spray exposure. The configuration of the joints for this test is the same given in Figure 5.7. The hybrid joints were placed vertically at an angle of 30° in a salt spray chamber for one, two, three, four, five, and six weeks. The time frame of the test was selected after a first assessment of the corrosion resistance of the joints. Thus, the different corrosion stages could be monitored until the final degradation of the joined area. In accordance with ASTM B117-16, the chamber was kept at 35°C with the pressure of 1 bar and concentration of 5% NaCl of the salty fog. Five replicates were tested for each time of exposure.

The residual strength of the joints after exposure was evaluated using lap shear test, as described in Section 5.2.5. The average residual shear strength of the joints was evaluated based on five replicates.

5.2.7 Electrochemical characterization

The base materials used to produce the joints were electrochemically characterized using potentiodynamic polarization. It is important to note that the electrochemical properties of CF-PPS vary according to the amount of exposed carbon fibers on its surface. Therefore, the measurements for CF-PPS were performed using a sample extracted from the PDZ of the joints to ensure maximum fiber exposition. For AA2024-T3, a standard sandblasted surface was used.

The electrochemical measurements were performed using an Interface 1000E Potentiostat/galvanostat/ZRA (Gamry) embedded with the Gamry framework system. The potentiodynamic polarization of AA2024-T3 and CF-PPS was conducted in a three-electrode system. The test sample was the working electrode, while platinum and silver/silver chloride (Ag/AgCl) were the counter and reference electrodes respectively. A scan rate of 1 mV/s was employed, and the measurements started after 6 minutes of immersion in E_{oc} (open circuit potential) conditions. The potentiodynamic polarization for AA2024-T3 samples was performed from -0.2 V to 1V vs. stable E_{oc} (~-0,58V) following the anodic direction, whereas for CF-PPS the scan was performed over the 0.2 V to –1 V range vs. stable E_{oc} (~0.08V) following the cathodic direction. The experiments were repeated at least three times. The measurements were performed at room temperature in a solution of 0.5 % NaCl.

5.2.8 Non-destructive inspection

Confocal laser scanning microscopy

Confocal laser scanning microscopy (VK-9700, Keyence, Japan) was employed to generate 3D profiles of the aluminum and the composite surfaces after the drop weight test. The area and depth of the damage generated due to the impact were measured from the 3D profiles. The three replicates from the drop weight test were evaluated.

Ultrasonic scanning

Another non-destructive inspection of the joints was performed using an automated ultrasonic scanning system (USPC 3040, Hilliger, Germany) based on a single pulse-echo sensor. The overlap area of the joints was scanned before and after the drop weight test. The scans of the overlap area were performed from the composite side of the joint to investigate the damage evolution through the plies of the composite. Additionally, the aluminum side of the joints was also scanned to evaluate the effective contact/adhesion at the metal-composite interface. A frequency of 1 MHz and speed of 2700 ms^{-1} and 1600

ms^{-1} were employed to scan the specimens from the composite and the aluminum side, respectively. The measurements were performed with a resolution of 0.1 mm with water as medium. Figure 5.11 exemplifies the ultrasonic scanning from the aluminum side of the joint.

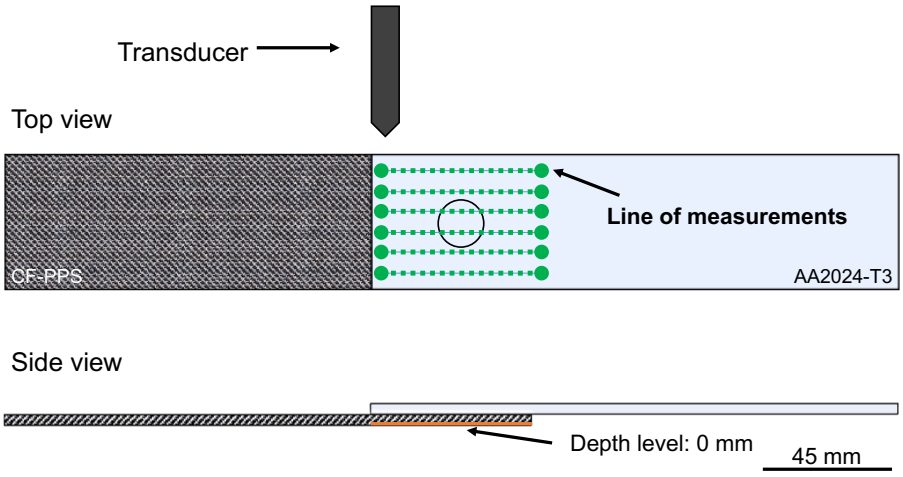

Figure 5.11 Schematics of the ultrasonic scanning, here depicting the scanning on the aluminum surface of the friction spot joint.

5.2.9 Fracture surface analysis

Scanning electron microscopy (SEM)

The failure micro-mechanisms of the joints were analyzed using scanning electron microscopy (SEM). The fractured surfaces of the joints were gold-sputtered and then analyzed by SEM (FEI, QUANTA FEG 650, USA). A voltage of 10 kV and a working distance of 10 mm were utilized.

Energy dispersive spectroscopy (EDS)

Energy dispersive spectroscopy, coupled with SEM, was employed to identify and characterize the corrosion sites in the joints exposed to the salt spray. In this case, the top surface and the fracture surface of the joints were analyzed. The software EDAX TEAM was used to evaluate the obtained spectra. The specimens were gold-sputtered prior to the examination to guarantee surface conductivity. The measurements were performed with a voltage of 10 kV, working distance of 10 mm, and spot size of 4.

5.2.10 Finite element modeling

Finite element modeling (FEM) was used in this work to predict the damage evolution in the different bonding zones of the friction spot joints. The software Abaqus was used to perform the simulations. The specimen geometry corresponds to the one used for the lap shear test (Figure 5.7), since the validation of the model was performed using this test.

Discretization of the interface

The joined area of the joints was modelled based on the discretization of its bonding zones and the metallic nub geometry. As discussed in Section 3.1, the joined area of a friction spot joint consists of three bonding zones: PDZ, TZ, and AZ. For simplification purposes and owing to its reduced area compared to both AZ and PDZ, the TZ was coupled with the PDZ in this study (Figure 5.12). The area of each zone was approximated to the values obtained from the fracture surfaces of the joints after mechanical testing. The PDZ has an area of 197 ± 12 mm^2 and the AZ of 268 ± 9 mm^2. Figure 5.12 presents (A) a real fracture surface along with the bonding zones and (B) the discretized zones in the model for a friction spot joint. In addition to the discretization of the bonding zones, the geometry of the metallic nub was also included. The nub geometry was modeled based on a typical cross-section of a friction spot joint, as indicated in Figure 5.13.

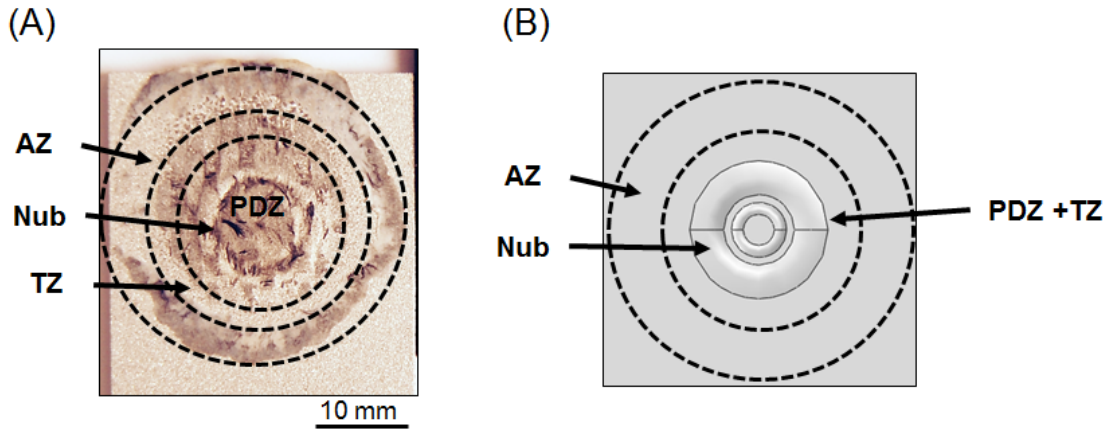

Figure 5.12 (A) Typical fracture surface of friction spot joints and (B) discretized bonding zones and nub geometry on the surface of the aluminum part for the finite element model.

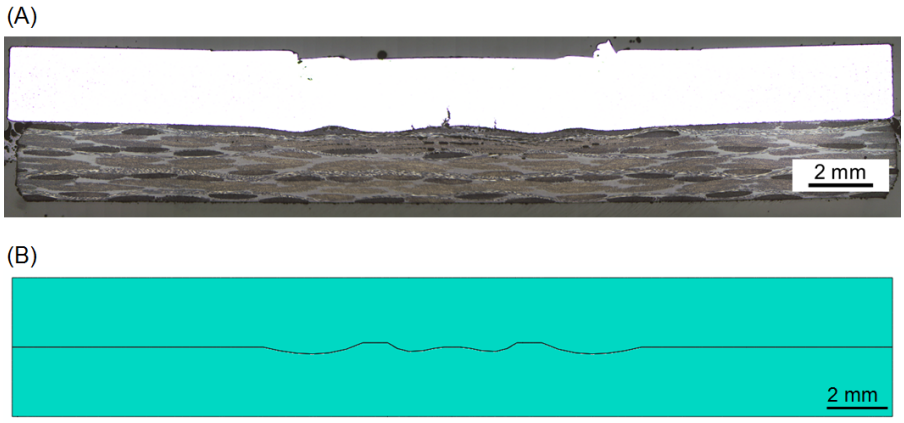

Figure 5.13 Cross-sections showing the nub geometry of (A) a real friction spot joint and (B) the joint in the finite element model.

Interface interaction

A variety of options is offered by Abaqus to define contact and model the interface of the joints [150]. In this study, the cohesive behavior feature was employed. This feature applies the fundaments of damage mechanics to model the behavior of an interface by using cohesive zone models. This strategy has been widely used to investigate the fracture behavior of composites and adhesive joints [151–157]. Cohesive behavior can be applied to surfaces having direct contact (cohesive surfaces) or to a layer of elements located between two surfaces (cohesive elements) [150]. Owing to its simplicity and good agreement with the failure mode of the joints, the cohesive surfaces option was employed in this study.

Cohesive behavior is ruled according to the traction-separation law [150,158]. The uncoupled traction-separation behavior was selected to simplify the model. In this way, the input to the law is just the cohesive stiffness coefficients in the pure normal (nn), tangential (tt), and shear (ss) directions. The force (t) at the contact interface is given through a linear elastic relation between the normal, tangential, and shear stiffness (K_{nn}, K_{tt}, K_{ss}) and separations (δ_{nn}, δ_{tt}, δ_{ss}), respectively [19]. Equation 5.1 [158] denotes the uncoupled traction-separation law.

Equation 5.1
$$t = \begin{Bmatrix} t_n \\ t_s \\ t_t \end{Bmatrix} = \begin{bmatrix} K_{nn} & 0 & 0 \\ 0 & K_{ss} & 0 \\ 0 & 0 & K_{tt} \end{bmatrix} \begin{Bmatrix} \delta_n \\ \delta_s \\ \delta_t \end{Bmatrix} = K\delta$$

The values of stiffness (K) were assigned to the bonding zones considering that the PDZ is the strongest region of the joint [35]. Primarily, the values were inferred from the elastic portion of the load-displacement curves of the joints under shear loading. Next, these initial values were optimized to obtain a better fit between the experimental and numerical force-displacement curves and the out-of-plane displacement of the joints observed during shear loading. Table 5.4 presents the final values of the stiffness coefficients applied to the different bonding zones modeled in this study.

Table 5.4 Cohesive stiffness coefficients used as input to model the different bonding zones of the joints in this work.

Bonding zone	K_{nn} [N.m^{-1}]	K_{ss} [N.m^{-1}]	K_{tt} [N.m^{-1}]
AZ	10^6	10^7	10^5
PDZ	3.6×10^{10}	3.6×10^{11}	3.6×10^9

Damage criteria

The traction-separation law applied to model the properties of the interface was complemented with a damage criterion to model the failure of the joint. The damage criterion employed is based on the separation (displacement) between the surfaces initially in contact. The displacement values for the initiation and completion of damage in a given bonding zone are provided as the input to control the damage evolution between the cohesive surfaces. Table 5.5 presents the values of separation applied to model the damage initiation and complete failure in the different bonding zones of the joint. These values were inferred from the experimental force versus displacement curves coupled with DIC.

Table 5.5 Displacements for initiation and completion of damage in the bonding zones of the joint in this model.

Bonding zone	Initiation - $\delta_{nn,\,ss,\,tt}$ [mm]	Complete failure - δ_{max} [mm]
AZ	10^{-3}	0.10
PDZ	0.08	0.62

Boundary conditions

The boundary conditions were set to simulate the lap shear test of the overlap joints. Therefore, the aluminum part was fixed, while the composite part was subjected to a constant and uniform displacement by imposing shear loading to the interface of the joint (Figure 5.7).

Modelling of the base materials

As discussed in Section 3.1, plastic deformation of the composite matrix in the PDZ of friction spot joints is the main micro-mechanism of failure in this zone [42]. Therefore, the composite was modeled with an elasto-plastic behavior, while the aluminum was assigned an elastic behavior. The elasto-plastic behavior of the CF-PPS was modeled by the load-displacement curve of the material under tensile load provided by its manufacturer. The elastic properties of the aluminum alloy as well as its Poisson ratio are given in Table 5.2.

Both base materials were meshed with hexahedrical eight-node elements with quadratic interpolation and reduced integration (Abaqus C3D20R).

Results and Discussions

The results obtained in this doctoral work are divided into five chapters to ensure a proper discussion. Chapter 6 deals with damage evolution at the interface of the friction spot joints which integrates FEM and experimental data. Chapter 7 is devoted to the characterization of the fracture energy and the fatigue damage tolerance of the friction spot joints. The impact resistance of the joints is investigated in Chapter 8. The corrosion behavior of the hybrid joints is addressed in Chapter 9. Finally, Chapter 10 provides an overview of the first steps for the upscaling of the Friction Spot Joining technology.

Chapter 6. Damage evolution and failure behavior of friction spot joints

This chapter is devoted to understand the damage evolution at the interface of the friction spot joints under shear stresses. For this purpose, FEM and analytical characterization of the joints were integrated. Firstly, a finite element model to predict the static strength of the friction spot joints is validated using lap shear testing. Next, the model is applied to assess the development of stresses at the interface regarding the shear load levels applied to the joint. Moreover, the finite element model is used to describe for the first time in the literature, the damage evolution at the interface of the friction spot joints. The damage evolution is described regarding levels of applied stress and the different bonding zones of the joints. Furthermore, the prediction of the damage evolution is integrated with loading-unloading hysteresis curves of the joint to clarify the damage micro-mechanisms in the different bonding zones according to load levels. The influence of the bonding zones on the mechanical behavior of the joints is also addressed using FEM. Finally, the chapter is concluded with the proposal of an updated theory of failure for the friction spot joints based on the new findings of this study.

6.1 Prediction of damage evolution at the interface of the joint using Finite Element Method

Figure 6.1 presents the force-displacement curves obtained from lap shear tests and the finite element model developed in this study (Section 5.2.10). One observes that the experimental average ultimate lap shear force (ULSF) is 3770 ± 288 N, while the simulation presents 4061 N of ULSF. It demonstrates that the model predicted the failure load of the friction spot joints with a deviation of 8%. Regarding the displacement at failure of the joints, the FE model showed 0.61 mm, while the experimental average was 0.62 ± 0.15 mm; a deviation of 1.6%. Both deviations, for ULSF and displacement at failure, are below 10%, indicating a very good agreement between the numerical output and the experimental data to evaluate the mechanical performance of the friction spot joints.

Figure 6.2 depicts the stress development at the interface and through the cross-section of the friction spot joint during shear loading. One observes that the stress concentration becomes asymmetrical as the loading of the joint progresses. The stress initiates to concentrate from the free edge of the CF-PPS (Figure 6.2-B and C). As the loading of the structure progresses, the composite bends in an attempt of its lower surface to displace in the loading direction despite the connection of the upper surface to the aluminum surface (Figure 6.2-D-G). The same phenomenon is observed for the aluminum part (Figure 6.2-D-G). This bending effect is known as secondary bending and it is a result of the eccentric load path induced by the overlap configuration of the joints [159,160]. McCarthy *et al.* [161] and Egan *et al.* [162] reported increased stress concentration and reduced joint

stiffness as a result of secondary bending in bolted joints. Also, Ekh *et al.* [163] demonstrated that secondary bending strongly influences the failure mode of composite bolted joints. In addition, the secondary bending has also proven to be a critical factor for the fracture behavior of adhesive bonded joints [164–167]. Lee *et al.* [165] investigated the mechanical behavior of adhesive bonded double-strap and supported single-lap GFRP joints. The authors showed that the joint strength was almost independent of the adhesive type. Nevertheless, the peeling effect created by the secondary bending of the structure was crucial to the failure behavior of the joints.

One observes that the out-of-plane displacement resultant from the secondary bending is less expressive for the aluminum part due to its higher stiffness in comparison to the CF-PPS ($E_{AA2024\text{-}T3}$ = 73 GPa, $E_{CF\text{-}PPS}$ = 53 GPa). The cross-sectional views of the joint in Figure 6.2 display a more pronounced bending at the free edge of the composite on the right-hand side of the overlap area. The secondary bending of the composite implies the opening of the interface, thereby increasing the concentration of tractive stresses in this half of the joined area (yellow-red field in Figure 6.2-D-G). Hence, a strong stress concentration is seen around the nub on the right-hand side of the joined area (bright red fields in Figure 6.2-F and G). It indicates the bearing of load through the anchoring effect provided by the metallic nub into the composite. Finally, a small field of compression stress is identified on the left-hand side of the joined area, close to the free edge of the aluminum part (dark blue fields in Figure 6.2-D-G). It is believed that such compression stresses are generated due to the bending of the composite part, which leads to the compression of the aluminum surface by the composite in that region. Additionally, the relative movement between aluminum and composite also squeezes the walls of the metallic nub against the composite during shear loading, thus contributing to the compressive stresses in this region. Note that the compressive stresses are also observed through the thickness of the aluminum part in Figure 6.2-F and G due to the anchoring of the nub into the composite.

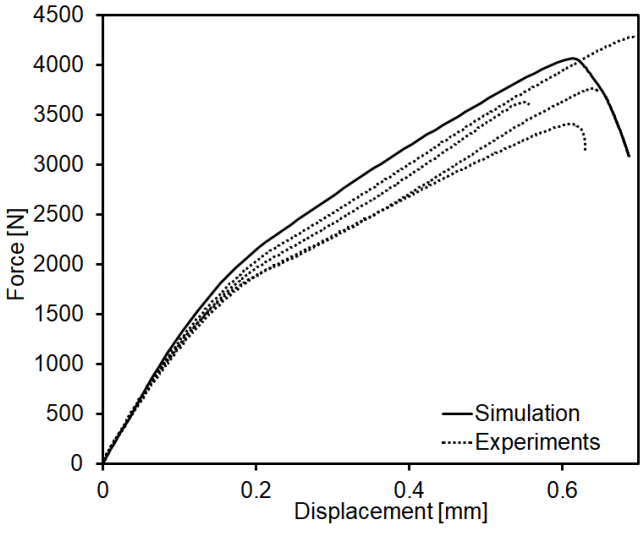

Figure 6.1 Force-displacement curves obtained from lap shear tests and the finite element model.

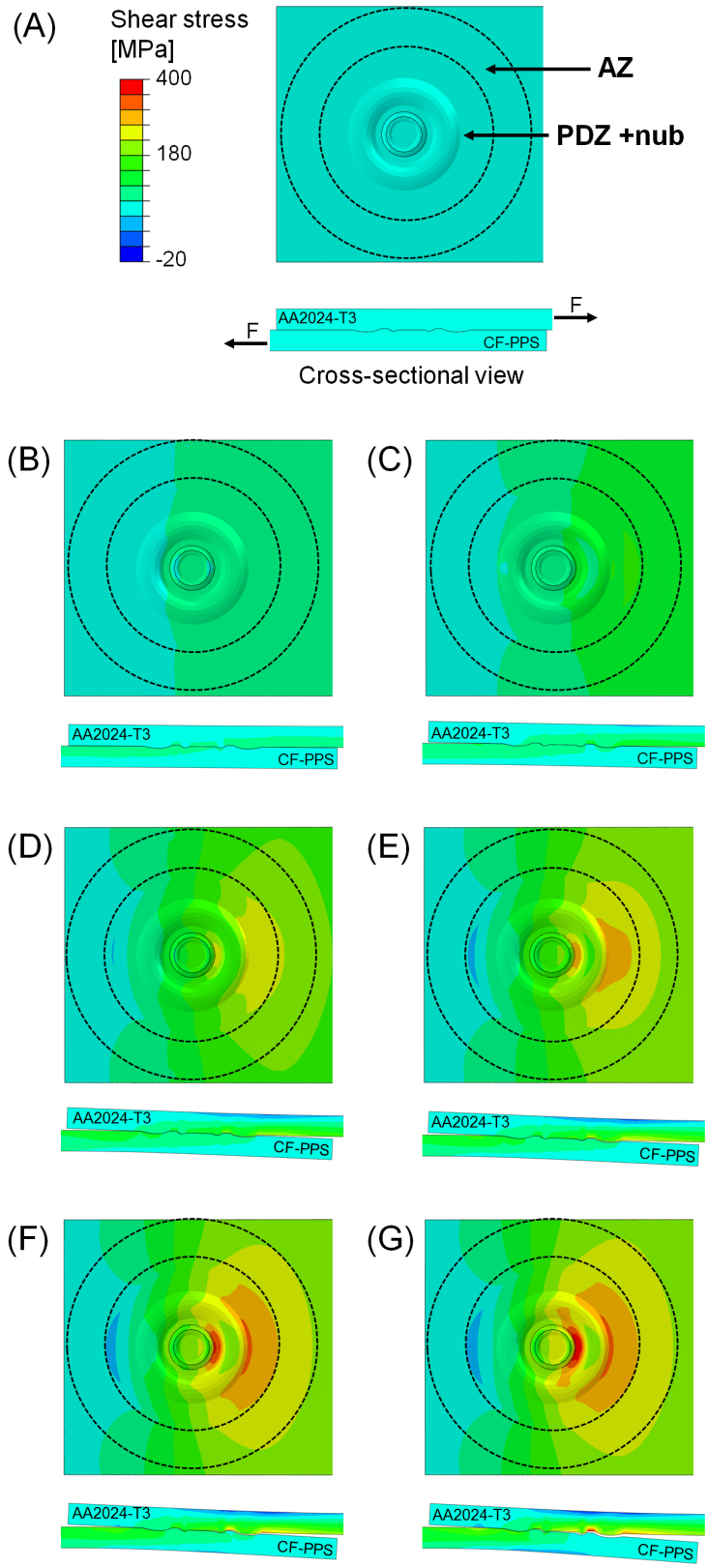

Figure 6.2 Shear stress profile at the interface (aluminum surface) and through the cross-section of the joint during loading. (A) 0 N, (B) 500 N, (C) 1500 N, (D) 2500 N, (E) 3000 N, (F) 3500 N, and (G) 4000 N.

The damage evolution at the interface of the joints is given in Figure 6.3. One observes that the damage of the interface initiates at the borders of the AZ (Figure 6.3-B). Further, the damage propagates with a linear front symmetrically from the edges to the center of the joined area (Figure 6.3-B). One observes that the damage in the AZ evolves rapidly, demonstrating the low load-bearing capability of this bonding zone. The finite element model showed that the damage initiates at approximately 30 N and completes at 750 N in the AZ (Figure 6.3-B-E). From 750 N until 1500 N, it is believed that the stresses are borne by the mechanical anchoring of the metallic nub. Thus, at 1500 N, damage starts to occur inside the PDZ (Figure 6.3-F). As the damage advances inside the PDZ, one observes that its propagation turns into an asymmetrical linear front (Figure 6.3-G-H). The damage evolves preferably from the free edge of the composite part as a result of the asymmetrical out-of-plane-displacement expressively developed for loads superior than 1500 N (Figure 6.2-D-G**)**. It is possible to observe that, at 3500 N, the damage starts to propagate also on the opposite side of the PDZ, close to the free edge of the aluminum part (Figure 6.3-I). Nevertheless, the damage in the PDZ already reached the nub at 3500 N, propagating from the free edge of the composite (Figure 6.3-I). Therefore, rapid damage propagation is observed, leading to the total failure of the interface at approximately 4000 N (Figure 6.3-J).

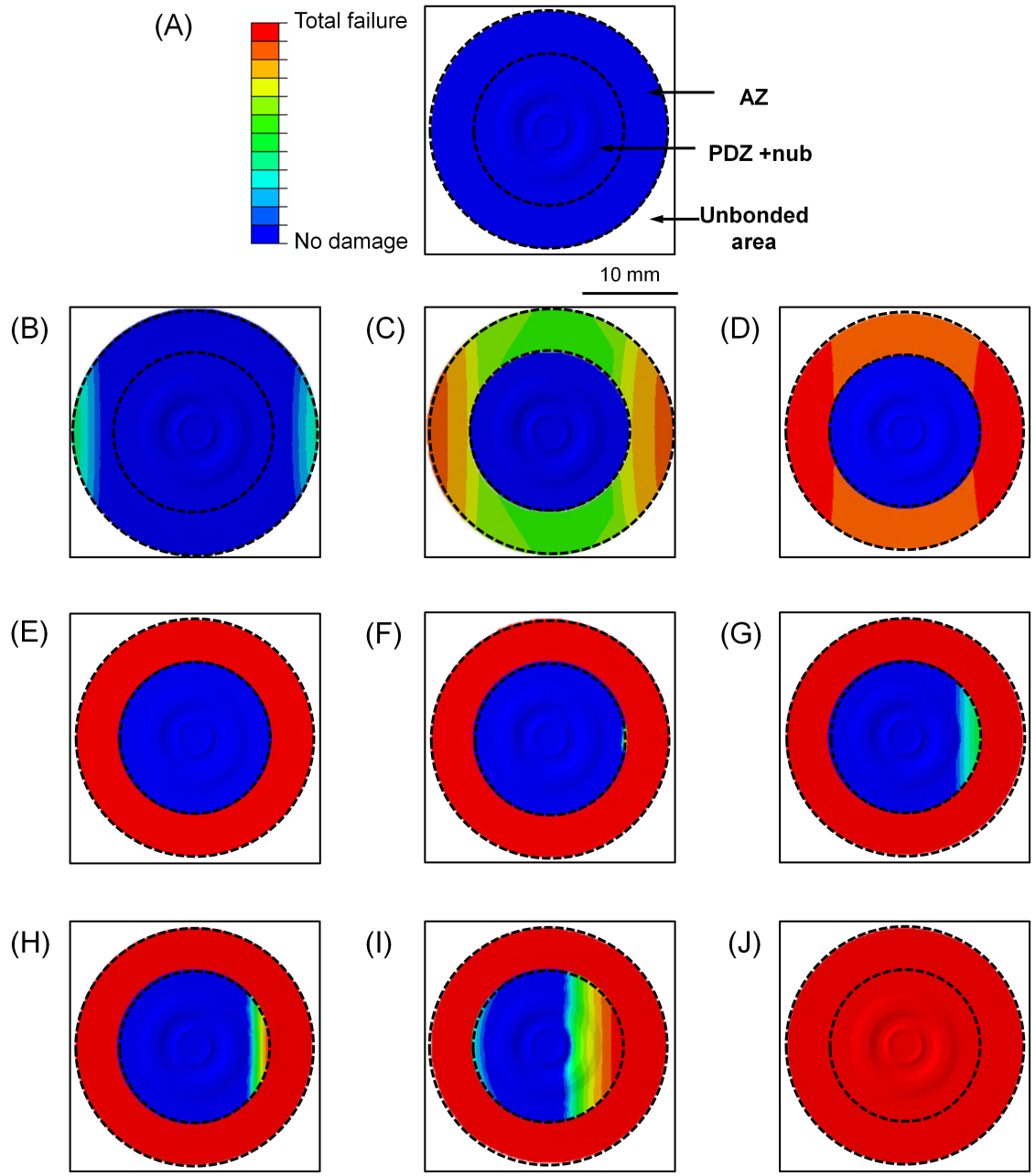

Figure 6.3 Damage evolution at the interface of the joints during shear loading. (A) 0 N, (B) 30 N, (C) 150 N, (D) 500 N, (E) 750 N, (F) 1500 N, (G) 2500 N, (H) 3000 N, (I) 3500 N, and (J) 4000 N.

6.2 Influence of the bonding zones in the mechanical behavior of friction spot joints

Combining the force-displacement curves (Figure 6.1) and the damage evolution presented in Figure 6.3, it is possible to infer the damage evolution rate at the AZ and the PDZ. Table 6.1 summarizes the initiation and completion of the damage in each bonding zone. The AZ presents a damage evolution rate of 0.14 % N^{-1}, while the PDZ fails at a rate of 0.04

% N^{-1}; approximately three times slower than the degradation rate of the AZ. It demonstrates once more that the PDZ is the strongest zone of the friction spot joints [22]. As discussed in Section 3.1, in the PDZ the main bonding mechanism in the PDZ is the mechanical interlocking provided by the metallic nub (macro scale), and the polymer and fiber attachment to the aluminum surface (micro scale). In contrast, in the AZ the parts are connected through adhesion forces. Thus, a higher level of efficiency is expected from the mechanical interlocking in comparison to the adhesion forces, leading to a lower degradation rate of the PDZ than that of the AZ.

Table 6.1 Damage evolution rate of the bonding zones of the friction spot joints obtained using FEM.

Bonding zone	Damage initiation [N]	Complete failure [N]	Damage evolution rate [% N^{-1} of applied force]
AZ	29	726	0.14
PDZ (includes TZ and nub)	1532	4061	0.04

These observations indicate significant differences in the contributions of the different bonding zones to the mechanical performance of the friction spot joints. Using FEM, the mechanical behavior of the joints without the AZ and without the metallic nub (flat interface) under shear loading was investigated. Figure 6.4 displays the force-displacement curves obtained for the joints without AZ and without the metallic nub and compares them with a standard joint containing all the typical features of friction spot joints.

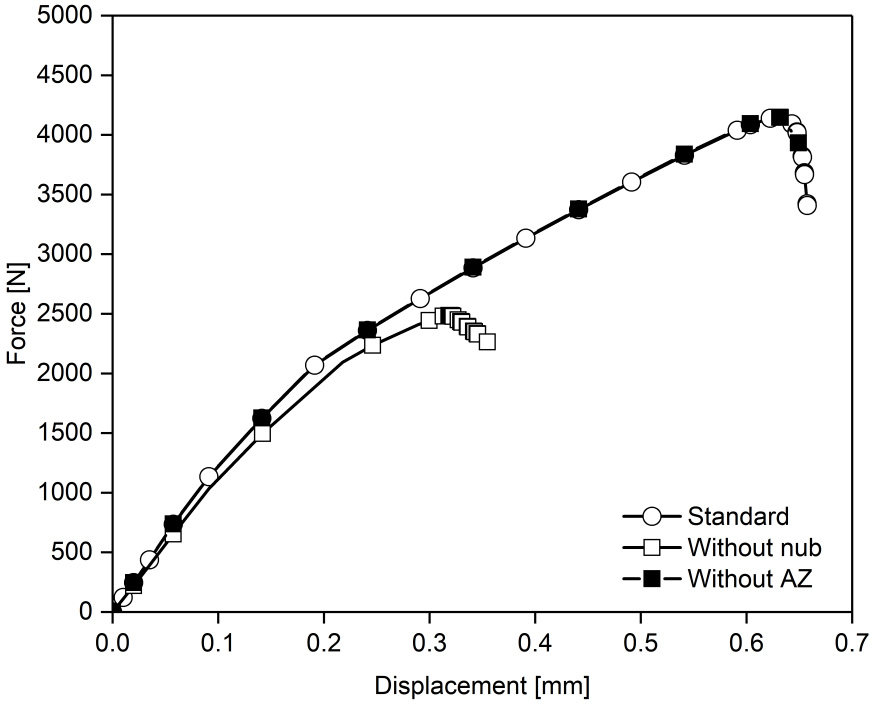

Figure 6.4 Prediction of the influence of the bonding zones and the metallic nub in the mechanical behavior of friction spot joints using FEM.

One observes that the joint without AZ presents a mechanical behavior practically identical to the standard joint (Figure 6.4). No changes in stiffness, ultimate lap shear force, or displacement at failure are observed. It suggests that the AZ does not contribute to the global mechanical performance of friction spot joints. The crack growth resistance of friction spot joints is evaluated in Chapter 7 to validate this prediction. Additionally, it is important to note that although AZ does not seem to contribute to the mechanical performance of the joints, this zone has an important role in the corrosion protection of friction spot joints. This aspect of AZ is discussed in Chapter 9.

In contrast, the mechanical behavior of the joint without the metallic nub strongly differs to the mechanical behavior observed for the standard joint (Figure 6.4). The initial stiffness of the joint without the nub is slightly lower than that of the standard joint; approximately 8.3 kN mm^{-1} for the standard joint and 8.0 kN mm^{-1} for the joint without nub. This result suggests that the initial stiffness of friction spot joints is mainly dictated by the PDZ, since it did not significantly change when AZ and the nub were removed (Figure 6.4). Additionally, one observes that the elongation of the joint decreased drastically when the nub was removed. The joint without nub prematurely failed at 0.32 mm of displacement, while the standard joint extended until 0.61 mm (Figure 6.4). Considering the damage evolution presented in Figure 6.3, this result suggests that the joint without nub failed rapidly after the damage reached the PDZ. The bearing of load in the PDZ seems to be majorly due to the shearing between the metallic nub and the volume of composite around it. Therefore, this zone is weakened without the nub. This observation indicates that the nub strongly contributes to the bearable load of the PDZ and consequently to the ductility of the joint.

The geometry of the nub also demonstrated to have strongly influenced the mechanical behavior of friction spot joints. Details of this investigation are found in [36] (Appendix B).

6.3 Damage evolution and its mechanisms

In this section, the damage mechanisms are described considering the different load levels and bonding zones of the joints. Additionally, correlations with FEM predictions, presented in Section 6.1, are established. For these purposes, one friction spot joint was subjected to subsequent loading and unloading steps. Six levels of maximum load were investigated: 500 N, 1000 N, 1500 N, 2000 N, 2500 N, and 3000 N. At the attempt of a final load level of 3500 N, the joint failed due to the accumulated damage. The hysteresis curves are presented in Figure 6.5-A.

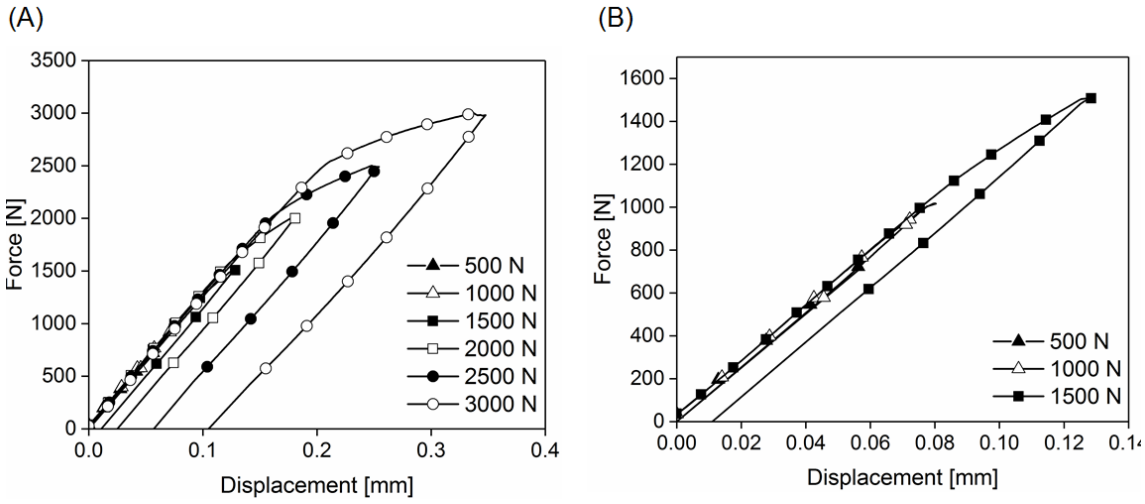

Figure 6.5 (A) Hysteresis curves for shear loading and unloading of friction spot joints. (B) Detail of (A) for the load levels 500 N, 1000 N and 1500 N.

The unloading section of the hysteresis curves demonstrates that up to 1000 N there was no permanent displacement when the joint was totally unloaded, as indicated by the close-up in Figure 6.5-B. It demonstrates that the joint did not plastically deform up to this load level. Considering the damage evolution presented in Figure 6.3, the damage propagation at 1000 N is retained in the AZ. Therefore, it is concluded that the damage mechanism in this bonding zone does not include plastic deformation. Figure 6.6 shows details of the fracture surface of a friction spot joint in the AZ. The reconsolidated polymer layer that composes the AZ is identified in Figure 6.6-B with a featureless surface. As also reported by Goushegir *et al.* [42], the featureless fracture surface in the AZ indicates that the crack propagated through the interface in this region. In this case, the adhesive failure mode is predominant and the main failure mechanism is the simple decoupling of the interface. Nevertheless, Figure 6.6-C and D show signs of plastic deformation and tearing at the borders of the polymer layer in the AZ. Therefore, it is expected that the mechanism of damage changed as the damage evolves from the AZ to the center of the joint as the load increases.

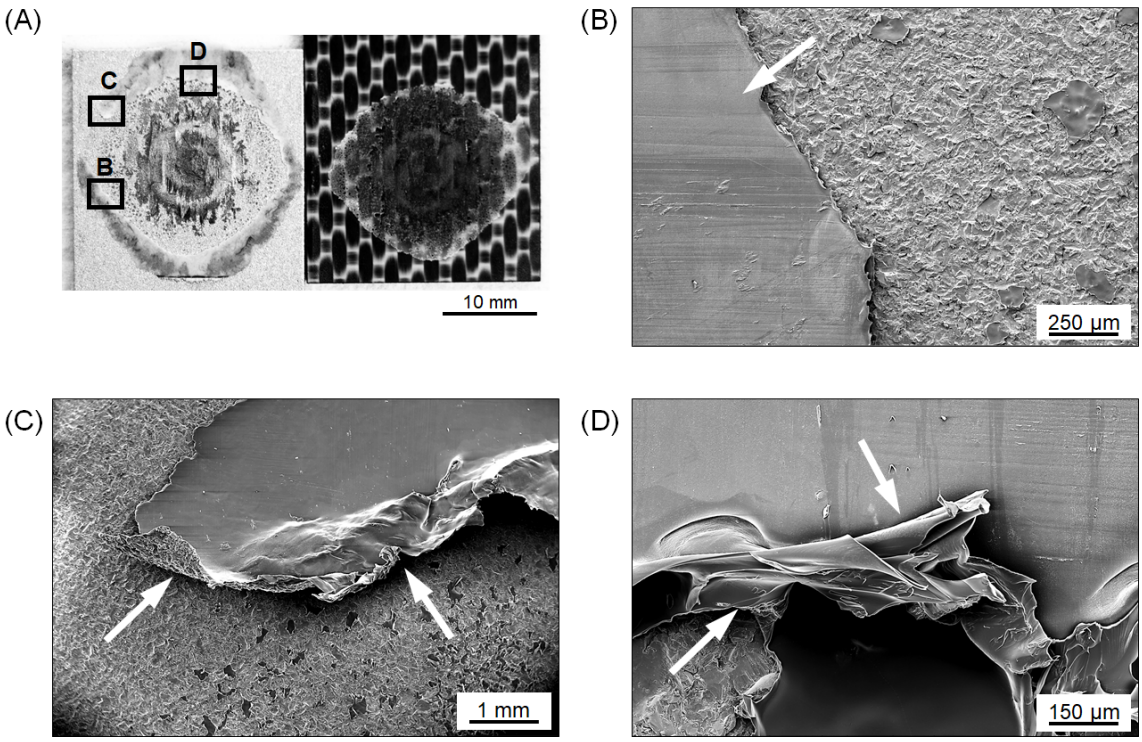

Figure 6.6 (A) Typical fracture surface of a friction spot joint showing details of AZ. (B) Featureless fracture surface of the polymer layer in AZ. (C) Detachment of the borders of the polymer layer in AZ. (D) Signs of plastic deformation at the borders of the polymer layer in AZ.

Starting from the load step of 1500 N, permanent displacements are observed after the unloading of the joint (Figure 6.5-B). The impossibility to return to zero displacement after the complete unloading indicates the occurrence of plastic deformation during the loading of the joint to 1500 N (1). In addition, Figure 6.3 demonstrates that the damage starts to propagate into the PDZ also at 1500 N (2). The observations (1) and (2) indicate that the main failure mechanism in the PDZ is plastic deformation. The fracture surface analysis of the joint shows the plastic deformation of the PPS matrix in different regions inside the PDZ (Figure 6.7). Plastic deformation of the PPS in a matrix-rich area on the composite fracture surface is observed in Figure 6.7-B. Figure 6.7-C shows fibrils of PPS close to the center of the joint (nub region), indicating extensive plastic deformation in this area. Additionally, plastic deformation of the PPS matrix around the fibers attached to the aluminum surface is observed in Figure 6.7-D. As discussed in Section 3.1, plastic deformation was also identified in the PDZ by Goushegir *et al.* [42] in the failure mechanism analysis for friction spot joints.

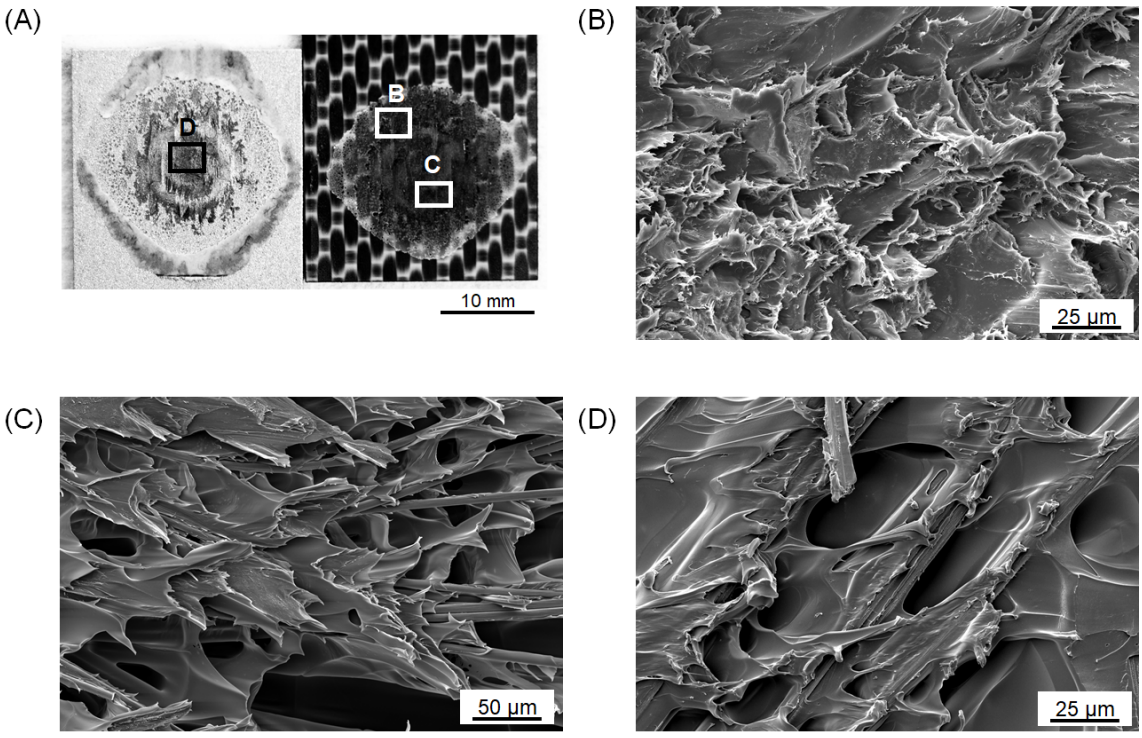

Figure 6.7 (A) Typical fracture surface of a friction spot joint showing details of the PDZ. (B) Plastic deformation of PPS in a matrix-rich area in the PDZ. (C) Fibrils of PPS in the PDZ. (D) Plastic deformation of the PPS matrix around the fibers.

Figure 6.5-A also shows that the permanent displacement after unloading continuously increased from 0.01 mm (1500 N) up to 0.11 mm (3000 N), indicating progressive plastic deformation in the PDZ until the final failure of the joint. Although the damage at the interface progressively increases at each loading step, the initial stiffness of the joint did not significantly change until the load level of 2500 N was reached (Figure 6.8). The joint presented an initial stiffness of 13.1 kN mm^{-1} until the loading step of 2500 N. After this step, the stiffness decreased to 12.5 kN mm^{-1} until the final failure of the joint; a decrease of approximately 5%.

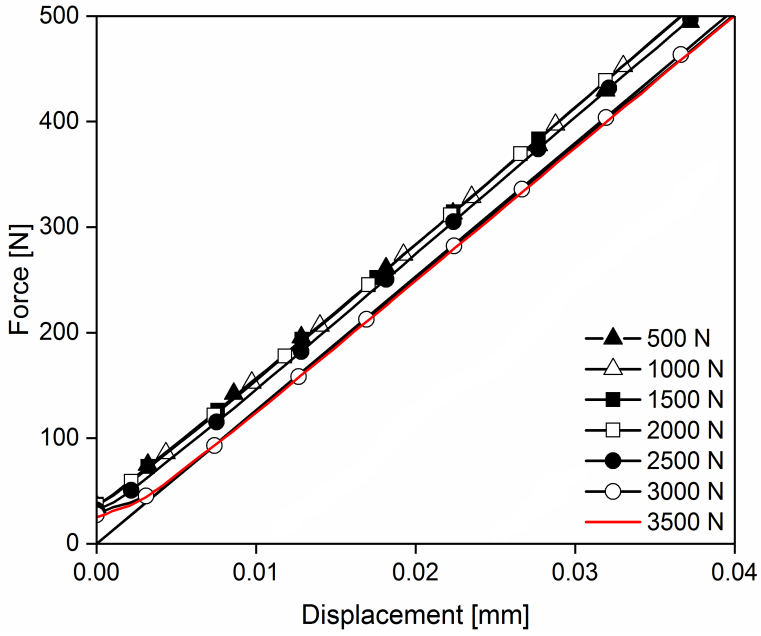

Figure 6.8 Detail of Figure 6.5-A showing the devolution of the initial stiffness of the joint in accordance with the loading steps. The joint failed during the load step of 3500 N.

As discussed in Section 6.2, the finite element model indicated that the initial stiffness of the friction spot joints is mainly dictated by the PDZ (Figure 6.4). In addition, the main damage mechanism of the PDZ was demonstrated to be plastic deformation (Figure 6.5 and Figure 6.7). The plastic deformation of semi-crystalline polymers, such as the PPS in this study, is a complex phenomenon and it is still discussed nowadays [168,169]. Nevertheless, several authors have agreed on the occurrence of strain hardening due to the orientation of the amorphous phase in semi-crystalline polymers [168,170]. Such phenomenon occurs through the disentanglement and orientation of the macromolecules in the amorphous phase between the crystallites [168,171]. This strengthening mechanism comprises overcoming the secondary bonds between the entangled macromolecules in the amorphous phase, thereby orientating the chains in the direction of load. At the maximum orientation of the chains, the load is borne by the primary bonds in the highly oriented bundles of macromolecules [169,172]. Therefore, strengthening is observed for the material under load before its failure.

Thus, the minimal decrease in stiffness of the joint (Figure 6.8), even at stages of extensive damage at the interface (Figure 6.3), may be a result of strain hardening due to the plastic deformation of PPS in the PDZ (Figure 6.7). Evidences of strain hardening were also identified for the friction spot joints under cyclic loading (Section 7.3.1). In this case, bundles of the stretched PPS matrix were found widely distributed in the fracture surface (Figure 7.4). Besides, the cyclic loading initiated crazes in the deformed PPS matrix. Crazes are a result of localized yielding of the polymer [171]. They appeared as apertures between bundles of highly oriented macromolecules, indicating the occurrence of strain hardening [19] (Figure 7.4).

6.4 Failure theory for friction spot joints: A summary

In 2016 Goushegir *et al.* [42] proposed a failure theory for friction spot joints based on the fracture surface analysis. The authors reported that the failure of friction spot joints occur in four stages, which could be identified in the force-displacement curve of the joints. Figure 6.9 depicts the typical force-displacement curve for friction spot joints divided into the four stages of failure, previously proposed by Goushegir.

Stage 1 corresponded to the high-stiffness linear-elastic behavior of the joints. It was believed that the crack radially nucleates at the periphery of AZ in this stage.

Stage 2 comprised the region of reduction in stiffness of the joint. In this stage, the crack would radially propagate through the AZ until the TZ. The authors believed that the stiffness reduction was due to the complete failure of the AZ.

Stage 3 corresponded to the low-stiffness linear-elastic behavior of the joints. In this stage, it is believed that the crack propagated through the TZ and in the PDZ.

Finally, stage 4 comprised the final catastrophic failure of the joint as the ULSF is reached.

The failure theory proposed by Goushegir has greatly contributed to the understanding of the damage evolution in friction spot joints and instigated further investigations in this topic. Thus, the findings of the present study add and clarify important aspects of the failure behavior of the joints, thereby refining Goushegir's failure theory for friction spot joints.

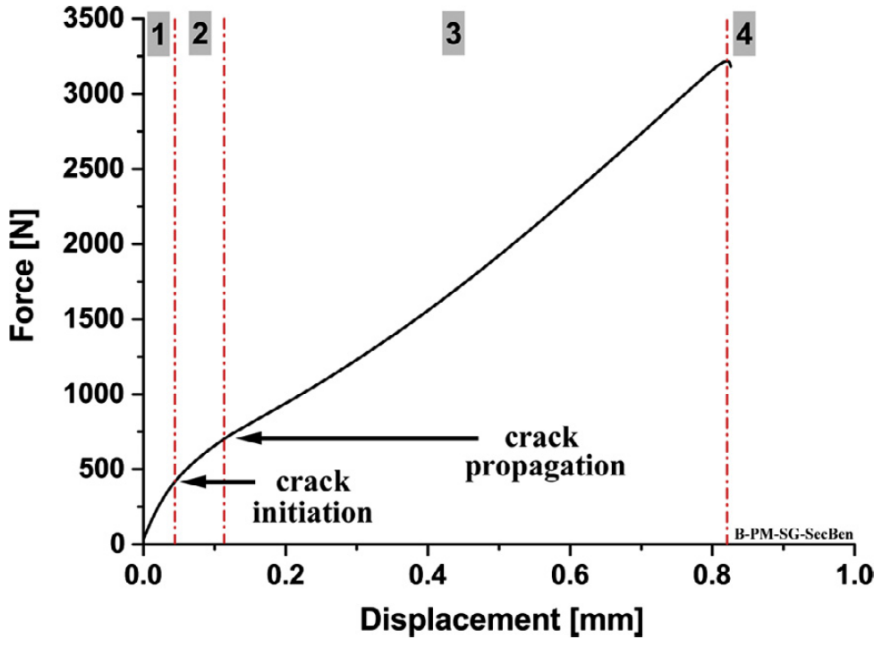

Figure 6.9 Four stages of the failure theory proposed by Goushegir *et al.* [42] for friction spot joints (Reproduced with permission).

Based on the results discussed earlier in this chapter, modifications and reaffirmations are proposed to the four stages of the failure theory of Goushegir *et al.* [42]. Figure 6.10 summarizes the new failure theory for friction spot joints based on the findings of this study.

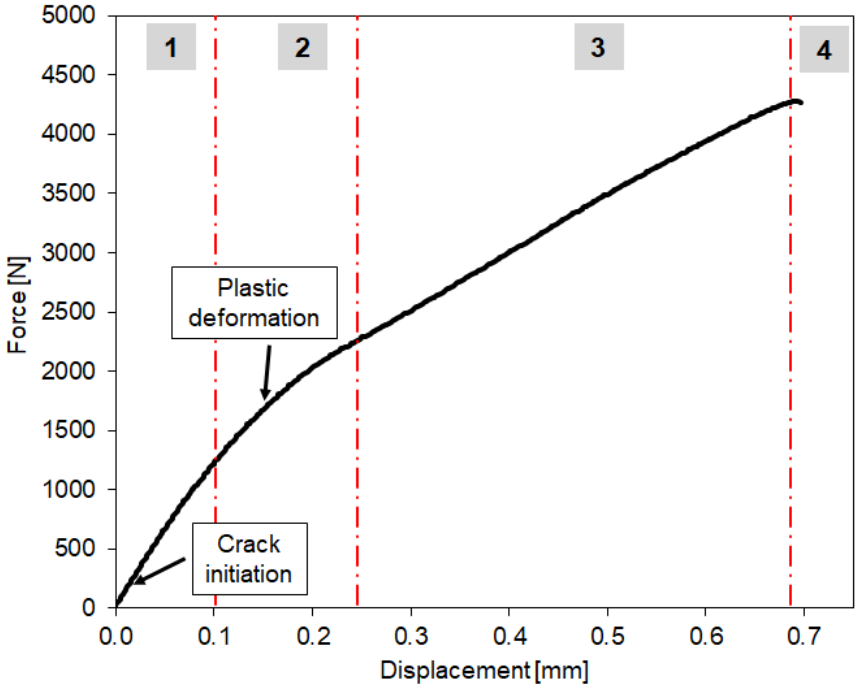

Figure 6.10 Proposal of failure theory for friction spot joints based on the new findings of this study.

Stage 1 comprises the high-stiffness linear-elastic behavior of the joints, as previously proposed [42] (Figure 6.10). The hysteresis curves presented in Figure 6.5 do not indicate the occurrence of plastic deformation until 1000 N, thus confirming the linear-elastic behavior up to this load. Thus, Stage 1 occurs approximately from 0 N to 1000 N (Figure 6.10). Additionally, the damage evolution prediction using FEM demonstrated that the crack initiates and propagates through the AZ, leading to the total failure of this zone at 750 N (Figure 6.3). Therefore, it is believed that Stage 1 actually comprises the complete failure of the AZ. This contradicts the previous theory, which assumed only nucleation of the crack at the borders of the AZ in this stage. In addition, the crack was shown to have a linear front of propagation (Figure 6.3), contradicting the radial crack propagation formerly suggested by Goushegir *et al.* [42].

Stage 2 remains characterized by the reduction in stiffness of the joint. This stage occurs approximately from 1000 N to 2000 N (Figure 6.10). Previously, it was believed that such stiffness reduction was due to the complete failure of the AZ. However, the FEM damage prediction indicates that the stiffness reduction matches with the evolution of the damage from the AZ to the PDZ. Both phenomena occur around 1500 N (Figure 6.1 and Figure 6.3). Concomitantly, the hysteresis curves presented in Figure 6.5 demonstrate the onset

of plastic deformation at this load level. These observations indicate that the stiffness reduction observed in the force-displacement curves is actually due to the damage initiation in the PDZ through plastic deformation.

Stage 3 comprises the propagation of the damage in the PDZ, as depicted in Figure 6.3. This stage occurs approximately from 2000 N until the ULSF is reached (Figure 6.10). The hysteresis curves presented in Figure 6.5 confirm the progress of plastic deformation in this stage. Starting from 1500 N, the permanent displacement after unloading continuously increases from 0.01 mm (1500 N) up to 0.11 mm (3000 N) (Figure 6.5). Therefore, this stage may no longer be characterized as a low-stiffness linear-elastic behavior, since plastic deformation is observed. Additionally, one also notes that Stage 3 becomes practically non-existent when the nub is removed from the PDZ (Figure 6.4). Therefore, it is believed that the plastic deformation in this stage is majorly due to shearing between the metallic nub and the volume of composite around it. This demonstrates the major role of the metallic nub in the ductility of friction spot joints.

Finally, Stage 4 remains as the fraction of second when the USLF is reached and the joint catastrophically fails, as previously formulated in [42].

Chapter 7. Fracture energy and fatigue damage tolerance of friction spot joints

This chapter applies the fundamentals of linear elastic fracture mechanics to investigate the fracture energy and fatigue damage tolerance of friction spot joints. The joints were subjected to a mixed-mode I/II loading to simulate in-service loads. The crack was monitored throughout the static and fatigue life of the joint. The strain energy release rate at the crack tip was calculated using a linear beam theory that incorporates transverse shear and elastic foundation effects. Thus, the mode-mixity of the fracture test was evaluated. Further, the typical R-curve of friction spot joints is presented for the first time in the literature. Additionally, the influence of the different bonding zones of the joint on the strain energy release rate and the fatigue crack growth were addressed. The chapter is concluded with a preliminary model developed to predict the fatigue crack growth behavior of friction spot joints.

7.1 Mode-mixity characterization

Overlap joints are widely used in aerospace, aircraft, and automotive applications [173,174]. Among the singularities of this type of joint, the overlap configuration is known to create an eccentric load path which results in the secondary bending of the components of the joint [175,176]. Therefore, a combination of in-plane tension and shear stresses (modes I and II respectively) are generated as the overlap joints are loaded [177]. Thus, a mixed-mode I/II of loading was employed in this study to simulate the in-service loading conditions of the single lap friction spot joint. Quasi-static single leg bending was used to investigate the crack growth resistance of the joints, as described in Section 5.2.5. Additionally, the fatigue damage tolerance of the joints was assessed using the cyclic single leg bending test (Section 5.2.5). The mode-mixity of the single leg bending tests was evaluated for both static and cyclic loading. The ratio between the strain energy release rate in mode I and II (G_I/G_{II}) obtained throughout the fracture tests is presented in Figure 7.1 as a function of the crack extension.

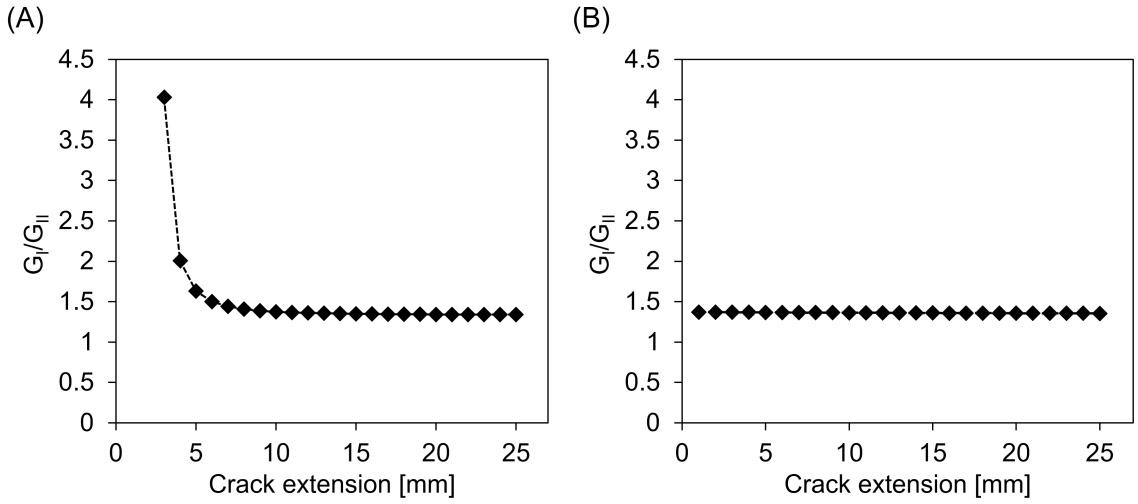

Figure 7.1 Mode-mixity average variation during (A) static and (B) cyclic (50 % of static strength) mixed-mode I/II fracture test.

One observes that, at the beginning of the static test, the G_I/G_{II} ratio is around 4.01 ± 0.01 and then rapidly decreased to the stabilized value of 1.37 ± 0.07 (Figure 7.1-A). It demonstrates that the static fracture test was performed with a quasi-fixed ratio in which the strain energy release rate throughout the test comprises 57.8 ± 1.1 % G_I. Figure 7.1-B presents the mode-mixity for the fracture test under cyclic loading. Since the applied load consists of 50% of the ultimate load obtained from the static strength, there is no variation in the mode-mixity at the beginning of the fracture test. The cyclic fracture test was performed with a quasi-fixed G_I/G_{II} ratio of 1.36 ± 0.01, where the strain energy release rate throughout the test comprises 57.6 ± 0.1 % G_I. It shows that the stresses in mode I (about 58%) are slightly higher than the stresses in mode II (approximately 42%) for the selected geometry of specimens in both static and cyclic SLB tests.

Fernandez *et al.* [76] reported a G_I/G_{II} ratio of 1.35 for the composite bonded joints under cyclic single leg bending. Also, Razavi *et al*. [77] achieved G_I/G_{II} ratios of 1.38–1.40 for metallic fiber-reinforced epoxy adhesive joints under static single leg bending. These values for G_I/G_{II} ratio are very similar to those obtained in the present study for the friction spot joints. Along with other studies [178–182], it demonstrates that the fracture tests performed in this work are in good agreement with the literature of fracture mechanics under mixed-mode loading of composites and adhesive bonded joints.

7.2 Crack growth resistance: the R-curve of friction spot joints

The crack growth resistance of friction spot joints was investigated in this section under quasi-static mixed-mode I/II loading. The strain energy release rate ($G_{I/II}$) at the crack tip was calculated according to Equation 3.5. A representative crack growth resistance curve (R-curve) for friction spot joints is presented in Figure 7.2. A typical R-curve rising

behavior [183] is observed for the friction spot joints. Therefore, the fracture behavior of the joints cannot be characterized by a critical value of the strain energy release rate ($G_{I/IIc}$). One observes that $G_{I/II}$ rises as the crack advances into the PDZ (Figure 7.2). Such observation reflects the high load-bearing capability of this zone as the most resistant zone of friction spot joints. The macro- and micro-mechanical interlocking, as predominant bonding mechanisms in PDZ, oppose the growth of the crack resulting in increased strain energy release rates at the crack tip. The metallic nub acts as a solid energetic barrier on the crack path, imposing resistance to the crack propagation. Combined with the nub, the effective micro-mechanical interlocking at the metal-composite interface shifts the crack path into the first plies of the composite (Section 3.1.4), forcing the crack tip to face the PPS matrix and its carbon-fiber reinforcement.

Rising R-curves are typically found for ductile materials [184,185]. In these cases, the fracture involves the development of a plastic deformation zone at the crack tip which progressively increases the resistance to the propagation of the crack through local strengthening mechanisms [184,185]. Thus, the rising behavior of the R-curve for friction spot joints complies with the ductile failure micro-mechanisms of these joints discussed in Chapter 6. As previously discussed, the plastic deformation of semi-crystalline polymers, such as the PPS in this study, is a complex phenomenon and is still discussed nowadays [168,169]. Nevertheless, several authors have agreed on the occurrence of strain hardening due to the orientation of the amorphous phase in semi-crystalline polymers [168,170]. Such phenomenon occurs through the disentanglement and orientation of the macromolecules in the amorphous phase between the crystallites [168,171]. This strengthening mechanism consists of overcoming the secondary bonds between the entangled macromolecules in the amorphous phase, thereby orientating the chains in the direction of load. At the maximum orientation of the chains, the load is borne by the primary bonds in the highly oriented bundles of macromolecules [169,172]. Therefore, strengthening is observed for the material under load before its failure. Heide-Jørgensen, Freitas and Budzik [186] also identified a rising R-curve for CFRP bonded joints as a result of the micro-mechanisms of failure involving plastic deformation. Similar behavior was also observed by Razavi *et al.* [77] for metallic-fiber-reinforced adhesive joints, while Chen *et al.* [179] observed it for automotive adhesive bonding systems.

Additionally, one observes that strain energy release rates up to 525 J m^{-2} were observed at the crack tip of friction spot joints (Figure 7.2). The literature reports maximum strain energy release rates of approximately 100 J m^{-2} for metallic fiber-reinforced adhesive bonded CF-epoxy joints [77], 350 J m^{-2} for AA5754-O adhesive bonded joints [179], 630 J m^{-2} for GF-epoxy laminates [73], and 508 J m^{-2} for carbon fiber metal laminates [187]. Generally, it indicates that the friction spot joints present similar/superior resistance to crack growth than adhesive bonded joints and layered materials under mixed-mode I/II loading.

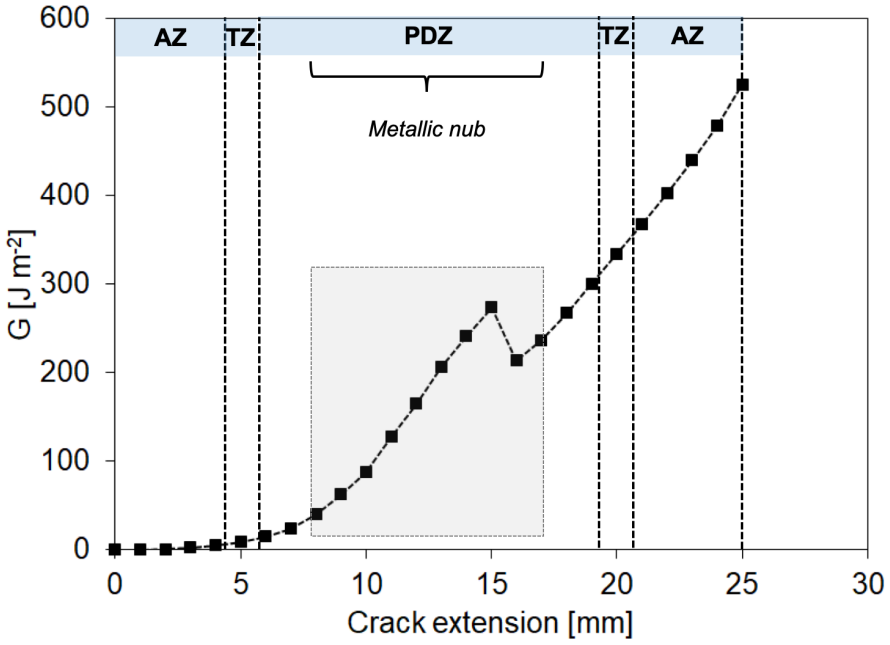

Figure 7.2 Crack growth resistance curve of the friction spot joint under quasi-static mixed-mode I/II loading. The light gray rectangle represents the metallic nub region inside PDZ.

Figure 7.2 shows that crack growth resistance (here denoted as the strain energy release rate, $G_{I/II}$) changes as the crack advances through the different bonding zones of the friction spot joint. Due to the geometry of the single leg bending test (Figure 5.8), the crack is induced to initiate at the borders of the AZ. As the crack propagates in the AZ, the strain energy release rate is extremely low; approximately 0.85 ± 0.01 J m^{-2}. Such low values of strain energy release rate for the crack propagation in this zone demonstrate that AZ imposes practically no resistance to the crack growth at the interface of the joint. This result confirms the FEM prediction given in Section 6.2 that the AZ does not contribute to the global mechanical performance of friction spot joints.

The strain energy release rate at the crack tip rises as the crack advances to the TZ and reaches the PDZ of the joint. It achieves a maximum of 274 ± 1 J m^{-2} as the crack extension reaches approximately 80% of the metallic nub inside of the PDZ. At this point, the interface of the joint is no longer able to support a stable crack propagation. The loss of the metallic nub causes a sudden drop in the strain energy release rate and the unstable crack propagates rapidly until the total failure of the joint. This result also confirms the prediction presented in Section 6.2 that the metallic nub is essential to the maximum bearable load of friction spot joints. The bearing of load in the PDZ seems to be majorly due to the anchoring between the metallic nub and the volume of composite around it. Therefore, without the nub contribution, this zone is weakened and the catastrophic failure of the joint is observed.

Similar observations were made by Ranade *et al.* [188] in their investigation of the crack growth resistance of bonded joints with locally weakened interfaces. The authors used physical vapor deposition of cooper to create well-defined and quantifiable localized flaws at the interface of AA6061-T6511 bonded joints. They reported a falling (or reverse) R-curve in the weakened regions of the interface. Nevertheless, as the crack tip approached the standard region, a rising R-curve was observed. An analogy can be made between the weakened and standard regions in those adhesive joints and the bonding zones in friction spot joints. For the friction spot joint, the weakened region corresponds to the AZ, where the strain energy release rates at the crack tip are close to zero. In contrast, the PDZ - including the metallic nub - is the strongest and most damage-tolerant zone of the joint, where rising values of strain energy release rates at the crack tip are observed (Figure 7.2).

7.3 Fatigue damage tolerance of friction spot joints

7.3.1 Fatigue crack growth: The influence of the bonding zones and their fracture energy

Preexisting and in-service generated damages can strongly influence the performance of materials, hence the safety of structural components [189]. The application of cyclic loads can lead to the accumulation of damage and premature failure of materials and structures [190–194]. Thus, the prediction of the load/or time to a sub-critical damage to accumulate enough to cause a premature failure is of major importance to ensure a robust and safe joined structure [185]. Therefore, the fatigue damage tolerance of the friction spot joints is addressed in this section. For this purpose, the joints were subjected to mixed-mode I/II fatigue loading using the single leg bending test. The strain energy release rate at the crack tip ($G_{I/II}$) and the crack propagation rate (da/dN) were computed throughout the fatigue life of the joints, as described in Section 5.2.5.

Figure 7.3-A correlates the strain energy release rate at the crack tip and the crack propagation rate to describe the fatigue crack growth in friction spot joints. Figure 7.3-B supports this analysis by discretizing the crack propagation rate in the respective bonding zones of the joints. One observes that the fatigue crack propagation occurs in three well-defined stages: I – Initiation, II – Linear behavior, and III- Final fracture, as indicated in Figure 7.3.

Stage I corresponds to the initial phase of the crack propagation. In this stage, the strain energy release rate rapidly rises from 253 ± 6 J m^{-2} to 389 ± 10 J m^{-2} (Figure 7.3-A). This stage comprises the crack propagation in the AZ, as indicates Figure 7.3-B. Thus, the initial low strain energy release rates are a result of the failure of AZ, which presents a low resistance to crack growth (Figure 7.2). Nevertheless, the presence of the PDZ ahead of the crack tip may induce the rapid increase in the strain energy release rate in this stage. As demonstrated in Figure 7.2, the PDZ is the most damage-tolerant zone of the friction

spot joints and presents higher crack growth resistance than the AZ. Increases in the strain energy release rate during crack propagation in weak regions, which are followed by resistant regions, were also observed by Ranade *et al.* [188]. The authors investigated the crack growth resistance of AA6061-T6511 bonded joints with localized patterns of flaws at the interface. They observed a well-defined rising behavior of the strain energy release rate in the weakened regions, followed by a defect-free region. This study suggests that the strain energy release rate at the crack tip is, in fact, affected by the resistance of the interface ahead of the site of propagation. The scaling effect of the strain energy release rate in the weakened regions occurred when the defect-free regions were up to 25 mm away from the weakened region. In case of friction spot joints, the AZ has only 4 ± 1 mm of ring width and is adjacent to the PDZ (Figure 3.6). Therefore, the increase in the strain energy release rate as the crack propagates in this zone is possibly an effect of the presence of the PDZ ahead in the crack path.

In addition, one observes that despite the rising behavior of the strain energy release rate, the crack propagation rate is very steady in Stage I (Figure 7.3-A). An average crack growth rate of 0.10 ± 0.03 mm/cycle is observed as a result of the low crack growth resistance of the AZ (Figure 7.3-B).

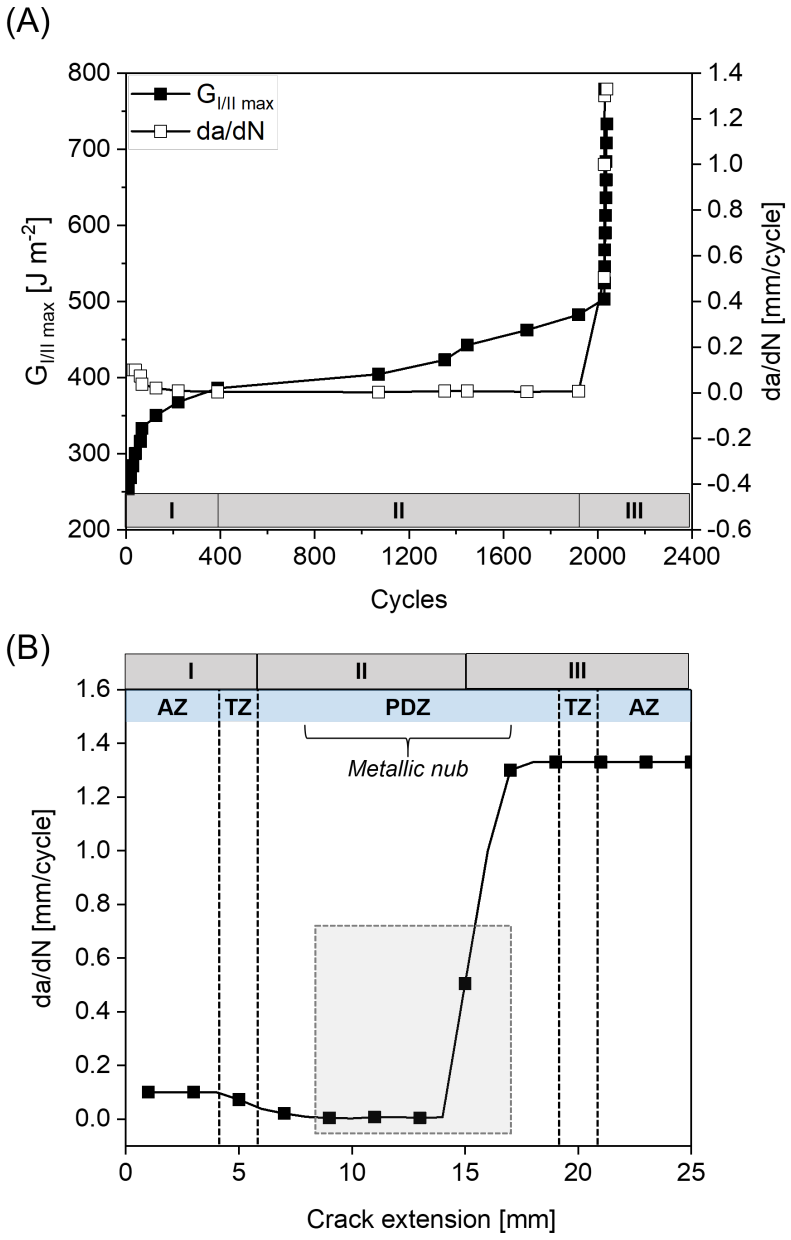

Figure 7.3 (A) Stages of fatigue crack propagation in friction spot joints. (B) Evolution of the crack propagation rate through the bonding zones of the friction spot joint. The light gray rectangle highlights the metallic nub region inside the PDZ.

Stage II comprises the region of linear behavior for $G_{I/II}$ and da/dN. In this stage, the strain energy release rate increases linearly from 389 ± 10 J m^{-2} to 462 ± 9 J m^{-2} as the damage accumulates (Figure 7.3-A). The rise of $G_{I/II}$ in Stage II is attributed to the propagation of the crack inside the PDZ, as determined in Figure 7.3-B. Figure 7.4 shows details of the fracture surface of the joint after fatigue. As demonstrated in Chapter 6 for static loading, the failure in the PDZ also occurs through plastic deformation under fatigue (Figure 7.4). Plastic deformation of the PPS matrix is shown in Figure 7.4-B, where bundles of the stretched PPS matrix are found widely distributed. Besides, the cyclic loading initiated

crazes in the deformed PPS matrix, as indicated by the arrows in Figure 7.4-C and D. Crazes are a result of localized yielding of the polymer [171]. They appear as apertures between bundles of highly oriented macromolecules, thus indicating the occurrence of strain hardening in these regions [19]. Therefore, the progressive increase of crack resistance in Stage II may be a result of strain hardening due to the plastic deformation of the PPS in the PDZ (Figure 7.4-C and D). Heide-Jørgensen, Freitas and Budzik [186] also reported increases in the strain energy release rate as a result of the micro-mechanisms of failure involving the plastic deformation of CFRP bonded joints.

One also observes that the crack growth rate stabilizes in Stage II (Figure 7.3-A). An average crack growth rate of 0.006 ± 0.001 mm/cycle is registered; approximately 16 times slower than the growth rate in Stage I when the crack propagated mostly in the AZ. It demonstrates once more that the PDZ is the most damage-tolerant zone of the friction spot joints.

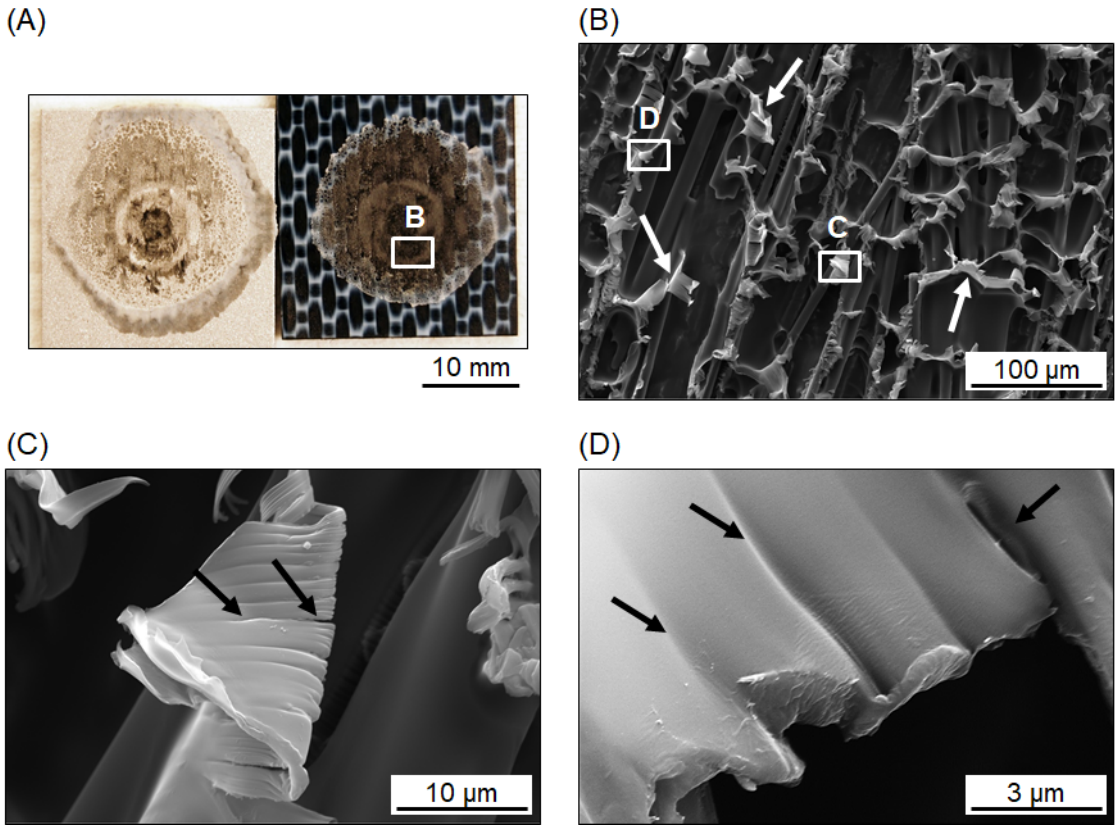

Figure 7.4 (A) Typical fracture surface of a friction spot joint after mode I/II fatigue loading. (B) The stretched PPS matrix showing plastic deformation at the center of the joint. (C) Initiation of crazes in the stretched PPS matrix. (D) Initiation of crazes and failure of the deformed PPS matrix at the center of the joint.

Stage III comprises the unstable crack propagation that occurs as the crack reaches approximately 80% of the metallic nub region (Figure 7.3-B). Similar behavior was also observed for the joints under static loading (Figure 7.2). The failure of the metallic nub

region results in an exponential increase in the crack propagation rate. It reaches 1.24 ± 0.22 mm/cycle as the crack advances through the second half of the joined area (Figure 7.3-B). Thus, an unstable crack propagates rapidly through the remaining PDZ, TZ, and AZ, thereby leading to the complete failure of the joint (Figure 7.3-B). This observation also confirms the prediction presented in Chapter 6 that the metallic nub is essential to the mechanical performance of friction spot joints. The loading capability of the PDZ seems to be mostly due to the anchoring between the metallic nub and the volume of composite around it. Therefore, without the nub contribution, this zone is weakened and the catastrophic failure of the joint is observed.

It is also important to note that the crack propagation rates presented steady values inside the AZ (0.10 ± 0.03 mm/cycle) and the PDZ (0.006 ± 0.001 mm/cycle) during the stable crack propagation in Stages I and II. In TZ, however, a variation is observed (Figure 7.3-B). Nevertheless, since the TZ is a small and transient zone, such behavior was expected. This fact confirms that the main bonding zones of friction spot joints have defined properties. Thus, the mechanical performance of the joints can be tailored as a function of such zones. Additionally, adhesive bonded joints are extensively reported to present crescent crack propagation rates during their fatigue life [80,178,192]. The typical range of stable crack propagation rates for adhesive bonded joints lies between 10^{-4} – 1 mm/cycle [59,60]. This broad variation in the crack propagation rate is often modeled by different equations like the Paris law [50,76]. Nevertheless, it is believed that the steady crack propagation rates presented by friction spot joints could certainly simplify the design of joined structures and components.

7.3.2 Fatigue crack propagation rate as a function of the fracture energy: A preliminary model for friction spot joints

The relationship between the crack propagation rate and the strain energy release rate (or the equivalent stress intensity factor) has been investigated for many decades in order to establish a law to predict the fatigue crack growth in materials [63,195]. One of the most popular models in this field is the Paris–Erdogan law or simply the Paris law [195]. The Paris law was originally developed to model and predict the crack propagation rate in bulk materials as a function of the stress intensity factor [195]. This fatigue crack growth model is denoted by Equation 7.1, where da/dN is the crack propagation rate, ΔK is the variation of the stress intensity factor in the fatigue cycle (K_{max}–K_{min}), and C and m are constants related to the material properties and the stress state [195].

Equation 7.1

$$\frac{da}{dN} = C * (\Delta K))^m$$

Equation 7.1 demonstrates a power law relationship between the crack growth rate and the stress intensity factor at the crack tip of a material during cyclic loading. This law can be linearized using a log-log plot to simplify its graphical representation of da/dN versus ΔK.

Owing to its efficiency and simplicity, the Paris law is also often adapted and applied to model the fatigue crack propagation in adhesive joints, composites, and fiber-metal laminates [196–200]. In these cases, the variation in strain energy release rates (ΔG) is used instead of the stress intensity factor (ΔK) in Equation 7.1. The main reason for the substitution is that the strain energy release rate is easier to compute than the stress intensity factor [62]. This fact is especially expressive when the crack propagates close to the interface, as discussed in Section 3.2. The linear elastic fracture mechanics (LEFM) has been extensively applied to determine G in the substitution of K [50]. In this way, the typical interlaminar fracture of adhesive joints and layered materials can easily be assessed [50]. The similarities between the failure modes in adhesive joints and friction spot joints lead to the use of the same approach in this work.

Figure 7.5-A shows an attempt to correlate the crack propagation rate and the strain energy release rate using the Paris law. One observes that the typical linear behavior obtained through the log-log plot of da/dN versus $\Delta G_{I/II}$, proposed by the Paris law [201], is not observed for friction spot joints (Figure 7.5-A). The deceleration of the crack propagation in Stage II due to the high crack growth resistance of the PDZ is the main reason for this discrepancy (Figure 7.5-A). Therefore, although largely applied to model fatigue crack growth in adhesive joints, composites, and fiber-metal laminates [196–200], the Paris law cannot model the behavior of friction spot joints.

Nonetheless, the distribution of da/dN versus $\Delta G_{I/II}$ resembles a sigmoidal distribution for friction spot joints when plotted in linear-linear scale (Figure 7.5-B). Therefore, a sigmoidal function was used to model the fatigue crack growth of friction spot joints. The fitting equation was obtained using a non-linear fitting tool of *OriginPro* (Table 7.1). The red line in Figure 7.5-B represents the fitting curve of the experimental data points using the sigmoidal model presented in Table 7.1. The fitting of the model demonstrates an R^2 value of 0.9955, while the adjusted R^2 value was 0.9949 (Table 7.1). The exceptional high values of R^2 indicate a good predictability of the data by the sigmoidal model [202].

Nevertheless, it is important to note that the model did not predict the accelerated crack propagation in Stage I of the fatigue crack propagation of the joints. Instead, it considered the crack propagation rate to be constant through Stages I and II (Figure 7.5-B). It is believed that for a complete and more accurate modeling of the fatigue crack growth behavior, the different stages of fatigue crack propagation of the joints should be modeled separately. Additionally, the physical meaning of the constants A_1, A_2, B, and p must be clarified (Table 7.1). However, these topics are beyond the scope of this work.

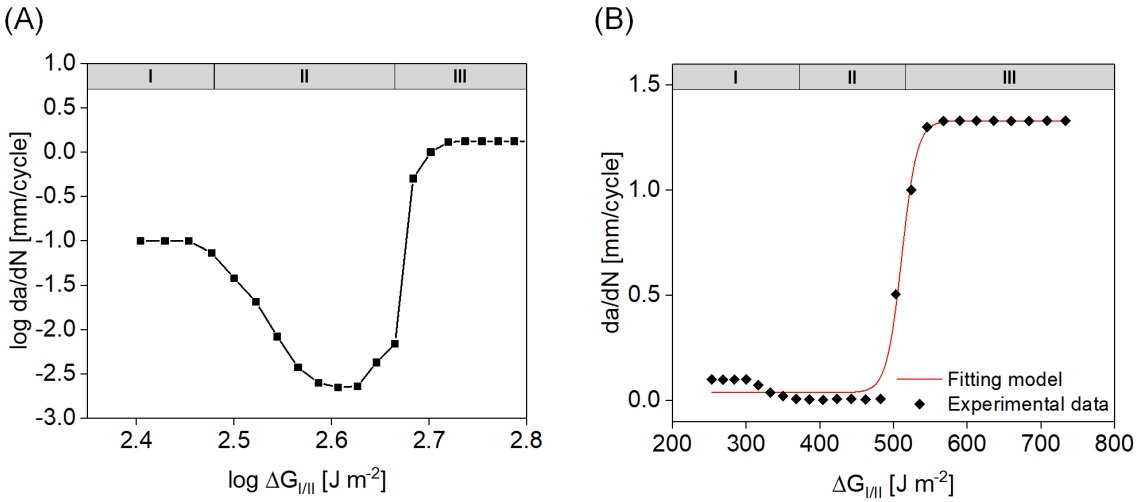

Figure 7.5 (A) Attempt to correlate the crack propagation rate and the strain energy release rate using the Paris law. (B) Sigmoidal model to correlate the crack propagation rate and the strain energy release rate of friction spot joints.

Table 7.1 Fitting model for the prediction of the fatigue crack propagation rate as a function of the strain energy release rate in friction spot joints.

Model	Sigmoidal
Equation	$\frac{da}{dN} = \frac{A_1 + (A_2 - A_1)}{1 + 10^{((B-\Delta G)*p))}}$
A_1	0.03732 ± 0.0123
A_2	1.3298 ± 0.0154
B	511.2773 ± 1.3413
p	0.04211 ± 0.00454
R^2	0.9955
Adjusted R^2	0.9949

Chapter 8. Impact resistance of metal-composite friction spot joints

In this chapter, the impact resistance of friction spot joints is discussed for the first time in the literature. Four levels of impact energy were tested: 2 J, 4 J, 6 J, and 8 J. The joints were aluminum-side (AS) and composite-side (CS) impacted to provide a preliminary design guideline regarding the impact damage tolerance of such hybrid joints. At first, the impact loading and the energy absorption of the joints during the impact event is presented. Next, the development of the damage on the aluminum and composite surfaces was analyzed for the different impact energies under study. Laser scanning microscopy was used to monitor the damage evolution on the surfaces. Ultrasonic echo scanning was applied to evaluate internal damages at the interface and through the composite part of the joints. Finally, the transfer of the impact energy to the interface of the joint was assessed and correlated with the residual strength of the joints according with the side of the joint under impact.

8.1 Impact loading and energy absorption

Figure 8.1 presents the representative force-time curves obtained during the impact events for the different energy levels and configurations investigated in this work. The curves show the loading and unloading of the joint during the impact event. They present a few oscillations during loading and unloading. One notes that the density of oscillations increases significantly from 2 J to 6 J, and then decreases at 8 J when the failure under impact of the joints occurred. Such oscillations can be related either to vibrations of the structure due to acceleration and deceleration of the joint during the impact event and/or occurrence of internal damage in the joint [97,107]. The internal damages created during the impact on the joint interface and the composite part are discussed in Section 8.2.

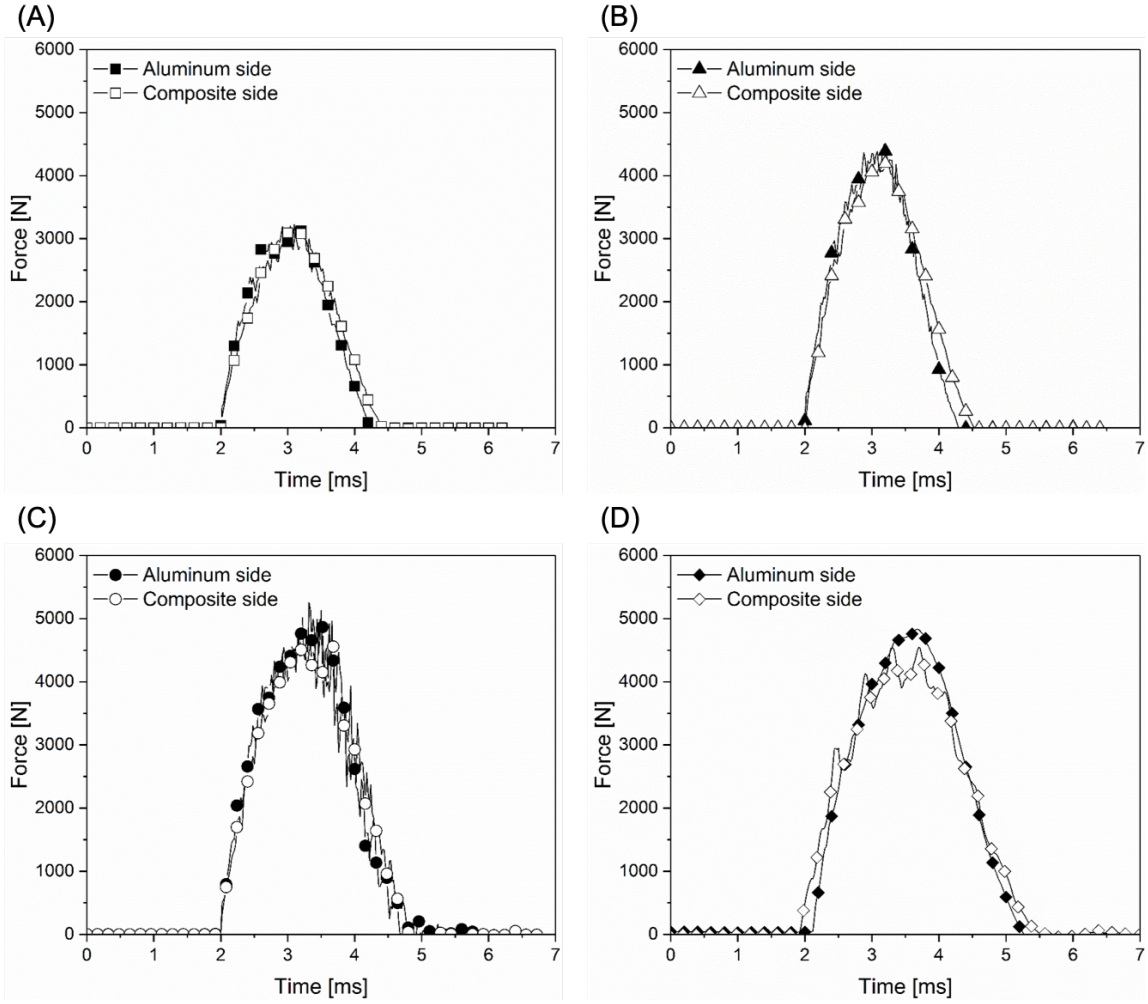

Figure 8.1 Representative force-time histories of aluminum-side (AS) and composite-side (CS) impacted joints for (A) 2 J, (B) 4 J, (C) 6 J, and (D) 8 J of potential energy. The failure of the joints occurred at 8 J for both AS and CS cases.

Figure 8.2 summarizes the maximum forces achieved in each energy level for the aluminum-side and composite-side impacted joints. The maximum force achieved during the impact increases linearly from 2 J to 6 J of impact energy. At 8 J, the failure under impact of the joints occurred. At this energy level, it is observed that the maximum force achieved is statistically the same as the force achieved at 6 J (6 J: 5440 ± 186 N (AS)/5085 ± 162 N (CS); 8 J: 5305 ± 125 N (AS)/4987 ± 345 N (CS)). Thus, it suggests that the failure threshold for the impact force is approximately 5204 ± 178 N for a single friction spot joint.

It is important to note that, for each energy level, the load applied by the impactor in the joint is very similar independent of the surface under impact (Figure 8.1 and Figure 8.2). One observes that, when impacted from the aluminum side, the joint is subjected to a force slightly higher (Figure 8.2). However, considering the standard deviation of such values, the difference between the maximum force achieved from the aluminum and composite impacted surfaces are statically insignificant.

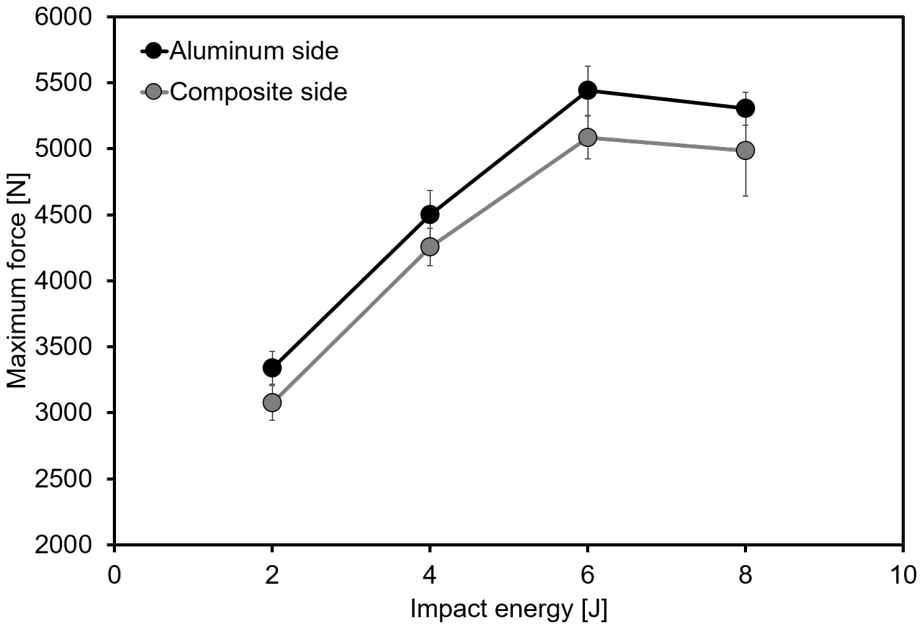

Figure 8.2 Maximum force applied to the joints during impact for different energy levels. The failure of the joints occurred at 8 J of impact energy for both AS and CS cases.

The absorbed energies during impact were calculated from the force-time curves depicted in Figure 8.1. Based on the Energy Profile Method (EPM) [94–97] introduced in Section 3.3, Figure 8.3 depicts the energy profile obtained for the single friction spot joints in this study. Figure 8.3 demonstrates that the joints presented rebounding behavior for all the investigated energy levels independent of the surface under impact. It implies that for all cases the impact energy was not totally absorbed for the joints, i.e. all impacted joints are situated under the equal energy line in Figure 8.3. In contrast, one observes that the joints fail at 8 J of impact energy. It suggests that aluminum and composite could further absorb energy during an impact event. Nevertheless, the interface of the joint reached its threshold at 8 J of impact energy, when 6.5 J is absorbed, independently of the surface under impact (Figure 8.3). It indicates that a single friction spot joint could absorb up to 103 $kJ.m^{-2}$ of joined area (considering a nominal area of 63.6 mm^2).

Machado *et al.* [109] investigated several combinations of adhesives to maximize the impact resistance of CF-epoxy bonded joints for automotive applications. They demonstrated that the combination of a flexible adhesive (at the edges of the overlap) and a stiff adhesive (in the center of the overlap) leads to optimized energy absorption during impact. In that case, energy absorption up to 48 $kJ.m^{-2}$ of bonded area was achieved which accounts for approximately half of the intake of a friction spot joint.

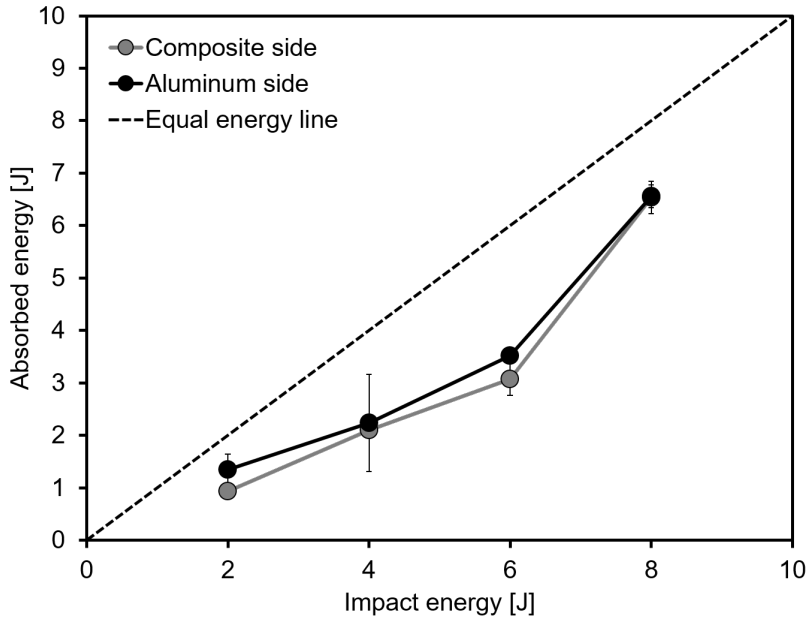

Figure 8.3 Energy profile obtained for single friction spot joints in this study. The failure of the joints occurred at 8 J of impact energy for both AS and CS cases.

8.2 Impact damage and its transfer to the joint interface

Figure 8.4 presents the area and maximum depth of the impact damage identified on the aluminum and composite surfaces for different levels of impact energy under investigation. One observes that both area and depth of damage increase as the impact energy rises independent of the side (AS or CS) under impact. The damage area increased from 4.6 ± 0.3 mm^2 (2 J) to 12.7 ± 0.2 mm^2 (8 J) for the aluminum-side impacted joints; an increase of 64%. For the composite-side impacted joints, the increase in the damage area was 44%; 10.4 ± 1.4 mm^2 (2 J) to 18.8 ± 0.7 mm^2 (8 J). Simultaneously, the damage depth increased 90% when the impact energy was raised from 2 J to 8 J for the aluminum-side impacted joints (5.1 ± 0.3 μm (2 J) to 47.3 ± 0.2 μm (8 J)). For the composite-side impacted joints, the increase in the damage depth was 69% [81.2 ± 8.7 mm (2 J) to 260.3 ± 7.4 μm (8 J)].

These observations from Figure 8.4 demonstrate that the damage evolves differently regarding the side of the joint subjected to impact. One observes that, at the same level of impact energy, the damage caused on the composite surface is deeper and roughly twice the damage caused on the aluminum surface (Figure 8.4). Such differences in damage development were just as expected, considering the diverse structure and mechanical properties of aluminum alloys and fiber-reinforced thermoplastics [203]. While the aluminum alloys present a well-defined elastic-plastic transition denoted by the yield strength of the materials, the fiber-reinforced thermoplastics typically present a viscoelastic behavior [203]. The damage development and its consequences to the transfer

of the impact energy to the interface of the joint are discussed for both cases (aluminum-side and composite-side impact) as the following.

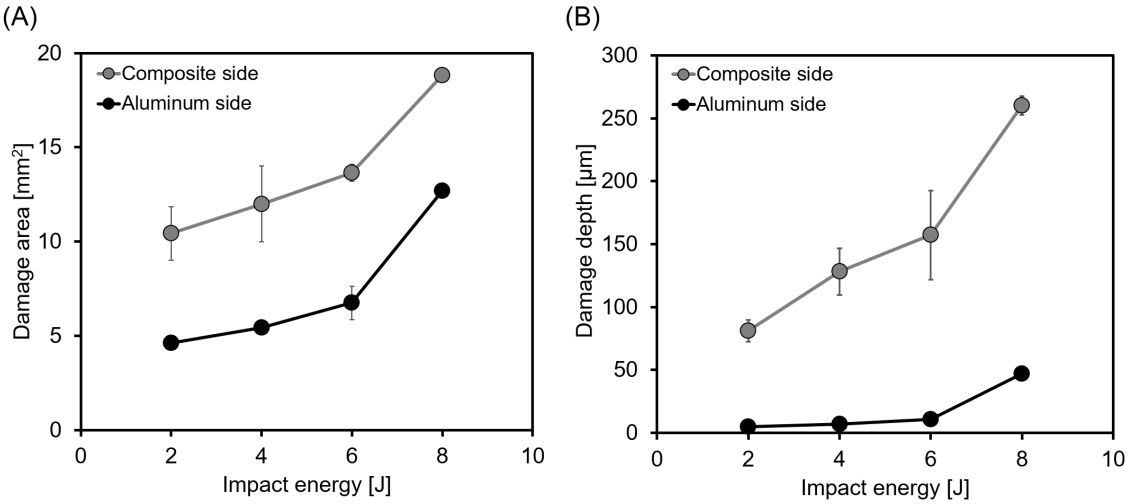

Figure 8.4 (A) Area and (B) maximum depth of impact damage for the joints impacted from the aluminum and the composite side for different levels of energy.

8.2.1 Damage development for aluminum-side impact

Figure 8.5 shows the damage caused by the aluminum-side impact for 2 J, 4 J, 6 J, and 8 J. The indentations left on the aluminum surfaces are hardly identified in Figure 8.5. Therefore, the dashed lines were used to highlight the impression on the aluminum surfaces after impact. In accordance with aircraft regulations, barely visible indentation damage (BVID) should not be identified at a distance of 50 cm during inspection [149]. Accordingly, the damages in this study were classified as BVID for all the energy levels investigated.

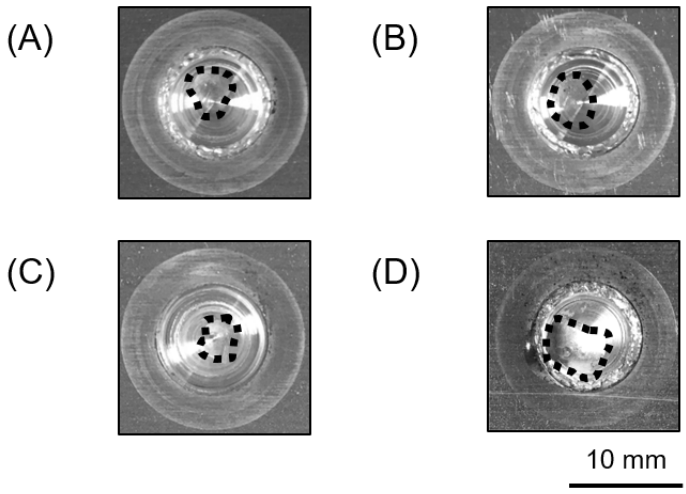

Figure 8.5 Damage evolution on the aluminum surface after (A) 2 J, (B) 4 J, (C) 6 J, and (D) 8 J of impact energy. The dashed lines highlight the damage imprint on the aluminum surface.

On the one hand, it is observed that the impactor locally generated very shallow impressions on the aluminum surfaces after the impact (Figure 8.5). The damages deepened from 5.1 ± 0.3 µm to 47.3 ± 0.2 µm as the impact energy increased from 2 J to 8 J; the depths were evaluated using an adapted roughness measurement performed by laser confocal microscopy (Figure 8.4-B). On the other hand, a global bending of the aluminum part is noted (Figure 8.6). It is observed that the angle of bending increases as the impact energy rises. At 2 J, the bending angle is nearly 0° and aluminum and composite presented full contact in the overlap area of the joint (Figure 8.6-A). At 8 J, the bending angle reached approximately 10° (Figure 8.6-D). In this case, it is even observed partial perforation in the composite part by the plastically deformed aluminum (arrow in Figure 8.6-D), thus leading to the detachment of the interface and failure of the joint during the impact.

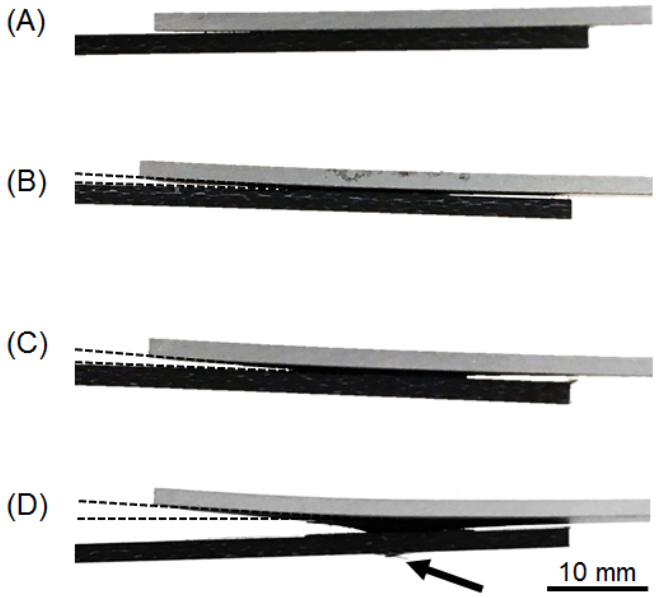

Figure 8.6 Representative side view of the joints after the impact on the aluminum surface for (A) 2 J, (B) 4 J, (C) 6 J, and (D) 8 J (failed during the impact).

After the impact, the joints were scanned with an ultrasound source to evaluate in a non-destructively the damage in the joints. No internal flaws could be observed in the aluminum part after the impact. Nevertheless, the background echo from the measurement provided a qualitative comparison of the joint interface before and after the impact. Since the output was very similar for all levels of the investigated impact energy, only a representative example is shown in Figure 8.7. The joint impacted with 4 J was selected for this purpose. The c-scans of all energy levels are included in Appendix C for documentation.

Figure 8.7 shows c-scans of the overlap area of a joint before and after the impact on the aluminum surface. Before the impact event, it is possible to identify the unbonded areas of the overlap area along with the circular joined area, including the metallic nub at its center (Figure 8.7-B). After the impact event, the echo signal inside the joined area became

equal to the echo signal of the unbonded area (dark grey areas indicated by white arrows in Figure 8.7-C). It indicates that the contact between aluminum and composite is no longer present, suggesting the occurrence of detachment in the outer joined area. Additionally, a decrease in the intensity of the echo in the nub region is noted, indicating the occurrence of damage in that area as well.

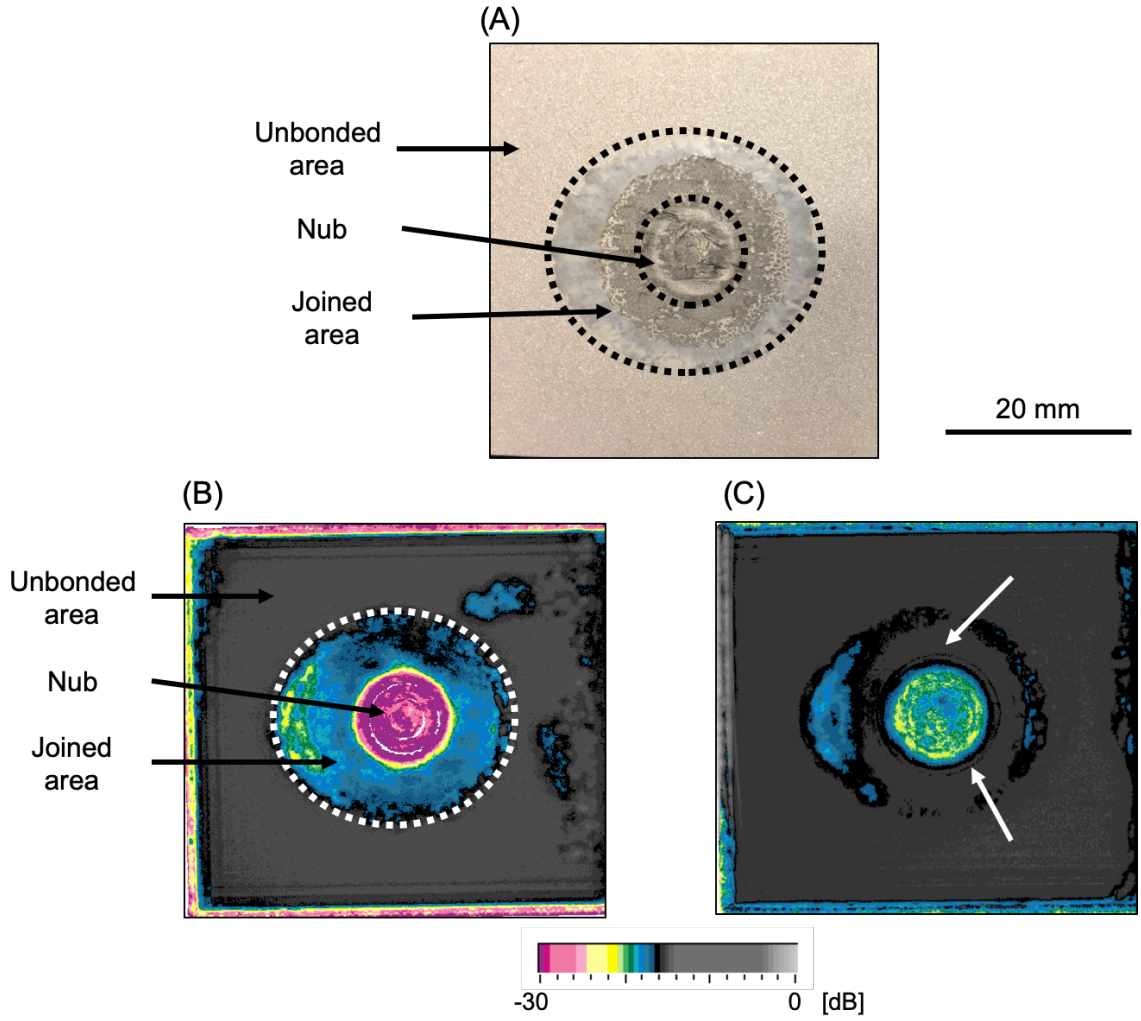

Figure 8.7 (A) Typical fracture surface of the aluminum part of a friction spot joint. Representative c-scans of the overlap area of a friction spot joint (A) before and (B) after the impact on the aluminum surface. A joint impacted with 4 J was selected as a representative example in this qualitative analysis.

These observations suggest that in case of the aluminum-side impact, the impact energy is mostly being absorbed by the joint as plastic deformation (bending) of the aluminum part. The bending of the aluminum introduces peeling stresses at the interface which will progressively promote the detachment of the interface and the failure of the joint. Similar behavior is reported in the literature for bonded joints. Harris and Adams [204] investigated three types of aluminum alloys (soft, mild and hard) substrates to produce impact-resistant adhesive bonded joints. Silva *et al.* [108] investigated steels (mild- and

high-strength) and their impact behavior as substrates for adhesive bonded joints. In both studies, the global deformation of the metallic substrates due to the impact was responsible for introducing stresses at the adhesive layer, thereby decreasing the impact failure load of the joints. As a result, higher residual strengths were reported for the bonded joints produced with the stiffest substrates in [204] and [108].

8.2.2 Damage development for composite-side impact

Figure 8.8 shows the 3D profile of the damage in case of the composite-side impact for 2 J, 4 J, 6 J, and 8 J. As it was observed for the joints impacted from the aluminum side, the damages in this case are also classified as BVID for all the investigated energy levels according to [149].

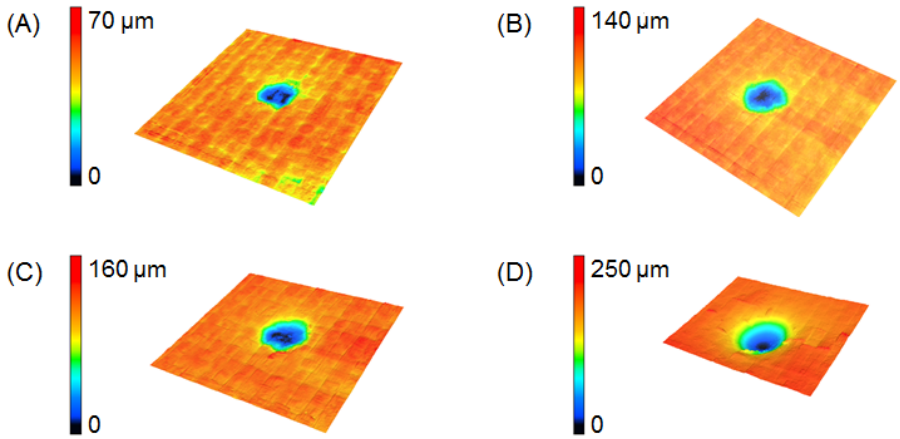

Figure 8.8 3D images of the damage on the composite surface of the joints after (A) 2 J, (B) 4 J, (C) 6 J, and (D) 8 J of the impact energy.

One observes that the impactor locally penetrated the composite part during the impact, controversially to the imprint observations on the aluminum-side impacted joints. It is possible to identify a depression on the composite surface after the impact (Figure 8.8). Naturally, the CF-PPS presents a lower hardness than the aluminum in this study (AA2024-T3: 1.4 GPa; CF-PPS: 0.4 GPa [205]), thereby facilitating the penetration of the impactor.

Additionally, no global distortion was observed for the composite part after the impact. Figure 8.9 shows that composite and aluminum are still entirely in contact after the impact, except for 8 J of impact energy. At 8 J, it is observed a distortion on the aluminum part due to the high energy of impact applied to the composite part (Figure 8.9-D). Such distortion of the aluminum results in the detachment of the interface and the failure of the joint during the impact. The absence of distortion in the composite, even at high levels of impact energy, is considered a result of its layered structure [97]. It favors the energy absorption through the creation of internal and localized damage rather than a global path of energy dissipation [108,204].

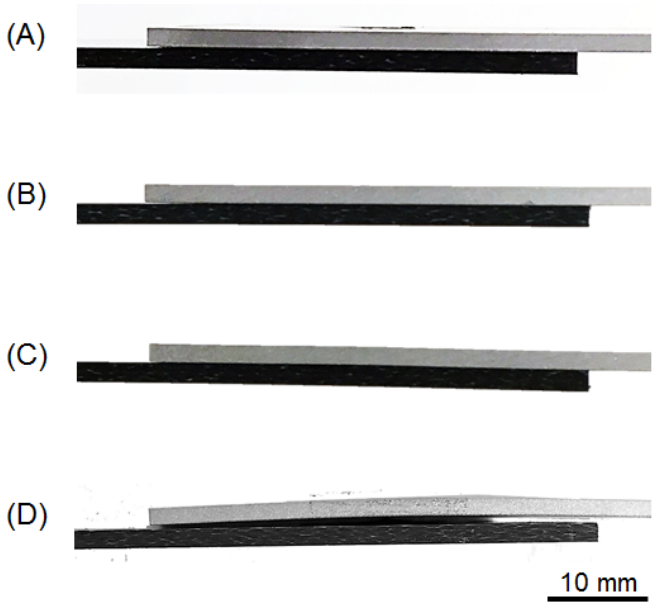

Figure 8.9 Representative side view of the joints after the impact on the composite surface for (A) 2 J, (B) 4 J, (C) 6 J, and (D) 8 J (failed during impact).

Figure 8.10 shows c-scans of the composite part before and after the impact event. The c-scans provided a qualitative comparison of the internal flaws in the composite part before and after the impact. Since the output was very similar for all levels of the investigated impact energy, only a representative example is shown in Figure 8.10. The joint impacted with 4 J was selected for this purpose. The c-scans of all energy levels are included in Appendix C for documentation.

Before the impact (Figure 8.10-A), it is possible to identify the presence of process-related defects through the thickness of the composite. It is observed that such flaws are distributed at the center of the joint, inside a perimeter that corresponds to the area affected by the sleeve plunging during the joining process. At the center of the joint, the highest temperatures are achieved during the joining process due to the proximity to the rotating tool [22]. As a result, more profound defects (middle-thickness of the composite part, approximately 1 mm, deep) were identified at the center of the joint, while superficial defects (close to the metal interface, approximately 2 mm deep) are found in its periphery. These process-related defects are basically microvoids originated from air entrapment during the outflow of the molten/softened PPS matrix during the FSpJ process. Details of the formation of such flaws are found in [22,23,206]. After the impact event (Figure 8.10-B), one observes that the density of microvoids increased, especially at the center of the joint (at depths around 1 mm, green-colored defects). This is an indication of the occurrence of delamination and/or coalescence of previously damaged volumes due to the impact in that region.

These observations suggest that the impact energy is being partially absorbed on the creation/extension of internal damage through the plies of the composite in the case of the

composite-side impact. Therefore, the impact energy is only partially transferred to the interface of the joint. This mechanism of energy absorption through internal damage creation has been extensively reported in the literature for composite materials and adhesive bonded joints [94,95,97,207,208].

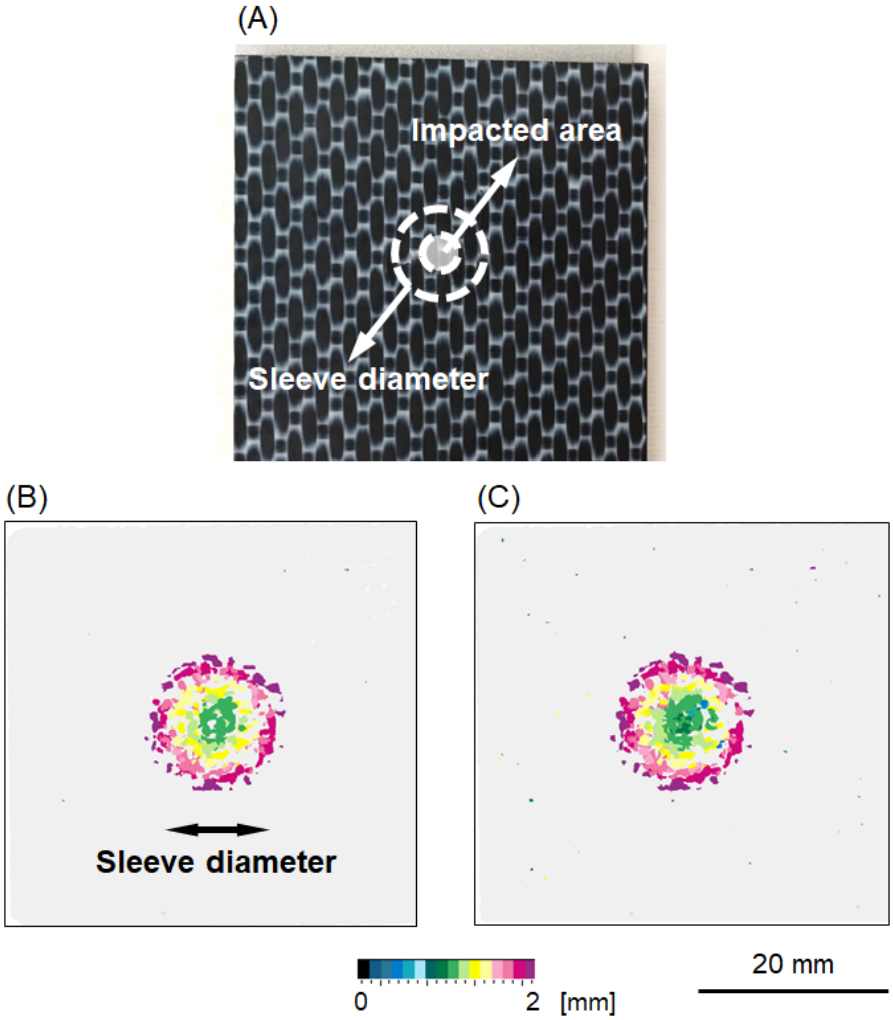

Figure 8.10 (A) Typical impacted composite surface showing the impacted area and the sleeve diameter used to perform the joining process. Representative c-scans through the thickness of the composite part in the overlap area of a friction spot joint (B) before and (C) after the impact on the composite surface (4 J). (0 mm: composite surface under the impact, and 2 mm: composite surface in contact with aluminum).

8.3 Residual shear strength of the joints after impact

Figure 8.11 presents the residual lap shear strength of the joints after the impact for the different impact levels investigated. One observes that the ShAI of the joints decreased progressively as the impact energy increased (Figure 8.11). The joints impacted from the aluminum side presented residual strengths of 84% (1735 ± 151 N) for 2 J, 30 % (624 ± 82 N) for 4 J, and 25% (523 ± 29 N) for 6 J impacts. For composite-side impacted joints,

the residual strengths were 80% (1657 ± 86 N) for 2 J, 54% (1124 ± 45 N) for 4 J, and 45% (936 ± 242 N) for 6 J impact. The joints impacted with 8 J, for both AS and CS cases, failed during the impact event.

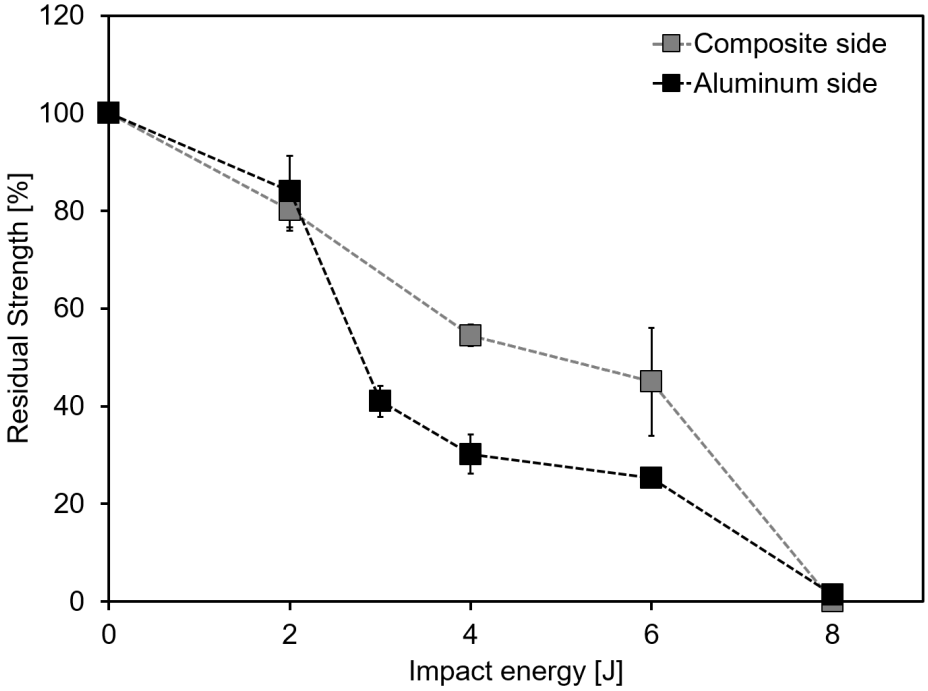

Figure 8.11 Residual lap shear strength of the joints after the impact.

In general, the joints impacted from the aluminum side presented lower residual strength after the impact than those impacted from the composite side (Figure 8.11). As previously discussed, the impact energy introduced from the aluminum side is mostly absorbed in the plastic deformation of the aluminum part. The bending of the aluminum promotes the detachment between aluminum and composite, advancing the damage at the interface as the bending angle increases (Figure 8.6). Otherwise, the impact energy introduced from the composite side is partially absorbed on the creation/extension of internal damage through the plies of the composite (Figure 8.10). Thus, it is expected that the impact energy is only partially transferred to the interface of the joint in the case of the composite-side impact, preserving its mechanical integrity. Consequently, the composite-side impacted joints presented higher residual strength after the impact.

A similar trend is found on the evaluation of the impact resistance of adhesive bonded joints. Silva *et al.* [108] assessed the impact behavior of adhesively bonded high strength steel joints. In that study, the joints were produced with a mixed-adhesive strategy (rigid and flexible) to improve the impact resistance of the joints. The study showed that in the case of mixed adhesives, 100% of the impact energy was absorbed by the joints in contrast to only 50% of absorption when only one type of adhesive was employed. In another investigation, Machado *et al.* [109] performed a similar study for CFRP bonded joints. The effects of combining flexible and rigid adhesives were found to be similar as those

observed for the steel joints. Nevertheless, the impact failure load for the CFRP joints was up to 20% higher than the failure load of the steel joints. The authors reported that the internal damages created in the CFRP substrates reduced the stresses in the adhesive layer of these joints compared to the steel joints, thereby preserving its integrity.

Nevertheless, one also observes that for the impact energy of 2 J, the aluminum-side- and composite-side impacted joints have similar residual strength: 80 ± 4 % for the CS and 84 ± 7 % for the AS impact (Figure 8.11). As shown in Figure 8.6, the impact energy of 2 J was not sufficient to significantly bend the aluminum part of the joint. Therefore, it is expected that no additional peeling stresses were introduced to the interface when the aluminum side of the joints was impacted in comparison with the composite-side impact case. As a result, the residual strength of the joints in this case is comparable.

These observations indicate that, for low impact energy (2 J, in this study), the side of the joint under the impact does not strongly affect the residual strength of the joint. Nevertheless, as the impact energy increases, the different impact behaviors of aluminum and composite played a more significant role in the strength degradation of the joint. The author is aware that such observations are strongly influenced by the geometry of the coupons. Although this study assessed for the first time the damage behavior of the friction spot joints under impact, the upscaling of such results requires further investigation.

Chapter 9. Corrosion behavior of metal-composite friction spot joints

In this chapter, the corrosion behavior of friction spot joints is assessed. For this purpose, the investigation was divided into two main topics: the corrosion development on the top surface and at the interface of the joint. Firstly, the process-related changes in the microstructure, precipitation state, and local mechanical performance of the aluminum part are investigated using microhardness and small-angle X-ray scattering (SAXS). Such findings are correlated with the corrosion development on the top surface of the joints. Further, the corrosion at the aluminum-composite interface is addressed. The understanding of the corrosion phenomenon at the interface of the joints is supported by the electrochemical characterization of the AA2024-T3/CF-PPS galvanic couple. Scanning electron microscopy (SEM) and energy dispersive spectroscopy (EDS) are used to identify the different stages in the corrosion process at the interface. Finally, the global strength degradation of the joints is correlated with the corrosion damage in the bonding zones of the joints.

9.1 Corrosion development on the top surface of the joints

9.1.1 Process-related changes on the microstructure and precipitation state of the aluminum part

Figure 9.1 presents the typical temperature evolution during the FSpJ process. During the joining process, the maximum temperature measured was 375 ± 15 °C at the borders of the tool on the aluminum surface. This temperature corresponds to 75% of the incipient melting temperature of AA2024-T3 (502 °C) [144], therefore no melting of the metallic part is expected. Nevertheless, the combination of such high temperatures and shear rates applied by the tool resulted in changes in the microstructure as well as the precipitation state of the AA2024-T3.

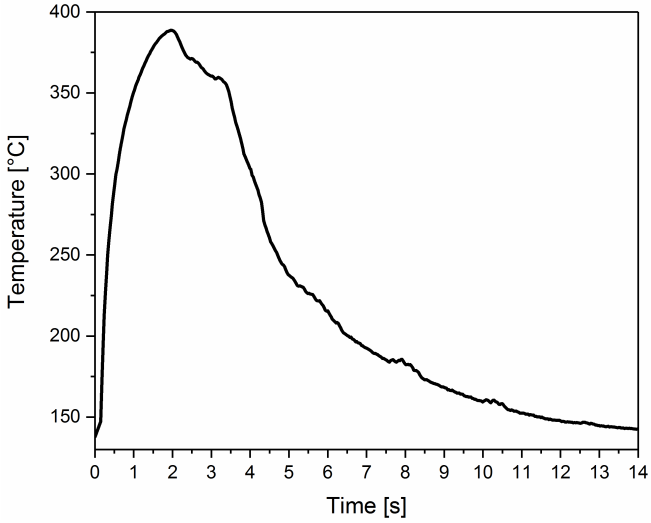

Figure 9.1 Representative example of the temperature evolution on the aluminum surface during FSpJ for the joining parameters used in this study.

As previously reported in the literature [25], FSpJ generates three different microstructural zones in the metallic part of the joints: stir zone (SZ), thermo-mechanically affected zone (TMAZ), and heat-affected zone (HAZ). These zones are displayed in Figure 9.2-A. In this study, the corrosion behavior of the joint is the main concern. Thus, the surface of the joint is the region of interest. Considering the top surface of the joint, the TMAZ corresponds to a limited area between the SZ and the HAZ. Therefore, only the latter two will be analyzed in detail in this section; the TMAZ is considered as the outer border of the SZ.

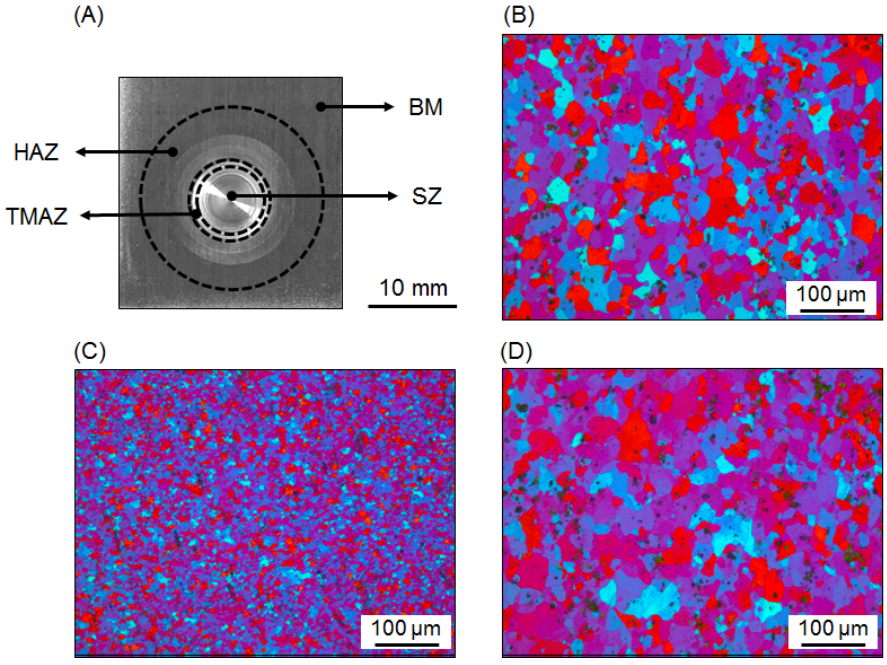

Figure 9.2 (A) Typical top surface of friction spot joints showing the delimitations for the microstructural zones. Microstructural details of (B) base material, (C) SZ, (D) HAZ.

The combination of high temperature (375 °C > 0.60T_m of AA2024-T3) and high shear rate imposed by the rotating sleeve leads to the dynamic recrystallization of the AA2024-T3 in the SZ. Therefore, fine grains are observed in this zone (Figure 9.2-C). One may also note that the coarse intermetallic particles present in the base material (BM) (black dots in Figure 9.2-B) were stirred and refined in the SZ (Figure 9.2-C). Additionally, above 250°C, the precipitation state of the alloy changes. The GPB zones are dissolved around 250°C, and as a result S'(S) metastable phase precipitates around 300°C [132]. Nevertheless, as the process temperature increases further (supposedly above 375 °C in the SZ), partial dissolution of S'(S) can increase the Cu content in the matrix of the alloy and lead to re-precipitation of the GPB zones in the SZ during cooling or at room temperature [132]. As a result, the fraction of GPB and S'(S) phases are similar between SZ/TMAZ and BM (Figure 9.3). The combination of grain refinement and precipitation sequence also results in similar hardness for SZ/TMAZ and BM (ca. 150 HV, Figure 9.4).

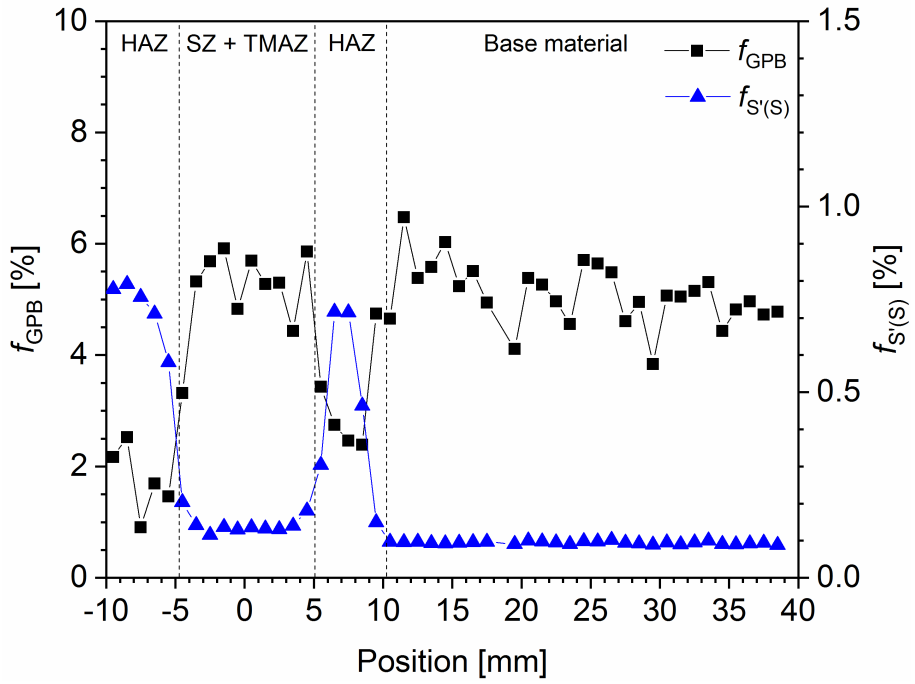

Figure 9.3 Volume fraction of GPB and S'(S) precipitates along a line across the friction spot joint determined by SAXS.

In contrast, in case of the HAZ, no visible changes are observed in the microstructure. The shape and size of the grains, as well as the presence of coarse intermetallic particles, are identical to the BM (Figure 9.2-D). Nevertheless, the hardness of the HAZ is lower than that of the BM (ca. 128 HV, Figure 9.4). This decrease in hardness is caused by the dissolution of coherent GPB zones above 250°C due to the FSpJ process. Figure 9.3 demonstrates a decrease of approximately 30% in the volume fraction of GPB zones in the HAZ in comparison with those of the BM and the SZ/TMAZ. It is also observed that the volume of semicoherent S'(S) precipitates strongly increases in the HAZ when compared to BM and SZ/TMAZ; an increase of approximately 700% (Figure 9.3). This demonstrates

that the maximum temperature of 375°C measured in the HAZ during FSpJ promoted the precipitation of a significant volume of S'(S) after the dissolution of the GPB zones at 250°C. One may also observe that, although the dissolution temperature of the S'(S) phase was achieved (350°C) in the HAZ, the time of exposure was not enough for Cu-saturation and re-precipitation of GPB zones, as observed in the SZ (Figure 9.3). This result is consistent with other observations of the non-isothermal precipitation kinetics of this alloy for other friction-based joining processes, such as friction stir welding in [132,209].

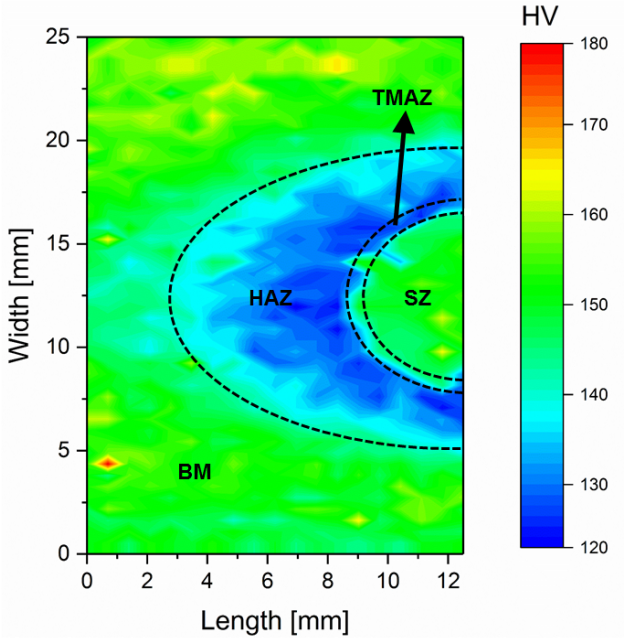

Figure 9.4 Typical microhardness profile of the top surface of friction spot joints.

9.1.2 Corrosion evolution at the top of the spot joint: Influence of the FSpJ process

Figure 9.5 presents the corrosion evolution on the top surface of the spot joint. It is possible to notice that the corrosion process starts heterogeneously through the formation of pits (Figure 9.5-B). Figure 9.6-A shows two developed pits on the aluminum surface after one week of exposure. As the time of exposure increases, the pits become deeper and start to connect themselves through a network of intergranular corrosion paths (Figure 9.6-B). Thus, the corrosion evolves beneath the surface, causing superficial exfoliation (black arrows in Figure 9.5-B to G). An overview of the exfoliation on the surface after six weeks of exposure is shown in Figure 9.6-D. This corrosion process has been reported in the literature for AA2024-T3 [28–30], including its welds produced by friction stir welding [213,214].

In addition, it is observed that the corrosion process does not evolve homogeneously on the top surface of the joint. This is a result of the different microstructural zones created during the thermo-mechanical cycle imposed by the joining process. Figure 9.5

demonstrates that the corrosion evolves rapidly at the HAZ, while the coupled region comprising TMAZ and SZ is barely attacked after six weeks of exposure.

As discussed earlier, GPB zones are the predominant precipitates in the SZ/TMAZ, as indicated in Figure 9.3. These zones comprise fine precipitates that are often distributed in the matrix of the alloy instead of the grain boundaries [132]. During their precipitation, these zones decrease the Cu content in the matrix, thereby reducing the matrix breakdown potential [215]. The lower content of Cu in the matrix also decreases the differential potential between the matrix and the Cu-depletion zones formed around the grain boundaries due to S'(S) precipitation [215]. Therefore, both pitting and intergranular attacks are unfavorable in this zone.

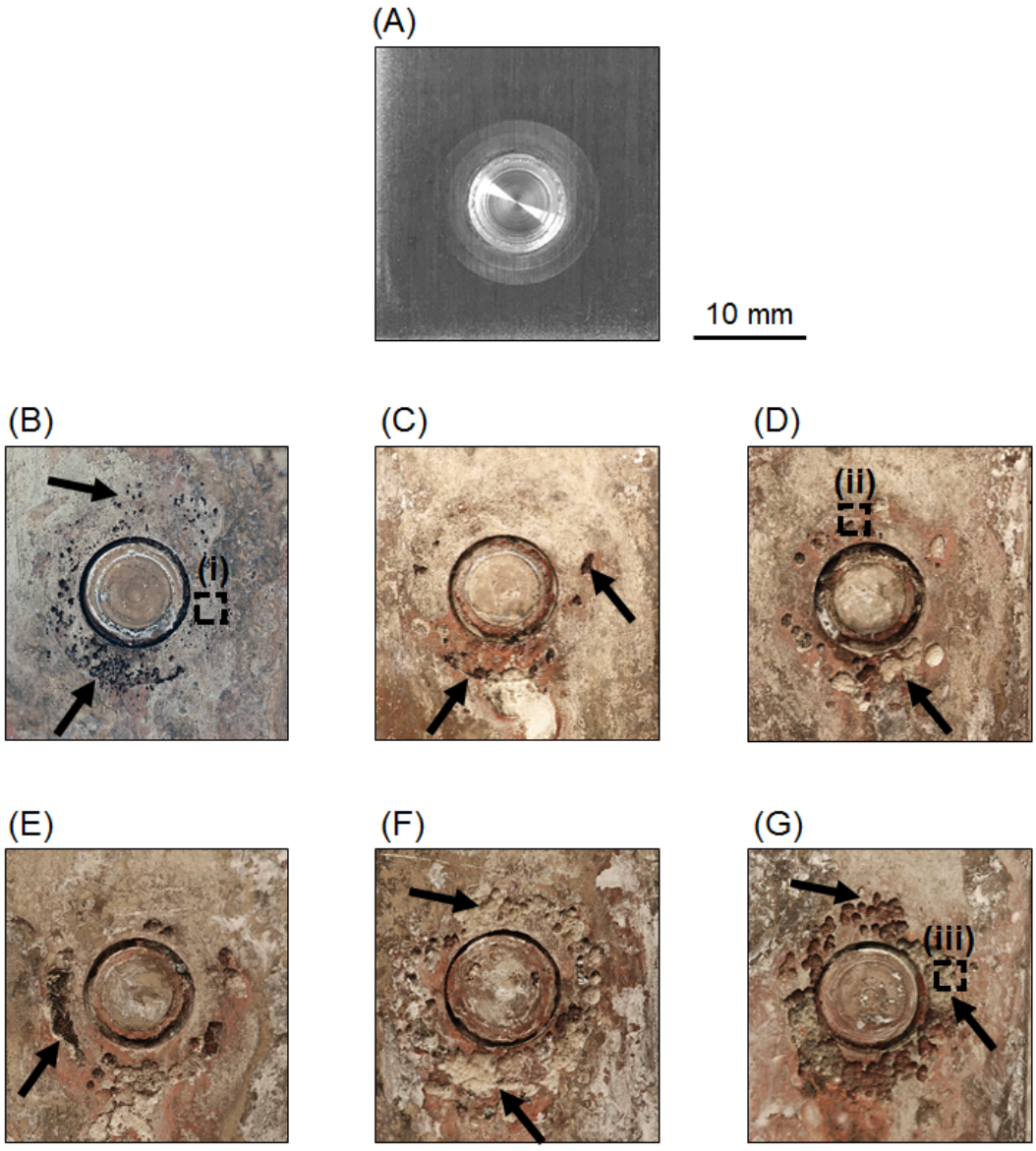

Figure 9.5 Top surface of the spot joint (A) as joined and after (B) one week, (C) two weeks, (D) three weeks, (E) four weeks, (F) five weeks, and (G) six weeks of exposure.

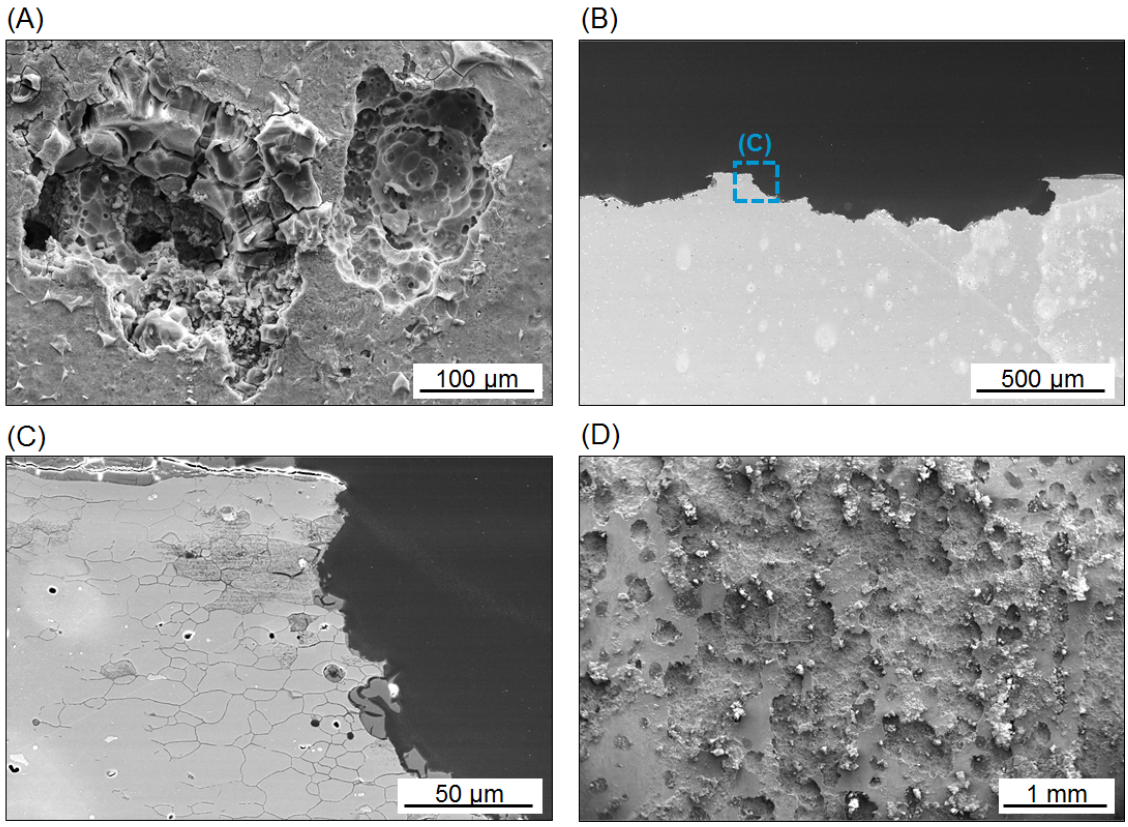

Figure 9.6 (A) Pits developed at the aluminum surface after one week of exposure (Region i from Figure 9.5-B). (B) The cross-sectional view of the connection between two pits after three weeks of exposure (Region ii from Figure 9.5-D). (C) Detail from (B) showing intergranular corrosion of the aluminum part. (D) Overview of exfoliation on the aluminum surface as a result of pitting and intergranular corrosion after six weeks of exposure (region iii from Figure 9.5-G).

In contrast, the HAZ presented coarse intermetallic particles and high volume of the S'(S) phase in its microstructure (Figure 9.2 and Figure 9.3). Coarse intermetallic particles and S'(S) phase precipitation create active sites in the alloy, thereby increasing the corrosion susceptibility of the HAZ in comparison with the SZ/TMAZ [133,134]. The coarse intermetallic particles lead to pitting corrosion due to their high self-corrosion potential through dissolution (or surrounding matrix dissolution depending on the composition of the particles) [133]. The S'(S) precipitates are often associated with the formation of precipitate-free and Cu-depletion zones around the grain boundaries during their formation [133]. These zones create a potential gradient at the region around the grain boundaries, consequently increasing the susceptibility of intergranular corrosion [133]. Besides, macro-galvanic coupling may also potentialize the corrosion in the HAZ. BM and SZ/TMAZ display similar profile of particles with lower volume fraction of S'(S) than the HAZ (Figure 9.3). Therefore, one expects that a macro-difference of potential is established when BM and SZ/TMAZ are coupled with HAZ in a corrosive environment. Macro-galvanic coupling was identified in friction stir welds of AA2024-T3 as a result of microstructural and precipitate state gradients between SZ and HAZ of the weld [133,134].

9.2 Corrosion development at the interface of the friction spot joints

9.2.1 Electrochemical characterization of the AA2024-T3/CF-PPS couple

The potentiodynamic polarization curves obtained for both AA2024-T3 and CF-PPS are represented in Figure 9.7. The window of the scan was reduced to focus mostly on the cathodic branch related to CF-PPS and the anodic branch of AA2024-T3. Using the Tafel fitting procedure, provided by the Gamry Echem software, the potential of corrosion (E_{corr}) was estimated to be close to 0.15 V for CF-PPS and -0.57 V for AA2024-T3. This result is expected and in accordance with the ASTM G82-98 galvanic series, which reports values from -0.4 to -1.0 V for aluminum alloys and 0.2 V for pure graphite [122]. These observations demonstrate the pronounced anodic activity of the aluminum compared to that of the composite. Therefore, one expects that, when electrically connected, the aluminum part of the joints corrodes while the composite part serves as a cathode.

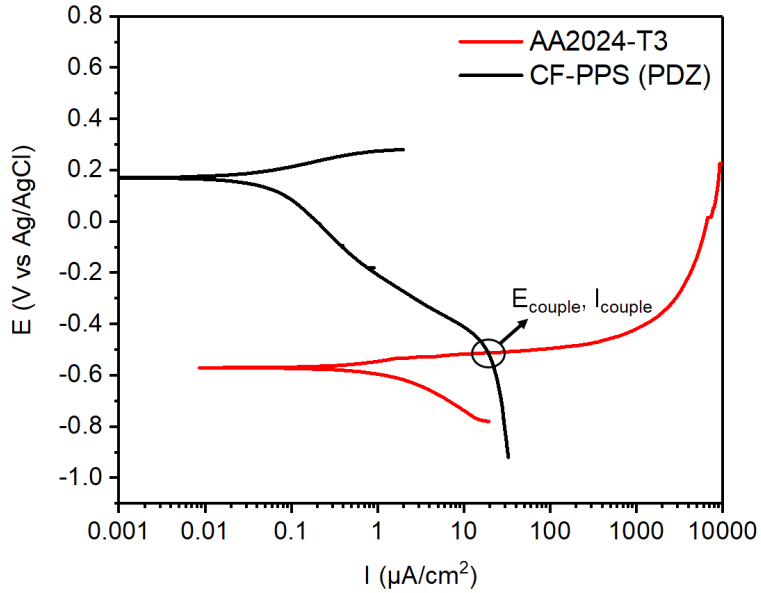

Figure 9.7 Potentiodynamic polarization curves of CF-PPS and AA2024-T3.

Additionally, according to the mixed potential theory [122], the intersection between the cathodic polarization curve of the CF-PPS and the anodic polarization curve of the AA2024-T3 allows to deduce the potential and current of the galvanic couple AA2024-T3/CF-PPS, which has been used in this work. Such properties were found to be E_{couple} = -0.52 V and I_{couple} = 19 µA/cm² (Figure 9.7). Pan *et al.* [125] reported I_{couple} = 56 µA/cm² for the AZ31/CF-epoxy couple. In another study, Mandel *et al.* [116] investigated the corrosion behavior of self-pierced hybrid joints. In that case, the authors measured an I_{couple} = 170 µA/cm² for AA6060-T6/CF-epoxy. In both studies, the corrosion currents were

significantly higher than those measured for the couple AA2024-T3/CF-PPS in this work. Magnesium alloys are known to present higher anodic activity than aluminum alloys [119]. Nevertheless, the corrosion resistance of AA2024-T3 is usually not as good as the other aluminum alloys, such as the 6XXX series [119]. Therefore, this result suggests that the carbon fibers are better isolated by the PPS matrix in the composite used in this work than in the CF-epoxy of that work. The reason may be related the production process of thermoset laminates, which usually consists of prepregging and lay-up processes while the lamination of the PPS involves several hours of the material under pressure [49].

9.2.2 Corrosion evolution at the interface of the friction spot joint: The role of the bonding zones

Figure 9.8 shows the residual strength, while Figure 9.9 presents the fracture surfaces of the joints after salt spray exposure. It is observed that the strength degradation occurred at different paces during the six weeks of exposure to salt spray. The development of the corrosion at the interface of the joints was divided into four stages.

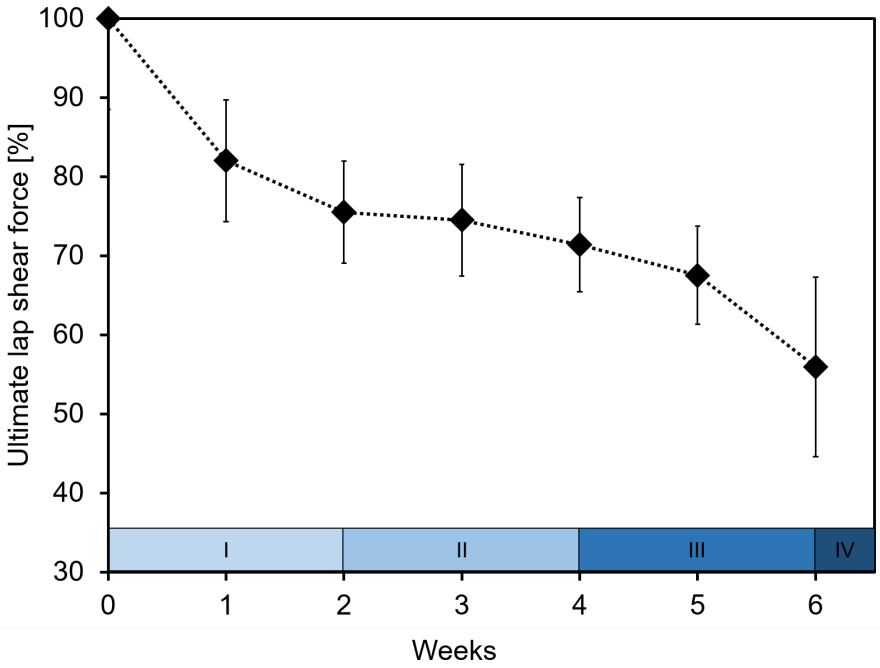

Figure 9.8 Residual strength of friction spot joints after salt spray. Stage I: PPS water absorption and protection by the AZ. Stage II: Transposition of the AZ. Stage III: Corrosion inside the PDZ. Stage IV: Final degradation of the joint.

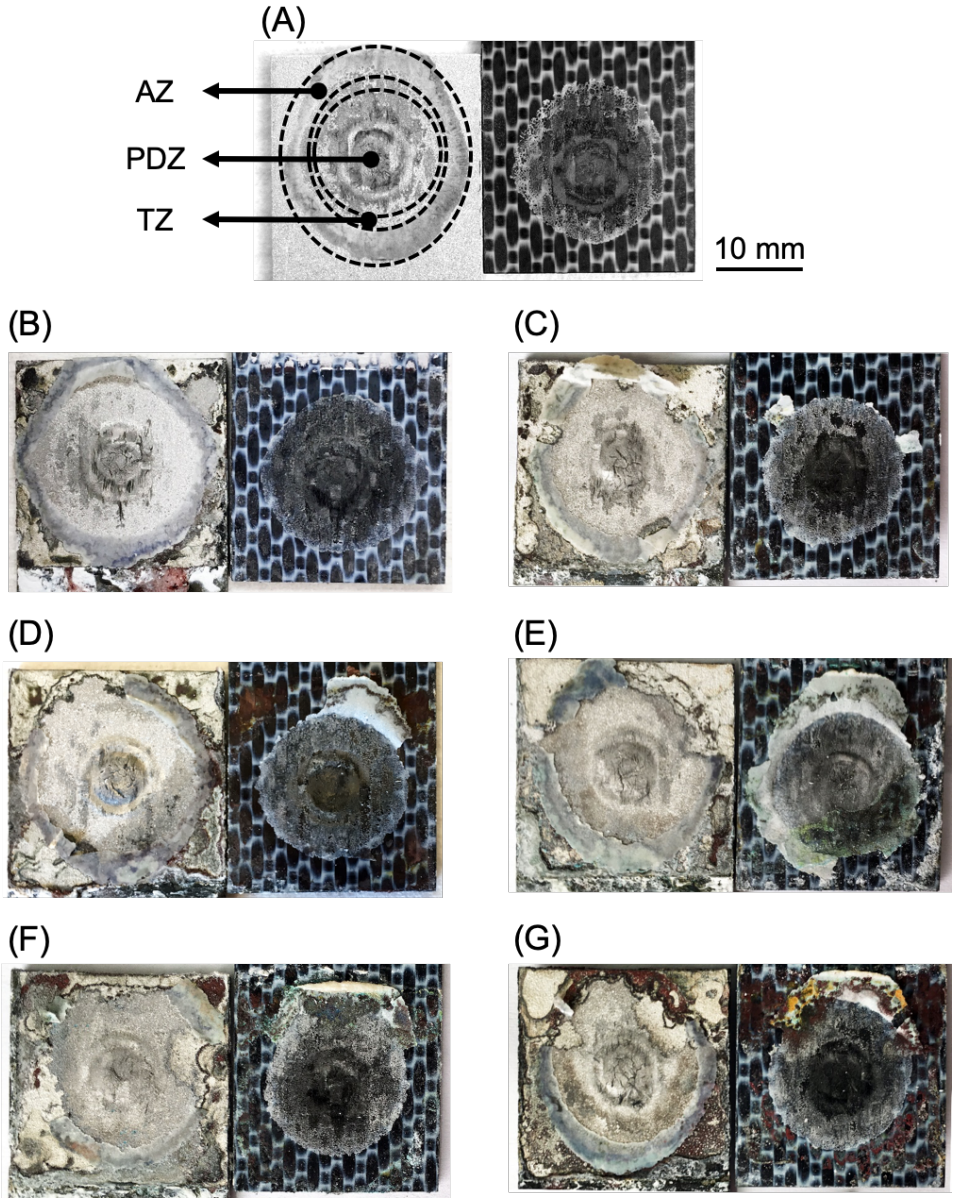

Figure 9.9 (A) Typical fracture surface of friction spot joints, the bonding zones are delimited by the dashed ellipses. Fracture surfaces after (B) one week, (C) two weeks, (D) three weeks, (E) four weeks, (F) five weeks and (G) six weeks of salt spray exposure.

Stage I comprises the first and second weeks of exposure. At this early stage, a decrease of -24 % in the ultimate lap shear force (ULSF) of the joints was observed (no exposure: 3619 ± 132 N; two weeks: 2750 ± 229 N, Figure 9.8). The fracture surface analysis demonstrates that at this exposure time there was no sign of corrosion inside the bonding area of the joint. Figure 9.10-B shows a typical sandblasted aluminum surface close to the polymeric layer inside the PDZ. Nevertheless, the aluminum surface is severely corroded outside the bonding area as a result of self-corrosion and galvanic coupling with the CF-PPS (Figure 9.10-C). It is possible to note that, right outside the AZ, the oxide shape of the aluminum surface around the layer of reconsolidated polymer (Figure 9.10-C). These

observations demonstrate that the layer of reconsolidated polymer in the AZ protected the core of the joint from being corroded. In this case, as no corrosion was found inside the bonding area, the decrease in strength of the joints is attributed to the degradation of the mechanical properties of the composite part. CF-PPS can absorb water and NaCl ions. This phenomenon has been observed in several studies in the literature [216–218]. Batista *et al.* [216] observed plasticization effects in CF-PPS after the salt spray exposure due to water absorption. Decreases in T_g and increases in dumping were among the main plasticization effects. The NaCl migration in the composite also reduced the stiffness of the composite due to the degradation of the fiber-matrix interface [216]. Besides the deterioration of the mechanical properties of the composite matrix, the water absorption and NaCl intake can also induce swelling of the polymeric part, resulting in interface decoupling [114].

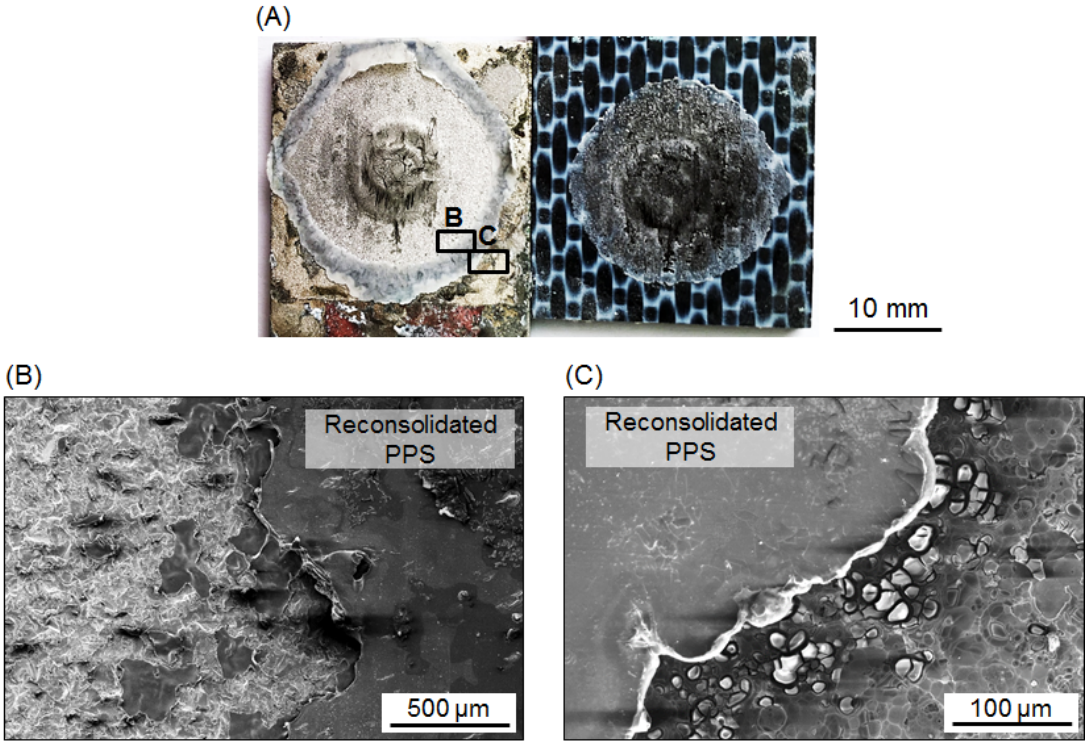

Figure 9.10 **(**A) Fracture surface of a friction spot joint after one week of salt spray exposure. (B) Detail showing no sign of corrosion inside the PDZ. (C) Detail showing the oxidized surface of the aluminum in the outside of the bonding zone after corrosion.

Stage II is characterized for arresting the strength degradation of the joints. From the second until the fourth week of exposure, the strength of the joints decreased only 4% (Figure 9.8). In two weeks of exposure, the reduction in strength was -24 % (2750 ± 229 N), reaching -28 % (2605 ± 193 N) after four weeks of exposure. In this stage, the fracture surface analysis demonstrates that the corrosion process started to degrade the bonding area of the joints. The high temperature at the aluminum surface, combined with the pressure applied during the FSpJ process, promotes the adhesion of the molten layer of

polymer and the aluminum surface [22]. Therefore, the layer of reconsolidated polymer is typically strongly attached to the aluminum surface after the failure of the joints (indicated by AZ in Figure 9.9-A). However, the white arrow in Figure 9.11-A shows a fragment of the polymer layer that remained attached to the composite part after the failure of the joint. It indicates a weakening of the aluminum-polymer layer interface in that region, as a result of the progress of the aluminum corrosion underneath the layer of polymer in the AZ. Figure 9.11-B exhibits signs of aluminum corrosion in the area from where the polymer layer was removed in the AZ. Nevertheless, no corrosion morphologies were identified in the PDZ of the joints (Figure 9.11-C). These observations suggest that the slower strength degradation in this stage is a result of two phenomena: water and NaCl saturation of the composite, and delay of the corrosion process by the presence of the polymeric layer in the AZ. The polymer layer in the AZ acts as a barrier to be transposed by the corrosion process, since the layer of PPS functions as a protective coating that well adheres to the aluminum surface.

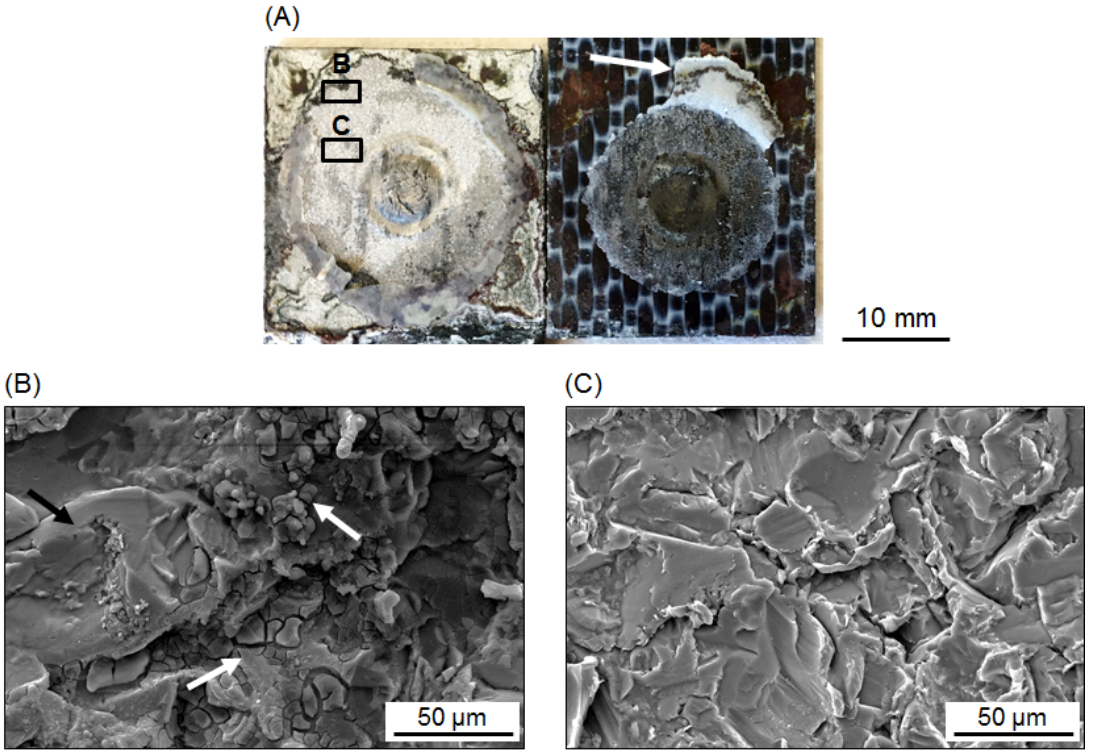

Figure 9.11 (A) Fracture surface of a friction spot joint after three weeks of salt spray exposure; the white arrow indicates a fragment of the polymer layer that remained attached to the composite surface after the failure of the joint. (B) Details showing corrosion morphologies in the area from where the polymer layer was removed at the AZ. (C) Details showing a typical sandblasted aluminum surface in the PDZ; no corroded sites.

Stage III corresponds to the final weeks of this study, the fifth and the sixth weeks. In this stage, the strength of the joints degraded rapidly, reaching a reduction of -44 % (2388 ± 741 N) of ULSF after six weeks of exposure. The fracture surface analysis demonstrated

that the barrier imposed by the AZ to the corrosion process was transposed in this stage. The white arrow in Figure 9.12-A indicates that, close to the free edge of the aluminum part, the AZ is completely detached from the aluminum surface. In such areas, it is possible to observe the nuances of the corrosion process at the interface of the joints due to the presence of the polymer layer in the AZ. Figure 9.12-B shows the transition between the new corroded surface formed after the AZ barrier was transposed (i), and the corroded surface that was previously under the PPS layer (ii). It is noted that in Region ii the corrosion process is more advanced than that in Region i. A flake-like surface is found in Region i (Figure 9.12-B). This type of surface is usually found in initial stages of corrosion [219]. In contrast, Region ii displays an oxide-like surface, showing the further development of the corrosion process in this area.

Additionally, Figure 9.13 presents the EDS analysis of Regions i and ii. For Region i, Al and O were identified as the main elements in the corrosion product. It indicates that in that region aluminum oxide/hydroxide is majorly formed due to the corrosion process [219]. For Region ii, a strong peak of Cu is observed, in addition to Al and O. The presence of Cu in the corrosion product demonstrates the de-alloying of the aluminum part, thus indicating severer corrosion in this region [210]. These observations indicate that the presence of the polymer layer in the AZ postponed the corrosion development inside the PDZ. As discussed earlier, the polymer layer works as a barrier to the corrosion process and acts as a protective coating at the aluminum surface. Nevertheless, as the corrosion slowly advances underneath the polymer layer, a weak layer of oxides is formed at the aluminum-PPS layer interface. Consequently, the polymeric layer detaches from the aluminum surface and the corrosion advances freely to the PDZ.

Therefore, corrosion sites were identified inside the PDZ after six weeks of exposure (white arrows in Figure 9.12-D and E). It is observed that such regions present flake-like surface, indicating an early stage of corrosion [219]. Besides, the corrosion is not widely spread in the PDZ. It is possible to observe non-corroded areas in Figure 9.12-E (green arrows). Thus, it is believed that Stage IV would comprise the generalized corrosion in the PDZ, leading to the final degradation of the quasi-static strength of the joints.

It is worth noting that no sign of corrosive damage was found on the composite surface at all stages (Appendix E). Such observation is quite expected, given the higher anodic activity of AA2024-T3 in comparison with CF-PPS, as discussed in Section 9.2.

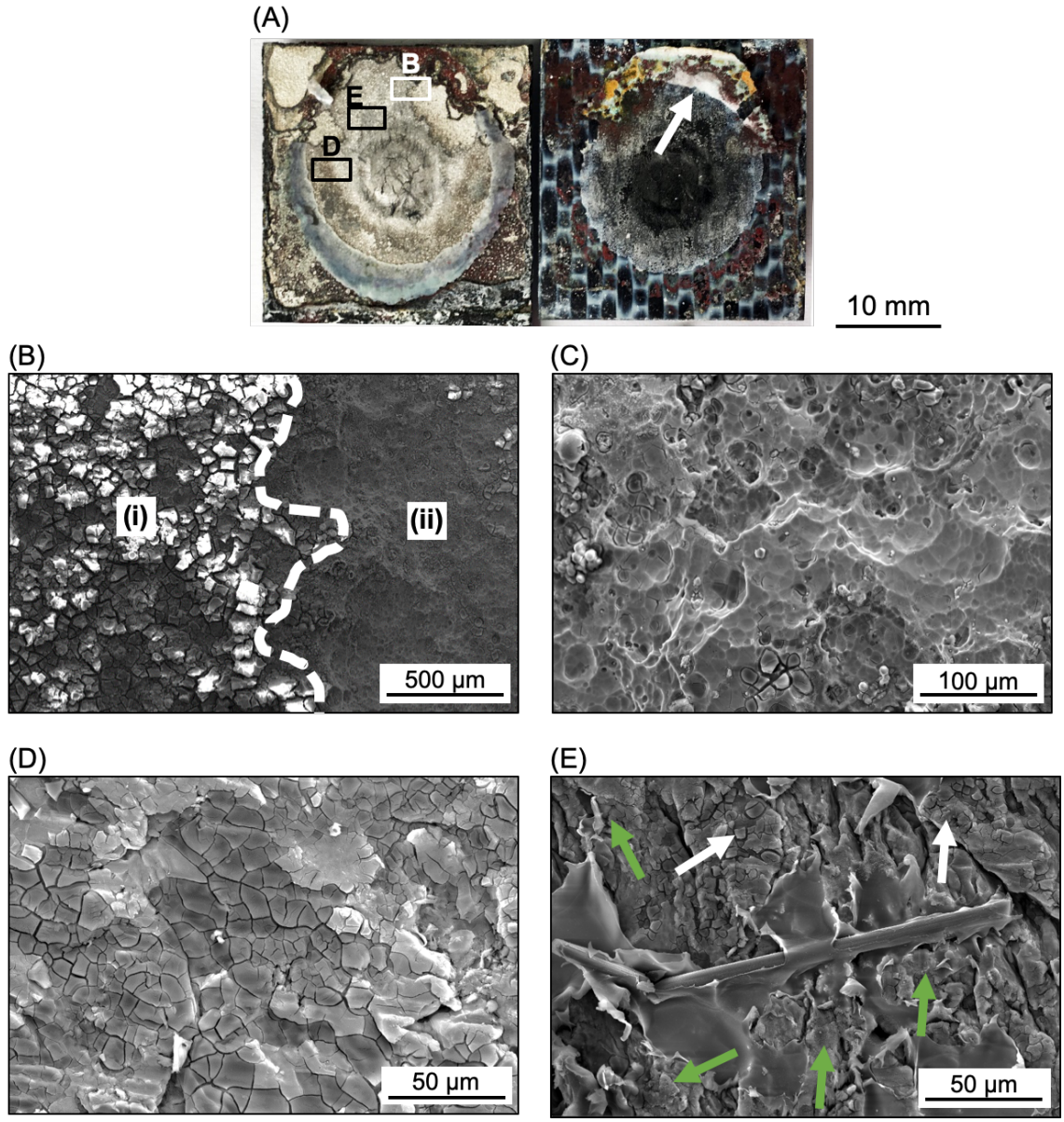

Figure 9.12 (A) Fracture surface of a friction spot joint after six weeks of salt spray exposure; the white arrow indicates a fragment of the polymer layer that remained attached to the composite surface after the failure of the joint. (B) Details showing different corroded areas due to the presence of the PPS layer in the AZ. (C) Detail showing region ii from Figure 9.12-B. (D) and (E) Details showing initial stages of corrosion inside the PDZ (white arrows), green arrows indicate non-corroded areas.

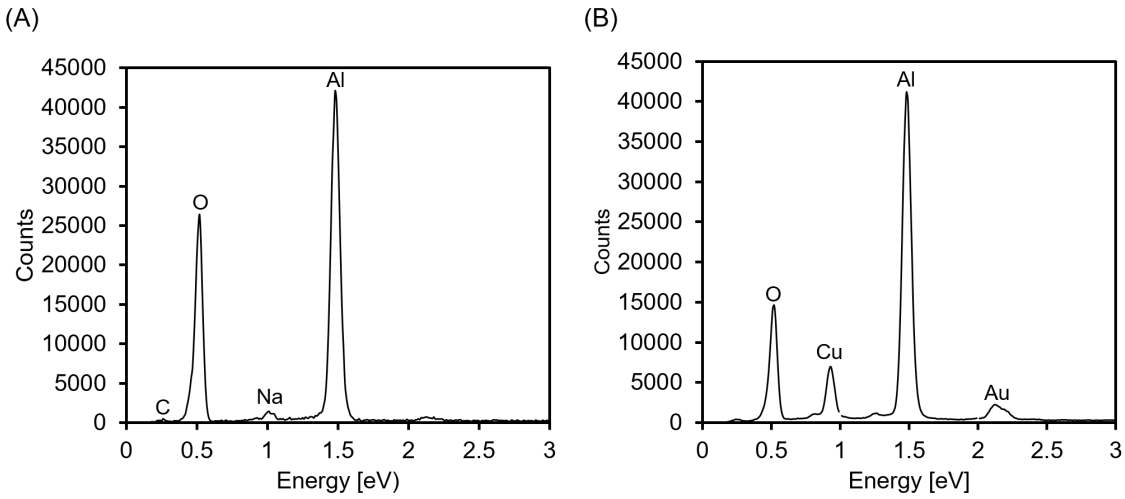

Figure 9.13 EDS analysis of the aluminum surface in (A) Region i and (B) Region ii from Figure 9.12-B.

Chapter 10. Upscaling of the Friction Spot Joining technology: Proof of the FSpJ concept

The construction of robust and safe structures demands advanced engineering and designing efforts [220,221]. Naturally, such requirements cannot simply be achieved through the coupon joints analysis [222]. The "Building Block" approach is a strategy normally adopted for the development of new structural components in the aerospace and automotive industry [223]. This upscaling strategy comprises modeling and testing of coupons, elements, subcomponents, and components to integrate the scientific findings with the requirements and responsibilities of the industry [222]. In this context, the current chapter presents the first results obtained in the upscaling of the FSpJ technology. Here a demonstrator part of an aircraft fuselage was built using FSpJ as one of the joining methods, as a proof of concept for the use of FSpJ in aircraft structures.

The acquired knowledge in this PhD work and previous investigations on friction-based technologies within the Solid-State Joining Processes department and the Young Investigator Group "Advanced Metal-Polymer Hybrid Structures" of the German research center Helmholtz-Zentrum Geesthacht (HZG) were integrated to design and construct a part of an aircraft fuselage with other joining technology experts at HZG. The design was based on the vast experience and diverse projects with partners from the aerospace industry developed at HZG. The fuselage sub-component comprised a hybrid metal-composite skin reinforced with metallic stringers and frames. Figure 10.1 depicts the parts used to the construction of the sub-component along with their main dimensions.

The skin of the part consists of a hybrid combination of 3.4-mm thick AA2024-T3 and CF-PEEK (carbon fiber-reinforced polyether ether ketone) curved panels. The two parts possessed equal dimensions, apart from the window located in the metallic skin, as presented in Figure 10.1-A and B. The stringers consist of 1.6-mm thick AA7050-T7. The stringers in the current design were optimized to minimize the weight of the structure. Therefore, the faying surface of the stringers comprises equally spaced rectangles instead of a continuous interface (Figure 10.1-C). Such design of the faying surface perfectly accommodates the friction spot joints and also promote material and weight savings. Figure 10.1-D shows the frames used in the construction of the part. The frames were made of 2-mm thick AA6016-T6. This combination of materials was selected due to its extensive application in aerospace structures [3,111,221,224].

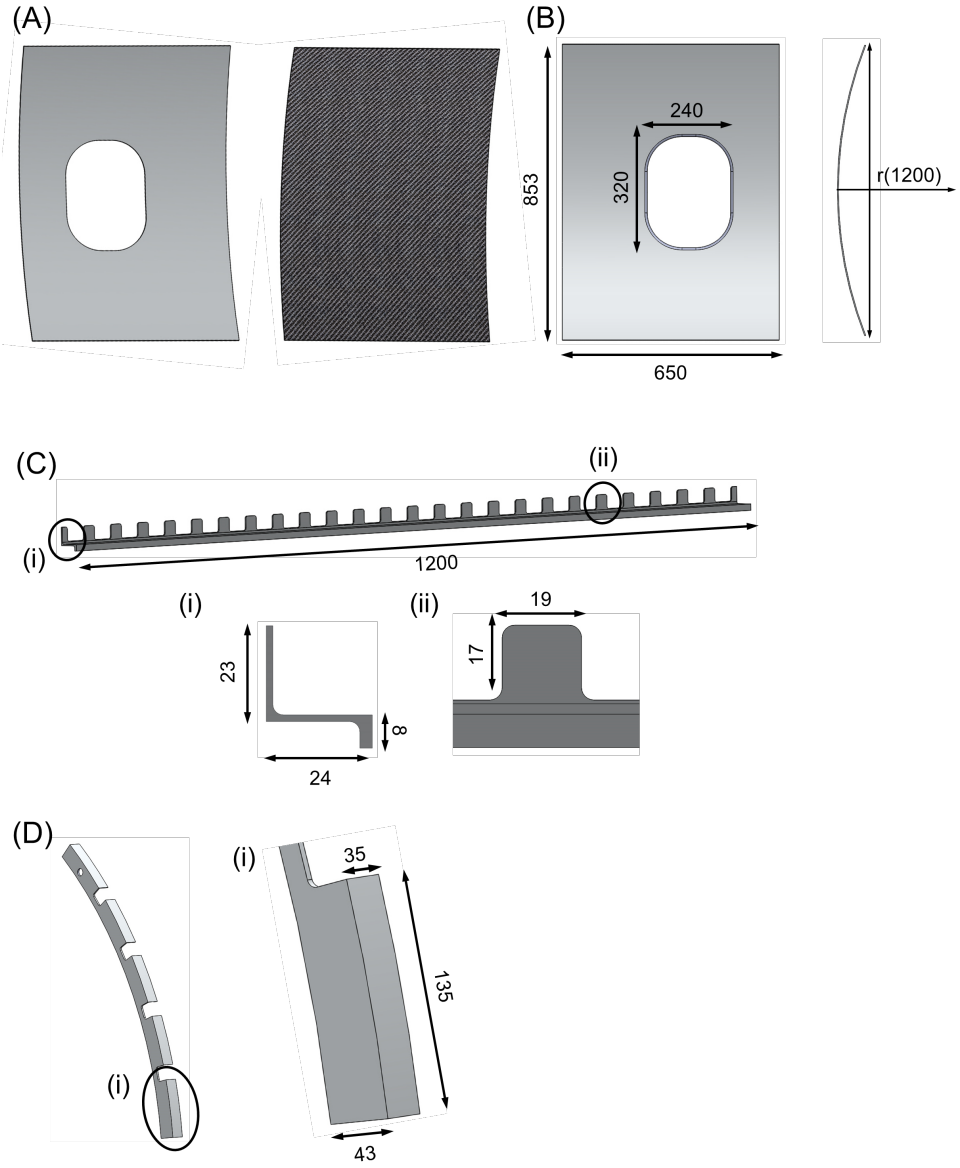

Figure 10.1 (A) Isometric view of the aluminum and composite skins. (B) Front and side view of the skin with the main dimensions of the part. (C) Stringer and (D) frame used to produce the sub-component along with their dimensional details (Dimensions in mm).

Six different technologies were employed to produce the fuselage part. Regarding the metallic section of the fuselage, Bobbin Tool Friction Stir Welding (BT-FSW) [225] was used to weld two units of curved aluminum skin, as depicted in Figure 10.2-B. Stationary Shoulder Friction Stir Welding (SS-FSW) [226] was applied to weld the aluminum skin to the window frame (Figure 10.2-C). Additionally, Refill Friction Stir Spot Welding (RFSSW) [227,228] was employed to weld the aluminum skin with the stringers and frames (Figure 10.2-D and E, respectively).

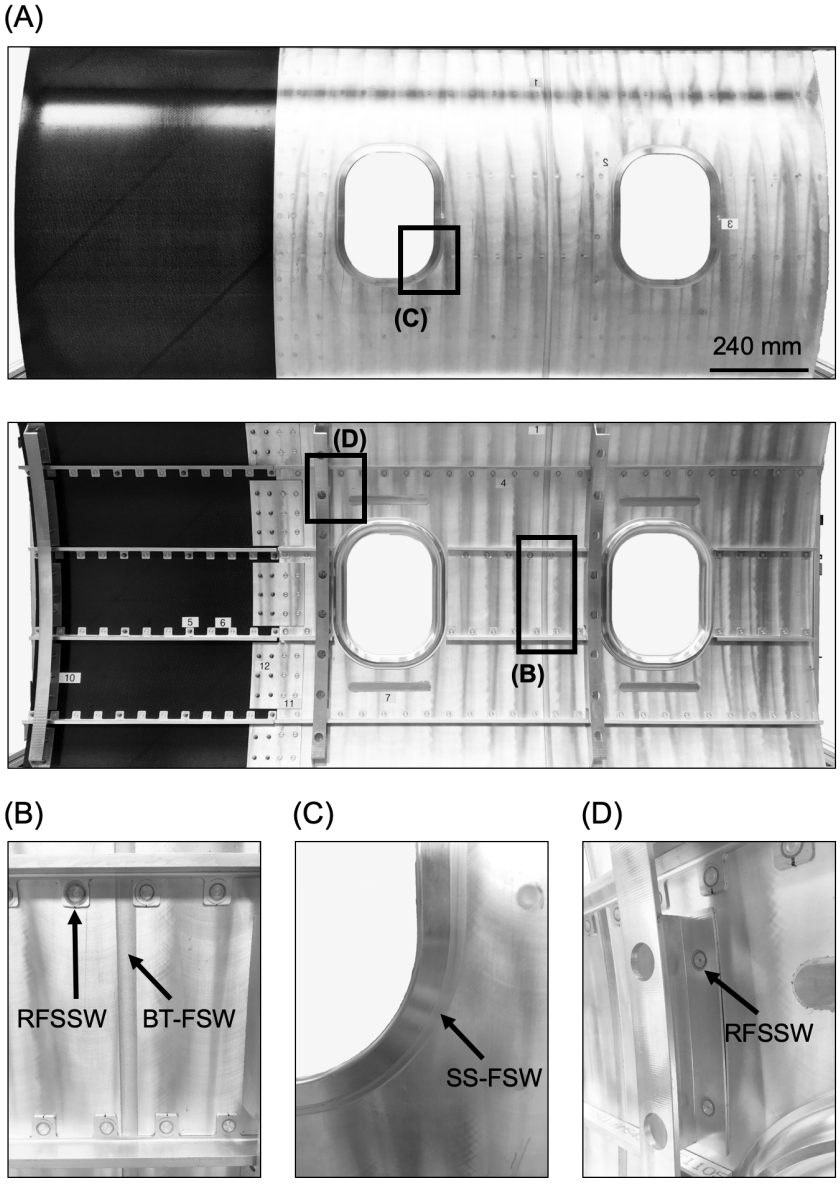

Figure 10.2 (A) Frontal and back overview of the demonstrator produced entirely with friction-based joining technologies. Metallic connections: (B) skin-skin by BT-FSW and skin-stringer by RFSSW, (C) skin-window frame by SS-FSW, (D) skin-frame by RFSSW.

Regarding the hybrid section of the fuselage, Friction Riveting (FricRiveting) [229] and Friction Spot Joining were used to produce the metal-composite connections. FricRiveting was applied to join the aluminum frames to the composite skin using pure titanium rivets (Figure 10.3-B). Additionally, FricRiveting – in combination with RFSSW – was applied to connect the composite skin to the aluminum skin by means of aluminum doublers (Figure 10.3-C). Friction Spot Joining was used to join the stringers to the composite skin, as depicted in Figure 10.3-D. The process parameters used for this combination of materials and thicknesses is given in Appendix G. In the stringers, one friction-riveted joint was added for every two friction spot joints. The friction-riveted joints work as

chicken rivets in the structure. The addition of chicken rivets in adhesive bonded areas of the structure is a common design practice in the aircraft industry to ensure the fail-safe of the structure [29,230]. Thus, if the adhesive fails, the chicken rivets can carry the main load and prevent the premature failure of the structure [29,230]. In this demonstrator, the friction-riveted joints were employed as chicken rivets for the friction spot joints, while the FSpJ as substitute for adhesive bonding.

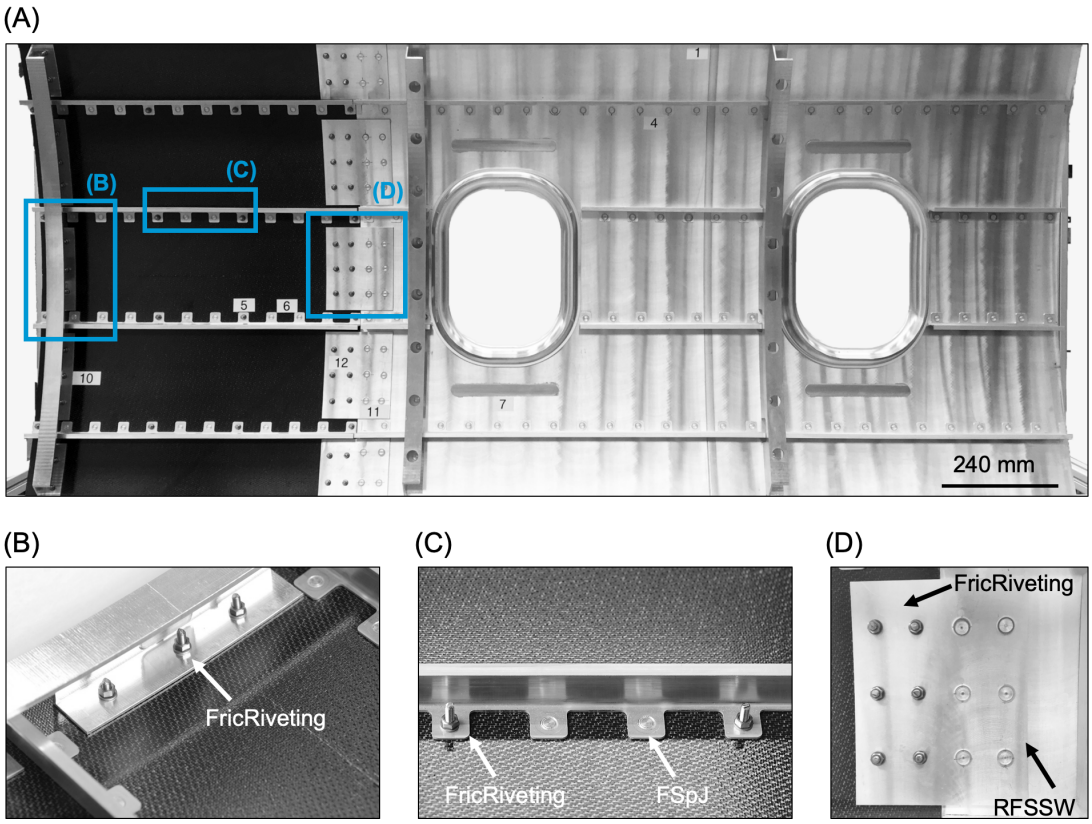

Figure 10.3 (A) Overview of the demonstrator produced entirely with friction-based joining technologies. Hybrid connections: (B) composite skin-metallic frame joined by FricRiveting, (C), composite skin-metallic stringer joined by FSpJ (D) composite skin-metallic doubler joined by FricRiveting and RFSSW.

A preliminary assessment of the weight savings provided by the composite introduction in the traditional metallic design of the fuselage, as well as by the absence of traditional fasteners, was performed. The weight of the structural parts used to build the sub-component (Figure 10.1) were estimated using the mass properties tool in *SolidWorks* software and the respective densities of the materials from the software library. Table 10.1 lists the estimated weight for the structural parts used to build the sub-component, as well as standard fasteners used in traditional designs for aircraft structures [29].

Considering the weight of the parts given by Table 10.1, three different designs for the sub-component were compared in terms of structural weight: 1: full-metallic and fastener-

free (**Table 10.2**), 2: full-metallic and assembled by traditional fasteners (Table 10.3), and 3: hybrid and assembled by friction-based joining technologies (Table 10.4).

Table 10.1 Structural parts and their estimated weights for the design of the sub-component.

Part	Weight [kg]
Stringer (1 unit = 25 spots)	0.291
Frame	0.581
AA2024-T3 skin with window	4.2
AA2024-T3 skin without window	4.8
CF-PEEK skin	2.4
Long AA2024-T3 doubler	0.247
Short AA2024-T3 doubler	0.124
Ti6Al4V bolt (EN6114, 6.35 mm diameter, 13 mm length)	0.005
Low alloy steel nut (EN3536, 6.35 mm diameter)	0.002
Window frames, AA2024-T3	1.05

Table 10.2 Structural parts and their estimated weights for the full-metallic and fastener-free design of the sub-component.

Part	Unit	Weight [kg]
Stringers	5.92	1.75
Frames	3	1.74
AA2024-T3 skin with window	2	8.4
AA2024-T3 skin without window	1	4.8
Long doubler	3	0.74
Short doubler	2	0.25
Window frame	2	2.1
TOTAL		**19.78**

Table 10.3 Structural parts and their estimated weights for the full-metallic design of the sub-component assembled by traditional fasteners.

Part	Unit	Weight [kg]
Stringers	5.92	1.75
Frames	3	1.74
AA2024-T3 skin with window	2	8.4
AA2024-T3 skin without window	1	4.8
Long doubler	3	0.74
Short doubler	2	0.25
Window frame	2	2.1

Bolts and nuts	568	1.98
TOTAL		**21.77**

Table 10.4 Structural parts and their estimated weights for the sub-component produced in this work.

Part	Unit	Weight [kg]
Stringers	5.92	1.75
Frames	3	1.74
AA2024-T3 skin with window	2	8.4
CF-PEEK skin	1	2.4
Long doubler	3	0.74
Short doubler	2	0.25
Window frame	2	2.1
TOTAL		**17.38**

The construction of the hybrid sub-component using purely friction-based joining technologies promoted a total weight reduction of approximately 20% (approximately 4.4 kg) compared to the full-metallic and state-of-the-art bolted design (Tables 10-3 and 10-4). One-third of the AA2024-T3 skin was replaced by a CF-PEEK panel resulting in a decrease of 12% in weight; approximately 2.4 kg. In this case, the introduction of the CF-PEEK in the structure is aided by the FSpJ technology, which provided a fastener-free alternative of assembly. Additionally, the elimination of traditional fastener connections throughout the structure provided 8% decrease in the structural weight (around 2 kg). Approximately 284 fastened connections were avoided in the production of this sub-component by using friction-based technologies, such as FSpJ. Naturally, the design of such a sub-component must be further optimized to maximize the damage tolerance of the structure. Besides, mechanical tests must be conducted to assess the mechanical performance of the demonstrator part. Nevertheless, the successful construction of this sub-component demonstrates the potential of FSpJ as a joining solution for the manufacturing of aircraft hybrid structures in future developments.

Chapter 11. Summary and Conclusions

This doctoral work aimed to fulfill the knowledge gaps related to the mechanical integrity and corrosion behavior of AA2024-T3/CF-PPS friction spot joints for future aircraft applications. The damage evolution at the interface of the joints was investigated along with the fatigue and impact damage tolerance. The corrosion behavior of the joints was also assessed and correlated with the precipitation state and the bonding zones of the joints. Finally, as a first step for the upscaling of this technology, an aircraft sub-component was constructed using FSpJ, among other friction-based technologies. In accordance with the objectives of the work presented in Chapter 2, the main conclusions were drawn from the results obtained:

Damage evolution and failure behavior

FEM and experiments were integrated to understand the damage evolution at the interface of friction spot joints under shear stresses. It was observed that the stresses developed asymmetrically in the joined area due to the asymmetrical secondary bending of the structure. The out-of-plane displacement due to secondary bending was less expressive for the aluminum part due to its higher stiffness in comparison with that of the CF-PPS ($E_{AA2024\text{-}T3}$ = 73 GPa, $E_{CF\text{-}PPS}$ = 53 GPa). The damage initiated at the AZ and propagated as a linear front from the edges to the center of the joined area. Nevertheless, as the damage advanced inside the PDZ, its propagation became an asymmetrical linear front. In the PDZ, the damage evolved preferably from the free edge of the composite part due to the asymmetrical stress concentration in the joints.

The influence of the bonding zones in the mechanical behavior of the joints was also evaluated. The AZ presented a damage evolution rate of 0.14 % N^{-1}, while the PDZ fails at a rate of 0.04 % N^{-1}; approximately three times slower than the degradation rate of the AZ. This result demonstrated a higher efficiency of the bonding mechanisms of the PDZ (the nub and micro-mechanical interlocking) compared to the adhesion forces of AZ. Using FEM, the mechanical behavior of joints without the AZ and without the metallic nub (flat interface) under shear loading was predicted. The joint without AZ presented a mechanical behavior identical to the standard joint, suggesting that the AZ does not contribute to the global mechanical performance of the friction spot joints. In contrast, the joint without the nub prematurely failed at 0.32 mm of displacement, while the standard joint extended until 0.61 mm. It was observed that the joint without the nub failed rapidly after the damage reached the PDZ. It indicates that the load bearing in the PDZ is majorly due to the shearing between the metallic nub and the volume of composite around it. This indicates that the nub strongly contributes to the bearable load of the PDZ, and consequently to the ductility of the joint.

Based on the new findings of this study, several modifications were proposed to the failure theory of friction spot joints proposed by Goushegir *et al.* [42]. The failure of the joints

was summarized into four stages, which can be identified in the force-displacement curve of the joints. Stage 1 comprised the initiation and propagation of a symmetric and linear front crack through the AZ. No plastic deformation is observed in this stage and the failure occurred through simple decoupling of the interface. Stage 2 was characterized by the reduction in stiffness of the joint due to the damage initiation in the PDZ. The damage in the PDZ mostly comprises the plastic deformation of the composite. Stage 3 comprised the progressive plastic deformation in the PDZ. Finally, Stage 4 corresponded to the fraction of second in which the USLF is reached and the joint catastrophically fails.

Fracture energy and fatigue damage tolerance

The crack growth resistance of friction spot joints was investigated under quasi-static mixed-mode I/II loading. The R-curve of friction spot joints presented a typical rising behavior. The crack growth resistance increased as the crack advanced through the different bonding zones of the joint. As the crack propagated in the AZ, the strain energy release rate was extremely low; approximately 0.85 ± 0.01 J m^{-2}. Such low values of strain energy release rate in this zone demonstrate that AZ provides practically no resistance to the crack propagation at the interface of the joint. This result confirms the previously discussed FEM prediction that the AZ does not contribute to the global mechanical performance of friction spot joints. The strain energy release rate greatly increased as the crack advanced to the TZ and PDZ of the joint. A maximum of 274 ± 1 J m^{-2} was achieved as the crack extension reached approximately 80% of the metallic nub inside the PDZ. Nevertheless, at this point, the interface of the joint is no longer able to support stable crack propagation. The loss of the metallic nub caused a sudden decrease in the strain energy release rate and the unstable crack propagated rapidly until the total failure of the joint. This result demonstrates that the PDZ - including the metallic nub - is the strongest and most damage-tolerant zone of the friction spot joints.

The fatigue crack growth of friction spot joints was evaluated and summarized into three well-defined stages. Stage I comprises the crack propagation in the AZ. In this stage, the strain energy release rate rapidly rises from 253 ± 6 J m^{-2} to 389 ± 10 J m^{-2} due to the presence of the PDZ ahead the crack tip. An average crack growth rate of 0.10 ± 0.03 mm/cycle is observed in this stage as a result of the low crack growth resistance of AZ. Stage II comprised the region of linear behavior for G and da/dN. In this stage, the strain energy release rate increased linearly from 389 ± 10 J m^{-2} to 462 ± 9 J m^{-2} as the plastic deformation of the PPS occurred in the PDZ of the joint. A stabilized crack growth rate of 0.006 ± 0.001 mm/cycle is registered in this stage; approximately 16 times slower than the growth rate in Stage I. Finally, Stage III comprised the unstable crack propagation that occurs as the crack reached approximately 80% of the metallic nub region. It is important to note that the friction spot joints presented steady crack propagation rates during the stable Stages I (0.10 ± 0.03 mm/cycle) and II (0.006 ± 0.001 mm/cycle). The typical range of stable crack propagation rates for adhesive bonded joints reported in the literature lies between 10^{-4} – 1 mm/cycle. This broad variation of crack propagation rate is often modeled

by different equations like the Paris law. Nevertheless, it is believed that the steady crack propagation rates presented by friction spot joints could certainly simplify the design of structures and components.

Impact resistance

The impact resistance of AA2024-T2/CF-PPS hybrid joints was investigated. Four levels of impact energy were tested: 2 J, 4 J, 6 J, and 8 J. The joints were aluminum-side and composite-side impacted to provide a preliminary design guideline on the impact damage tolerance of such hybrid joints. It was observed that for each energy level, the load applied by the impactor on the joint is very similar independent of the surface under impact. The maximum force achieved during the impact increases linearly from 2 J to 6 J of impact energy. At 8 J, the failure under impact of the joints occurred. At this energy level, it is observed that the maximum force achieved is statistically the same as the force achieved at 6 J (6 J: 5440 ± 186 N (AS)/5085 ± 162 N (CS); 8 J: 5305 ± 125 N (AS)/4987 ± 345 N (CS)). Thus, the threshold for impact force is approximately 5204 ± 178 N for a single friction spot joint.

The joints presented rebounding behavior for all the investigated energy levels, thereby implying that the impact energy was not totally absorbed for the joints, even though the joints failed at 8 J of impact energy. It suggests that aluminum and composite could further absorb energy during an impact event. Nevertheless, the interface of the joint has its threshold for absorption of impact energy around 6.5 J, which was reached when the joint is impacted with 8 J of potential energy independent of the surface under impact. Thus, this study shows that a single friction spot joint could absorb up to 103 $kJ.m^{-2}$ of joined area. The literature reported energy absorption up to 48 $kJ.\ m^{-2}$ in CF-epoxy bonded joints for automotive applications which accounts to approximately half of the intake of friction spot joints.

Shear after impact was employed to evaluate the residual strength of the joints. Generally, the aluminum-side impacted joints presented lower residual strength after the impact than the composite-side impacted joints. The impact energy introduced from the aluminum side is mostly absorbed in the plastic deformation of the aluminum part, bending the aluminum and promoting the detachment of the interface. Otherwise, the impact energy introduced from the composite side is mostly absorbed on the creation/extension of internal damage through the plies of the composite. Thus, the impact energy is only partially transferred to the interface of the joint in the case of the composite-side impact. Consequently, those joints presented higher residual strength after the impact.

Corrosion behavior

The corrosion behavior of metal–composite friction spot joints was investigated using salt spray exposure. Regarding the top surface of the joints, the aluminum part corroded preferentially in the HAZ. It was demonstrated that BM and SZ+TMAZ displayed a

similar profile of particles, thus presenting a lower volume fraction of S'(S) phase than the HAZ. The higher fraction of S'(S) and coarse intermetallic particles in the HAZ increased the anodic activity in this zone. The coarse intermetallic particles lead to pitting corrosion (high self-corrosion potential), while the S'(S) precipitates are associated with intergranular corrosion (formation of precipitate-free and Cu-depletion zones around the grain boundaries). The macro-galvanic coupling between the BM, HAZ, and SZ may also potentialize the corrosion in the HAZ.

In addition, the corrosion development at the interface of the joints was evaluated. Four stages were identified and correlated with the global strength degradation of the joints. Stage I comprises the first two weeks of exposure. In Stage I, a fast strength degradation of the joints was observed (0% to -24% of ULSF). Nevertheless, no corrosion was identified in the joined area of the joints. Therefore, it is believed that water absorption and NaCl-migration into the composite caused plasticization and the consequent deterioration of the mechanical properties of the composite. Stage II corresponds to the third and fourth weeks of exposure. In Stage II, the strength degradation rate of the joints decreased. In two weeks of exposure, the reduction in strength was -24%, reaching -28% after four weeks of exposure. The slower strength degradation in this stage is a result of two phenomena: water and NaCl-saturation of the composite and the protection of the PDZ by the presence of the PPS layer in the AZ. The polymer layer acted as a protective coating that adheres well to the aluminum surface. Stage III comprises the fifth and sixth weeks of exposure. In this stage, the strength of the joints degraded rapidly, reaching a reduction of -44% of ULSF after six weeks of exposure. The development of corrosion underneath the PPS layer created a weak layer of oxides at the aluminum-PPS layer interface. Consequently, the polymeric layer was detached from the aluminum surface, and the corrosion could advance into the PDZ. Finally, Stage IV allegedly comprises the generalized corrosion in the PDZ and the final strength degradation of the joint.

Upscaling of the Friction Spot Joining technology

Part of an aircraft fuselage was built using FSpJ as one of the joining methods. The fuselage sub-component comprised a hybrid metal-composite skin reinforced with metallic stringers and frames. Six different technologies were employed to produce the fuselage part. The construction of such sub-component using purely friction-based joining technologies promoted a reduction of approximately 20% (4.4 kg) in its weight compared to the full-metallic and state-of-the-art bolted design. The weight reduction is provided mainly by the partial substitution of the metallic skin for a composite skin (12%) and the elimination of traditional fasteners (8%). Despite the future mechanical assessments of this structure, the construction of this demonstrator successfully demonstrates the potential of FSpJ as a joining solution for hybrid aircraft structures in the future.

Chapter 12. Recommendations for future work

Although this PhD thesis fulfills the proposed objectives, it also revealed topics that must be further investigated for the increase of the technological readiness level of the FSpJ technology. These may include:

- Development of a finite element model which considers the initiation and propagation of the crack using J-Integral solutions. Thus, the occurrence/influence of the plasticity at the crack tip and the crack-closure phenomenon for the friction spot joints could be evaluated. In addition, the model would also support the fatigue damage tolerance of friction spot joined structures, as the experimental crack monitoring becomes highly complex for multiple-spot FSpJ structures.

- Modeling and validation of a crack growth law for friction spot joints, as a complementation of the preliminary model presented in Chapter 7.

- Evaluation of the impact resistance and energy absorption of elements and sub-components produced by FSpJ based on the findings presented in Chapter 8.

- Development of protection systems for the AA2024-T3/CF-PPS joints to stall the mechanisms of strength degradation associated with the galvanic corrosion discussed in Chapter 9.

- Optimization of the stress distribution in the friction spot joints in terms of geometry and load path (secondary bending) to maximize the damage tolerance of the joints.

- Evaluation of the residual stresses generated due to the highly dissimilar physical properties (e.g. thermal expansion, diffusivity, specific heat, thermal conductivity) of metal and composites. In this topic, efforts should be put in the modeling of heat development during the FSpJ process. Thus, the effect of additional thermal cycles on adjacent spots during the production of multi-spot structures could be understood in a better way.

References

[1] Amancio-Filho ST, dos Santos JF. Joining of Polymers and Polymer-Metal Hybrid Structures: Recent Developments and Trends. Polym Eng Sci 2009;49:1461–76. doi:10.1002/pen.21424.

[2] Mallick PK. Materials, design and manufacturing for lightweight vehicles. 1st ed. Cambridge, UK: Woodhead Publishing Limited; 2010.

[3] Boeing 787: from the ground up. <www.boeing.com/commercial/aeromagazine/articles/qtr_4_06/article_04_2.html. Access: June 2018.

[4] Flight Airworthiness Technology, Airbus Technical Magazine, vol. FAST 30, 2011.

[5] Tencate Advanced will provide ballisct solutions for Embraer KC-390". <http://www.compositesworld.com/news/tencate-advanced-armour-will-provide-ballistic-solutions-for-the-embraer-kc-390>. Access: June 2018.

[6] BMW i3, the inside story: what it's made of, how it's made - SAE International. <http://articles.sae.org/12056>. Access: June 2018.

[7] Rotheiser J. Joining of Plastics 3E: Handbook for Designers and Engineers. 3 edition. Munich; Cincinnati, Ohio: Hanser; 2009.

[8] Habenicht G. Applied Adhesive Bonding: A Practical Guide for Flawless Results. 1 edition. Weinheim: Wiley-VCH; 2009.

[9] Chang B, Shi Y, Shijie D. Comparative studies on stresses in weld-bonded, spot-welded and adhesive-bonded joints. Journal of Materials Processing Technology 1999:230–6.

[10] Messler RW. Joining of Materials and Structures: From Pragmatic Process to Enabling Technology. 1 edition. Butterworth-Heinemann; 2000.

[11] McKnight SH, McBride MG, Gillespie JW. Joining of Polypropylene and Aluminum: Evaluation of Environmental Durability. 25th International SAMPE Technical Conference, Covina: 1993, p. 26–8.

[12] Chen M-A, Li H-Z, Zhang X-M. Improvement of shear strength of aluminium-polypropylene lap joints by grafting maleic anhydride onto polypropylene. International Journal of Adhesion and Adhesives 2007;27:175–87. doi:10.1016/j.ijadhadh.2006.01.008.

[13] Marinelli JM, Lambing CLT. Advancement in Welding Technology for Composite-to-Metallic Joints. Journal of Advanced Materials 1994;25:20–7.

[14] Wagner G, Balle F, Eifler D. Ultrasonic Welding of Hybrid Joints. JOM 2012;64:401–6. doi:10.1007/s11837-012-0269-5.

[15] Villegas IF, Moser L, Yousefpour A, Mitschang P, Bersee HE. Process and performance evaluation of ultrasonic, induction and resistance welding of advanced thermoplastic composites. Journal of Thermoplastic Composite Materials 2013;26:1007–24. doi:10.1177/0892705712456031.

[16] Costa AP da, Botelho EC. A Review of Welding Technologies for Thermoplastic Composites in Aerospace Applications. Journal of Aerospace Technology and Management 2012;4:255–65. doi:10.5028/jatm.2012.04033912.

[17] Ageorges C, Ye L. Resistance Welding of Metal/Thermoplastic Composite Joints. Journal of Thermoplastic Composite Materials 2001;14:449–75. doi:10.1106/PN74-QXKH-7XBE-XKF5.

[18] Mitschang P, Velthuis R, Didi M. Induction Spot Welding of Metal/CFRPC Hybrid Joints. Advanced Engineering Materials 2013;15:804–13.

[19] Messler RW, Bell J, Craigue O. Laser beam weld bonding of AA5754 for automobile structures. Welding Journal 2003;82:151s–9s.

[20] Amancio-Filho ST, dos Santos J. European Patent EP2329905B1, 2012.

[21] Amancio-Filho ST, Bueno C, dos Santos JF, Huber N, Hage Jr. E. On the feasibility of friction spot joining in magnesium/fiber-reinforced polymer composite hybrid structures. Materials Science and Engineering: A 2011;528:3841–8. doi:10.1016/j.msea.2011.01.085.

[22] Goushegir SM, dos Santos JF, Amancio-Filho ST. Friction Spot Joining of Aluminum AA2024 / Carbon-Fiber Reinforced Poly(phenylene sulfide)composite single lap joints: microstructure and mechanical performance. Materials & Design 2014;50:196–206. doi:10.1016/j.matdes.2013.08.034.

[23] André NM, Goushegir SM, dos Santos JF, Canto LB, Amancio-Filho ST. Friction Spot Joining of aluminum alloy 2024-T3 and carbon-fiber-reinforced poly(phenylene sulfide) laminate with additional PPS film interlayer: Microstructure, mechanical strength and failure mechanisms. Composites Part B: Engineering 2016;94:197–208. doi:10.1016/j.compositesb.2016.03.011.

[24] Esteves JV, Goushegir SM, dos Santos JF, Canto LB, Hage Jr. E, Amancio-Filho ST. Friction spot joining of aluminum AA6181-T4 and carbon fiber-reinforced poly(phenylene sulfide): Effects of process parameters on the microstructure and mechanical strength. Materials & Design 2015;66:437–45. doi:10.1016/j.matdes.2014.06.070.

[25] Goushegir SM. Friction spot joining (FSpJ) of aluminum-CFRP hybrid structures. Weld World 2016;60:1073–93. doi:10.1007/s40194-016-0368-y.

[26] Schmidt HJ, Schmidt B. Fatigue & Damage Tolerance and Composite Training, Helmholtz-Zentrum Geesthacht: Geesthacht. 2012.

[27] Balle F, Huxhold S, Wagner G, Eifler D. Damage Monitoring of Ultrasonically Welded Aluminum/ CFRP-Joints by Electrical Resistance Measurements. Procedia Engineering 2011;10:433–8. doi:10.1016/j.proeng.2011.04.074.

[28] Niu MC. Composite Airframe Structures: Practical Design Information and Data. 1st edition. Hong Kong Conmilit Press limited; 1992.

[29] Niu MC. Airframe Stress Analysis and Sizing. 3rd edition. Hong Kong Conmilit Press limited; Los Angeles, Calif.: Adaso/Adastra Engineering Center; 2011.

[30] "2015 GHTC ALUMNI IN DALLAS", award in Lightweight Design, prize of Germany Trade & Invest (GTAI) for GHTC® Alumni to present the Friction Spot Joining. <http://www.research-in-germany.org/en/campaigns-and-activities/ghtc-award/2015-ghtc-meets-gtai/Amancio.html>, Dallas, USA: 2015.

[31] "Rising Star, Category Joining Techniques" Automotive Circle International, Nürnberg, Germany: 2015.

[32] "Georg-Sachs-Preis", German Society for Materials Science (Deutsche Gesellschaft für Materialkunde –DGM), Darmstadt, Germany: 2014.

[33] "German High Tech Champions 2013 in Lightweight Design", award in the category joining technology. <http://www.research-in-germany.org/en/campaigns-and-activities/ghtc-award/2013-lightweight-design-v2/Amancio.html>, Munich: Federal Ministry of Education and Research (BMBF); 2013.

[34] Amancio-Filho ST. Raiser Innovation Award for Friction Welding« Category: Auszeichnung. Friction Spot Joining of Lightweight Metals and Fiber-Reinforced Polymer Hybrid Structures, Munich: 2011.

[35] Goushegir SM. Friction Spot Joining of Metal-Composite Hybrid Structures.PhD thesis. Technical University of Hamburg, 2015.

[36] Manente André N, F. dos Santos J, T. Amancio-Filho S. Evaluation of Joint Formation and Mechanical Performance of the AA7075-T6/CFRP Spot Joints Produced by Frictional Heat. Materials 2019;12:891. doi:10.3390/ma12060891.

[37] Goushegir SM, Scharnagl N, dos Santos JF, Amancio-Filho ST. XPS analysis of the interface between AA2024-T3/CF-PPS friction spot joints. Surf Interface Anal 2015;10.1002/sia.5816. doi:10.1002/sia.5816.

[38] Balle F, Emrich S, Wagner G, Eifler D, Brodyanski A, Kopnarski M. Improvement of Ultrasonically Welded Aluminum/Carbon Fiber Reinforced Polymer-Joints by Surface Technology and High Resolution Analysis. Adv Eng Mater 2013;15:814–20. doi:10.1002/adem.201200282.

[39] Jung KW, Kawahito Y, Takahashi M, Katayama S. Laser direct joining of carbon fiber reinforced plastic to zinc-coated steel. Materials & Design 2013;47:179–88. doi:10.1016/j.matdes.2012.12.015.

[40] André NM, Goushegir SM, Canto LB, Amancio-Filho, Dos Santos JF. Improvement of fatigue performance of metal-composite friction spot joints based on the weld-bonding concept. ANTEC technical conference, society of Plastic Engineers, Orlando, USA: 2018.

[41] Dubé M, Hubert P, Gallet JNAH, Stavrov D, Bersee HEN, Yousefpour A. Fatigue performance characterisation of resistance-welded thermoplastic composites. Composites Science and Technology 2008;68:1759–65. doi:10.1016/j.compscitech.2008.02.012.

[42] Goushegir SM, dos Santos JF, Amancio-Filho ST. Failure and fracture micro-mechanisms in metal-composite single lap joints produced by welding-based joining techniques. Composites Part A: Applied Science and Manufacturing 2016;81:121–8. doi:10.1016/j.compositesa.2015.11.001.

[43] Rosenfeld M, editor. Damage Tolerance in Aircraft Structures. 100 Barr Harbor Drive, PO Box C700, West Conshohocken, PA 19428-2959: ASTM International; 1971.

[44] Mahadevan S, Ni K. Damage tolerance reliability analysis of automotive spot-welded joints. Reliability Engineering & System Safety 2003;81:9–21. doi:10.1016/S0951-8320(03)00057-7.

[45] Qing X, Sun H-T, Dagba L, Chang F-K. Damage-Tolerance-Based Design of Bolted Composite Joints. In: Grant P, Rousseau C, editors. Composite Structures: Theory

and Practice, 100 Barr Harbor Drive, PO Box C700, West Conshohocken, PA 19428-2959: ASTM International; 2001, p. 243-243–30.

[46] Gere JM, Goodno BJ. Mechanics of Materials. 8th edition. Stamford, CT: Cengage Learning; 2012.

[47] Dillard DA. Improving adhesive joint design using fracture mechanics. Advances in Structural Adhesive Bonding, Woodhead Publishing; 2010, p. 350–88. doi:10.1533/9781845698058.3.350.

[48] Callister WDJr. Materials Science and Engineering: An Introduction. 7th ed. Wiley Publishers; 2006.

[49] Degarmo PE, Black JT, Kohser RA. Materials and Processes in Manufacturing. Wiley; 2003.

[50] Chaves FJP, Silva LFM da, Moura MFSF de, Dillard DA, Esteves VHC. Fracture Mechanics Tests in Adhesively Bonded Joints: A Literature Review. The Journal of Adhesion 2014;90:955–92. doi:10.1080/00218464.2013.859075.

[51] Carta F, Pirondi A. Damage tolerance analysis of aircraft reinforced panels. Frattura Ed Integrità Strutturale 2011;16:34–42.

[52] Sanford RJ. Principles of Fracture Mechanics. 1st edition. Upper Saddle River, NJ: Pearson; 2002.

[53] Dieter GE. Mechanical Metallurgy. 3rd edition. McGraw-Hill; 1986.

[54] Liu M, Gan Y, Hanaor DAH, Liu B, Chen C. An improved semi-analytical solution for stress at round-tip notches. Engineering Fracture Mechanics 2015;149:134–43. doi:10.1016/j.engfracmech.2015.10.004.

[55] Rice JR. A Path Independent Integral and the Approximate Analysis of Strain Concentration by Notches and Cracks. J Appl Mech 1968;35:379–86. doi:10.1115/1.3601206.

[56] Zehnder AT. Griffith Theory of Fracture. Encyclopedia of Tribology, Springer, Boston, MA; 2013, p. 1570–3. doi:10.1007/978-0-387-92897-5_259.

[57] Application of the end loaded split and single-leg bending tests to the mixed-mode fracture characterization of wood : Holzforschung. <https://www.degruyter.com/view/j/hfsg.2009.63.issue-5/hf.2009.088/hf.2009.088.xml?format=INT>. Acessed: March, 2018.

[58] Jiang Z, Wan S, Wu Z. Calculation of energy release rate for adhesive composite/metal joints under mode-I loading considering effect of the non-

uniformity. Composites Part B: Engineering 2016;95:374–85. doi:10.1016/j.compositesb.2016.04.001.

[59] Moroni F, Alfano M, Romoli L. Fatigue analysis of adhesive joints with laser treated substrates. Procedia Structural Integrity 2016;2:120–7. doi:10.1016/j.prostr.2016.06.016.

[60] Campos AAMA, de Jesus AMP, Correia JAFO, Morais JJL. Fatigue Crack Growth Behavior of Bonded Aluminum Joints. Procedia Engineering 2016;160:270–7. doi:10.1016/j.proeng.2016.08.890.

[61] Reeder JR, Rews JH. Mixed-mode bending method for delamination testing. AIAA Journal, Aerospace Research Central 1990;28:1270–6. doi:10.2514/3.25204.

[62] Kinloch AJ. Adhesion and Adhesives: Science and Technology. 1987 edition. London ; New York: Chapman & Hall; 1987.

[63] Broek D. Elementary engineering fracture mechanics. Springer Netherlands; 1982.

[64] Davidson BD, Schapery RA. A technique for predicting mode I energy release rates using a first-order shear deformable plate theory. Engineering Fracture Mechanics 1990;36:157–65. doi:10.1016/0013-7944(90)90105-P.

[65] Suo Z, Hutchinson JW. Interface crack between two elastic layers. Int J Fract 1990;43:1–18. doi:10.1007/BF00018123.

[66] Williams JG. On the calculation of energy release rates for cracked laminates. Int J Fract 1988;36:101–19. doi:10.1007/BF00017790.

[67] Timoshenko SP. History of Strength of Materials. McGraw-Hill Inc.,US; 1953.

[68] Park S, Dillard DA. Development of a simple mixed-mode fracture test and the resulting fracture energy envelope for an adhesive bond. Int J Fract 2007;148:261–71. doi:10.1007/s10704-008-9200-z.

[69] Tong L, Luo Q. Analysis of Cracked Lap Shear (CLS) Joints. Modeling of Adhesively Bonded Joints, Springer, Berlin, Heidelberg; 2008, p. 25–51. doi:10.1007/978-3-540-79056-3_2.

[70] John H. Crews J, James R. R. A Mixed-Mode Bending Apparatus for Delamination Testing. NASA Langley Technical Report Server; 1998.

[71] Hong CS, Yoon SH. Modified End Notched Flexure Specimen for Mixed Mode Interlaminar Fracture in Laminated Composites. INTERNATIONAL JOURNAL OF FRACTURE 1990;43:R3–9.

[72] Ozdil F, Carlsson LA, Davies P. Beam analysis of angle-ply laminate end-notched flexure specimens. Composites Science and Technology 1998;58:1929–38. doi:10.1016/S0266-3538(98)00018-9.

[73] Szekrényes A, Uj J. Beam and finite element analysis of quasi-unidirectional composite SLB and ELS specimens. Composites Science and Technology 2004;64:2393–406. doi:10.1016/j.compscitech.2004.05.002.

[74] Lopes RM, Campilho RDSG, da Silva FJG, Faneco TMS. Comparative evaluation of the Double-Cantilever Beam and Tapered Double-Cantilever Beam tests for estimation of the tensile fracture toughness of adhesive joints. International Journal of Adhesion and Adhesives 2016;67:103–11. doi:10.1016/j.ijadhadh.2015.12.032.

[75] de Moura MFSF, Cavaleiro PMLC, Silva FGA, Dourado N. Mixed-mode I+II fracture characterization of a hybrid carbon-epoxy/cork laminate using the Single-Leg Bending test. Composites Science and Technology 2017;141:24–31. doi:10.1016/j.compscitech.2017.01.001.

[76] Fernández MV, de Moura MFSF, da Silva LFM, Marques AT. Mixed-mode I+II fatigue/fracture characterization of composite bonded joints using the Single-Leg Bending test. Composites Part A: Applied Science and Manufacturing 2013;44:63–9. doi:10.1016/j.compositesa.2012.08.009.

[77] Razavi SMJ, Ayatollahi MR, Esmaeili E, da Silva LFM. Mixed-mode fracture response of metallic fiber-reinforced epoxy adhesive. European Journal of Mechanics - A/Solids 2017;65:349–59. doi:10.1016/j.euromechsol.2017.06.001.

[78] de Moura MFSF, Campilho RDSG, Goncalves JPM. Mixed-Mode Cohesive Damage Model Applied to the Simulation of the Mechanical Behaviour of Laminated Composite Adhesive Joints. J Adhes Sci Technol 2009;23:1477–91. doi:10.1163/156856109X433036.

[79] Allix O, Corigliano A. Modeling and simulation of crack propagation in mixed-modes interlaminar fracture specimens. Int J Fract 1996;77:111–40. doi:10.1007/BF00037233.

[80] de Moura MFSF, Gonçalves JPM. Cohesive zone model for high-cycle fatigue of composite bonded joints under mixed-mode I+II loading. Engineering Fracture Mechanics 2015;140:31–42. doi:10.1016/j.engfracmech.2015.03.044.

[81] Chen J. Predicting Progressive Delamination of Stiffened Fibre-Composite Panel and Repaired Sandwich Panel by Decohesion Models. Journal of Thermoplastic Composite Materials 2002;15:429–42. doi:10.1177/0892705702015005736.

[82] Chandra N, Li H, Shet C, Ghonem H. Some issues in the application of cohesive zone models for metal–ceramic interfaces. International Journal of Solids and Structures 2002;39:2827–55. doi:10.1016/S0020-7683(02)00149-X.

[83] Schellekens JCJ, de Borst R. A non-linear finite element approach for the analysis of mode-I free edge delamination in composites. International Journal of Solids and Structures 1993;30:1239–53. doi:10.1016/0020-7683(93)90014-X.

[84] de Moura MFSF, Gonçalves JPM, Magalhães AG. A straightforward method to obtain the cohesive laws of bonded joints under mode I loading. International Journal of Adhesion and Adhesives 2012;39:54–9. doi:10.1016/j.ijadhadh.2012.07.008.

[85] Sørensen BF. Cohesive law and notch sensitivity of adhesive joints. Acta Materialia 2002;50:1053–61. doi:10.1016/S1359-6454(01)00404-9.

[86] Yang QD, Thouless MD, Ward SM. Numerical simulations of adhesively-bonded beams failing with extensive plastic deformation. Journal of the Mechanics and Physics of Solids 1999;47:1337–53. doi:10.1016/S0022-5096(98)00101-X.

[87] Xu X-P, Needleman A. Numerical simulations of fast crack growth in brittle solids. Journal of the Mechanics and Physics of Solids 1994;42:1397–434. doi:10.1016/0022-5096(94)90003-5.

[88] de Moura MFSF, Gonçalves JPM, Marques AT, de Castro PMST. Prediction of compressive strength of carbon–epoxy laminates containing delamination by using a mixed-mode damage model. Composite Structures 2000;50:151–7. doi:10.1016/S0263-8223(00)00091-X.

[89] Turon A, Costa J, Camanho PP, Dávila CG. Simulation of delamination in composites under high-cycle fatigue. Composites Part A: Applied Science and Manufacturing 2007;38:2270–82. doi:10.1016/j.compositesa.2006.11.009.

[90] Schellekens JCJ. Computational strategies for composite structures. PhD thesis. TU Delft, 1992.< http://resolver.tudelft.nl/uuid:ecc16ece-34b5-4df3-90aa-83f8e8bc31a7>. Access: June, 2018.

[91] Allix O, Ladevèze P. Interlaminar interface modelling for the prediction of delamination. Composite Structures 1992;22:235–42. doi:10.1016/0263-8223(92)90060-P.

[92] Flight Airworthiness Technology. Airbus Technical Magazine 2011;Volume 48.

[93] Engle R. Damage Accumulation Techniques in Damage Tolerance Analysis. In: Chang J, Rudd J, editors. Damage Tolerance of Metallic Structures: Analysis Methods and Applications, 100 Barr Harbor Drive, PO Box C700, West Conshohocken, PA 19428-2959: ASTM International; 1984, p. 25-25–11.

[94] Aktaş M, Atas C, İçten BM, Karakuzu R. An experimental investigation of the impact response of composite laminates. Composite Structures 2009;87:307–13. doi:10.1016/j.compstruct.2008.02.003.

[95] Machado JJM, Marques E a. S, da Silva LFM. Adhesives and adhesive joints under impact loadings: An overview. J Adhes 2018;94:421–52. doi:10.1080/00218464.2017.1282349.

[96] Boria S, Scattina A, Belingardi G. Impact behavior of a fully thermoplastic composite. Composite Structures 2017;167:63–75. doi:10.1016/j.compstruct.2017.01.083.

[97] Liu D. Impact-Induced Delamination—A View of Bending Stiffness Mismatching. Journal of Composite Materials 1988;22:674–92. doi:10.1177/002199838802200706.

[98] Liu D. Characterization of Impact Properties and Damage Process of Glass/Epoxy Composite Laminates. Journal of Composite Materials 2004;38:1425–42. doi:10.1177/0021998304042741.

[99] Liu Y, Liaw B. Effects of Constituents and Lay-up Configuration on Drop-Weight Tests of Fiber-Metal Laminates. Appl Compos Mater 2010;17:43–62. doi:10.1007/s10443-009-9119-1.

[100] Allazadeh MR, Itani MK, Wosu SN. Compression of the Material Characteristics of Steel, Aluminum, Wood and Woven Graphite Epoxy Composites in Response to High Strain Rate Load. Advances in Materials Science and Applications. < http://www.academicpub.org/amsa/paperInfo.aspx?PaperID=11933>. Access: June, 2018.

[101] Potter D. Durability and Damage Tolerance Behavior of Adhesively Bonded Primary Structure. In: Abelkis P, Hudson C, editors. Design of Fatigue and Fracture Resistant Structures, 100 Barr Harbor Drive, PO Box C700, West Conshohocken, PA 19428-2959: ASTM International; 1982, p. 373-373–35.

[102] Alderliesten RC, Homan JJ. Fatigue and damage tolerance issues of Glare in aircraft structures. International Journal of Fatigue 2006;28:1116–23. doi:10.1016/j.ijfatigue.2006.02.015.

[103] Johnson W, Masters J, Wilson D, Graesser D, Tuttle M. Damage Tolerance Predictions for Stiffened Composite Panels—Part II: Application of a Failure Criteria. Journal of Composites Technology and Research 1996;18:102. doi:10.1520/CTR10521J.

[104] Richardson MOW, Wisheart MJ. Review of low-velocity impact properties of composite materials. Composites Part A: Applied Science and Manufacturing 1996;27:1123–31. doi:10.1016/1359-835X(96)00074-7.

[105] Mikulik Z, Haase P. Composite Damage Metrics and Inspection. EASA; 2012.< https://www.easa.europa.eu/document-library/research-projects/easa20111>. Access: June, 2018.

[106] Nakatani H, Kosaka T, Osaka K, Sawada Y. Damage characterization of titanium/GFRP hybrid laminates subjected to low-velocity impact. Composites Part A: Applied Science and Manufacturing 2011;42:772–81. doi:10.1016/j.compositesa.2011.03.005.

[107] Bieniaś J, Jakubczak P, Surowska B, Dragan K. Low-energy impact behaviour and damage characterization of carbon fibre reinforced polymer and aluminium hybrid laminates. Archives of Civil and Mechanical Engineering 2015;15:925–32. doi:10.1016/j.acme.2014.09.007.

[108] Silva MRG, Marques E a. S, Silva LFM da, Silva MRG, Marques E a. S, Silva LFM da. Behaviour under Impact of Mixed Adhesive Joints for the Automotive Industry. Latin American Journal of Solids and Structures 2016;13:835–53. doi:10.1590/1679-78252762.

[109] Machado JJM, Gamarra PM-R, Marques EAS, da Silva LFM. Improvement in impact strength of composite joints for the automotive industry. Composites Part B: Engineering 2018;138:243–55. doi:10.1016/j.compositesb.2017.11.038.

[110] Jamasri, Ilman MN, Soekrisno R, Triyono. Corrosion Fatigue Behavior of Resistance Spot Welded Dissimilar Metal Welds between Carbon Steel and Austenitic Stainless Steel with Different Thickness. Procedia Engineering 2011;10:649–54. doi:10.1016/j.proeng.2011.04.108.

[111] Faivre V, Morteau E. Airbus Tech Mag (FAST). Damage Tolerant Composite Fuselage Sizing, Characterization of Accidental Damage Threat 2011;48:10–6.

[112] L. F. M. da Silva (editor). Hybrid Adhesive Joints. Springer, 2011.

[113] Bauer A, Grundmeier G, Steger H, Weitl J. Corrosive delamination processes of CFRP-aluminum alloy hybrid components. Mater Corros 2018;69:98–105. doi:10.1002/maco.201709637.

[114] Arhant M, Le Gac P-Y, Le Gall M, Burtin C, Briançon C, Davies P. Effect of sea water and humidity on the tensile and compressive properties of carbon-polyamide 6 laminates. Composites Part A: Applied Science and Manufacturing 2016;91:250–61. doi:10.1016/j.compositesa.2016.10.012.

[115] Zhang C, Zheng D-J, Song G-L. Galvanic Effect Between Galvanized Steel and Carbon Fiber Reinforced Polymers. Acta Metall Sin (Engl Lett) 2017;30:342–51. doi:10.1007/s40195-017-0539-x.

[116] Mandel M, Krüger L. Long-term Corrosion Studies of a CFRP/EN AW-6060-T6 Self-piercing rivet Joint and a Steel/EN AW-6060-T6 Blind Rivet Joint. Materials Today: Proceedings 2015;2:S131–40. doi:10.1016/j.matpr.2015.05.030.

[117] Bellucci F, Martino AD, Liberti C. Electrochemical behaviour of graphite-epoxy composite materials (GECM) in aqueous salt solutions. J Appl Electrochem 1986;16:15–22. doi:10.1007/BF01015979.

[118] American Society for Metals. Metals Handbook. Volume 2. Metals Park, Ohio: American Society for Metals; 1981.

[119] Davis JR. Aluminum and Aluminum Alloys. Materials Park, OH: ASM International; 1993.

[120] GHOSH KS, HILAL Md, BOSE S. Corrosion behavior of 2024 Al-Cu-Mg alloy of various tempers. Transactions of Nonferrous Metals Society of China 2013;23:3215–27. doi:10.1016/S1003-6326(13)62856-3.

[121] Francis R. Galvanic corrosion: a practical guide for engineers. 2nd edition. NACE International; 2017.

[122] American Society for Testing and Materials. Standard guide for development and use of a galvanic series for predicting galvanic corrosion performance. West Conshohocken, PA: ASTM; 1998.

[123] Roberge PR. Corrosion Engineering: Principles and Practice. New York: Mechanical Engineering; 2008.

[124] Hakansson E. Galvanic corrosion of aluminum/carbon composites systems. PhD thesis. University of Denver, 2016. < https://digitalcommons.du.edu/cgi/viewcontent.cgi?referer=&httpsredir=1&article=2120&context=etd>. Access: June, 2018

[125] Pan Y, Wu G, Cheng X, Zhang Z, Li M, Ji S, et al. Galvanic corrosion behaviour of carbon fibre reinforced polymer/magnesium alloys coupling. Corrosion Science 2015;98:672–7. doi:10.1016/j.corsci.2015.06.024.

[126] Miller J, Bennie A. The Galvanic Corrosion of Graphite Epoxy Composite Materials Coupled with Alloys. Air Force Institute of Technology Wright-Patterson, 1975.< https://apps.dtic.mil/dtic/tr/fulltext/u2/a019322.pdf>. Access: June, 2018.

[127] Fiore V, Calabrese L, Proverbio E, Passari R, Valenza A. Salt spray fog ageing of hybrid composite/metal rivet joints for automotive applications. Composites Part B: Engineering 2017;108:65–74. doi:10.1016/j.compositesb.2016.09.096.

[128] Charai A, Walther T, Alfonso C, Zahra A-M, Zahra CY. Coexistence of clusters, GPB zones, S″-, S′- and S-phases in an Al–0.9% Cu–1.4% Mg alloy. Acta Materialia 2000;48:2751–64. doi:10.1016/S1359-6454(99)00422-X.

[129] Jena AK, Gupta AK, Chaturvedi MC. A differential scanning calorimetric investigation of precipitation kinetics in the Al-1.53 wt% Cu-0.79 wt% Mg alloy. Acta Metallurgica 1989;37:885–95. doi:10.1016/0001-6160(89)90015-1.

[130] Wang SB, Liu ZR, Xia SL, Key J, Chen JH. Tetragonal-prism-like Guinier Preston Bagaryatsky zones in an AlCuMg alloy. Mater Charact 2017;132:139–44. doi:10.1016/j.matchar.2017.08.014.

[131] Zuiko I, Kaibyshev R. Aging behavior of an Al-Cu-Mg alloy. J Alloy Compd 2018;759:108–19. doi:10.1016/j.jallcom.2018.05.053.

[132] Genevois C, Deschamps A, Denquin A, Doisneau-cottignies B. Quantitative investigation of precipitation and mechanical behaviour for AA2024 friction stir welds. Acta Materialia 2005;53:2447–58. doi:10.1016/j.actamat.2005.02.007.

[133] Bousquet E, Poulon-Quintin A, Puiggali M, Devos O, Touzet M. Relationship between microstructure, microhardness and corrosion sensitivity of an AA 2024-T3 friction stir welded joint. Corrosion Science 2011;53:3026–34. doi:10.1016/j.corsci.2011.05.049.

[134] Yasakau KA, Zheludkevich ML, Lamaka SV, Ferreira MGS. Mechanism of Corrosion Inhibition of AA2024 by Rare-Earth Compounds. J Phys Chem B 2006;110:5515–28. doi:10.1021/jp0560664.

[135] Tencate Advanced Composites. CETEX® PPS Technical Datasheet and Guidelines, Tencate Advanced Composites 2009.

[136] Lage LG, Kawano Y. Polímeros: Ciência e Tecnologia. Estudo Sobre a Cinética de Decomposição Térmica Do Poli(Sulfeto de Fenileno) 1999;9:82–5.

[137] Ma C-CM, Hsia H-C, Liu W-L, Hu J-T. Polymer Composites. Thermal and Rheological Properties of Poly(Phenylene Sulfide) and Poly(Ether Etherketone) Resins and Composites 1987;8:256–64.

[138] Tanthapanichakoon W, Hata M, Nitta K, Furuuchi M, Otani Y. Mechanical degradation of filter polymer materials: Polyphenylene sulfide. Polymer Degradation and Stability 2006;91:2614–21. doi:10.1016/j.polymdegradstab.2006.05.005.

[139] Nohara LB, Nohara EL, Moura A, Gonçalves JMRP, Costa ML, Rezende MC. Study of crystallization behavior of poly(phenylene sulfide). Polímeros 2006;16:104–10. doi:10.1590/S0104-14282006000200009.

[140] Jachowicz J, Kryszewski M, Sobol A. Thermal degradation of poly(2-methylphenylene oxide), poly(2,5-dimethylphenylene oxide) and poly(1,4-phenylene oxide). Polymer 1979;20:995–1002. doi:10.1016/0032-3861(79)90198-8.

[141] Budgell DR, Day M, Cooney JD. Thermal degradation of poly(phenylene sulfide) as monitored by pyrolysis—GC/MS. Polymer Degradation and Stability 1994;43:109–15. doi:10.1016/0141-3910(94)90232-1.

[142] Vieille B, Aucher J, Taleb L. Carbon fiber fabric reinforced PPS laminates: Influence of temperature on mechanical properties and behavior. Advances in Polymer Technology 2011;30:80–95. doi:10.1002/adv.20239.

[143] Deng S. Tensile deformation of semi-crystalline polymers by molecular dynamics simulation. Iran Polym J 2017;26:903–11. doi:10.1007/s13726-017-0577-2.

[144] Aluminium AA2024-T3 technical datasheet. Constellium France; 2012.

[145] André NM, Goushegir SM, Scharnagl N, Santos JF dos, Canto LB, Amancio-Filho ST. Composite surface pre-treatments: Improvement on adhesion mechanisms and mechanical performance of metal–composite friction spot joints with additional film interlayer. The Journal of Adhesion 2017;0:1–20. doi:10.1080/00218464.2017.1378101.

[146] Hammersley AP, Svensson SO, Hanfland M, Fitch AN, Hausermann D. Two-dimensional detector software: From real detector to idealised image or two-theta scan. High Pressure Research 1996;14:235–48. doi:10.1080/08957959608201408.

[147] Pedersen JS. Determination of size distribution from small-angle scattering data for systems with effective hard-sphere interactions. J Appl Cryst, J Appl Crystallogr 1994;27:595–608. doi:10.1107/S0021889893013810.

[148] Chen Q, Guo H, Avery K, Kang H, Su X. Mixed-mode fatigue crack growth and life prediction of an automotive adhesive bonding system. Engineering Fracture Mechanics 2018;189:439–50. doi:10.1016/j.engfracmech.2017.11.004.

[149] Airbus. Composites Airbus: Damage Tolerance Methodology, Chicago, USA: 2006.<https://www.niar.wichita.edu/chicagoworkshop/Chicago%20Damage%20Tolerance%20Workshop%20%20July%201921,%202006/Wednesday%20%20Session%201%20Presentations/Airbus%20Composites%20%20Damage%20Tolerance%20Methodolgy%20-%20Fualdes.pdf>. Access: June 2018.

[150] Abaqus v. 6.14-1 Documentation, under license for Helmholtz-Zentrum Geesthacht (formerly GKSS Forschungszentrum Geesthacht GmbH), Germany, 2010–2011.

[151] Cui W, Wisnom MR. A combined stress-based and fracture-mechanics-based model for predicting delamination in composites. Composites 1993;24:467–74. doi:10.1016/0010-4361(93)90016-2.

[152] Needleman A. A Continuum Model for Void Nucleation by Inclusion Debonding. J Appl Mech 1987;54:525–31. doi:10.1115/1.3173064.

[153] Xu X-P, Needleman A. Numerical simulations of fast crack growth in brittle solids. Journal of the Mechanics and Physics of Solids 1994;42:1397–434. doi:10.1016/0022-5096(94)90003-5.

[154] J. Chen YQ M Crisfield, AJ Kinloch, EP Busso, FL Matthews. Predicting Progressive Delamination of Composite Material Specimens via Interface Elements. Mechanics of Composite Materials and Structures 1999;6:301–17. doi:10.1080/107594199305476.

[155] Mi Y, Crisfield MA, Davies GAO, Hellweg HB. Progressive Delamination Using Interface Elements, Progressive Delamination Using Interface Elements. Journal of Composite Materials 1998;32:1246–72. doi:10.1177/002199839803201401.

[156] Turon A, Costa J, Camanho PP, Dávila CG. Simulation of delamination in composites under high-cycle fatigue. Composites Part A: Applied Science and Manufacturing 2007;38:2270–82. doi:10.1016/j.compositesa.2006.11.009.

[157] Tvergaard V, Hutchinson JW. The relation between crack growth resistance and fracture process parameters in elastic-plastic solids. Journal of the Mechanics and Physics of Solids 1992;40:1377–97. doi:10.1016/0022-5096(92)90020-3.

[158] Barenblatt GI. The Mathematical Theory of Equilibrium Cracks in Brittle Fracture. In: Dryden HL, von Kármán Th, Kuerti G, van den Dungen FH, Howarth L, editors. Advances in Applied Mechanics, vol. 7, Elsevier; 1962, p. 55–129. doi:10.1016/S0065-2156(08)70121-2.

[159] McCarthy CT, Gray PJ. An analytical model for the prediction of load distribution in highly torqued multi-bolt composite joints. Composite Structures 2011;93:287–98. doi:10.1016/j.compstruct.2010.09.017.

[160] Ireman T. Three-dimensional stress analysis of bolted single-lap composite joints. Composite Structures 1998;43:195–216. doi:10.1016/S0263-8223(98)00103-2.

[161] McCarthy MA, McCarthy CT, Padhi GS. A simple method for determining the effects of bolt–hole clearance on load distribution in single-column multi-bolt composite joints. Composite Structures 2006;73:78–87. doi:10.1016/j.compstruct.2005.01.028.

[162] Egan B, McCarthy CT, McCarthy MA, Frizzell RM. Stress analysis of single-bolt, single-lap, countersunk composite joints with variable bolt-hole clearance. Composite Structures 2012;94:1038–51. doi:10.1016/j.compstruct.2011.10.004.

[163] Ekh J, Schön J. Effect of secondary bending on strength prediction of composite, single shear lap joints. Composites Science and Technology 2005;65:953–65. doi:10.1016/j.compscitech.2004.10.020.

[164] Yeh H-Y, Tandjung D. Mixed Mode Fracture Analysis of the Lap Shear Specimen Test Per ASTM D1002. Journal of Reinforced Plastics and Composites 2005;24:839–53. doi:10.1177/0731684405047771.

[165] Lee HK, Pyo SH, Kim BR. On joint strengths, peel stresses and failure modes in adhesively bonded double-strap and supported single-lap GFRP joints. Composite Structures 2009;87:44–54. doi:10.1016/j.compstruct.2007.12.005.

[166] da Silva LFM, das Neves PJC, Adams RD, Wang A, Spelt JK. Analytical models of adhesively bonded joints—Part II: Comparative study. International Journal of Adhesion and Adhesives 2009;29:331–41. doi:10.1016/j.ijadhadh.2008.06.007.

[167] da Silva LFM, das Neves PJC, Adams RD, Spelt JK. Analytical models of adhesively bonded joints—Part I: Literature survey. International Journal of Adhesion and Adhesives 2009;29:319–30. doi:10.1016/j.ijadhadh.2008.06.005.

[168] Hiss R, Hobeika S, Lynn C, Strobl G. Network Stretching, Slip Processes, and Fragmentation of Crystallites during Uniaxial Drawing of Polyethylene and Related Copolymers. A Comparative Study. Macromolecules 1999;32:4390–403. doi:10.1021/ma981776b.

[169] Liu AF. Mechanics and Mechanisms of Fracture: An Introduction. ASM International; 2005.

[170] Haward RN. Strain hardening of thermoplastics. Macromolecules 1993;26:5860–9. doi:10.1021/ma00074a006.

[171] Maes D, Groeninckx G, Ravenstijn J, Aerts L. A molecular model for structural changes during shear yielding and crazing in amorphous polymers. Polymer Bulletin 1986;16:363–70. doi:10.1007/BF00255010.

[172] Canevarolo SV. Ciência dos Polímeros. 2° edição. São Paulo: Artliber; 2006.

[173] Grandt A. Introduction to Damage Tolerance Analysis Methodology. In: Chang J, Rudd J, editors. Damage Tolerance of Metallic Structures: Analysis Methods and Applications, 100 Barr Harbor Drive, PO Box C700, West Conshohocken, PA 19428-2959: ASTM International; 1984, p. 3-3–22.

[174] Wang CH, Duong CN. Chapter 6 - Damage tolerance and fatigue durability of scarf joints. Bonded Joints and Repairs to Composite Airframe Structures, Oxford: Academic Press; 2016, p. 141–72.

[175] Olmedo A, Santiuste C, Barbero E. An analytical model for the secondary bending prediction in single-lap composite bolted-joints. Composite Structures 2014;111:354–61. doi:10.1016/j.compstruct.2014.01.015.

[176] Zhao L, Xin A, Liu F, Zhang J, Hu N. Secondary bending effects in progressively damaged single-lap, single-bolt composite joints. Results in Physics 2016;6:704–11. doi:10.1016/j.rinp.2016.08.021.

[177] Xu XX, Crocombe AD, Smith PA. Mixed-mode fatigue and fracture behaviour of joints bonded with either filled or filled and toughened adhesive. International Journal of Fatigue 1995;17:279–86. doi:10.1016/0142-1123(95)93540-I.

[178] de Moura MFSF, Gonçalves JPM, Fernandez MV. Fatigue/fracture characterization of composite bonded joints under mode I, mode II and mixed-mode I+II. Composite Structures 2016;139:62–7. doi:10.1016/j.compstruct.2015.11.073.

[179] Chen Q, Guo H, Avery K, Kang H, Su X. Mixed-mode fatigue crack growth and life prediction of an automotive adhesive bonding system. Engineering Fracture Mechanics 2018;189:439–50. doi:10.1016/j.engfracmech.2017.11.004.

[180] Santos MAS, Campilho RDSG. Mixed-mode fracture analysis of composite bonded joints considering adhesives of different ductility. Int J Fract 2017;207:55–71. doi:10.1007/s10704-017-0219-x.

[181] Shimamoto K, Sekiguchi Y, Sato C. Mixed mode fracture toughness of adhesively bonded joints with residual stress. International Journal of Solids and Structures n.d. doi:10.1016/j.ijsolstr.2016.10.011.

[182] Santos MAS, Campilho RDSG. Numerical Evaluation of the Mixed-Mode Fracture of Composite Bonded Joints. Porto: Inegi-Inst Engenharia Mecanica E Gestao Industrial; 2016.

[183] Gdoutos EE, Pilakoutas K, Rodopoulos CA. Failure Analysis of Industrial Composite Materials. McGraw Hill Professional; 2000.

[184] Waas AM, Sankar BV, Hyer MW. Failure in Composites. DEStech Publications, Inc; 2013.

[185] Moore DR, Williams JG, Pavan A. Fracture Mechanics Testing Methods for Polymers, Adhesives and Composites. Elsevier; 2001.

[186] Heide-Jørgensen S, Teixeira de Freitas S, Budzik MK. On the fracture behaviour of CFRP bonded joints under mode I loading: Effect of supporting carrier and interface contamination. Composites Science and Technology 2018;160:97–110. doi:10.1016/j.compscitech.2018.03.024.

[187] Bieniaś J, Dadej K, Surowska B. Interlaminar fracture toughness of glass and carbon reinforced multidirectional fiber metal laminates. Engineering Fracture Mechanics 2017;175:127–45. doi:10.1016/j.engfracmech.2017.02.007.

[188] Ranade SR, Guan Y, Moore RB, Dillard JG, Batra RC, Dillard DA. Characterizing fracture performance and the interaction of propagating cracks with locally weakened

interfaces in adhesive joints. International Journal of Adhesion and Adhesives 2018;82:196–205. doi:10.1016/j.ijadhadh.2017.12.006.

[189] Developments in fracture mechanics test methods standardization: a symposium presented at St. Louis, Mo., 4 May, 1976. American Society for Testing and Materials; 1977.

[190] Shiri S, Yazdani M, Pourgol-Mohammad M. A fatigue damage accumulation model based on stiffness degradation of composite materials. Materials & Design 2015;88:1290–5. doi:10.1016/j.matdes.2015.09.114.

[191] Ziemian CW, Ziemian RD, Haile KV. Characterization of stiffness degradation caused by fatigue damage of additive manufactured parts. Materials & Design 2016;109:209–18. doi:10.1016/j.matdes.2016.07.080.

[192] Cheuk PT, Tong L, Wang CH, Baker A, Chalkley P. Fatigue crack growth in adhesively bonded composite-metal double-lap joints. Composite Structures 2002;57:109–15. doi:10.1016/S0263-8223(02)00074-0.

[193] Patel VK, Bhole SD, Chen DL. Fatigue life estimation of ultrasonic spot welded Mg alloy joints. Materials & Design 2014;62:124–32. doi:10.1016/j.matdes.2014.05.008.

[194] Zhang Y, Vassilopoulos AP, Keller T. Stiffness degradation and fatigue life prediction of adhesively-bonded joints for fiber-reinforced polymer composites. International Journal of Fatigue 2008;30:1813–20. doi:10.1016/j.ijfatigue.2008.02.007.

[195] Pugno N, Ciavarella M, Cornetti P, Carpinteri A. A generalized Paris' law for fatigue crack growth. Journal of the Mechanics and Physics of Solids 2006;54:1333–49. doi:10.1016/j.jmps.2006.01.007.

[196] Syed AK, Zhang X, Fitzpatrick ME. A comparison of fatigue crack growth performance of two aerospace grade aluminium alloys reinforced with bonded crack retarders. Fatigue Fract Eng Mater Struct 2018;41:1237–42. doi:10.1111/ffe.12744.

[197] Glud JA, Carraro PA, Quaresimin M, Dulieu-Barton JM, Thomsen OT, Overgaard LCT. A damage-based model for mixed-mode crack propagation in composite laminates. Compos Pt A-Appl Sci Manuf 2018;107:421–31. doi:10.1016/j.compositesa.2018.01.016.

[198] Takamatsu T, Shimokawa T, Matsumura T, Miyoshi Y, Tanabe Y. Evaluation of fatigue crack growth behavior of GLARE3 fiber/metal laminates using a compliance method. Eng Fract Mech 2003;70:2603–16. doi:10.1016/S0013-7944(03)00063-8.

[199] Chang P-Y, Yeh P-C, Yang J-M. Fatigue crack growth in hybrid boron/glass/aluminium fibre metal laminates. Fatigue Fract Eng Mater Struct 2008;31:989–1003. doi:10.1111/j.1460-2695.2008.01288.x.

[200] Avanzini A, Petrogalli C, Battini D, Donzella G. Influence of micro-notches on the fatigue strength and crack propagation of unfilled and short carbon fiber reinforced PEEK. Mater Des 2018;139:447–56. doi:10.1016/j.matdes.2017.11.039.

[201] Costa M, Viana G, Silva LFM da, Campilho RDSG, Costa M, Viana G, et al. Effect of Humidity on The Fatigue Behaviour of Adhesively Bonded Aluminium Joints. Latin American Journal of Solids and Structures 2017;14:174–87. doi:10.1590/1679-78252976.

[202] Montgomery DC, Runger GC. Applied Statistics and Probability for Engineers. 4th edition. Hoboken, NJ: Wiley; 2006.

[203] Roesler J, Harders H, Baeker M. Mechanical Behavior of Engineering Materials: Metals, Ceramics, Polymers, and Composites. 1st ed. Germany: Springer; 2007.

[204] Harris JA, Adams RD. An Assessment of the Impact Performance of Bonded Joints for Use in High Energy Absorbing Structures, An Assessment of the Impact Performance of Bonded Joints for Use in High Energy Absorbing Structures. Proceedings of the Institution of Mechanical Engineers, Part C: Journal of Mechanical Engineering Science 1985;199:121–31. doi:10.1243/PIME_PROC_1985_199_102_02.

[205] André NM. Friction Spot Joining of aluminum alloy 2024-T3 and carbon-fiber-reinforced polyphenylene sulfide composite laminate with additional PPS film interlayer. Master thesis. Federal University of São Carlos, 2015.

[206] André NM, Goushegir SM, Dos Santos JF, Canto LB, Amancio-Filho S de T. Influência termomecânica do processo de União Pontual por Fricção na recristalizaçãodos componentes poliméricos de junta híbrida CF-PPS/Alumínio com filme intermediário de PPS. National conference of Polymers (CBPol), Natal - RN, Brazil: 2015.

[207] Ozdemir O, Oztoprak N. An investigation into the effects of fabric reinforcements in the bonding surface on failure response and transverse impact behavior of

adhesively bonded dissimilar joints. Composites Part B: Engineering 2017;126:72–80. doi:10.1016/j.compositesb.2017.06.005.

[208] Choudhry RS, Hassan SF, Li S, Day R. Damage in single lap joints of woven fabric reinforced polymeric composites subjected to transverse impact loading. International Journal of Impact Engineering 2015;80:76–93. doi:10.1016/j.ijimpeng.2015.02.003.

[209] Chen Y, Ding H, LI J, ZhaoJ, Fu M, Li X. Effect of welding heat input and post-welded heat treatment on hardness of stir zone for friction stir-welded 2024-T3 aluminum alloy. Transactions of Nonferrous Metals Society of China 2015;25:2524–32. doi:10.1016/S1003-6326(15)63871-7.

[210] Glenn AM, Muster TH, Luo C, Zhou X, Thompson GE, Boag A, et al. Corrosion of AA2024-T3 Part III: Propagation. Corrosion Science 2011;53:40–50. doi:10.1016/j.corsci.2010.09.035.

[211] Zhang X, Zhou X, Hashimoto T, Liu B. Localized corrosion in AA2024-T351 aluminium alloy: Transition from intergranular corrosion to crystallographic pitting. Materials Characterization 2017;130:230–6. doi:10.1016/j.matchar.2017.06.022.

[212] Zhou X, Luo C, Hashimoto T, Hughes AE, Thompson GE. Study of localized corrosion in AA2024 aluminium alloy using electron tomography. Corrosion Science 2012;58:299–306. doi:10.1016/j.corsci.2012.02.001.

[213] Kang J, Fu R, Luan G, Dong C, He M. In-situ investigation on the pitting corrosion behavior of friction stir welded joint of AA2024-T3 aluminium alloy. Corrosion Science 2010;52:620–6. doi:10.1016/j.corsci.2009.10.027.

[214] Seetharaman R, Ravisankar V, Balasubramanian V. Corrosion performance of friction stir welded AA2024 aluminium alloy under salt fog conditions. Trans Nonferrous Met Soc China 2015;25:1427–38. doi:10.1016/S1003-6326(15)63742-6.

[215] Jariyaboon M, Davenport AJ, Ambat R, Connolly BJ, Williams SW, Price DA. The effect of welding parameters on the corrosion behaviour of friction stir welded AA2024–T351. Corrosion Science 2007;49:877–909. doi:10.1016/j.corsci.2006.05.038.

[216] Batista NL, Rezende MC, Botelho EC. Effect of crystallinity on CF/PPS performance under weather exposure: Moisture, salt fog and UV radiation. Polymer Degradation and Stability 2018;153:255–61. doi:10.1016/j.polymdegradstab.2018.03.008.

[217] Lopes de Oliveira MC, Sayeg IJ, Ett G, Antunes RA. Corrosion behavior of polyphenylene sulfide–carbon black–graphite composites for bipolar plates of polymer electrolyte membrane fuel cells. International Journal of Hydrogen Energy 2014;39:16405–18. doi:10.1016/j.ijhydene.2014.07.175.

[218] Gellert EP, Turley DM. Seawater immersion ageing of glass-fibre reinforced polymer laminates for marine applications. Composites Part A: Applied Science and Manufacturing 1999;30:1259–65. doi:10.1016/S1359-835X(99)00037-8.

[219] Hughes AE, Boag A, Glenn AM, McCulloch D, Muster TH, Ryan C, et al. Corrosion of AA2024-T3 Part II: Co-operative corrosion. Corrosion Science 2011;53:27–39. doi:10.1016/j.corsci.2010.09.030.

[220] Prabhakaran R, Razzaq Z, Devara S. Load and resistance factor design (LRFD) approach for bolted joints in pultruded composites. Composites Part B: Engineering 1996;27:351–60. doi:10.1016/1359-8368(95)00021-6.

[221] Gudmundsson S. Chapter 5 - Aircraft Structural Layout. In: Gudmundsson S, editor. General Aviation Aircraft Design, Boston: Butterworth-Heinemann; 2014, p. 97–131.

[222] Rouse M. Utilization of the Building-Block Approach in Structural Mechanics Research, NASA, Austin, TX, United States: 2005.< https://ntrs.nasa.gov/archive/nasa/casi.ntrs.nasa.gov/20050199405.pdf>. Access: June, 2018.

[223] Gudmundsson S. General Aviation Aircraft Design: Applied Methods and Procedures. 1st edition. S.l.: Butterworth-Heinemann; 2013.

[224] Arakaki FK, Gonçalves WG. Embraer Composite Material Application, Kyoto, Japan: 2007.< https://www.iccm-central.org/Proceedings/.../MoAM1-03sp_arakakif224623p.pdf>. Access: June, 2018.

[225] Goebel J, Reimann M, Norman A, dos Santos JF. Semi-stationary shoulder bobbin tool friction stir welding of AA2198-T851. Journal of Materials Processing Technology 2017;245:37–45. doi:10.1016/j.jmatprotec.2017.02.011.

[226] Barbini A, Carstensen J, dos Santos JF. Influence of a non-rotating shoulder on heat generation, microstructure and mechanical properties of dissimilar AA2024/AA7050 FSW joints. J Mater Sci Technol 2018;34:119–27. doi:10.1016/j.jmst.2017.10.017.

[227] Plaine AH, Suhuddin UFH, Alcantara NG, dos Santos JF. Microstructure and mechanical behavior of friction spot welded AA6181-T4/Ti6Al4V dissimilar joints. Int J Adv Manuf Technol 2017;92:3703–14. doi:10.1007/s00170-017-0439-2.

[228] Plaine AH, Gonzalez AR, Suhuddin UFH, dos Santos JF, Alcantara NG. Process parameter optimization in friction spot welding of AA5754 and Ti6Al4V dissimilar joints using response surface methodology. Int J Adv Manuf Technol 2016;85:1575–83. doi:10.1007/s00170-015-8055-5.

[229] Borba NZ, Blaga L, dos Santos JF, Amancio-Filho ST. Direct-Friction Riveting of polymer composite laminates for aircraft applications. Materials Letters 2018;215:31–4. doi:10.1016/j.matlet.2017.12.033.

[230] Composite Materials Handbook: Polymer matrix composites guidelines for characterization of structural materials. vol. 1. United States of America: 2002.

Appendix A: Joining process assessment and optimization

Statistical analysis of the optimization of joining parameters

Table A.1 Joining parameters used to produce the joints in the full-factorial (2^4) design of experiments.

Condition	Rotational speed [rpm]	Plunge depth [mm]	Joining time [s]	Joining force [kN]
E1	1900	0.5	4	4
E2	2900	0.5	4	4
E3	1900	0.5	8	4
E4	2900	0.5	8	4
E5	1900	0.5	4	6
E6	2900	0.5	4	6
E7	1900	0.5	8	6
E8	2900	0.5	8	6
E9	1900	0.8	4	4
E10	2900	0.8	4	4
E11	1900	0.8	8	4
E12	2900	0.8	8	4
E13	1900	0.8	4	6
E14	2900	0.8	4	6
E15	1900	0.8	8	6
E16	**2900**	**0.8**	**8**	**6**
Center point	2400	0.65	6	5

Table A.2 Ultimate lap shear force (ULSF) obtained for the joints produced with the full-factorial (2^4) design of experiments.

Condition	ULSF [N]	Standard Deviation [N]
E1	2554.67	188.64
E2	2644.00	173.74
E3	2621.00	161.82
E4	2848.67	71.93
E5	2069.67	213.56
E6	3339.67	184.26
E7	2576.67	196.88
E8	3431.25	225.82
E9	2699.00	209.27
E10	3060.00	126.19
E11	3032.00	57.15
E12	3324.67	299.03
E13	2788.00	192.97
E14	2822.00	249.85
E15	3074.67	250.65
E16	3619.00	132.06
Center point	3441.50	369.34

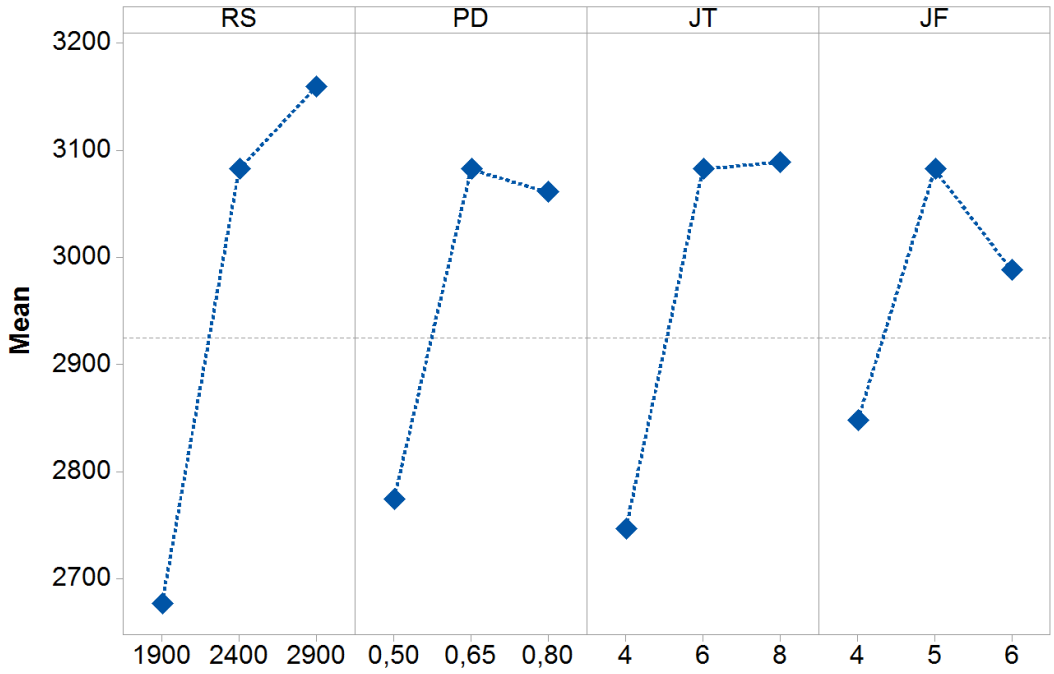

Figure A.1 Individual influence of the main joining parameters on the ULSF of the joints.

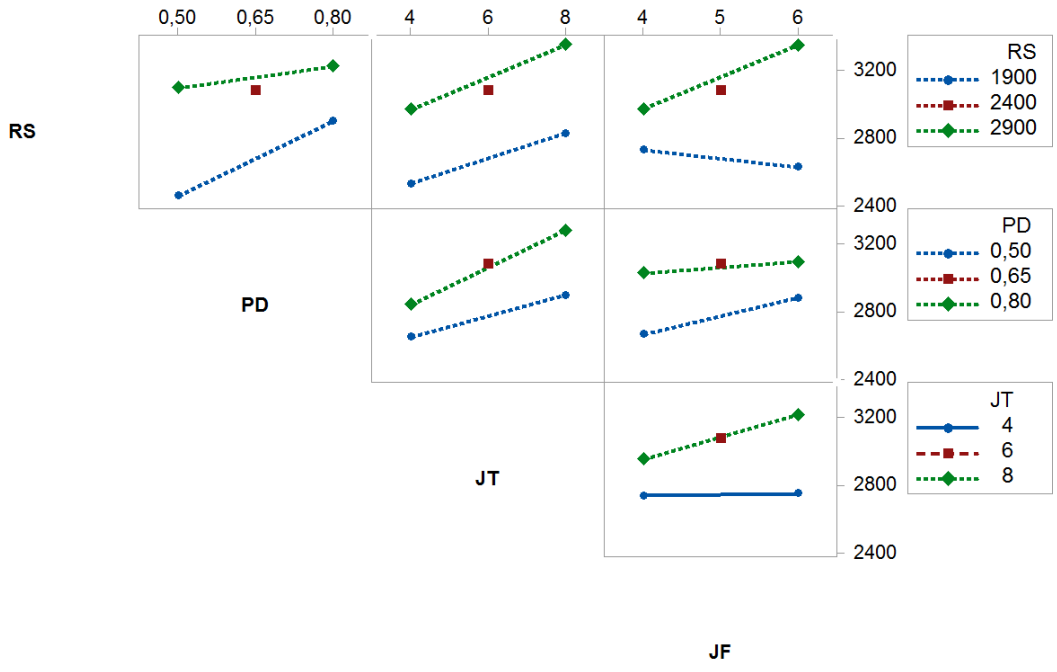

Figure A.2 Influence of the joining parameters interactions on the ULSF of the joints.

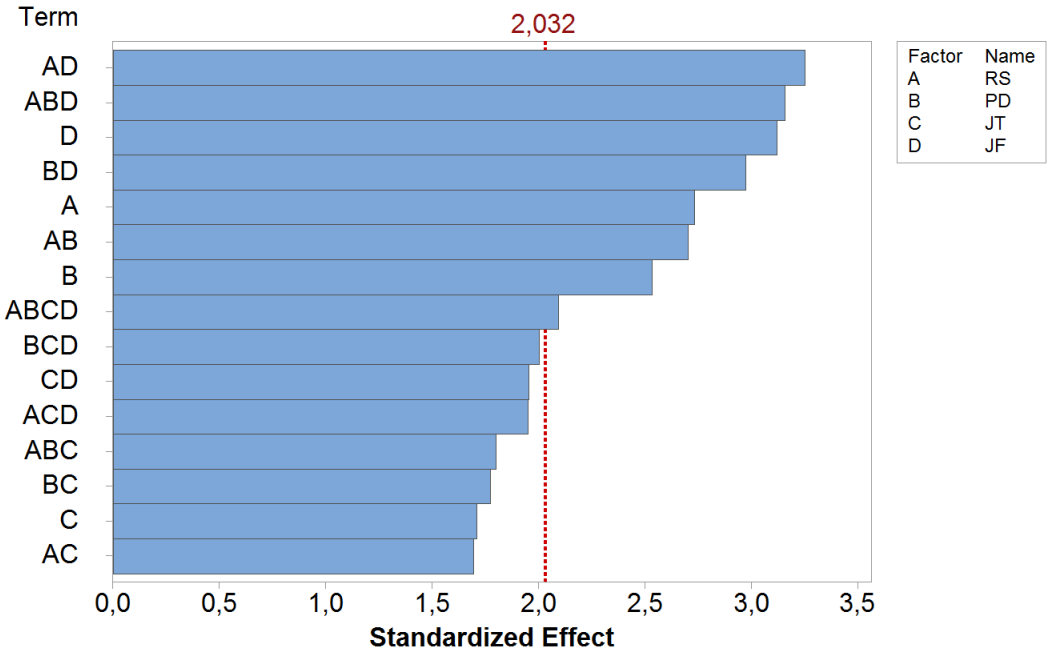

Figure A.3 Pareto chart showing the statistical significance of the influence of joining parameters and their interactions on the ULSF response (2^4) (95% of confidence level).

Table A.3 Analysis of variance (ANOVA) for ultimate lap shear force obtained for the full-factorial (2^4) design of experiments with a 95% confidence level ($\alpha = 0.05$).

Source	F	p-value
RS	7.46	0.010
PD	6.41	0.016
JT	2.92	0.096
JF	9.73	0.004
RS*PD	7.31	0.011
RS*JT	2.87	0.100
RS*JF	10.56	0.003
PD*JT	3.15	0.085
PD*JF	8.83	0.005
JT*JF	3.81	0.059
RS*PD*JT	3.23	0.081
RS*PD*JF	9.95	0.003
RS*JT*JF	3.80	0.060
PD*JT*JF	4.02	0.053
RS*PD*JT*JF	4.38	0.319

Table A.4 Estimated coefficients of the equation to predict the ULSF of the joints (95% of confidence level).

Term	Coefficient
Constant	32340
RS	-12.75
PD	-43414
JT	-3094
JF	-7000
RS*PD	18.91
RS*JT	1.249
RS*JF	2.98
PD*JT	4813
PD*JF	9994
JT*JF	693
RS*PD*JT	-1.99
RS*PD*JF	-4.33
RS*JT*JF	-0.282
PD*JT*JF	-1066
RS*PD*JT*JF	0.454

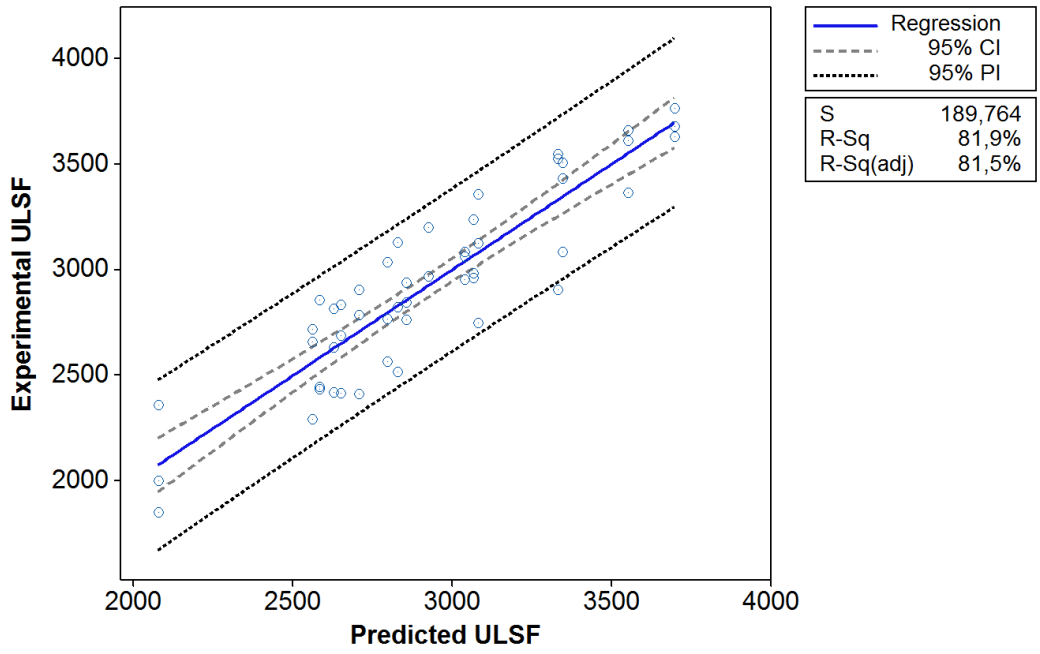

Figure A.4 Fitting plots of the ULSF of the joints predicted with the equation generated with the statistical model (Table A.4). CI: confidence interval. PI: predicted interval.

Influence of secondary parameters in the mechanical performance of the joints

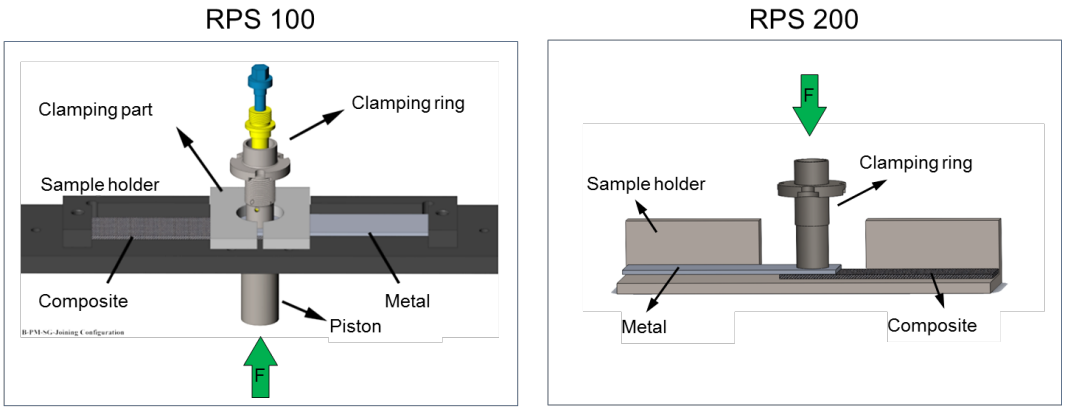

- Pressure applied by a piston
- The initial value of pressure is maintained during the whole process
- Force set by clamping ring position
- The position is maintained during the whole process

Figure A.5 Differences in the application of force during the FSpJ process between RPS100 and RPS 200.

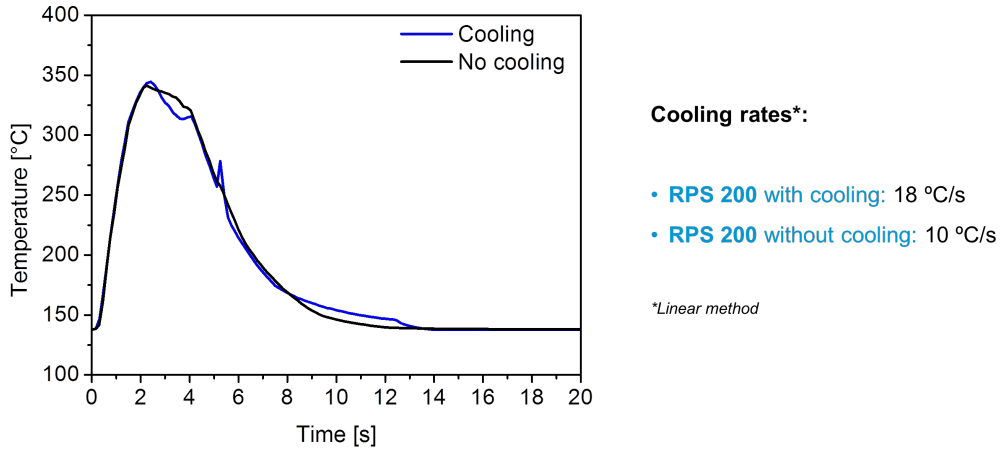

Figure A.6 Temperature evolution monitored with the infrared camera for the joints produced with and without manual cooling (compressed air at 10 bar for 10 seconds). Joining condition E16.

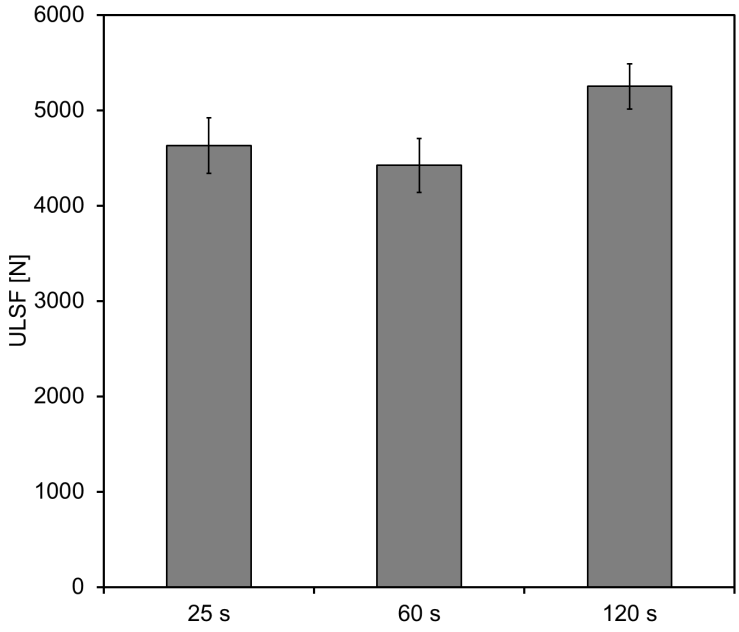

Figure A.7 Influence of the consolidation time in the mechanical performance of the joints. Joining condition E16.

As seen in Figure A.7, the mechanical performance of the joints increases about 5% when the consolidation time is incremented from 25s to 120s. It is believed that, when allowed longer times under the manual clamping system to reconsolidate, the pressure applied facilitates the entrapment of molten/soften polymer matrix into the irregularities of the aluminum surface. In this way, a more effective micro-mechanical interlocking is established at the aluminum-composite interface and an increase in the ULSF is observed.

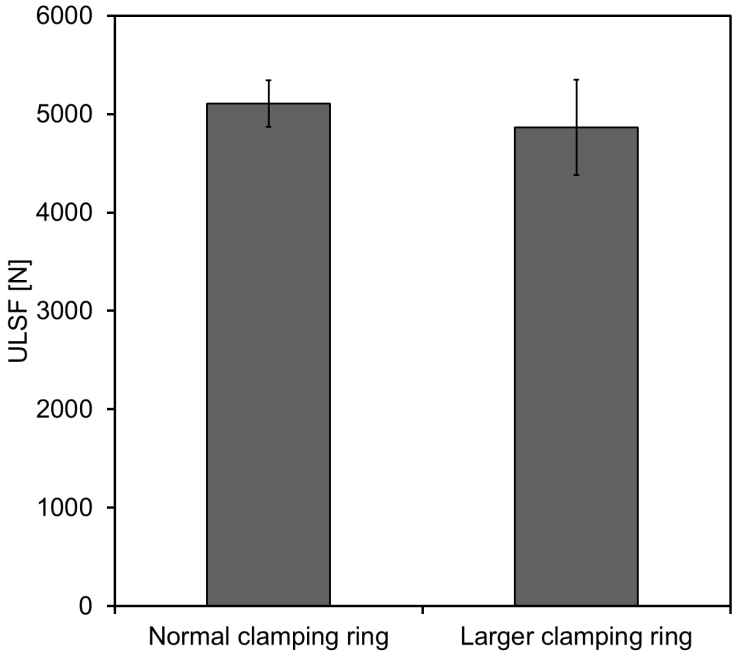

Figure A.8 Influence of the clamping ring in the mechanical performance of the joints (normal: 14 mm of diameter; larger: 17 mm of diameter). Joining condition E16.

Appendix B: Influence of the nub geometry on the mechanical performance of the joints

The cross-sections of the joints produced using different joining forces are presented in Figure B.1. Moreover, the fracture surface and the respective 3D images of the metallic nub (obtained from the fracture surface of the joints on the aluminum-side) are also presented in Figure B.2. In the images, different geometries of the metallic nub can be identified. In the joint produced with a lower level of joining force (4 kN), the deformation of the aluminum into the composite was very shallow (the metallic nub, Figure B.1-A). As a result, the macro-mechanical interlocking between aluminum and the composite is less effective. In this case, the volume of the composite entrapped into the nub was 51 ± 15 mm^3 (Figure B.2-A) and the joints reached the lowest ultimate lap shear force (2456 ± 60 N) for the joining conditions studied in this work. The joint produced with the intermediate joining force (6 kN) presented a more pronounced deformation of the aluminum into the composite (Figure B.1-B). In this case, the deformation of aluminum into the composite retained the shape of two rings (ellipses in Figure B.2-B). This geometry provides two sites of macro-mechanical interlocking between aluminum and the composite, thereby maximizing the volume of the composite entrapped into the nub (84 ± 8 mm^3). Therefore, the highest mechanical performance of the joints (4068 ± 184 N) was achieved in this study. The aluminum deformation in the joint produced with a higher level of joining force (8 kN) resulted in the shape with only one wide ring (Figure B.1-C). Such geometry provides only one site for macro-mechanical interlocking between aluminum and composite (Figure B.2-C). Moreover, the volume of the composite entrapped into the nub was 62 ± 7 mm^3. Therefore, a decrease in ULSF was observed for the joint produced with 8 kN (3102 ± 199 N) compared to those produced with 6 kN.

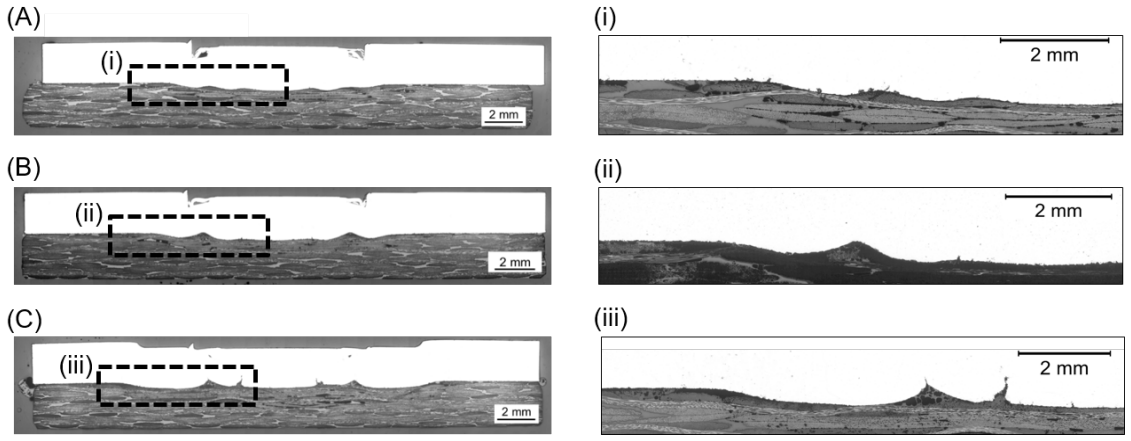

Figure B.1 Cross-sections of friction spot joints produced with (A) 4 kN, (B) 6 kN, and (C) 8 kN. Details of the metallic nubs are given in (i), (ii), and (iii) for the joints produced with 4, 6, and 8 kN respectively. (constant joining parameters RS: 1900 rpm, PD: 0.8 mm, JT: 4 s)

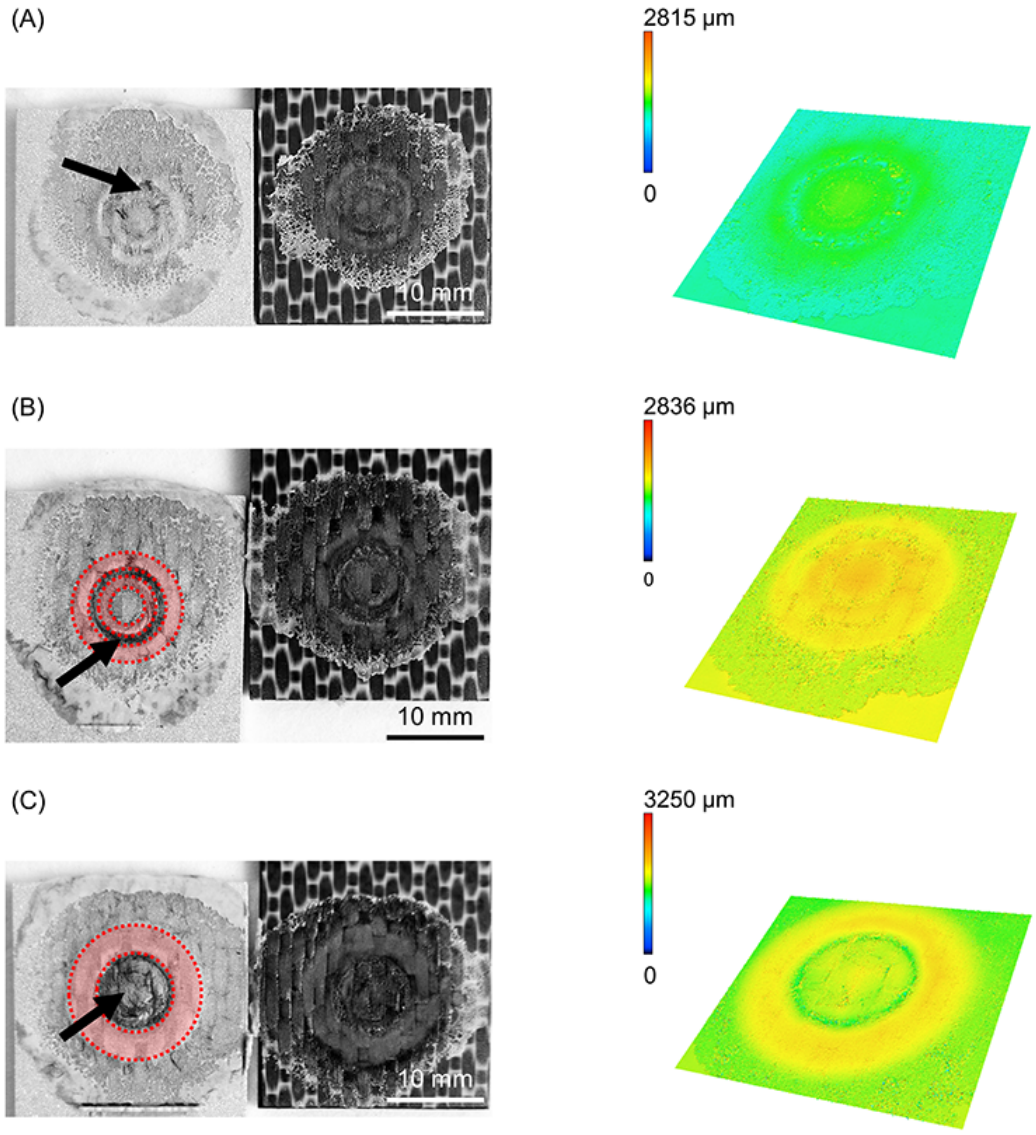

Figure B.2 Fracture surface and the 3D image of the deformation in the aluminum part (nub region) for joints produced with (A) 4 kN, (B) 6 kN, and (C) 8 kN of joining force. (constant joining parameters RS: 1900 rpm, PD: 0.8 mm, JT: 4 s)

It is worth noting that for all the joints investigated, the layer of reconsolidated molten PPS was formed and remained attached to the aluminum surface (Figure B.2), providing adhesion forces. Additionally, signs of fiber and matrix entrapment on the aluminum surface were also observed in all cases (black arrows in Figure B.2). These results indicate the importance of the nub geometry, its influence on the macro-mechanical interlocking between the joining parts, and hence, the mechanical performance of friction spot joints.

Appendix C: Identification of impact damage using ultrasonic scanning

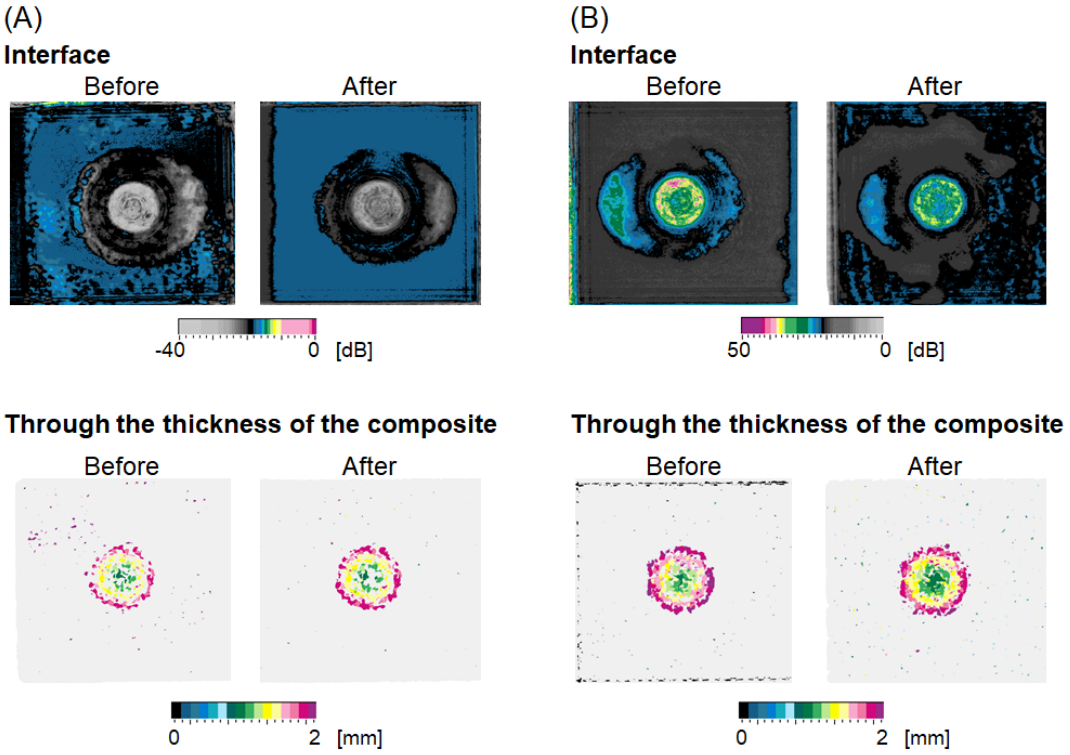

Figure C.1 C-scans of the overlap area of the joints before and after the impact energy of 2 J. (A) Impact from the aluminum side of the joints. (B) Impact from the composite side of the joints.

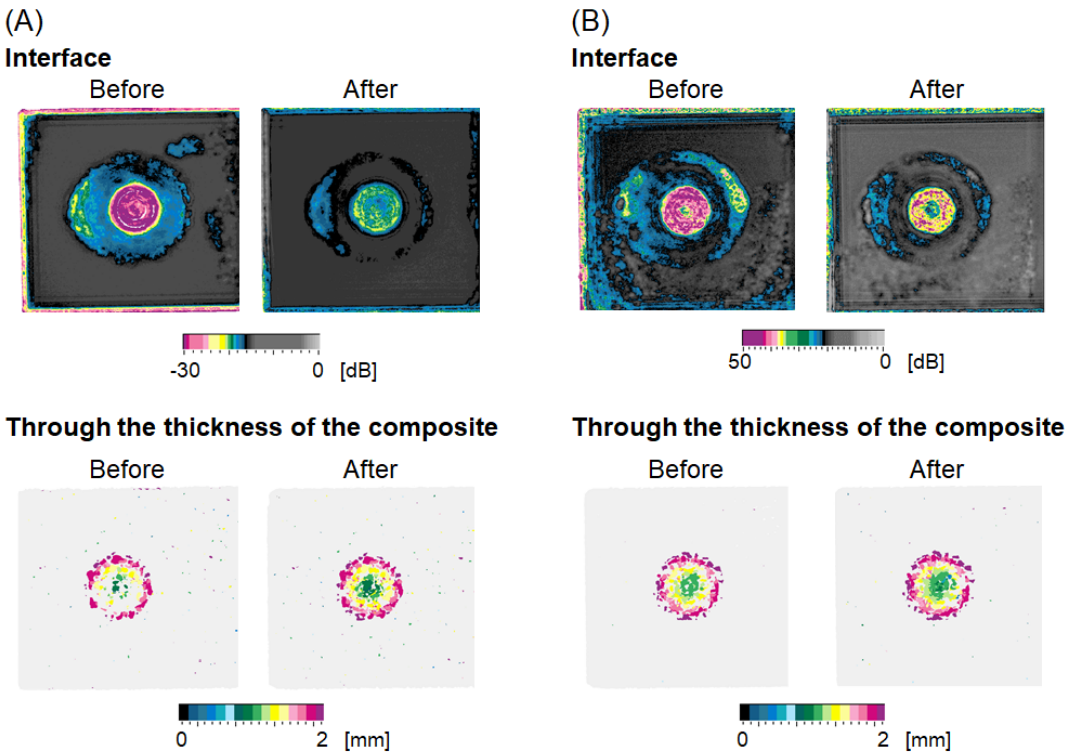

Figure C.2 C-scans of the overlap area of the joints before and after the impact energy of 4 J. (A) Impact from the aluminum side of the joints. (B) Impact from the composite side of the joints.

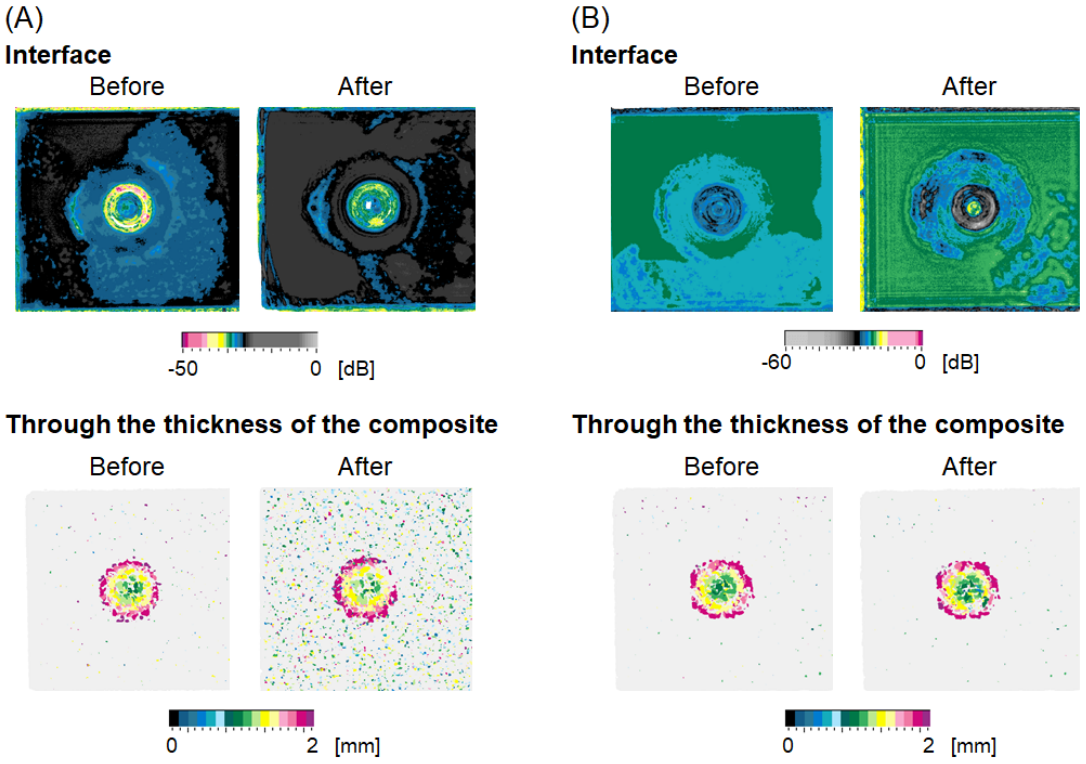

Figure C.3 C-scans of the overlap area of the joints before and after the impact energy of 6 J. (A) Impact from the aluminum side of the joints. (B) Impact from the composite side of the joints.

Appendix D: Replicates for mode-mixity analysis in single leg bending test

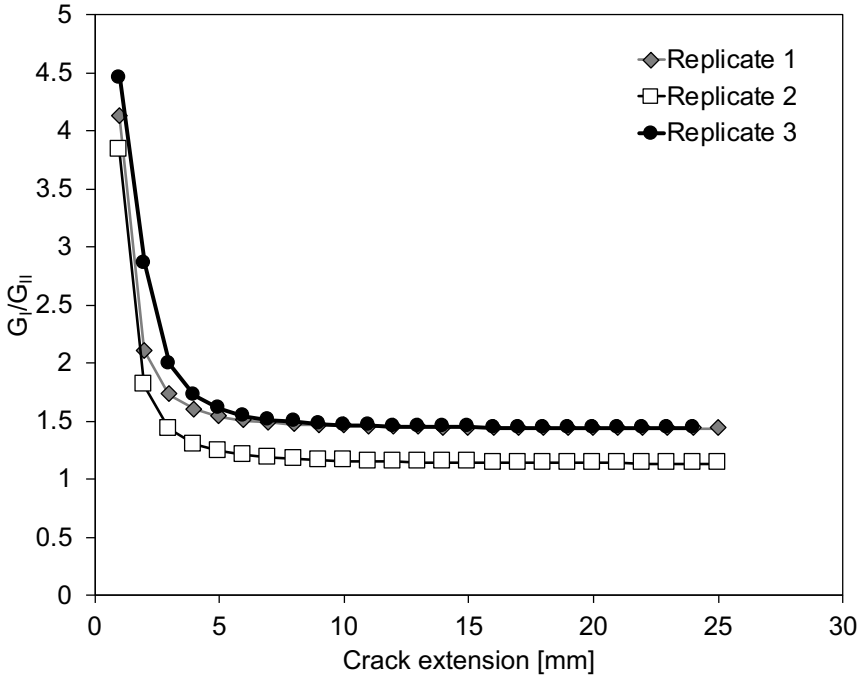

Figure D.1 Mode-mixity analysis for SLB test (static).

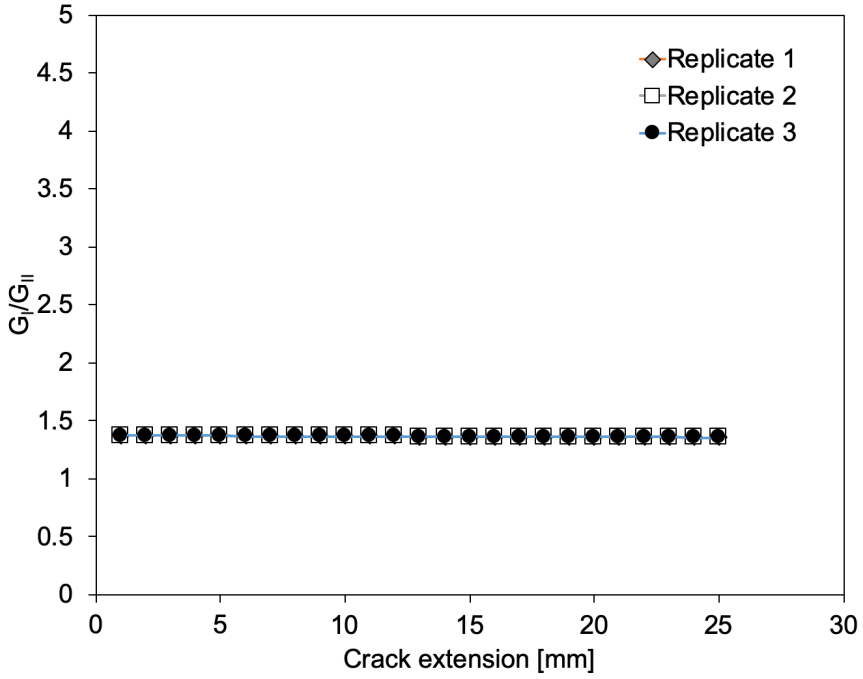

Figure D.2 Mode-mixity analysis for SLB test (fatigue).

Appendix E: Post-salt spray analysis of CF-PPS fracture surface

Figure E.1 shows the fracture surface of the composite after 6 weeks of exposure in salt spray; the worst condition studied in this investigation. Details are shown in Figure E.1-B-C. Figure E.1-D shows details of a fracture surface not exposed to salt spray for comparison. One observes that the profile of stretched PPS did not change after the exposure to salt spray. No superficial attacks or embrittlement signs of the PPS matrix were observed due to the exposure to salt spray.

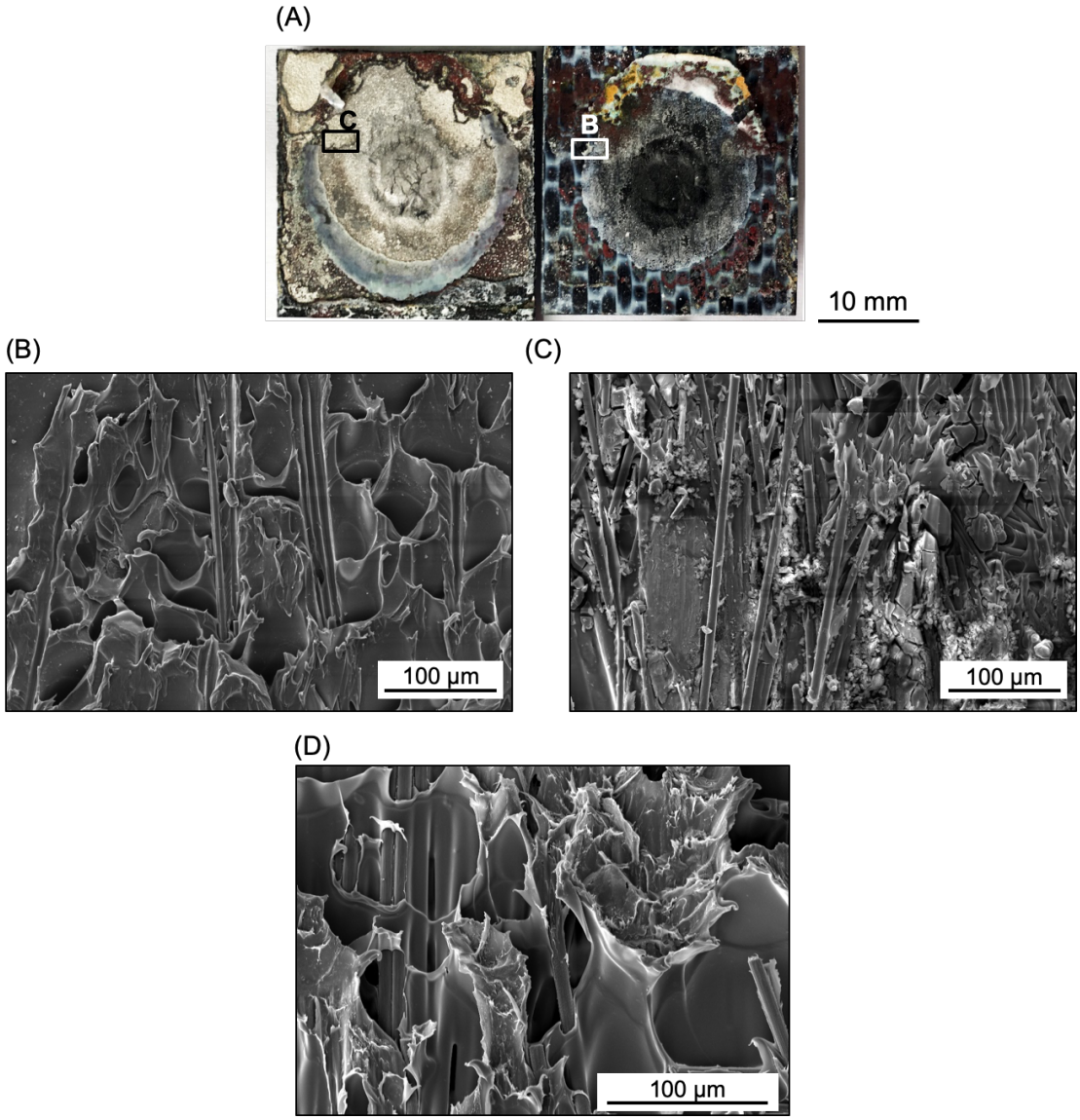

Figure E.1 (A) Overview of the fracture surface a friction spot joint after 6 weeks of salt spray exposure. (B) Detail of the fracture surface on the composite side of the joint. (C) Details of the fracture surface on the aluminum side of the joint. (D) Example of composite fracture surface before salt spray exposure.

Appendix F: Preliminary investigation on the residual stresses in friction spot joints

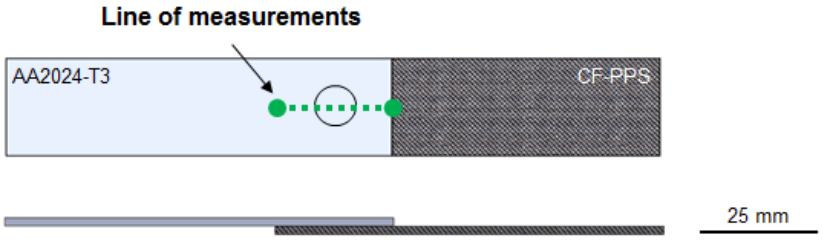

Figure F.1 Schematic illustration showing the central line where X-ray synchrotron diffraction was performed to measure the residual stresses in the joint.

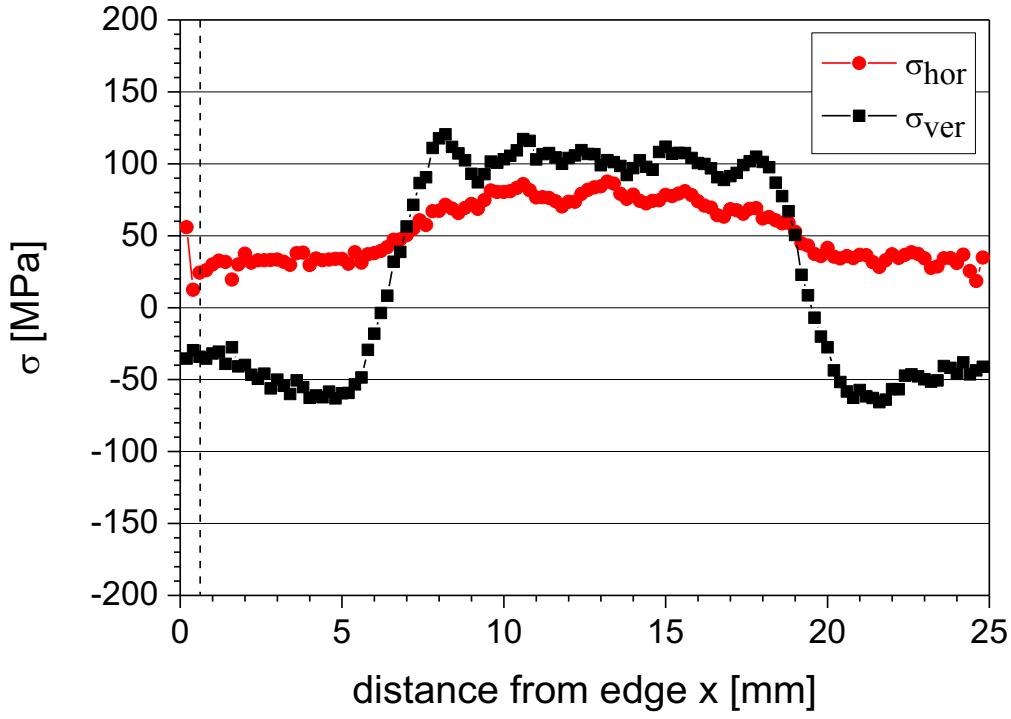

Figure F.2 Residual stresses obtained through X-ray synchrotron diffraction for a friction spot joint as joined. The highest stresses are located in the SZ of the joint.

Appendix G: Process parameter study for manufacturing the demonstrator

The FSpJ process parameters to join the demonstrator discussed in Chapter 10 were selected based on a one-factor-at-a-time approach as described in Table G.1. The joints were produced without any additional cooling or clamping ring. Nevertheless, the clamping ring was kept pressing the joint for 120 s (holding time) after the joining process to ensure pressure during the consolidation of the joint. The joining parameter C8 was selected based on the best superficial finish (flat and fulfilled keyhole).

Table G.1 One-factor-at-a-time approach to select the process parameters for the demonstrator discussed in Chapter 10.

Sample	Rotation Speed [rpm]	Plunge Depth [mm]	Joining time [s]	Joining Force [N]	Holding Time [s]
C1	1300	0.2	4	400	120
C2	1900	0.2	4	600	120
C3	1300	0.4	4	600	120
C4	1900	0.4	4	400	120
C5	1300	0.2	6	600	120
C6	1900	0.2	6	400	120
C7	1300	0.4	6	400	120
C8	**1900**	**0.4**	**6**	**600**	**120**

List of Figures

List of Tables